A Fundamental Study of $Pt_{100-x}Ni_x$ Nanoparticles: Synthesis and Characterization

Galina Tenkova Yavasheva

Master Thesis in Materials, Energy and Nanotechnology

60 credits

Department of Chemistry
Faculty of Mathematics and Natural Sciences

UNIVERSITY OF OSLO

May 2019

2019

A fundamental study of $Pt_{100-x}Ni_x$ nanoparticles: synthesis and characterization

Galina Tenkova Yavasheva

http://www.duo.uio.no/

Author Contribution

The candidate performed the following experiments and analysis:

- Kinetics experiments
- Synthesis of free-standing $Pt_{100-x}Ni_x$ NPs
- SEM imaging (DF-SEM and BF-STEM modes)
- In-house PXRD experiments and following data analysis
- Data analysis for providing histograms for particle sizes from BF-STEM images of $Pt_{100-x}Ni_x$ NPs
- Early in the master thesis, work on Au NPs was done, but this is not included in the main text and is reported in the Appendix (sections 9.3 and 9.4).

The candidate was supported on the following experiments:

- HAADF-STEM imaging and HAADF-STEM-EDX elemental mapping of free-standing NPs performed by PhD fellow Martin Jensen
- PPMS magnetization measurements by Dr. Susmit Kumar

Acknowledgements

I have had the great pleasure to be a part of the NAFUMA research group and to be introduced to the exciting process of scientific research during this Master thesis.

I would like to thank my supervisor Prof. Anja O. Sjåstad for excellent guidance and support throughout this master thesis. Sincerely thank you for the stimulating scientific discussions, insightful feedback and valuable advice. You have been a great source of inspiration and motivation.

I would also like to thank my co-supervisor PhD fellow Martin Jensen for exceptionally good training and guidance in the lab, for the work on the TEM, for many hours spent in intriguing discussions and for being a steady co-supervisor and a great colleague.

I would also like to thank Dr. Susmit Kumar for guidance with PPMS measurements and data analysis, Dr. David Wragg for the training and guidance with XRD measurements and data analysis, Dr. Kristian Lausund for training me on the SEM and Diamanta Ibishi and Sajjad Ahmadi for the uplifting conversations and good times in the office.

Last, but not least, a thank you to my parents, my sister and my partner, Vetle Løveng, for always believing in me and the many motivational talks during hard times. To my closest friends, Genoveva Yordanova and Karmil Marthinsen, thank you for the constant support.

Galina Tenkova Yavasheva

Abstract

In this master thesis, NPs with nominal composition $Pt_{100-x}Ni_x$ (x = 0, 10, 20, 30, 40, 50, 60, 70, 80, 90, 100) were produced via a polyol synthesis method. $Pt(acac)_2$ and $Ni(acac)_2$ were used as metal precursors, 1,4-BD as a solvent and PVP10 as a surfactant. A set of conditions referred to as our standard are: a total amount of 0.2 mmol of metal ions, 20 mL of solvent, metal ions/PVP monomer ratio 1/10, synthesis –temperature and –time 220 ^{0}C and 120 min, respectively.

All as-synthesized NPs were characterized by SEM (BF-STEM) imaging and particle size histograms were prepared. It was found that all bimetallic NPs gave bi- or trimodal particle size distributions. The overall trend is that average particle size and the difference between the particle size modes increase with increasing atomic % Ni in the nominal composition. The $Pt_{80}Ni_{20}$ NPs were found to be the most homogeneous of the samples series with respect to particle size. Further, characterization by PXRD was done for all as-synthesized NPs. The measurements in combination with Rietveld refinement revealed that all bimetallic samples contain multiple phases, all of the ccp-type. Hence, it was concluded that solid solution is not formed. PXRD did not provide information on the element distribution in the NPs.

HAADF-STEM-EDX-elemental mapping was performed on selected $Pt_{100-x}Ni_x$ NPs (x = 10, 50 and 90) to gain more insight to their element –composition and –distribution. It was found that core@shell configuration is formed in all investigated batches. It was noticed that the larger NPs are richer in Ni-content than the smaller ones in the same sample, which suggests that the Ni-metal precursors, $Ni(acac)_2$, has a faster kinetics than the Pt one, $Pt(acac)_2$. Additionally, the NPs become more heterogeneous with respect to element distribution with increasing atomic % Ni in their nominal composition.

The reduction kinetics of $Pt(acac)_2$ and $Ni(acac)_2$ towards formation of the monometallic NPs were explored and visual analysis combined with SEM imaging revealed that $Ni(acac)_2$ has a faster kinetics than $Pt(acac)_2$. Furthermore, attempts to modify the reduction kinetics of the Ni-precursor were done by changing the solvent from 1,4-BD to EG, the surfactant from PVP10 to PVP55 as well as NaOH was added. However, it was concluded that the standard polyol route gave most well-defined samples.

Further, the kinetics of formation of the bimetallic NPs was studied for the nominal composition $Pt_{50}Ni_{50}$. By collecting samples at 0, 15, 30, 60 and 120 minutes during the propagation of the

reaction. It was found by SEM imaging-histogram analysis that NPs from the first four samples give bimodal particle size distributions whereas the NPs from the last one gives a trimodal particle size distribution. Additionally, it was noticed that the ratio small/large NPs increases with increasing synthesis time, indicating that nucleation does not occur as a single event.

Following these findings, an attempt at modifying the reaction kinetics was made for the $Pt_{10}Ni_{90}$ NPs by changing the metal/PVP monomer ratio from 1/10 to 1/100. Analysis by SEM (BF-STEM) and TEM (HAADF-STEM-EDX) showed that an improved sample quality was obtained with respect to particle size distribution, but the produced NPs still gave phase segregation, i.e. a core@shell element distribution.

Magnetic measurements performed by PPMS on selected $Pt_{100-x}Ni_x$ NPs (x = 0, 10, 50, 90 and 100) showed diamagnetic signal for Pt NPs whereas the remainder of the analyzed samples give a saturation magnetization. This indicates that the alloyed NPs have at least one phase, which is ferromagnetic/superparamagnetic. Additionally, it was observed that the saturation magnetization increases with increasing atomic % Ni in the nominal composition, which shows that the metallic properties of ferromagnetic/superparamagnetic Ni are reflected in the bimetallic NPs.

Abbreviations

Ac – Acetate

Acac – Acetylacetonate

ADF – Annular dark-field

BD – Butanediol

BF / DF (SEM/TEM) – Bright-field / Dark-field

BSE – Backscattered electrons

CCP – cubic close packing

CTAB – Cetyltrimethylammonium bromide

CTAC – Cetyltrimethylammonium chloride

EDS – Energy dispersive X-ray spectroscopy

EG – Ethylene glycol

Et-OH – Ethanol

Exp. no. – Experiment number

HAADF (-STEM) – High angle annular dark-field

HCP – hexagonal close packing

Hfac – Hexafluoroacetylacetonate

HOPG – Highly Ordered Pyrolytic Graphite

MWCNTs – Multi-walled carbon nanotubes

Ni@Pt (NP) – core-shell structure with Ni in the core and Pt in the shell

Nominal comp. – Nominal composition

NP – Nanoparticle

PVP – Polyvinylpyrrolidone

Prec. – precursor

PXRD – Powder x-ray diffraction

RT – Room temperature

SE – Secondary electrons

SEM – Scanning electron microscopy

STEM – Scanning transmission electron microscopy

Synth. temp. – Synthesis temperature

TEM – Transmission electron microscopy

XRD – X-ray diffraction

Table of Contents

1 Introduction

The main objectives of this master thesis are to establish a synthesis route for the formation of $Pt_{100-x}Ni_x$ NPs and to explore their properties through a combination of relevant analysis techniques. In this section, a brief introduction to nanoparticles is given, including history and some changes in properties of bulk materials when they are confined to the nanoscale, followed by a limited review of literature on the formation and properties of free-standing Pt and Ni NPs via the polyol synthesis route. Then, important aspects of the Pt-Ni system in bulk materials and a more extensive literature evaluation on the formation and properties of $Pt_{100-x}Ni_x$ NPs are presented. The section ends with the motivation for this master thesis.

1.1 Change in Properties from Bulk to Nano

Materials which have at least one dimension confined to the nanoscale (typically from 1 nm to 100 nm) are defined as nanomaterials [1, p. 1]. This master thesis explores the preparation and properties of zero-dimensional nanomaterials, which means they are confined to the nanoscale in all three dimensions. These are also known as Nanoparticles (NPs) and nanocrystals in the case when they are crystalline. The history of NPs can be traced back to the Roman period where they prepared colloidal suspensions of metal NPs and used them to dye glass and fabrics. However, there was no understanding of nanoscale phenomena until much later when studies started appearing. In the seventeenth century, the preparation of colloidal gold suspension was described by an Italian priest, Antonio Neri in the work *L'Arte Vetraria* (The art of glass). The basis for understanding the behavior of colloidally dispersed metal NPs was established by Michael Faraday in 1857 [2] when he identified the formation of very small particles, which are thermodynamically unstable and must be stabilized against aggregation. Nowadays, there is extensive research on the formation of NPs via various synthesis routes and the understanding of their properties. The tremendous interest in nanomaterials originates from the size-dependency of their characteristic optical, electronic, magnetic, and chemical properties [3, p. 1-3]. The reasons for the significant changes in these properties are increase in specific surface area and appearance of quantum effects when going from the bulk material to the nanoscale [4, p. 16].

In chemistry and solid-state physics, it is common to assume that interfaces are absent and the reason for this is that the processes, which take place on the surface of a material, are different than the ones in the bulk. This approximation is only valid for bulk materials, in which the surface atoms make up a very small portion of the mass. In nanomaterials, a large portion of the constituent atoms are on the surface and Figure 1.1-1 illustrates the increase in ratio of surface/bulk atoms for a spherical NP with decreasing diameter [5, p. 12-13]. Hence, nanomaterials can have extremely large surface area per mass, i.e. specific surface area.

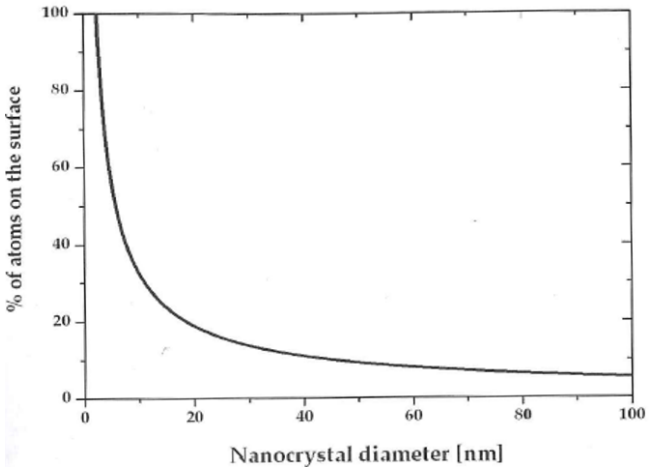

Figure 1.1-1: Approximated percentage of surface atoms as a function of particle size, assuming spherical NPs of PbS [5, p. 13]

Surface atoms possess unsatisfied bonds, aka dangling bonds, which have a partial electric charge and this results in surfaces having higher energy than the bulk. Nature tries to reduce the material's energy by saturating the surface bonds whereas we, as chemists, like to use them as reaction seats for targeted surface reactions. Naturally, the larger number of dangling bonds, the more reactive a material is and thus, reactivity increases with increasing surface area [5, p. 12-13]. Hence, NPs have a significantly higher efficiency for processes involving surface reactions like sensing and catalysis compared to the one of the same amount of bulk material [4, p. 16], [5, p. 17]. However, the preparation of nanoscale materials can be seen as trying to fight nature as they are not thermodynamically stable and hence, special techniques must be used to control the surface energy [5, p. 15]. In alloyed NPs, surface segregation can occur where one of the elements, which has lower surface energy, is diffused to the surface of the particles. This can result in a structure, denoted as core@shell, in which one phase is in the core

and another one is a shell. The change in element distribution in the NPs changes the properties of the NPs [5, p. 17].

Nanomaterials have sizes in the intermediate region between bulk and molecular systems and they exhibit a mixture of classical and quantum behavior. Generally, a property change is observed when the size of the object it affects becomes comparable to the dimension the property operates at [5, p. 21]. Hence, the influence of quantum effects becomes increasingly significant with decreasing particle size. An example is the weak intermolecular Van der Waals forces, which can cause NPs to agglomerate. They originate from the instantaneous shifts in electron density, which cause transient charge polarity in molecules, which in turn causes the attraction to a positive charge and repulsion by a negative charge. Agglomeration must be avoided in the preparation of nanomaterials, because it decreases the surface area of the material and thus, the properties are altered [4, p. 16].

Another example is the plasmon resonance effect, which gives rise to a variety of colors for metallic NPs. Metals have surface plasmons, which are defined as the collective oscillation of the sea of delocalized electrons and these are confined in metallic nanocrystals. Photons of a certain wavelength, which excite the surface plasmon at its resonance frequency, are absorbed whereas the rest are not. The absorbed wavelength decreases with decreasing size of the NPs. Metallic NPs have been used to stain glass because of this effect [3, p. 19-20].

Shape of nanoscale materials also affects size-dependent properties. An example is colloidal Au NPs. When it is reduced to the nanoscale, gold loses its metallic sheen and has bright colors, which originate from the plasmon resonance effect. Spherical NPs have a single resonance frequency whereas nanorods have two, transverse and longitudinal, corresponding to their diameter and length, respectively. Hence, nanorods have very different color [5, p. 22, 24].

Superparamagnetism is another quantum effect, which arises when the size of a ferromagnetic/ferrimagnetic material decreases to the nanoscale. The reason for this is the existence of magnetic domains in the nanoscale, i.e. regions in which magnetic dipoles are oriented in the same direction, and a NP becomes superparamagnetic when its size is comparable to that of the domains. Ferroelectrics behave in a similar way when size is decreased [5, p. 21].

1.2 Previous Work on Pt and Ni NPs

An overview of previous work on the production and characterization of Pt and Ni NPs is given in this section. Listed in Table 1.2-1 are the experimental details and some reported results on free-standing monometallic NPs prepared via the polyol method with the surfactant PVP. A more extensive literature review on the alloyed NPs will be presented in section 1.3.

Table 1.2-1: Previous work on free-standing Pt and Ni NPs prepared via the polyol route with the surfactant PVP. The following information is given: Metal precursor, solvent, additive, metal ions/PVP monomer molar ratio, metal ions/additive molar ratio, synthesis –temperature and –time, reported particle –morphology and –size, reported unit cell length and magnetism. See explanations of the alphabetical superscripts at the bottom of the table.

Reference	Metal precursor	Surfactant	Solvent	Additive	Metal ions/PVP monomer	Metal ions/additive	Synthesis temp. [°C]	Synthesis time [min]	Particle morphology	Particle size [nm]	Unit cell length [Å]	Magnetism
Alayoglu et al. [6]	$PtCl_2$	PVP55	EG	-	1/2.5	-	-	60	-	5.7	-	-
	H_2PtCl_6	-			-		130-180	120		2.2		
Bundli [7]	$Pt(acac)_2$	PVP10	1,4-BD	-	1/10	-	220	120	-	16.2 ± 5.2	-	-
Jensen [8]	$Pt(acac)_2$	PVP10	1,4-BD	-	1/10	-	220	120	-	17 ± 5	3.9228 ± 0.0009	-
Papa et al. [9]	H_2PtCl_6	PVP8	EG	NaOH	1/10	1/6.6	120	60	-	4.9	3.917	-
Long et al. [10]	$H_2PtCl_6{\cdot}6H_2O$	PVP55	EG	$AgNO_3$	1/12	1/0.16	160	10-30[a]	triangular plates and tetrahedra	< 35	-	-
									octahedra and bipyramids	20-30		
									nanorods	25		
Song et al. [11]	$H_2PtCl_6{\cdot}6H_2O$	PVP55	EG	$AgNO_3$	1/12	1/0.01	197[b]	16[a] + 5	cubes	9.4 ± 0.6	-	-
						1/0.11			cuboctahedra	9.1 ± 0.6		
						1/0.32			octahedra	9.8 ± 0.6		
Bathla et al. [12]	$NiCl_2{\cdot}6H_2O$	PVP[c]	EG	$NaBH_4$	1/1	≈ 1/25	140	120	-	10-12	-	Hc = 58.24 Oe
					1/3					7-9		Hc = 81.96 Oe
					1/5					3-5		Hc = 137.29 Oe

Tripathi et al. [13]	$Ni(Ac)_2{\cdot}4H_2O$	PVP[c]	EG	-	1/2.5	-	-	1080	-	29	3.526	-
					1/5			1200		28		
					1/7.5			1440		27		
					1/10			900		23		
Neiva et al. [14]	$Ni(Ac)_2{\cdot}4H_2O$	PVP[c]	EG	$NaBH_4$	1/3.2	1/4	140	120	-	3.4	-	-
						1/8				2.8		
						1/12				2.2		
Couto et al. [15]	$NiCl_2{\cdot}6H_2O$	PVP[c]	EG	$NaBH_4$	0	≈ 1/1200	140	120	-	7.7	-	-
					1/0.1					3.7		
					1/0.5					3.6		
					1/1					3.6		Superpara-magnetic-like
					1/5					3.4		-

[a]Metal precursor added in steps during the given period of time
[b]Temperature is given as the boiling point of EG
[c]Type of PVP is not specified

Upon close inspection of Table 1.2-1, it is noticed that Pt NPs formed following the polyol synthesis route in the presence of PVP are often reduced from the metal precursor $H_2PtCl_6 \cdot 6H_2O$ in the solvent EG at elevated temperature between 120-197 °C with varying synthesis time.

Further, additional chemicals such as NaOH and $AgNO_3$ are used for pH-regulation and as structure-modifying agent, respectively. When the latter is used, the produced NPs form with polyhedral shapes and attempts at controlled morphology have been made by Long et al. [10] and Song et al. [11]. In the work of Long et al. [10], Pt NPs with sharp polyhedral morphology were prepared at 160 °C via stepwise addition of metal precursor and they attempted to optimize these steps. On the other hand, Song et al. [11] were successful to control the NPs' morphology through variation in the ratio of metal ions/$AgNO_3$. The produced Pt NPs were cubes, cuboctahedra and octahedra with increasing ratio from 1/0.01 to 1/0.32.

Finally, in our research group, Pt NPs have been previously prepared from reduction of $Pt(acac)_2$ in the solvent 1,4-BD with surfactant PVP10 (metal ions/PVP monomer ratio 1/10) via a polyol route at 220 °C for 120 min by Bundli [7] and Jensen [8]. NPs with average sizes 16.2 ± 5.2 and 17 ± 5 were produced in the two works, respectively.

Table 1.2-1 shows that free-standing Ni NPs produced from the polyol method in the presence of PVP are often reduced from the metal precursors $NiCl_2 \cdot 4H_2O$ and $Ni(Ac)_2 \cdot 4H_2O$ in the solvent EG with an additional reducing agent $NaBH_4$ at 140 °C and synthesis time 120 min.

Further, Tripathi et al. [13] varied the molar ratio of metal ions/PVP monomer from 1/2.5 to 1/10 and the synthesis time from 1080 min to 900 min, respectively, and observed that the size of the prepared Ni NPs decreased from 29 nm to 23 nm. In the works of Bathla et al. [12] and Couto et al. [15], the molar ratio of metal ions/PVP monomer was varied similarly from 1/1 to 1/5 and from 1/0.1 to 1/5, respectively. Their findings confirm that the size of the prepared NPs decreases with increasing amount of PVP. In addition, Couto et al. [15] prepared NPs without the addition of PVP and they observed that the resulting size was 7.7 nm, which is a significantly larger than the size of 3.7 nm from the Ni NPs prepared with 1/0.1 ratio of metal ions/PVP monomer. On the other hand, the team of Neiva et al. [14] controlled the size of the Ni NPs from 3.4 nm to 2.2 nm through variations of the ratio of metal ions/$NaBH_4$ from 1/4 to 1/12. This suggests that the use of a larger amount of reducing agent increases the kinetics of NP formation.

Finally, the findings of Couto et al. [15] suggest a superparamagnetic-like behavior for the prepared Ni NPs (3.6 nm) with metal ions/PVP monomer ratio 1/1. This behavior is similar to that of several small superparamagnetic NPs, which form a larger 'apparent particle'. Further, Bathla et al. [12] revealed ferromagnetic behavior for the synthesized Ni NPs with increasing coercive field from 58 Oe to 137 Oe for decreasing particle size.

1.3 The Pt-Ni System

In this section some aspects of the Pt-Ni system are presented starting with the Pt-Ni phase diagram and reported lattice constants for various element compositions in the bulk alloy, followed by a literature review on the synthesis and characterization of $Pt_{100-x}Ni_x$ NPs.

1.3.1 Phase Diagram and Lattice Constants of Bulk $Pt_{100-x}Ni_x$

Nash and Singleton [16] derived a phase diagram of the bulk Pt-Ni system (Figure 1.3-1) based on previous reports and the thermodynamic calculations from that work. The liquidus has a shallow minimum at around 22.5 atomic % Pt and 1437 ^{0}C. The system has complete solid solubility at high temperature while there are two ordered phases below ≈ 700 ^{0}C. The ordered Pt-Ni phases have element composition ratios 1:1 and 1:3 and their critical temperatures are 645 ^{0}C and 580 ^{0}C, respectively. At lower than 30 atomic % Pt, the Pt-Ni solid solution is ferromagnetic and at higher atomic % Pt, the solid solution is a Pauli paramagnet. The variation of Curie temperature with atomic % Pt is reported to be approximately $T_c = 354.3\ ^0C - 9.413 * X_{Pt}$.

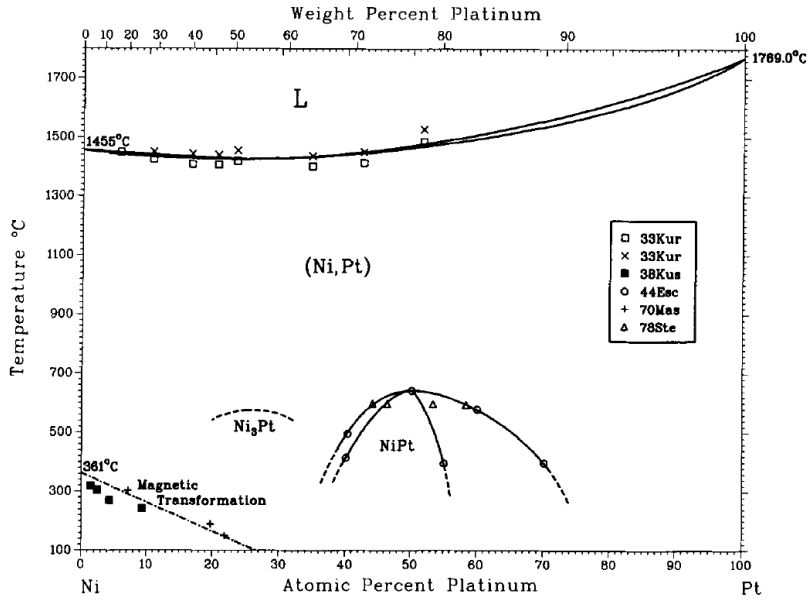

Figure 1.3-1: Pt-Ni binary phase diagram. The figure is taken from literature [16].

In table 1.3-1 are the previously reported Pt-Ni phases for bulk alloys listed. It can be noticed that pure cubic-close packed (ccp) Pt and ccp Ni have quite different *a*-axis lengths – 3.921 Å and 3.534 Å, respectively. Further, the lattice parameters for the alloyed phases have decreasing values with increasing atomic % Ni.

Table 1.3-1: Previously reported phases of bulk Pt-Ni alloys. In this table, the following information is given: Nominal composition, space group and unit cell dimensions of the Pt-Ni phase.

Reference	Element composition	Space group	Unit cell length [Å]
Manoun et al. (2005) [17]	Pt	Fm-3m	3.921
Jeon et al. (2009) [18]	$Pt_{28}Ni_{72}$	Fm-3m	3.743
Mishima et al. (1985) [19]	$Pt_{25}Ni_{75}$	Fm-3m	3.652
Buschow et al. (1983) [20]	$Pt_{8}Ni_{92}$	Fm-3m	3.564
Nikiforov et al. (2013) [21]	Ni	Fm-3m	3.534

1.3.2 Previous work on $Pt_{100-x}Ni_x$ NPs

In this section, a literature review on previous work on the formation and characterization of $Pt_{100-x}Ni_x$ NPs is given. In Table 1.3-1 are the experimental details and some of the reported results on both free-standing and supported alloyed NPs listed. The studies are sorted with focus on the polyol method as it is the one utilized in the practical work of this master thesis.

Table 1.3-2: Previous work on $Pt_{100-x}Ni_x$ NPs. In this table, the following information is given: Synthesis method (where FS – free-standing and OS – on substrate), precursors (in the order: metal precursors, surfactant, solvent, reducing agent, acid/base for pH regulation, substrate), synthesis –temperature and –time (for the specific step when bimetallic NPs are formed), nominal composition of the NPs, reported element distribution, reported particle –morphology and –size, reported unit cell length and control parameter. See explanations of the alphabetical superscripts at the bottom of the table.

Reference	Synthesis method		Precursors	Synthesis temperature [°C]	Synthesis time [min]	Nominal composition	Element distribution	Particle morphology	Particle size [nm]	Unit cell length [Å]	Control parameter
Galhardo et al. [22] (2018)	FS[a]	modified polyol	H_2PtCl_6, $NiCl_2$	160	180	$Pt_{75}Ni_{25}$	solid solution	-	2.5 ± 0.7	-	-
			EG								
		microwave-assisted polyol	Same	160	6				1.9 ± 0.5		
Jiang et al. [23] (2010)	FS[a]	modified polyol	$H_2PtCl_6{\cdot}6H_2O$, $Ni(NO_3)_2{\cdot}6H_2O$	180	240	$Pt_{75}Ni_{25}$	solid solution	-	2.8	3.90	-
			EG			$Pt_{67}Ni_{33}$			2.7	3.85	
			NaOH			$Pt_{50}Ni_{50}$			3.3	3.81	
Bao et al. [24] (2013)	FS[a]	modified polyol	$H_2PtCl_6{\cdot}6H_2O$, $Ni(NO_3)_2{\cdot}6H_2O$	180	240	$Pt_{75}Ni_{25}$	quasi core-shell (Pt@NiOx)	-	2.8	3.92	-
			EG			$Pt_{67}Ni_{33}$	solid solution		3.2	3.86	
			NaOH			$Pt_{50}Ni_{50}$			3.4	3.81	
Rudi et al. [25] (2012)	FS[a]	modified polyol	$H_2PtCl_6{\cdot}6H_2O$, $Ni(NO_3)_2{\cdot}6H_2O$	160	20	$Pt_{84}Ni_{16}$	solid solution	-	2.0 ± 0.6	-	-
			EG								
			NaOH, H_2SO_4								

			$Pt(acac)_2$, $Ni(ac)_2{\cdot}4H_2O$	200	60	$Pt_{32}Ni_{68}$			3.7 ± 1.0		
			1,2-tetradecanediol, diphenyl ether, 1,2-dichlorobenzene			$Pt_{26}Ni_{74}$			5.7 ± 0.7		
			oleyamine			$Pt_{14}Ni_{86}$			6.0 ± 0.8		
			oleic acid								
Xu et al. [26] (2012)	FS	modified polyol	H_2PtCl_6, $NiCl_2$	room temperature	20	$Pt_{80}Ni_{20}$	solid solution	-	-	-	-
			CTAB			$Pt_{75}Ni_{25}$				3.80	
			EG, Milli-Q water			$Pt_{67}Ni_{33}$				-	
			$NaBH_4$			$Pt_{50}Ni_{50}$					
Chen et al. [27] (2008)	FS	modified polyol	H_2PtCl_6, $Ni(ac)_2$	138	30	$Pt_{17}Ni_{83}$	core-shell	irregular polyhedrons	5.4	-	-
			1,2-PD								
			KBH_4								
			NaOH, oleic acid								
Wan et al. [28] (2014)	FS	one pot reduction	$H_2PtCl_6{\cdot}6H_2O$, $Ni(NO3)_2{\cdot}6H_2O$	230	10	$Pt_{75}Ni_{25}$	solid solution	urchin-like	60 ± 12	3.86	-
						$Pt_{50}Ni_{50}$			59 ± 6	3.75	
			ODA			$Pt_{25}Ni_{75}$			57 ± 8	3.67	
Carpenter et al. [29] (2012)	FS[a]	solvothermal	$Pt(acac)_2$, $Ni(acac)_2$	200	1440	$Pt_{75}Ni_{25}$	solid solution	cubes and cubocta-hedra	5.5	3.84	-
						$Pt_{67}Ni_{33}$	solid solution (2 phases)	-	3.1	3.86	
						$Pt_{60}Ni_{40}$			4.0	3.86	
			DMF			$Pt_{50}Ni_{50}$		octahedra and truncated octahedra	6.7	3.83	
						$Pt_{33}Ni_{67}$		-	3.8	3.79	
	FS		$Pt(acac)_2$, $Ni(acac)_2$	120	-	$Pt_{30}Ni_{70}$	-	-	-	-	

Ma et al. [30] (2018)		microwave-assisted solvothermal	DMF	140			solid solution	concave octahedra			temperature - to vary particle shape and degree of alloying
				160				octahedra			
				180			solid solution + Ni phase	-			
				190				octahedra with rounded corners			
				200			solid solution	-			
Banik et al. [31] (2016)	FS	aqueous reduction	$NiCl_2$, K_2PtCl_6	60	-	$Pt_{90}Ni_{10}$	solid solution	-	-	3.89	-
			Millipore water			$Pt_{80}Ni_{20}$				3.84	
						$Pt_{70}Ni_{30}$				3.80	
						$Pt_{50}Ni_{50}$		spherical	54	3.70	
			$NaBH_4$			$Pt_{30}Ni_{70}$		-	-	3.62	
						$Pt_{10}Ni_{90}$				3.51	
Kyung-Won et al. [32] (2002)	FS	aqueous reduction	$H_2PtCl_6 \cdot xH_2O$, $NiCl_2 \cdot 6H_2O$	room temperature	-	$Pt_{75}Ni_{25}$	solid solution + Ni oxides	-	-	-	-
			Millipore water			$Pt_{50}Ni_{50}$			3.5 ± 0.5		
			$NaBH_4$								
Du et al. [33] (2015)[c]	FS	galvanic displacement reaction and	K_2PtCl_6, $NiCl_2$	75	120	$Pt_{67}Ni_{33}$	solid solution	spherical	53	-	temperature - to vary size and composition
			PVP								
			H_2O								

		aqueous reduction	$NaBH_4$								
Zhang et al. [34] (2016)	FS	one pot reduction	$Pt(acac)_2$, $Ni(acac)_2$ FPD CO	210	60 2 + 58 4 + 56 10 + 50 20 + 40 60	$Pt_{75}Ni_{25}$	solid solution	-	8.2 6.3 6.3 6.4 6.5 6.4	-	CO exposure time - to vary particle size and shape
Santos et al. [35] (2006)	FS[a]	micro-emulsion reduction	H_2PtCl_6, $NiCl_2{\cdot}6H_2O$ heptane, water Brij 30	-	-	$Pt_{90}Ni_{10}$ $Pt_{75}Ni_{25}$ $Pt_{60}Ni_{40}$	solid solution	-	3.8 ± 0.8 3.6 ± 0.8 4.7 ± 0.9	3.84 3.82 3.82	-
Hwang et al. [36] (2015)	FS	one pot thermal decomposi-tion	$Pt(acac)_2$, $Ni(acac)_2$ CTAC 1-octadecene oleyamine oleic acid	250	180	$Pt_{96}Ni_4$ (core) $Pt_{71}Ni_{29}$ (shell)	solid solution core-shell	nano-dendrites	45.7	-	time and concentration of CTAC - to vary degree of alloying
Kim et al. [37] (2006)	FS	γ-irradiation	H_2PtCl_6, $NiCl_2$ PVP distilled water	-	-	$Pt_{80}Ni_{20}$ $Pt_{60}Ni_{40}$ $Pt_{40}Ni_{60}$ $Pt_{20}Ni_{80}$	solid solution	-	-	-	-
Kozejova et al. [38] (2017)[c]	FS	potentio-static electro-deposition	K_2PtCl_4, $NiCl_2$ deionized water NaCl, HCl, NaOH	-	-	Pt75Ni25 Pt25Ni75	solid solution	irregular, torn-like spherical	164 133	-	time - to vary size and density of NPs
Lee et al. [39] (2014)	OS	ultrasound-assisted polyol	$Pt(acac)_2$, $Ni(acac)_2$ EG Ketjen Black 300 J	room temperature	180	$Pt_{50}Ni_{50}$	core-shell	truncated octahedra	3.1 ± 0.5; (shell = 0.5 nm)	3.84	Ni precursors - to vary particle shape and shell thickness

			Same, except $Ni(hfac)_2$ instead of $Ni(acac)_2$			$Pt_{50}Ni_{50}$		octahedra	3.8 ± 0.6; (shell = 0.8 nm)	3.80	
Rusnaeni et al. [40] (2010)	OS	modified polyol	H_2PtCl_6, $NiCl_2{\cdot}6H_2O$	190	120	$Pt_{31}Ni_{69}$	solid solution	-	-	-	pH - to vary particle size and nominal composition
			EG			$Pt_{23}Ni_{77}$			5.7	3.64	
			NaOH			$Pt_{18}Ni_{82}$			5.5	3.64	
			Vulcan XC 72R			$Pt_{13}Ni_{87}$			-	-	
Lin et al. [41] (2018)	OS	microwave-assisted solvothermal	$Pt(acac)_2$, $Ni(ac)_2{\cdot}4H_2O$	-	33	$Pt_{25}Ni_{75}$	solid solution	octahedra and tetrahedra; corners round off with time	6.9	-	number of pulses - to vary particle shape
			EG		40				8.5		
			PPDA		50				8.9		
			Vulcan XC 72R		60				9.2		
Xiong et al. [42] (2013)	OS	modified polyol	H_2PtCl_6, $NiSO_4$	70	180	$Pt_{80}Ni_{20}$	solid solution	-	4.7	3.84	-
			EG			$Pt_{75}Ni_{25}$			-	3.82	
			$NaBH_4$								
			NaOH			$Pt_{67}Ni_{33}$			-	3.83	
			functionalized MWCNTs			$Pt_{50}Ni_{50}$			4.0	3.78	
Veera Manohara Reddy et al. [43] (2018)	OS	modified polyol	$H_2PtCl_6{\cdot}6H_2O$, $NiCl_2{\cdot}6H_2O$	120	120	$Pt_{50}Ni_{50}$	solid solution	-	4.5	-	-
			EG								
			KI								
			ascorbic acid								
			GO								
Wang et al. [44] (2015)	OS	modified polyol	$H_2PtCl_6{\cdot}6H_2O$, $Ni(NO_3)_2{\cdot}6H_2O$	room temperature	240	$Pt_{75}Ni_{25}$	solid solution	-	2.9 ± 0.5	-	-

			glycerol $NaBH_4$ HCl Vulcan XC-72			$Pt_{67}Ni_{33}$ $Pt_{50}Ni_{50}$			2.7 ± 0.4 2.4 ± 0.3		
Yano et al. [45] (2007)	OS	modified polyol	$Pt(acac)_2$, $Ni(acac)_2$ 1,2-hexadecanediol, diphenyl ether oleyamine, $LiBEt_3H$ oleic acid Ketjen Black EC	270	30	$Pt_{50}Ni_{50}$	solid solution	-	2.5	3.78 ± 0.01	-
Chiwata et al. [46] (2016)	OS	modified polyol[b]	$Pt(acac)_2$, $Ni(acac)_2$ 1,2-hexadecanediol, diphenyl ether oleyamine, $LiBEt_3H$ oleic acid Ketjen Black EC	270	30	$Pt_{50}Ni_{50}$ (core) Pt (shell)	solid solution core-shell	-	3.2 ± 0.4	-	-
Jeon et al. [47] (2009)	OS	alcohol reduction	$PtCl_4$, $NiCl_2{\cdot}6H_2O$ NaOAc anhydrous Et-OH $NaBH_4$ Vulcan XC 72R	room temperature	240 240 + 60 240 + 120 240 + 180	$Pt_{50}Ni_{50}$	solid solution	-	2.1 2.0 2.1 2.2	3.79 3.84 3.85 3.86	heat treatment time - to vary degree of alloying
Jeon et al. [48] (2010)	OS	alcohol reduction	$PtCl_4$, $NiCl_2{\cdot}6H_2O$ NaOAc anhydrous Et-OH	room temperature	240	$Pt_{67}Ni_{33}$ $Pt_{50}Ni_{50}$	solid solution	-	4.2 3.4	-	-

			$NaBH_4$			$Pt_{40}Ni_{60}$			2.7		
			Vulcan XC 72R								
Yang et al. [49] (2004)	OS	carbonyl complex route	Pt salt, Ni salt	200-500	-	$Pt_{83}Ni_{17}$	solid solution	-	3.1 ± 1.4	3.89	-
			NaOAc								
			Met-OH			$Pt_{75}Ni_{25}$			2.8 ± 1.2	3.85	
			CO, H_2			$Pt_{67}N_{i33}$			2.4 ± 1.1	3.82	
			Vulcan XC 72			$Pt_{50}Ni_{50}$			2.3 ± 1.3	3.80	
Hanprera-kriengkrai et al. [50] (2018)	OS	ion exchange reaction	$Ni(NO_3)_2$, $Pt(NH_3)_4Cl_2$	room temperature	1440	$Pt_{50}Ni_{50}$	solid solution	-	2.4	-	-
			NH_3			$Pt_{25}Ni_{75}$			2.3		
			resin WK-11								
Changlin et al. [51] (2014)	OS	solid state impregnation reduction	$Pt(acac)_2$, $Ni(acac)_2$	200	60	$Pt_{80}Ni_{20}$	solid solution	rhombic	-	-	-
						$Pt_{75}Ni_{25}$					
			CO, H_2			$Pt_{67}Ni_{33}$					
						$Pt_{60}Ni_{40}$			5.8 ± 1.5		
			C support			$Pt_{50}Ni_{50}$			-		

[a]Synthesis of free-standing NPs, but characterization of the NPs is done on a support
[b]The synthesis method and precursors are for the solid solution core of the NPs
[c]The magnetic properties of the NPs are characterized, but not included here

By inspecting Table 1.3-2, it is noticed that the polyol synthesis route is the most common for method for the production of both free-standing and supported $Pt_{100-x}Ni_x$ NPs. Further, the metal precursors $H_2PtCl_6 \cdot xH_2O$ and $Pt(acac)_2$ are often used for Pt-ions whereas the metal precursors $NiCl_2 \cdot xH_2O$ and $Ni(acac)_2$ are often used for Ni-ions. In addition, the most frequently utilized solvent is EG and there are few previous studies, in which the synthesis was performed without any other additives. Note that an additive is here used for chemicals other than the metal precursors, the solvent and the surfactant. The synthesis –temperature and –time vary significantly from one work to another and the most common intervals are 120-250 ^{0}C and 20-240 min, respectively. Naturally, the resulting $Pt_{100-x}Ni_x$ NPs and their properties element distribution, particle –size and –morphology, and lattice constant clearly vary depending on the preparation method and specific conditions. The following in-depth description of selected works from Table 1.3-2 is focused on the formation of NPs via the polyol method as it is the one used in the practical work of this thesis.

Element distribution

All previous works utilizing the polyol reduction route for synthesis of alloyed $Pt_{100-x}Ni_x$ NPs have reported element distribution. The most common one is solid solution followed by a core@shell. Jiang et al. [23] prepared alloyed NPs with nominal compositions $Pt_{50}Ni_{50}$, $Pt_{67}Ni_{33}$ and $Pt_{75}Ni_{25}$ from the simultaneous reduction of $H_2PtCl_6 \cdot 6H_2O$ and $Ni(NO_3)_2 \cdot 6H_2O$ in EG in the presence of NaOH at 180 °C for 240 min. They analyzed them by means of XRD and revealed that the reflections shifted to higher values for 2θ with increasing atomic % Ni; see Figure 1.3-2. This indicates that at least a partial alloy was formed. In addition, the reported lattice constants decrease from 3.90 Å to 3.81 Å with increasing atomic % Ni, which confirms the formation of the alloy. The same observations were made by Bao et al. [24], who used the same conditions for the synthesis of these three nominal compositions. However, they revealed that the $Pt_{75}Ni_{25}$ NPs, which they prepared formed a quasi core@shell structure with a Pt-core and a NiO-shell. Xiong et al. [42] made similar observations for $Pt_{100-x}Ni_x$ (x = 20, 25, 33 and 55) prepared from the simultaneous reduction of H_2PtCl_6 and $NiSO_4$ in EG with an additional reducing agent $NaBH_4$ in the presence of NaOH and functionalized MWCNTs at 70 ^{0}C for 180 min. Similar trend for the lattice constants found from XRD measurements were also made in the works of Wan et al. [28],

Carpenter et al. [29], Banik et al. [31], and Yang et al. [49], via other synthesis methods than the polyol.

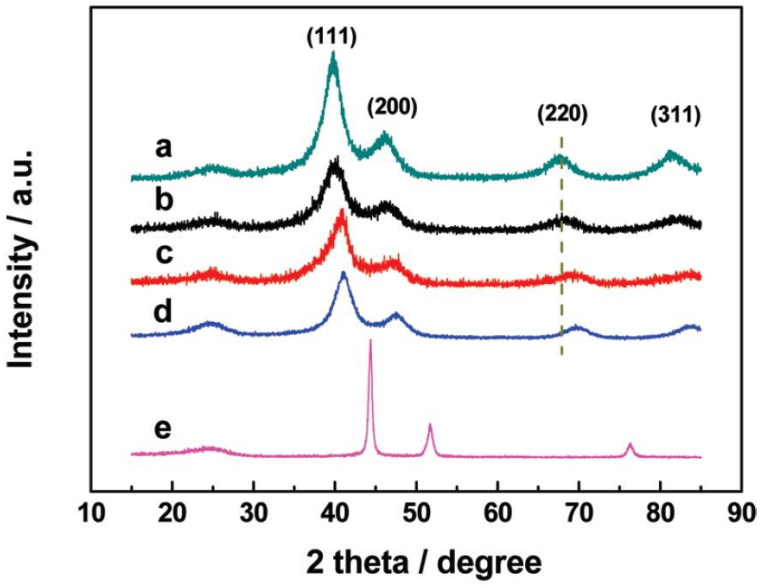

Figure 1.3-2: XRD patterns of Pt/C (a), $Pt_{75}Ni_{25}$/C (b), $Pt_{67}Ni_{33}$/C (c), $Pt_{50}Ni_{50}$/C (d) and Ni/C (e). The figure is taken from literature [23].

Particle –size and –morphology

The reviewed studies in Table 1.3-1, which use the polyol synthesis method, have reported quite similar particle size values for the alloyed NPs; all are in the range 2-6 nm. Galhardo et al. [22] analyzed by means of TEM the particle size of $Pt_{75}Ni_{25}$ NPs produced by the modified polyol method and the microwave-assisted polyol method. It was found that NPs with size 2.5 ± 0.7 nm were the product when H_2PtCl_6 and $NiCl_2$ were simultaneously reduced in ethylene glycol (EG) with reaction time of 180 min and reaction temperature of 160 ^{0}C while NPs with size 1.9 ± 0.5 nm were the product of the same reaction, but with reaction time of 6 min. TEM images of the results are presented in Figure 1.3-3.

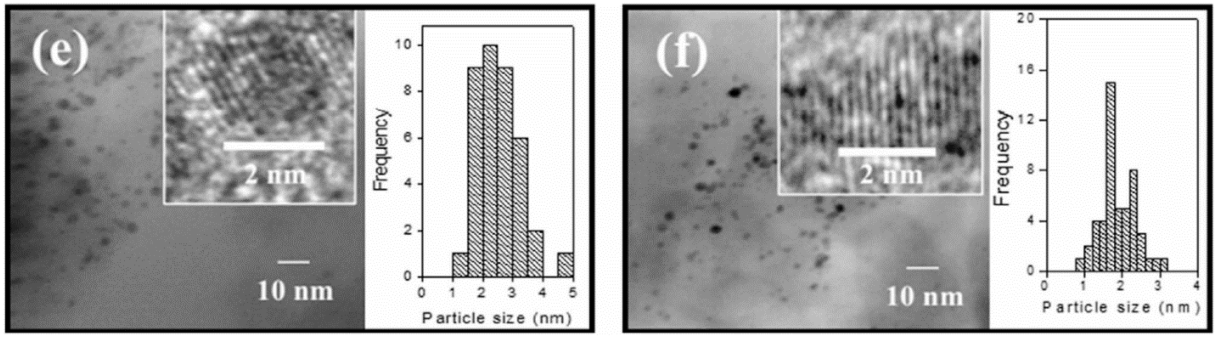

Figure 1.3-3: TEM and HR-TEM images and particle size distribution histograms of the $Pt_{75}Ni_{25}$ NPs produced by the modified polyol method (e) and the microwave-assisted polyol method (f) as synthesized by Galhardo et al. [22].

Rudi et al. [25] analyzed by means of TEM the particle size of $Pt_{32}Ni_{68}$, $Pt_{26}Ni_{74}$ and $Pt_{14}Ni_{86}$ NPs. It was found that NPs with sizes 3.7 ± 1.0 nm, 5.7 ± 0.7 nm and 6.0 ± 0.8 nm respectively, were the product of the reduction of $Ni(Ac)_2{\cdot}4H_2O$ and $Pt(acac)_2$ in 1,2-tetradecanediol, 1,2-dichlorobenzene, diphenyl ether and oleic acid with oleyamine as a capping agent, reaction time of 60 min and reaction temperature of 200 ^{0}C. The findings about particle size increasing with increasing atomic % Ni are consistent with the results found in the works of Jiang et al. [23] and Bao et al. [24], who prepared NPs with nominal compositions $Pt_{75}Ni_{25}$, $Pt_{67}Ni_{33}$ and $Pt_{50}Ni_{50}$ from the reduction of $H_2PtCl_6{\cdot}6H_2O$ and $Ni(NO_3)_2{\cdot}6H_2O$ in EG in the presence of NaOH with reaction –time and –temperature 240 min and 180 ^{0}C, respectively. The particle sizes reported by Jiang et al. [23] are 2.8 nm, 2.7 nm and 3.3 nm for the respective nominal compositions. This suggests the possibility of a minimum particle size somewhere along the Pt-Ni system. Santos et al. [35] observed a similar trend in particle size utilizing micro-emulsion reduction method.

Finally, few observations on particle morphology have been reported for the $Pt_{100-x}Ni_x$ NPs prepared via the polyol method. In the work of Chen et al. [27], the synthesized core@shell $Pt_{17}Ni_{83}$ NPs were irregular polyhedra whereas Lee et al. [39] and Lin et al. [41] attempted to control the particle shape. In the work of Lee et al. [39], core@shell $Pt_{50}Ni_{50}$ NPs were synthesized from $Pt(acac)_2$ and $Ni(acac)_2$ or $Ni(hfac)_2$ in EG on support material Ketjen Black 300 J and the resulting morphologies depending on the type of Ni-precursor were truncated octahedra and octahedra, respectively; see Figure 1.3-4. On the other hand, Lin et al. [41] controlled the shape of $Pt_{25}Ni_{75}$

NPs through number of pulses during the microwave-assisted solvothermal route. They revealed that octahedra and tetrahedra were formed with corners becoming more round with increasing pulse time.

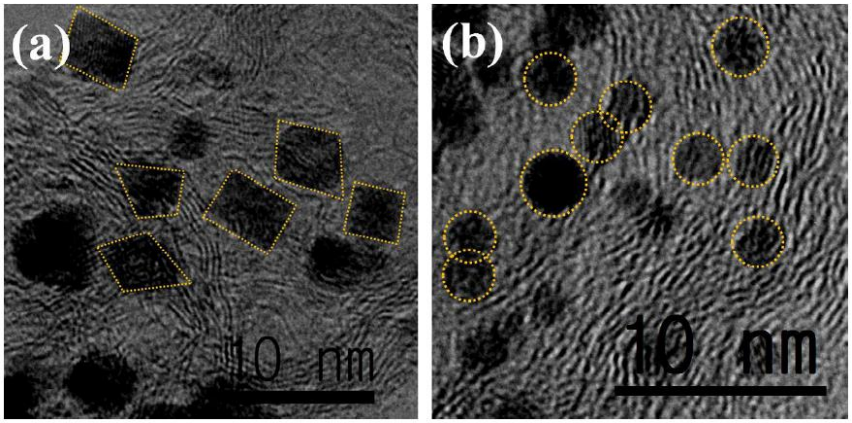

Figure 1.3-4: TEM images of $Pt_{50}Ni_{50}$/C prepared from $Ni(hfac)_2$ (a) and $Ni(acac)_2$ (b). The figure is taken from literature [39].

Magnetism

In addition to the work presented in Table 1.3-2, some few studies have explored the magnetic properties of the alloyed $Pt_{100-x}Ni_x$ NPs. Kozejova et al. [38] prepared NPs with nominal compositions $Pt_{75}Ni_{25}$ and $Pt_{25}Ni_{75}$ via an electrodeposition technique under potentiostatic conditions from metal precursors K_2PtCl_4 and $NiCl_2$ in ultrapure deionized water in the presence of NaCl, NaOH and HCl where the last two were used to control the pH = 2.5. The deposition time was 100 s and the element composition was controlled by the applied potential. The $Pt_{75}Ni_{25}$ and $Pt_{25}Ni_{75}$ had average particle size 164 nm and 133 nm, respectively, and the former were found to be diamagnetic whereas the latter exhibit superparamagnetic behavior with the blocking temperature (T_B) 225 K. In the work of Du et al. [33], $Pt_{67}Ni_{33}$ NPs were prepared using the galvanic displacement reaction from $NiCl_2$ and K_2PtCl_6 in water in the presence of PVP and by the addition of the reducing agent $NaBH_4$. The produced NPs had average particle size 53 nm and showed a superparamagnetic behavior with blocking temperature (T_B) 8.0 K; see Figure 1.3-5.

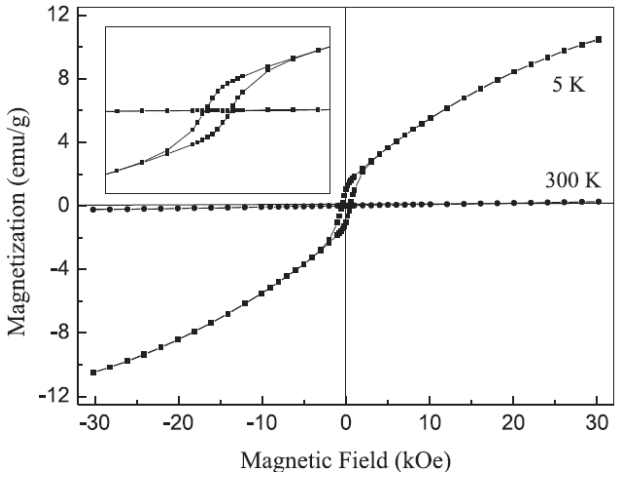

Figure 1.3-5: Magnetization of the $Pt_{67}Ni_{33}$ NPs as a function of applied field measured at 5 K and 300 K. In addition, an inset of an open-hysteresis loop in the low-field region (<4500 Oe). The figure is taken from the literature [33].

1.4 Motivation

In the NAFUMA research group at Department of Chemistry, UiO we have the last years explored colloidal routes for metallic nanoparticle (NP) synthesis in tandem with nanoscale materials characterization. For example, we are in position to synthesize monodisperse NPs of Co, Co-Re, Ni and Pt-Rh, whereof the element distribution of the bimetallic NPs are strictly controlled.

Currently, the NAFUMA group are running several projects devoted to utilization of mono- and bimetallic noble metal nanoparticles for NOx abatement and water purification. The metallic nanoparticles will act as the active component in metal supported catalysts in the NOx abatement process and as the antibacterial component in filters for water purification. Systems as Pd-Pt, Pt-Rh, Ag-Pt, Ag-Rh and Ag-Au are currently under investigation.

The motivation of this master project is to perform an initial screening of the bimetallic Pt-Ni system for NOx abatement and to provide recommendations on recipes on the synthesis, including details connected to the nucleation and growth of the nanoparticles. A part of the study is to introduce magnetic property investigations into the characterization toolbox for metallic NPs.

In the first part of the master project, our standard polyol synthesis route will be used to produce colloidal $Pt_{100-x}Ni_x$ NPs, and the obtained particle size and element distribution will be investigated in detail. Included to the experiments some simple kinetic experiments will be performed.

The second part of the study will involve correlating data obtained from the synthesis- and kinetic studies to propose a simple model to describe the nucleation and growth of the obtained $Pt_{100-x}Ni_x$ NPs. The model will subsequently be used to optimize the synthesis procedure with the purpose to fine tune the particle size distribution and element distribution/segregation.

Finally, since Ni and Pt have quite different magnetic properties, i.e. being ferromagnetic/ superparamagnetic and Pauli paramagnetic, respectively, attempts to implement magnetization data will be tried.

Methodologies used will be Schlenk-lines and glove box for inert handling of chemicals, the NP synthesis work and for the kinetics experiments. In addition, will powder X-ray diffraction (PXRD) for phase identification and unit cell dimensions from Rietveld refinements, high resolution scanning electron microscopy (SEM) imaging – particle size histograms analysis for morphology studies, transmission electron microscopy (TEM) for element distribution/segregation analysis and magnetization data from physical property measurement system (PPMS) be performed.

2 Methods and Theory

Methods and theory relevant for this thesis are presented in this chapter. In the beginning, nucleation and growth mechanisms of NPs are explained followed by description of synthesis methods and stabilization of colloidal suspensions. Finally, magnetism of metallic NPs and the principles behind the characterization techniques used in this work are explained.

2.1 Nucleation and Growth of Nanoparticles

In this section, the mechanisms of nucleation and growth of NPs are described in light of reduction in the total Gibbs free energy and the LaMer model is explained.

2.1.1 Nucleation of Nanoparticles

Nucleation is the process of formation of a thermodynamically stable phase, which may occur in liquid, gaseous and solid state. In this work, the focus is on formation of solid NPs in solution. The formation of NPs can be either homogeneous or heterogeneous depending on whether the nuclei form spontaneously in the solution or on a nucleation site, i.e. a solid surface.

Homogeneous nucleation is the process of spontaneous formation of a solid phase in a supersaturated solution, i.e. a solution in which the concentration of the solute exceeds its solubility equilibrium. The driving force for this process is reduction in the high Gibbs free energy, which the solution possesses. The reduction in Gibbs free energy per unit volume of the solid phase, ΔG_V, is given by the following relation:

$$\Delta G_V = -\frac{kT}{\Omega} \mathrm{LN}\left(\frac{C}{C_0}\right) \quad (1)$$

where k is the Boltzmann constant, T is temperature, Ω is the atomic volume, C is the concentration of the solute and C_0 is the solubility concentration of the solute. In addition, there is an increase in surface free energy upon particle formation due to the formation of surface area. The changes in both volume- and surface- free energy are size dependent and they are presented as functions of the radius, r, of spherical NPs in Figure 2.1-1. The total change in Gibbs free energy, ΔG, is given by the following relation:

$$\Delta G = \frac{4}{3}\pi r^3 \Delta G_V + 4\pi r^2 \gamma \quad (2)$$

where the first term represents the volume free energy and the second expresses the surface free energy. In addition, γ is the surface energy per unit surface area [52, p. 53-55]. Figure 2.1-1 shows the change in total Gibbs free energy of a supersaturated solution when nuclei are formed. The

overall energy decreases, which is the driving force for nucleation, but the change in energy is positive for nuclei with radius smaller than the critical radius, r^*, and hence these are not stable and are likely to dissolve back. The total Gibbs free energy, ΔG^*, for nuclei with critical radii (Figure 2.1-1) is the energy barrier for the nucleation process. Nuclei which exceed the critical radius are stable and will continue to grow. Hence, the critical radius for a supersaturated solution gives the minimum size for the prepared NPs. Factors like temperature, solvent, additives and impurities can change the critical radius.

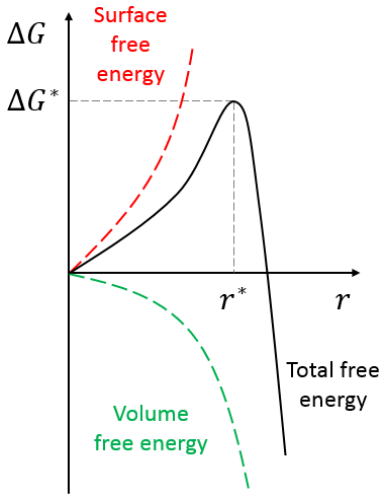

Figure 2.1-1: Plot illustrating the size dependency of volume free energy (green), surface free energy (red) and total free energy (black). The figure is made based on the literature [52, p. 55].

Heterogeneous nucleation is the process of formation of solid nuclei on nucleation sites, which in our case are solid surfaces. These can be already formed NPs, the walls of the flask containing the solution or impurities. Further, special additives can be introduced as seeds to promote heterogeneous nucleation. In addition, the energy barrier for heterogeneous nucleation is lower than the one for homogeneous nucleation; see Figure 2.1-2 [53].

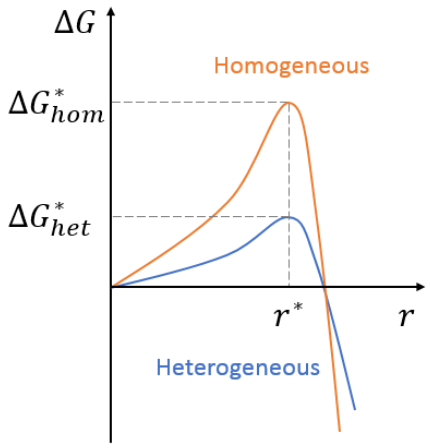

Figure 2.1-2: Plot illustrating the difference in total free energy as a function of particle size for homogeneous (orange) and heterogeneous (blue) nucleation. The figure is made based on the literature [53].

2.1.2 Growth of Nanoparticles

As mentioned in the previous section, nuclei with radii above the critical value, will continue to grow and the driving force for this process is the reduction in total Gibbs free energy. The growth process happens in a series of steps and the major ones are the formation of growth species, their diffusion towards a solid surface, their adsorption to it and the irreversible incorporation into the solid phase. The size distribution of the resulting NPs depends on which of these steps is controlled. A diffusion-limited growth promotes formation of NPs of uniform size. Some of the strategies to control the diffusion are to keep the concentration of the growth species low, to use a solvent with high viscosity and to introduce a diffusion barrier on the surface of the NPs. When the available growth species are used up, further growth of the NPs can occur through different mechanisms [52, p. 23-25].

Coalescence and Ostwald ripening are the two major mechanisms for further growth of the NPs; Figure 2.1-3. In the former, two NPs merge into whereas in the latter larger NPs grow at the expense of the smaller ones [52, p. 23-25].

Figure 2.1-3 (a) shows the mechanism of coalescence, in which two smaller NPs in a solid solution merge together to form a larger one. The driving force for this process is the reduction in the total

Gibbs free energy upon reduction of surface area. Figure 2.1-3 (b) shows the mechanism of Ostwald ripening. NPs in a solid solution are in equilibrium with the solvent surrounding them. Smaller particles have larger solubility due to their larger curvature and this causes them to dissolve and atoms are diffused towards larger particles. To maintain the equilibria around each of the particles, the diffused atoms are precipitated on the surface of the large ones whereas surface atoms from the small ones are dissolved. Once the small particles start to dissolve, the process would not stop until their elimination since the particle's solubility increases with decreasing size. The elimination of small NPs results in a narrower size distribution. [52, p. 29-31].

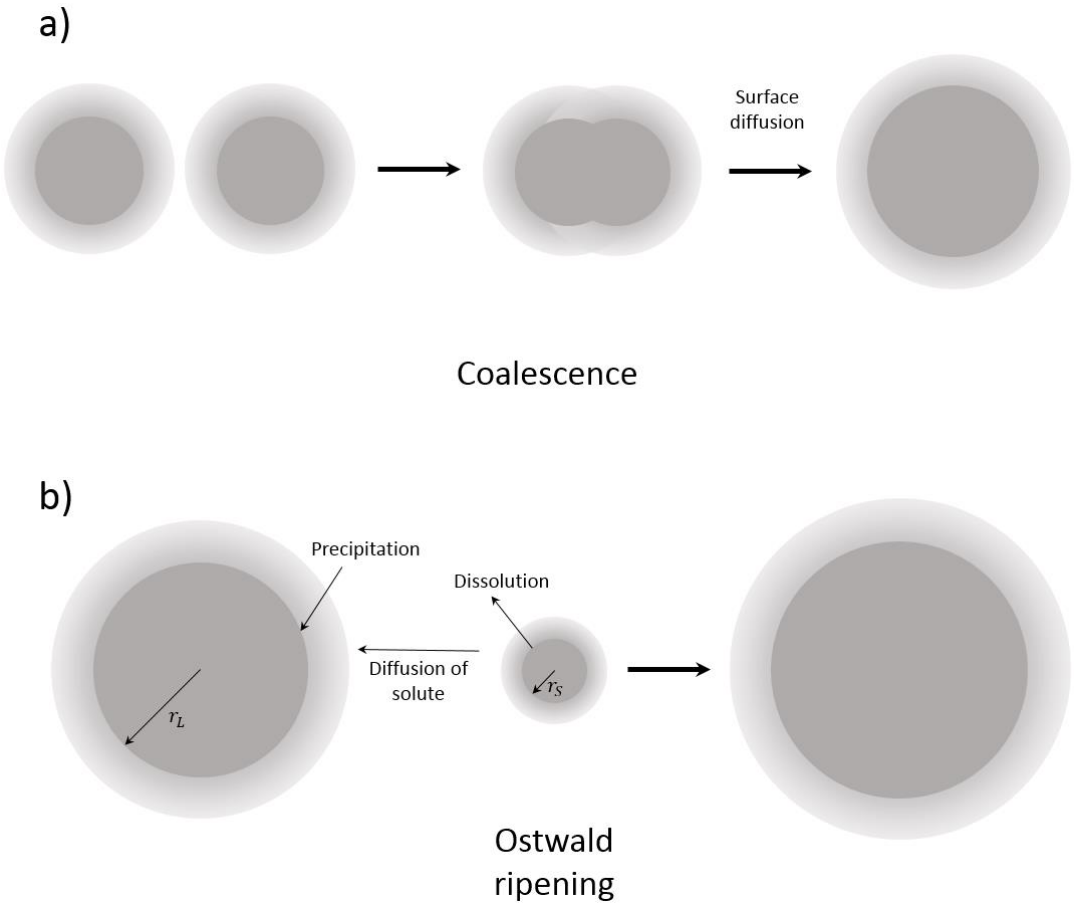

Figure 2.1-3: Schematic illustrations of the growth mechanisms coalescence (a) and Ostwald ripening (b). The figure is based on the references [54] and [52, p. 25, 30].

2.1.3 The LaMer Model

The famous LaMer diagram, proposed by LaMer and Dinegar [55], illustrates the mechanism of homogeneous nucleation and subsequent growth of the NPs with a plot of solute concentration (monomer concentration) as a function of time; Figure 2.1-4. The plot is divided into three regions, I, II and III. In the first one, the solution becomes supersaturated as the concentration of the solute increases above its solubility concentration, C_s. In region II, the solute's concentration goes over a minimum value, C_{min}. Hence, homogeneous nucleation is initiated. This results in decrease of supersaturation and the solution returns to a concentration that does not promote further nucleation; i.e. we are entering zone III in Figure 2.1-4. The remaining monomers are consumed in the growth phase.

It should be pointed out that both nucleation and particle growth occur simultaneously in the second region of the plot over a certain amount of time. The consequence of this is that the initially formed NPs would have grown quite a bit when new nuclei are still being formed, which results in NPs with a wide size distribution. For the preparation of NPs with a narrower size distribution, the time for which the concentration of the growth species exceeds the minimum value, C_{min}, has to be minimized. In this way, very quick nucleation process can be achieved also known as burst nucleation [52, p. 57]. Further, the size distribution can be altered during the subsequent growth in region III (Figure 2.1-4).

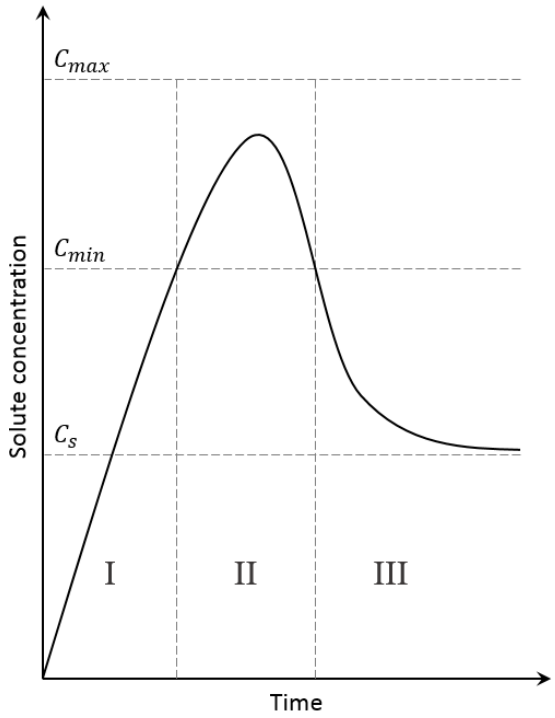

Figure 2.1-4: Schematic illustration of the LaMer theory via a plot of solute concentration as a function of time. The figure is made based on the literature [52, p. 57].

2.2 Nanoparticle Synthesis Methods

In this section, aspects of solution-based methods for the preparation of metallic NPs are described with focus on the polyol method, which was used in this work.

2.2.1 Solution-Based Methods

The most widely used method for the preparation of metallic NPs in colloidal suspensions is via reduction of salts containing cations of the metal(s) or via decomposition of complexes containing the targeted elements. In a general synthesis, the precursors are introduced into a solvent in a reaction flask, where they decompose or are reduced into atomic species, which then nucleate and form NPs. These processes are most often thermally activated. Further, surfactant molecules are added to the solvent prior to the nucleation step. These adsorb to the surface of the formed nuclei and are often used to control the NP growth. A good surfactant is one which is mobile enough to

allow for the addition of the reactive species, i.e. so the nuclei can grow, but it should be stable enough to prevent aggregation of the NPs [56, p. 28].

In aqueous solutions, a reducing agent has to be added or generated. However, in non-aqueous solutions, NPs can be formed without an additional reducing agent, i.e. the solvent can reduce the metal salts. Alcohols are solvents that fit this criterion, and the polyol method (section 2.2.2) utilizes the reductive properties of alcohols.

The alcohol reduction process, which was developed by Hirai and Toshima, is a general solution-based method in which alcohols are used as the solvent and the reducing agent and the resulting colloidal suspensions are often stabilized by organic polymers [56, p. 192]. Metal NPs can catalyze the oxidation of alcohols to aldehydes or acids and addition of a base can further catalyze the reaction. The mechanism of the reaction is initiated by the formation of alkoxides with an oxonium ion as the intermediate. Then, a carbonyl compound is formed via hydride elimination. The deprotonation of the oxonium intermediate is aided by the base [3, p. 34].

The particle size and size distribution of the prepared NPs vary with the type of reduction agent used in the synthesis because the strength of the reduction agent determines the rate of reaction and hence the particle size. A strong reducing agent aids the formation of small NPs, but it does not necessarily result in a small size distribution. The reason for this is that the size distribution width depends on the time period of the nucleation process – if quick nucleation occurs, a slow reaction rate leads to a diffusion-limited growth and hence a size narrow distribution whereas if the nucleation process takes a while the resulting NPs have very heterogeneous sizes [52, p. 67]. A common additional reducing agent used in the solution-based methods for NP preparation, is borohydride. The oxidation of borohydride donates electrons to the metallic cations, which are reduced to their zero-valent state and the reaction involves hydrogen gas evolution:

$$BH^-_{4\,(solv)} + \frac{4}{n}M^{n+}_{(solv)} + 4OH^-_{(solv)} \rightarrow 2H_{2\,(g)} + B(OH)^-_{4\,(solv)} + \frac{4}{n}M_{(solv)} \qquad (3)$$

The problems with using borohydride as a reducing agent are irreproducibility in aqueous systems and the incorporation of boron in the resulting NPs [3, p. 30-32].

There are different strategies in solution-based synthesis of NPs. The nucleation and subsequent growth processes should be separated in time to promote preparation of NPs with a narrow size distribution. The so-called “heat-up” and “hot-injection” methods are two ways in which this separation can be achieved and thus, a burst nucleation event can take place; see Figure 2.2-1.

In the heat-up method, the metallic precursors are dissolved in the solvent and thereafter brought to elevated temperature, which results in nucleation and subsequent growth of the NPs as observed by the color change of the solution (Figure 2.2-1 (a)). In this synthesis method, it is hard to separate the nucleation and growth steps since the reactive species are heated up continuously and these two processes overlap in time. The particle size and size distribution of the prepared NPs depends largely on the heating rate of the solution. If the heating is quick enough, burst nucleation can occur. Further, a heat-up method is reliable for reproducible synthesis if the heating rate is controlled [57, p. 1].

In the hot-injection method (Figure 2.2-1 (b)), the solvent is heated up to the desired temperature and the metallic precursors, which are dissolved in a small amount of solvent, are then injected into the hot liquid. This causes quick nucleation, i.e. many nuclei are formed simultaneously. This synthesis strategy yields NPs with a narrower size distribution because the nucleation and growth processes are separated better in time. Employing the burst nucleation approach, however, presents a few challenges. The main problem is the reproducibility from one batch to another, because the time taken for the injection of the dissolved precursors into the hot liquid will often vary between different batches and different users if not special care is taken [57, p. 1-2].

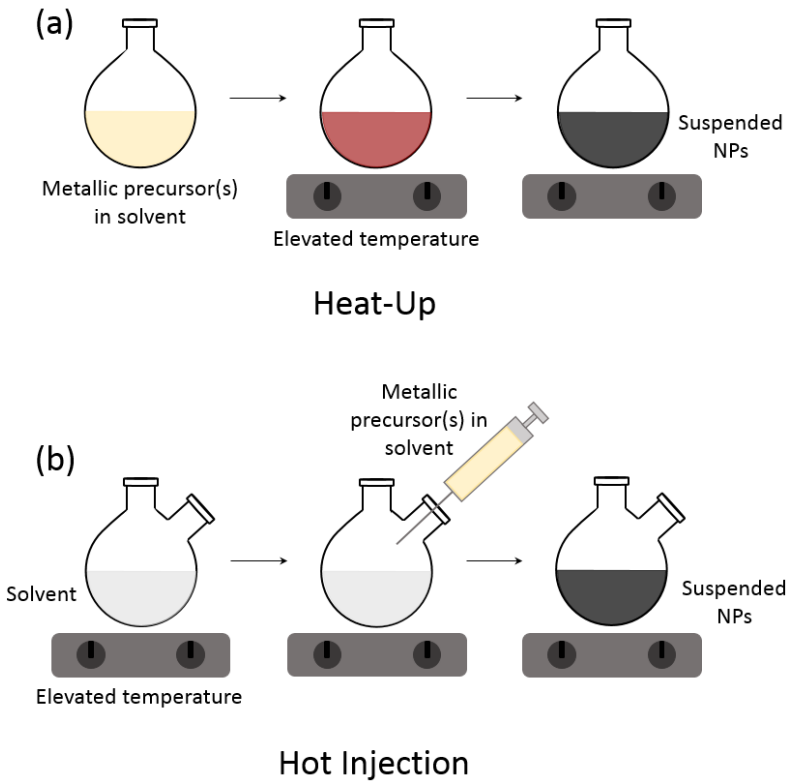

Figure 2.2-1: Schematic illustration of the strategies of a heat-up (a) and a hot-injection (b) solution-based synthesis methods. The figure was made based on the literature [57].

2.2.2 The Polyol Method

The polyol method, which was reported by Fievet et al. [58] in 1989, is a solution-based method in which inorganic precursors of the metals are reduced in liquid polyalcohols. Polyalcohols are alcohols, which contain multiple hydroxyl groups. The process involves the suspension of the precursor in the polyol solvent and heating of the solution to a temperature just below the polyol's boiling point, which in turn kicks-off the reduction of the metallic precursor(s). The starting material(s) for the metallic ions can be a hydroxide, an oxide or a salt. [58, p. 1]. In addition to acting as solvent and reducing agent, the polyalcohols can also serve as the stabilizing agent. Small NPs can be prepared more easily via the polyol method [3, p. 34]. The use of polyols has several advantages. Firstly, their solubility is comparable to that of water and hence, a large variety of metal precursors can be used successfully in this synthesis method. Further, they have high boiling

points up to 320 °C, which makes high temperature synthesis possible and thus, crystalline NPs can be produced at atmospheric pressure. In addition, polyols have reducing properties, which make the reduction of metal precursors for formation of metal NPs possible without an additional reducing agent. Finally, the chelating effect in polyols not only gives rise to their solubility properties, but it also contributes to the stabilization of the colloidal suspensions. Hence, a polyol synthesis can be performed without an additional stabilization agent. However, the most common surfactant used in this method is Poly(vinylpyrrolidone) (PVP) (section 2.3) [59, p. 1]

An illustration of the oxidation of a secondary polyalcohol is presented in Figure 2.2-2.

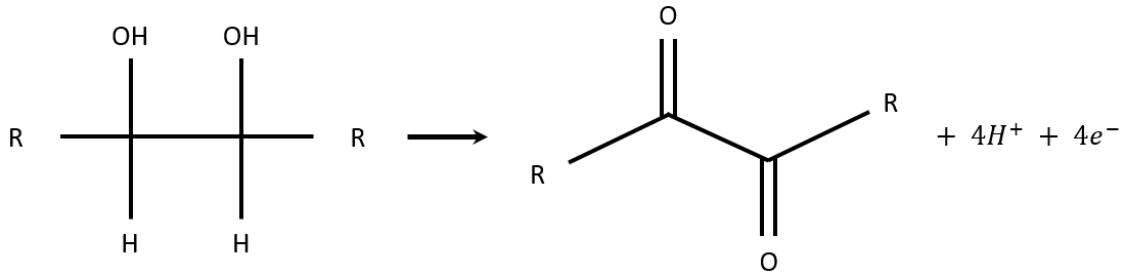

Figure 2.2-2: Oxidation reaction of a polyalcohol. The figure is made based on the literature [8, p. 51].

The electrons from the oxidation of polyalcohols (Figure 2.2-2) are donated to the metallic cations, which are reduced to their zero-valent state:

$$M^{n+} + ne^{-} \rightarrow M_{(s)} \quad (4)$$

2.3 Stabilization of Colloidal Suspensions

As described in the previous sections, the reduction in total Gibbs free energy is the driving force for nucleation and growth of NPs from a supersaturated solution. Formation of agglomerates and aggregates of the NPs in the produced colloidal solution is another mechanism for energy reduction. In the former, the NPs are joined together by van der Waals attraction and can be dispersed, whereas in the latter the NPs are joined by chemical bonds, which makes the formation of aggregates irreversible. In order to prepare well-dispersed NPs, the colloidal solution has to be

stabilized and the three stabilization mechanisms are electrostatic, steric and electrosteric. Electrostatic stabilization gives a kinetically stable system whereas employing steric stabilization results in a thermodynamically stable system [52, p. 31].

In this work steric stabilization is utilized, and thus, is described in more detail. For further reading on electrostatic and kinetically stabilized systems, see reference [52, p. 32-42]. Since the NPs are stabilized thermodynamically, they can be redispersed. Further, this mechanism is suitable for multiple phases and the adsorbed layer of polymer on the surface of the NPs serves as a barrier for diffusion. The latter results in diffusion-limited growth, which in turn results in a narrower size distribution [52, p. 42-43].

When choosing the precursors for the synthesis of NPs, the polymer-solvent and polymer-solid surface interactions must be considered. Firstly, a "good" or a "bad" solvent is one in which the dissolved polymer expands or contracts, respectively, to reduce the overall Gibbs free energy. Further, this property is temperature dependent, and the Flory-Huggings theta temperature is the point below which the polymer coils up and above which it expands. Depending on the type of the polymer-solid surface interaction, the polymers can be anchored, adsorbed or non-adsorbed. Only the first two of these can be used for steric stabilization with the former attaching to the surface of the NPs by one of its ends whereas random parts of the latter adsorb weakly onto the NPs' surface; Figure 2.3-1 [52, p. 43-44].

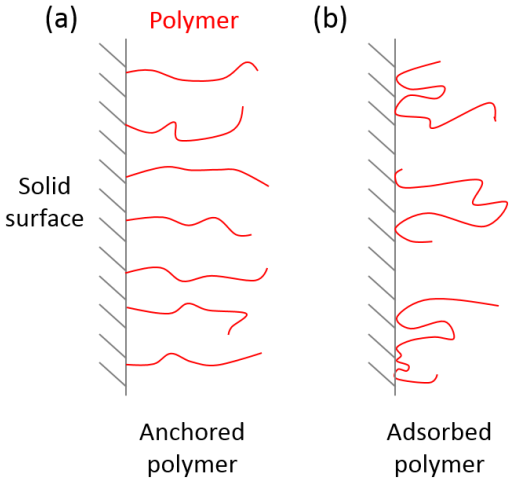

Figure 2.3-1: A schematic illustration of the two types of polymers, anchored (a) and adsorbed (b), which can be used to sterically stabilize a colloidal suspension in respect to the polymer-solid surface interaction. The figure is made based on the literature [52, p. 46-47].

The interactions between the polymer layers of two NPs as they approach each other determine whether the forces between the two are attractive or repulsive. The interactions between adsorbed polymers (Figure 2.3-1) are described here. Firstly, bridging can occur when a single polymer chain attaches to two NPs and if given enough time, polymer chains can desorb from the surface of a particle. Further, the interactions between two polymer layers depend on the degree of coverage and the type of solvent; see Figure 2.3-2 [52, p. 46-47].

For a full coverage of strongly adsorbed polymer chains, when the distance between the surfaces of two NPs is $< 2L$, i.e. twice the distance of the polymer layer, the Gibbs free energy increases and thus, there are repulsive forces (orange curve in Figure 2.3-2). For a partial coverage of the adsorbed polymer chains, the interaction between two NP depends on the nature of the solvent. In a good solvent (dark green curve in Figure 2.3-2), when the distance between the NPs is $< 2L$ the forces are repulsive, because the polymer layers interpenetrate, which results in reduced entropy, i.e. $\Delta S < 0$, and hence, increased Gibbs free energy according to:

$$\Delta G = \Delta H - T\Delta S > 0 \tag{5}$$

where the change in enthalpy, ΔH, from the interpenetration of the polymer layers is assumed to be negligible. In a poor solvent, interpenetration promotes further coiling up of the polymers, resulting in increased entropy and thus, lowered Gibbs free energy. Hence, the forces between the two particles are attractive when the distance is $L < D < 2L$ (light green curve in Figure 2.3-2). However, when the distance is $< L$, i.e. under the thickness of one polymer layer, Gibbs free energy increases and the forces are repulsive [52, p. 46-47].

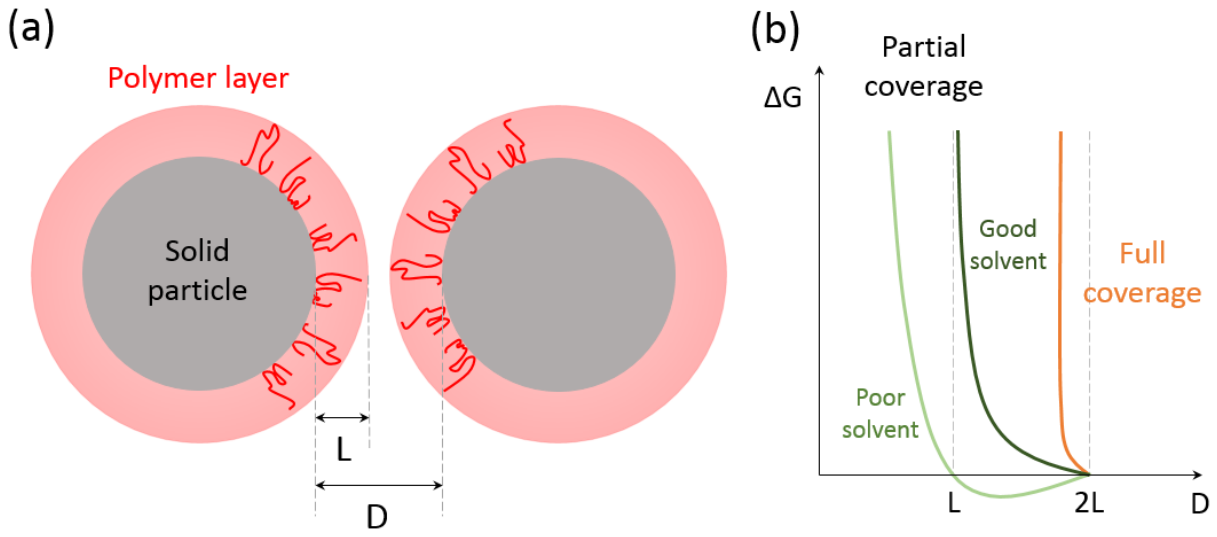

Figure 2.3-2: Schematic illustration of the adsorbed polymer layers of two NPs (a) where L is the thickness of one polymer layer and D is the separation distance between the two NPs. In addition, a plot illustrating the interaction between the two layers (b). The figure is made based on the literature [52, p. 46-47].

In this work, Poly(vinylpyrrolidone) (PVP) is utilized as a stabilizer for the produced colloidal suspensions. It is a non-ionic water-soluble polymer with C=O, C–N and CH_2 functional groups. It consists of the monomer *N*-vinylpyrrolidone, which consists of a hydrophobic (alkyl group) and a hydrophilic (pyrrolidone ring) part; see Figure 2.3-3. Since the ends of the molecule are terminated with hydroxyl groups, PVP can also act as a reducing agent. The metal-PVP interaction for noble metals takes place through the carbonyl group and nitrogen atom of the pyrrolidone ring [60, p. 2].

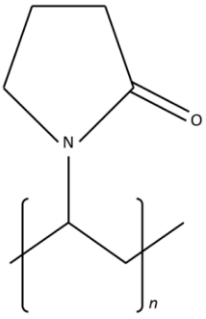

Figure 2.3-3: The structure of the *N*-vinylpyrrolidone monomer, which is used to build PVP. The figure is made based on the literature [61].

2.4 Magnetism

In this section a brief description of magnetic properties are given with focus on how various magnetic phenomena depend on particle size, temperature and applied magnetic field.

Magnetism arises mainly from the motion of electrons, which have intrinsic magnetic moments also known as spin. All materials are affected to some extent by an applied magnetic field, and the interactions between the two depend on the arrangements of the individual atomic magnetic moments in the materials. Hence, the various types of magnetism are defined by the arrangement of electron spins; see Figure 2.4-1. Firstly, diamagnetism, which is produced by the movement of electrons (in fully occupied orbitals) causes a weak repulsion from a magnetic field. This occurs in all materials, but its contribution is very small compared to the rest of the phenomena [56, p. 220-221], [62, p. 342]. Paramagnetism refers to the random arrangement of atomic magnetic moments whereas ferro-, antiferro- and ferri-magnetism have well-arranged electron spins, which are parallel and equal, antiparallel and equal and antiparallel and not equal, respectively (Figure 2.4-1). Ideally, in antiferromagnetic materials, there is no net magnetic moment since the individual moments cancel out whereas there is a net magnetic moment in the ferromagnetic and ferrimagnetic ones [63, p. 394].

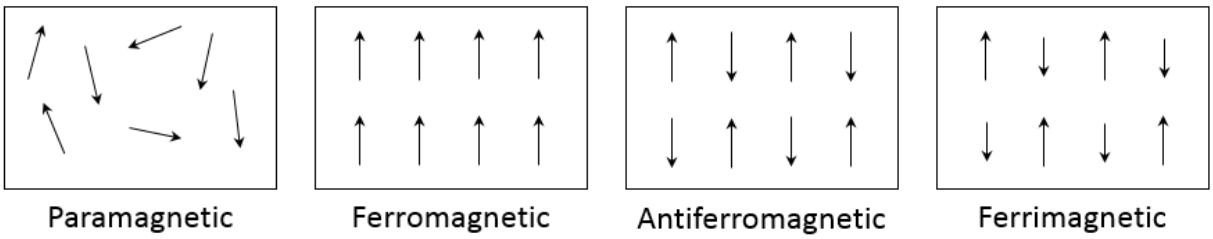

Figure 2.4-1: Illustration of the various arrangements of magnetic moments of individual atoms, which result in paramagnetism, ferromagnetism, antiferromagnetism and ferrimagnetism. The figure is made based on the literature [63, p. 394].

The applied magnetic flux density, *B*, is a property of the applied magnetic field, which defines the density of force lines produced by the field, and it is expressed by the following relation (in vacuum):

$$B = \mu_0 H \tag{6}$$

where μ_0 is the permeability of free space and *H* is the magnetic field strength. When a material is placed in the magnetic field, it changes the magnetic flux density of the field:

$$B = \mu_0 (H + M) \tag{7}$$

where *M* is the magnetization of the material. Diamagnetic materials reduce the density of the force lines whereas paramagnetic ones increase it [62, p. 342]. The relationship of magnetization and applied field can be expressed by magnetic susceptibility, χ:

$$\chi = \frac{M}{H} \tag{8}$$

When an external field is applied to a paramagnetic material, its magnetic moments align with the field, which is opposed by the randomizing effect of thermal energy. The relationship between the two results in the temperature dependency of the magnetic susceptibility, which is described by the Curie law:

$$\chi = \frac{C}{T} \tag{9}$$

where *C* is the Curie constant. The temperature dependency is different for the various types of magnetism. For ferromagnetism, it becomes:

$$\chi = \frac{C}{(T - T_C)} \tag{10}$$

where T_C is the Curie temperature at which there is a changeover from independent to cooperative behavior. For antiferromagnetism, the magnetic susceptibility is:

$$\chi = \frac{C}{(T + T_N)} \tag{11}$$

where T_N is the Néel temperature. The temperature dependency of magnetic susceptibility and the field-dependent magnetization curves for diamagnetic, paramagnetic, ferromagnetic, and antiferromagnetic materials are illustrated in Figure 2.4-2.

Figure 2.4-2 (a) shows that diamagnetic materials have a temperature-independent susceptibility whereas paramagnets have a decreasing susceptibility with increasing temperature. Further, the susceptibilities of ferro- and antiferro- magnets correspond to that of a paramagnet over the Curie- and Néel- temperatures, respectively. On the other hand, under the Curie temperature, the susceptibility of a ferromagnet increases with decreasing temperature whereas under the Néel temperature, the susceptibility of an antiferromagnet decreases with decreasing temperature.

Figure 2.4-2 (b) shows that magnetization of diamagnetic (black) and paramagnetic (black) materials is linearly dependent on the applied field and it decreases and increases, respectively, with increasing field strength. Finally, the magnetization curves of ferromagnetic/ferrimagnetic (red) and antiferromagnetic (green) materials are similar in shape, and are increasing with increasing applied field and reaching a saturation magnetization. However, the magnetization of the former is strong whereas it is weak for the latter [64, p. 12].

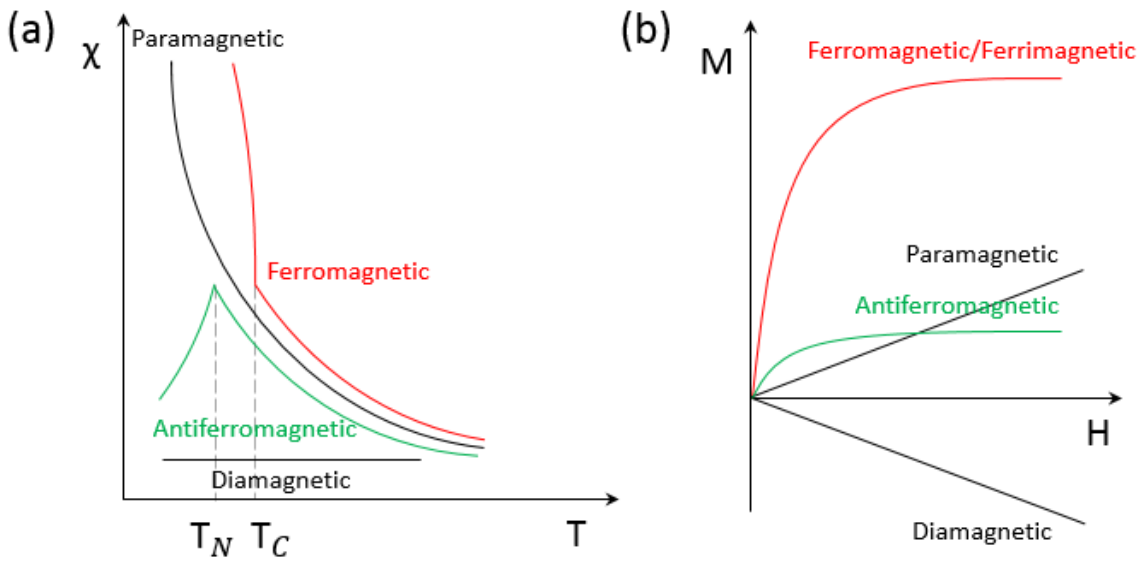

Figure 2.4-2: Plot of magnetic susceptibility, χ, versus temperature, T, (a) and magnetization, M, curves for applied magnetic field, H, (b) for diamagnetic, paramagnetic, ferromagnetic, ferrimagnetic and antiferromagnetic materials. The figure is made based on the literature [62, p. 343] and [64, p. 12].

Most metals display weak paramagnetic behavior, which is quite different from paramagnetism as it is small and temperature-independent. This phenomenon is called Pauli paramagnetism and it can be explained on the basis of the band theory. The electrons in a metal, which occupy the conduction band, are spin paired and equal number of spin-up and spin-down are present; see Figure 2.4-3 (a). This makes the metal diamagnetic. However, when an external magnetic field is applied, the electrons with spin parallel to the field have less energy than the ones with spin antiparallel to the filed; Figure 2.4-3 (b). Further, the electrons at the Fermi level, i.e. the electrons occupying the highest molecular orbitals in the conduction band, are the only ones which can reorient in the applied field. This produces a small imbalance in the number of spin-up and spin-down electrons and the material becomes paramagnetic. The magnetic susceptibility, χ, for Pauli paramagnetism depends on the density of states at the Fermi level, $N(E_F)$ [65, p. 373-374]:

$$\chi \propto \mu_0 \mu_B N(E_F) \tag{12}$$

where μ_0 is the vacuum permittivity and μ_B is the Bohr magneton. The reason for the temperature-

independency of the magnetic susceptibility of a Pauli paramagnet is that temperature does not change the density of states significantly.

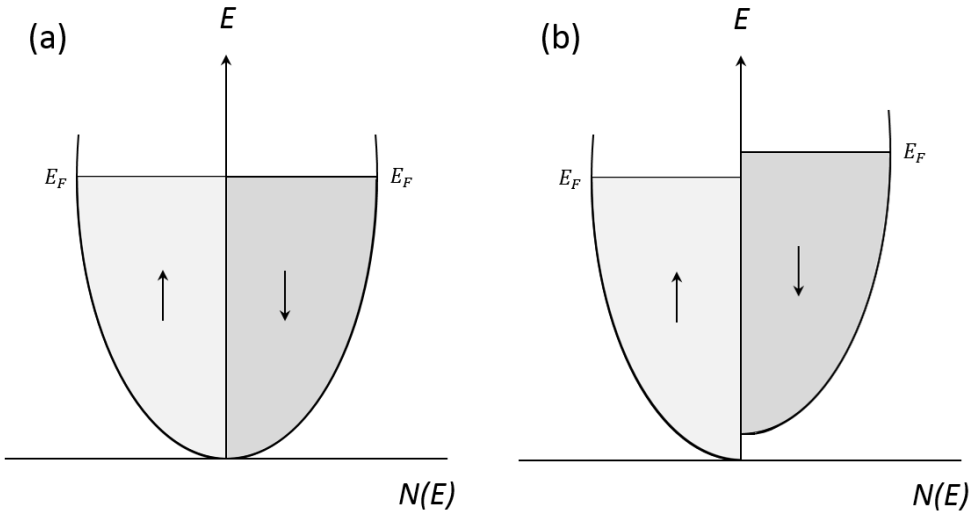

Figure 2.4-3: An illustration of the density of states for electrons in a metal in the absence of an external magnetic field (a) and in an applied external magnetic field (b). The figure is based on the literature [65, p. 375].

Both ferro- and antiferro- magnetic materials (below T_C and T_N, respectively) possess a hysteresis loop when exposed to an external magnetic field; see Figure 2.4-4 for a ferromagnetic material. The reason for this is the existence of magnetic domains (also known as Weiss domains), which are regions of perfectly aligned atomic moments. The lower net magnetic moment stems from the different orientation of these domains. When an external field is applied, the Weiss domains align resulting in increasing magnetization of the material until a saturation point, M_s, is reached. However, when the field is removed, the initial orientations are not fully restored, causing a remnant magnetization, M_r. The difference in the initial and final magnetizations is called hysteresis loop, and is illustrated in Figure 2.4-4 (a). A second magnetic field has to be applied in the opposite direction of the first one in order to remove the remnant magnetization, i.e. to demagnetize the material. The field required for this is called the coercive field, H_c. [63, p. 396-397]. If ferromagnetic NPs are cooled in a magnetic field, the magnetic moments align with the field resulting in maximum magnetization. Then, as the temperature is raised, a certain point is reached called the blocking temperature, T_B, where the thermal energy is greater than the energy

of interaction with the magnetic field and the individual magnetic moments become disordered [63, p. 402].

The size of the magnetic domains is of the order of 10-1000 nm and thus, ferromagnetic/ferrimagnetic NPs composed of single domains can be synthesized. Demagnetization of such NPs becomes harder because the spin-spin coupling within the domain has to be disrupted rather than returning the domains to their original orientations as in bulk ferromagnetic materials. As the size of the NPs becomes even smaller, there are fewer electron spins and thus, the force aligning them is weaker. Superparamagnetism occurs when the particle size is sufficiently small for the spins to flip over to their other orientation under the influence of temperature and in the absence of a magnetic field. Superparamagnetism is different from paramagnetism as it occurs below the Curie temperature [62, p. 396-397]. The variation in coercive field with particle size is illustrated in Figure 2.4-4 (b) where D_c is the size of a single domain. For NPs with coercive field zero, the hysteresis observed in Figure 2.4-4 (a) disappears.

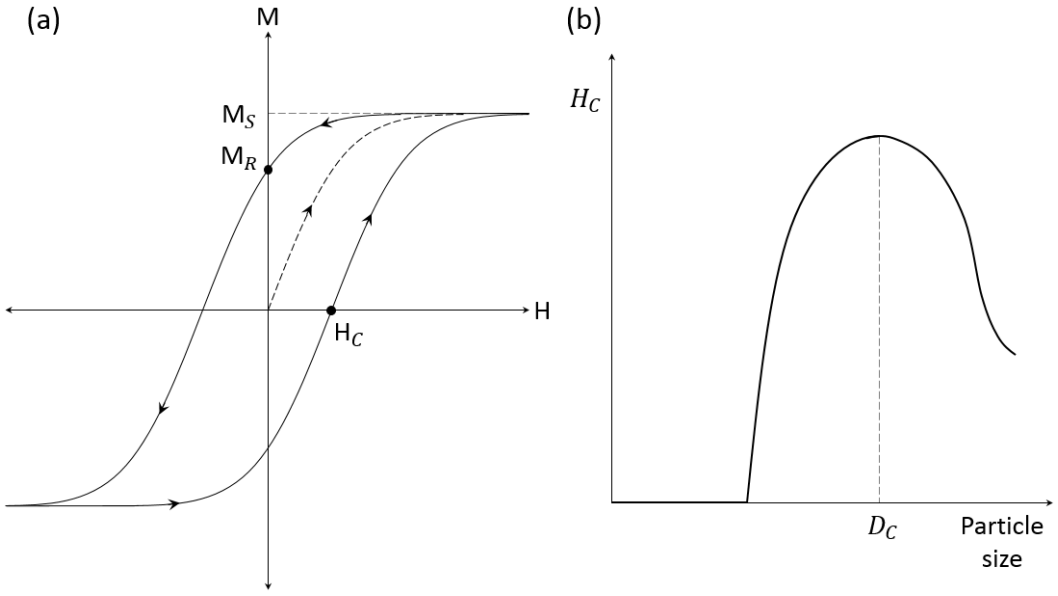

Figure 2.4-4: Plot of magnetization, *M*, of a ferromagnetic material with applied magnetic field, *H*, (a). In addition, plot of the coercive field, H_c, for ferromagnetic NPs with varying particle size (b) The figures are made based on the literature [63, p. 398] and [62, p. 397].

2.5 Characterization of Nanoparticles

The basic working principles of the various characterization techniques used in this thesis are explained in this section along with the type of information that can be extracted for the NPs.

2.5.1 Electron Microscopy

Electron microscopy is a common method for analysis of NPs as it provides information about the particle size and size distribution, morphology and elemental composition. As the name suggests, electrons are used for imaging. In this thesis, two types of electron microscopes are used; the Scanning Electron Microscope (SEM) and Transmission Electron Microscope (TEM). Further, a technique referred to as Scanning Transmission Electron Microscopy (STEM), which combines the working principles of the two was employed. This technique can be used on either of the two microscope types. In this section, some operational modes of the SEM and TEM microscopes are described in light of their relevance to this thesis.

Both instruments consist of an electron source, a system of electromagnetic lenses and apertures, a specimen stage and different types of detectors [4, p. 101-105]. Further, electrons are extracted from a filament forming an electron beam followed by acceleration towards the specimen. The most significant difference between a SEM and a TEM is the maximum energy of the incident electron beam. In the former, it is 30 keV whereas in the latter it is 400 keV. Common for SEM and STEM is that the electron beam is focused to a very small spot and scanned in a raster pattern over the specimen surface. The final image in S(T)EM is assembled from the signal collected at each point in the scanned area of the sample.

Generally, when electrons interact with a specimen, various signals are generated as illustrated in Figure 2.5-1. The volume in the specimen from which the signals are generated is called the interaction volume (Figure 2.5-1). The depth and diameter of the interaction volume depend on the acceleration voltage of the electrons and the specimen density and thus, its shape varies from a tear-drop to a semi-circle [66].

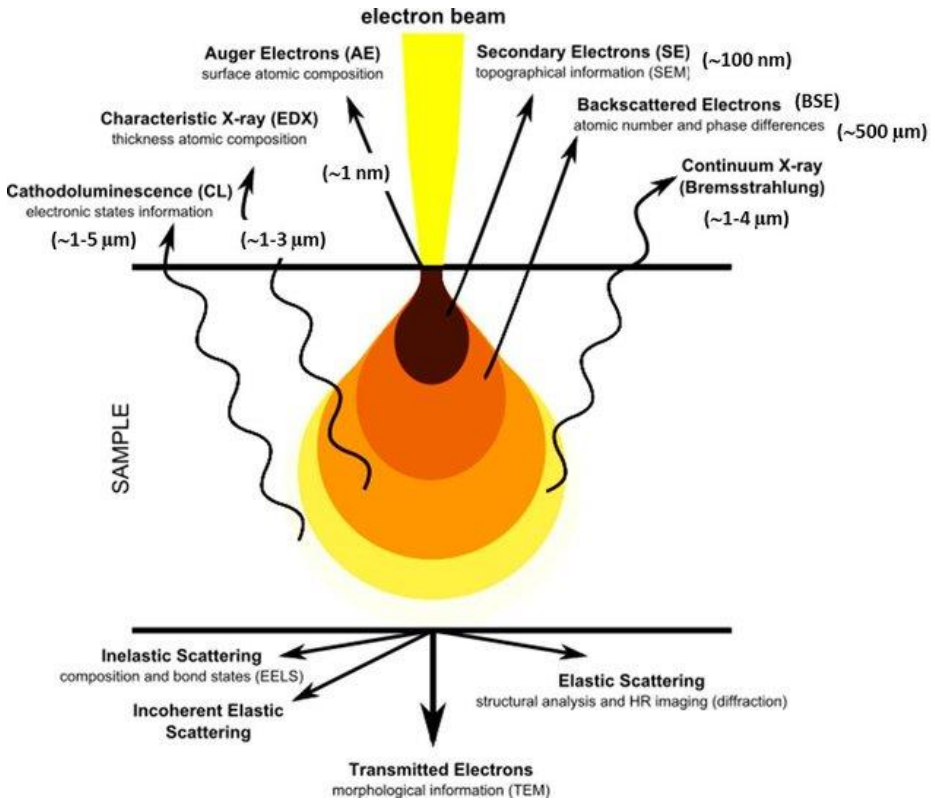

Figure 2.5-1: A schematic illustration of the generated signals and the interaction volume from the interaction between an incident electron beam and a specimen. The figure is taken from literature [67].

In this work, SE and transmitted electrons are used for imaging in SEM whereas transmitted electrons and characteristic X-rays were used for imaging and elemental analysis, respectively, in TEM.

The SEs (Figure 2.5-1) are one type of signal arising from the interaction of an incident electron beam with a specimen. They are ejected from atoms in the specimen as shown in Figure 2.5-2 and are scattered inelastically at small angles. These can be used for topographical information in imaging [68, p. 130].

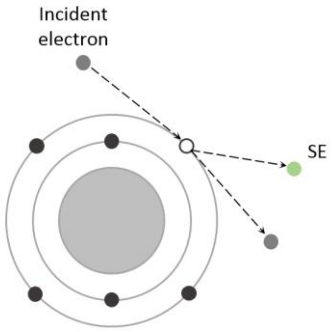

Figure 2.5-2: A schematic diagram of the mechanism of ejecting SEs from a specimen by an incident electron beam. The figure is made based on the literature [68, p. 130].

Another type of signal, which is emitted from a specimen upon exposure to an incident electron beam is characteristic X-rays (Figure 2.5-1) and an illustration of the mechanism of their emission is shown in Figure 2.5-3 (a) and (b). The process happens in two consecutive steps. In the first an incident electron collides with an electron from an inner atomic orbital in an atom of the specimen giving it enough energy to make it leave the atom (Figure 2.5-3 (a)). Then, an electron from an outer orbital drops down to the vacant spot and emits an X-ray with energy equal to the energy difference between the two atomic orbitals (Figure 2.5-3 (b)). The energy gaps between atomic orbitals are characteristic to the specific element as they depend on core charge and the emitted X-rays have energies specific to the element. In addition, there are different types of characteristic X-rays and they are marked according to the orbital which the electron (Figure 2.5-3 (b)) occupies before and after the drop in energy; see Figure 2.5-3 (c). Further, there is less signal emitted from thicker parts of a specimen, because the longer path to the surface gives rise to higher chance of absorbance of the X-rays. However, this is mostly a problem for elements with low atomic number as their characteristic X-rays have lower energy. Another type of X-rays called Bremsstrahlung are also emitted from a specimen when it is illuminated by an incident electron beam (Figure 2.5-1). Figure 2.5-3 (d) shows the mechanism in which they are extracted; an incident electron passing through an atom is accelerated due to electrostatic attraction to the positive nucleus and emits an X-ray in the process [69].

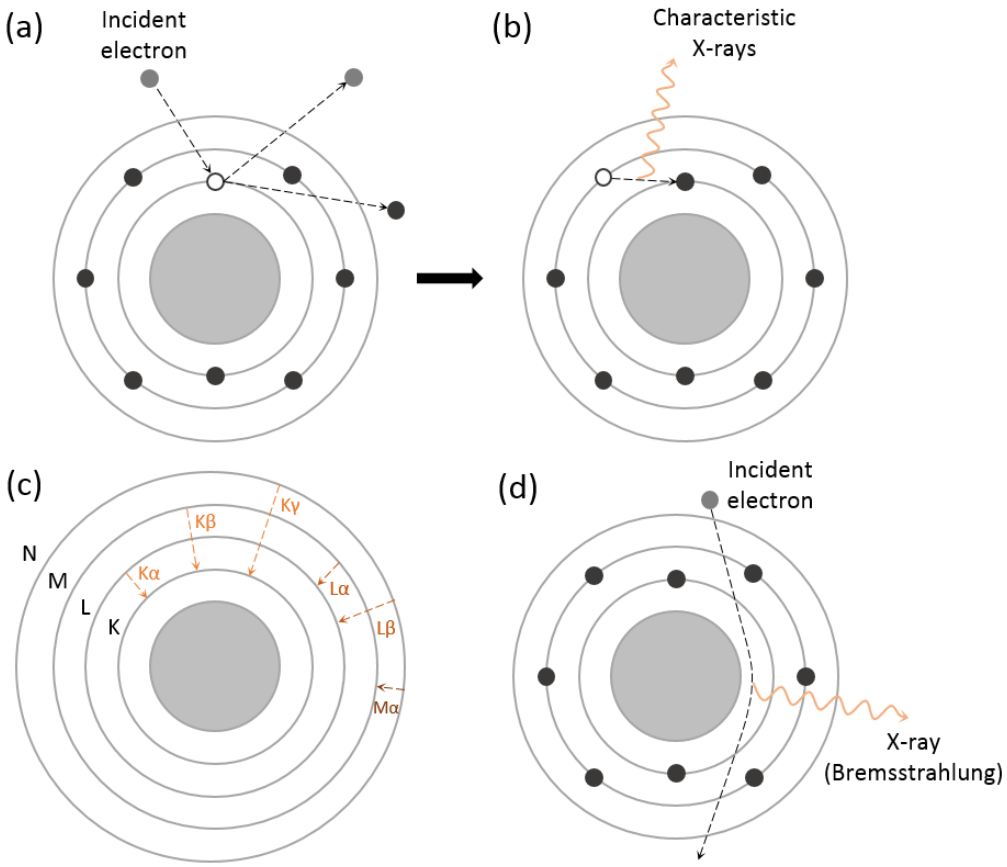

Figure 2.5-3: A schematic diagram of the mechanism of generation of characteristic X-rays from a specimen by an incident electron beam (a) and (b). In addition, illustrations of the different types of characteristic X-rays (c) and the mechanism of emission of Bremsstrahlung X-rays (d). The figure is made based on literature [70, p. 27] and [69].

The SEM allows for surface and elemental analysis of materials, and a really important feature of the instrument is its large depth of field, which is the reason for the three-dimensional appearance of SEM images [68, p. 127]. A schematic illustration of the key components in the SEM is shown in Figure 2.5-4. The electron gun consists of a filament, a Wehnelt electrode and an anode (Figure 2.5-4). The electrons can be extracted by heating of the filament or application of electric field in a thermionic emission or field emission gun (FEG), respectively. In the case of a Schottky FEG, a combination of heating and electric field are used. The Wehnelt electrode and the anode are used to focus the electrons to a crossover and to accelerate them, respectively. The range of acceleration voltages in a SEM is 0-30 keV. The preferred electron sources are FEGs as they provide higher resolution, but they also require higher vacuum and are more expensive [70, p. 16].

The system of electromagnetic lenses in a SEM consists of two condenser lenses and an objective lens (Figure 2.5-4). The purpose of the former two is to reduce the crossover diameter of the electron beam whereas the latter focuses the beam to a point on the surface of the specimen. It is important to minimize the probe diameter as it controls the resolution of the SEM images. The deflection coils control the displacement of the electron beam across the specimen's surface so that it moves in a straight line and it hops over to the next line in a raster motion [68, p. 128-129].

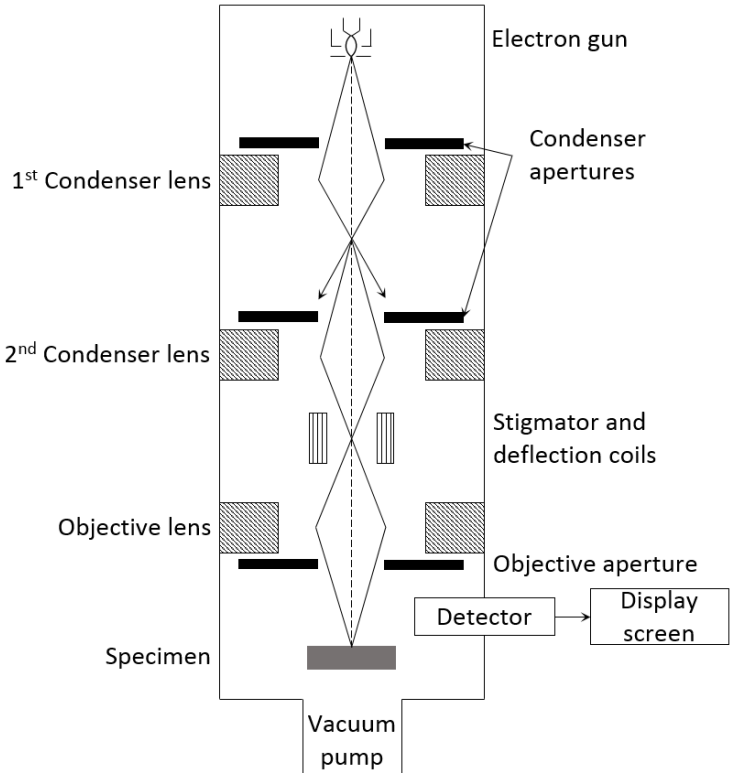

Figure 2.5-4: A schematic diagram of the structure of a SEM. The figure is made based on the literature [68, p. 128].

The electron beam is focused to a point on the specimen's surface after passing through an ideal objective lens whereas in reality the focused probe has aberrations, which result in a blur around it [70, p. 18]. There are different types of aberrations, some of which are spherical and chromatic; see Figure 2.5-5. These two types stem from varying convergence angles for the electrons in the incident beam when passing through a lens depending on the distance between the electrons and the optical axis of a lens for the former and the energy of the electrons for the latter. Figure 2.5-5

(a) shows that the longer the distance from the passing electrons to the optical axis of a lens is, the stronger the convergence angle is, causing spherical aberration. Figure 2.5-5 (b) illustrates that electrons with higher energy converge less than the ones with lower energy resulting in chromatic aberration [69]. A smaller objective aperture and larger acceleration voltage can be used to decrease spherical aberration and chromatic aberration, respectively [70, p. 18]. In addition, a FEG produces a more monochromatic electron beam, which decreases the chromatic aberration [69].

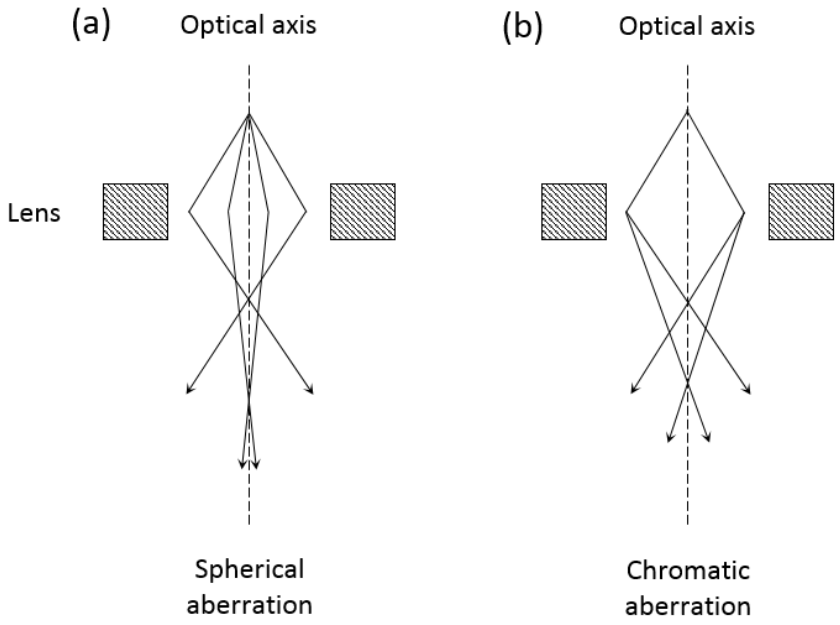

Figure 2.5-5: A schematic diagram of spherical (a) and chromatic (b) aberrations. This figure is made based on the literature [69].

The resolution in a SEM depends on the accelerating voltage of the incident electrons, the type of filament and the lens system. For some SEMs, there is an additional detector for transmitted electrons, which is positioned under the specimen and is called Bright-Field STEM (BF-STEM). BF images are produced from the collection of transmitted electrons. The magnification of the images produced from S(T)EM depends on the ratio between the linear size of the display and the linear size of the area of the specimen which is scanned. Hence, the SEM can provide a wide variation of image magnifications [68, p. 129].

In a TEM, much higher magnification and resolution can be achieved compared to a SEM and one may observe the specimen close to its atomic structure. This is a result from the much higher acceleration voltages which can be used; 60-400 keV. Further, there are two main operational modes. Transmitted electrons are used for imaging whereas the microscope can be used to obtain structural data of the specimen when it is in diffraction mode. In this work, the TEM has been used for imaging in forms of High-Angle Annular Dark-Field STEM (HAADF-STEM) along with Energy Dispersive X-ray Spectroscopy (EDX) element mapping.

A STEM mode in electron microscopy combines the scanning used in SEM with the high resolution which is achieved in TEM. For this technique, the incident electron beam has to be focused to a spot smaller than 1-10 nm and the prepared specimen has to be very thin since the transmitted electrons are collected. When the TEM is operated in STEM mode, there are electrons, which are diffracted at high angles and these can be very useful. The imaging when these electrons are collected is called HAADF-STEM. Figure 2.5-6 shows the relative positions of the BF and the HAADF detectors in TEM. Note that what appears to be two HAADF detectors in the illustration is in fact a ring around the low-angle diffracted beam. The high-angle diffraction signal gives rise to the so-called Z-contrast, which stems from the element composition of a specimen. I.e. the intensity (brightness) of a position in the produced image represents the relative atomic number of the column of atoms in this position in the object. The reason for this can be explained via Bragg's law (section 2.5.2). The coherently scattered electron beam from incident electrons with very short wavelength will be at small angles, i.e. the low-angle diffraction (Figure 2.5-6) whereas the high-angle scattered electrons are produced by deflection from the nuclei in the specimen and hence, this signal is very sensitive to atomic number [62, p. 108-109].

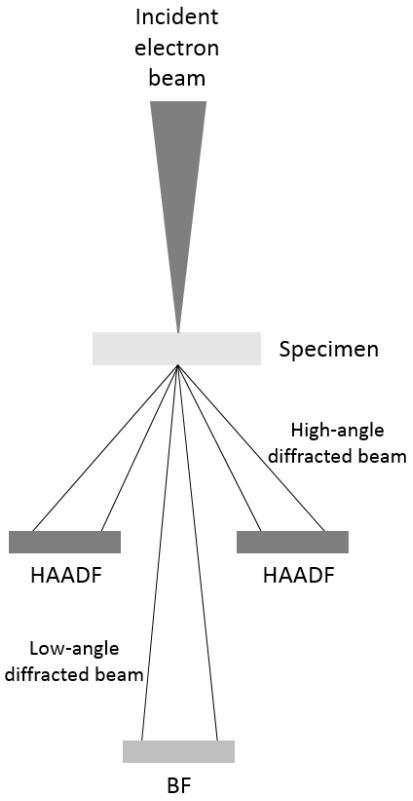

Figure 2.5-6: Schematic diagram of the relative position of a HAADF- and a BF-detector in a TEM. The figure is made based on literature [62, p. 109].

The characteristic X-rays (Figure 2.5-3 (a-c)) can be collected in an EDX detector for analysis of element composition in the specimen. Bremsstrahlung X-rays (Figure 2.5-3 (d)) are also collected in an EDX detector, forming background, which needs to be accounted for during data analysis. Another signal, which is collected by the detector is system X-rays, which are characteristic X-rays generated from the sample holder and for a TEM grid, the elements are often Cu and C [69].

An illustration of the most common EDX detector, which is the Si(Li) type, is reported in Figure 2.5-7. The characteristic X-rays enter the detector and create a number of electron/hole-pairs depending on their energy. These pairs are then separated by an applied bias and the current is measured. Further, the detectors are cooled to -196 ^{0}C to avoid diffusion of dopants in the strong applied bias and thermal noise. In addition, the sample is tilted to avoid shadowing from sample holder. A typical resolution of the energy dispersion is ≈ 150-200 eV and O is the lightest element which can be detected [68, p. 203-204].

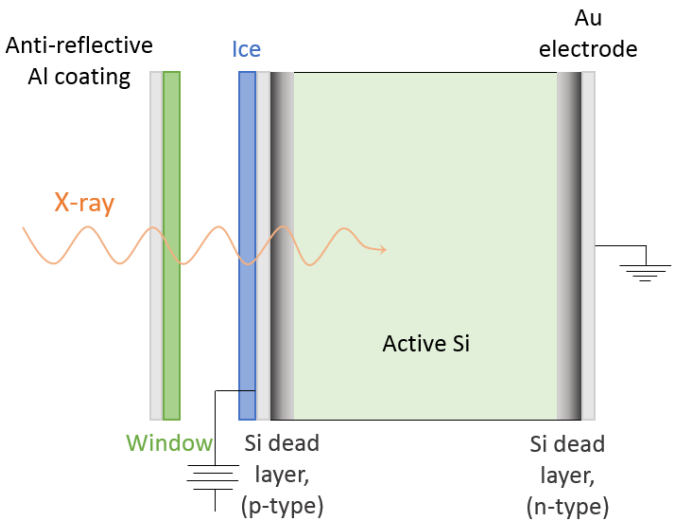

Figure 2.5-7: Illustration of an EDX detector. The figure is made based on the literature [69].

Some of the significant detector artefacts are escape peaks, sum peaks and energy resolution. Sometimes when an X-ray enters the detector, a Si Kα photon is generated and when it leaves the detector it takes some of the energy, which should have gone to the formation of electron/hole-pairs. Hence, the incoming X-ray is interpreted as having less energy than it does and this artefact is called escape peaks. For sum peaks to occur, two X-ray photons must enter the detector with very small time difference, which results in the detector interpreting the information as one X-ray with energy equal to the sum of these two. Finally, two X-rays with energy difference smaller than the energy resolution of the detector cannot be separated and are seen as the same signal [69].

Along with identification of the elements in a specimen, one can also estimate their relative concentrations through quantitative analysis. The result from an EDX element mapping is a spectrum with different peak intensities for the various collected signals and the concentrations of the constituent elements in the specimen are related to these intensities [68, p. 213-215]. The Cliff-Lorimer equation gives the relationship between peak intensities and the corresponding element concentration:

$$\frac{c_A}{c_B} = k_{AB}\frac{I_A}{I_B} \tag{13}$$

where c_A and c_B are the concentrations of elements A and B, k_{AB} is the Cliff-Lorimer k-factor, which is a sensitivity factor for a certain setup and I_A and I_B are the intensities of the peaks originating from elements A and B. Note that this is only valid for thin samples.

2.5.2 Powder X-ray Diffraction

X-ray powder diffractometry is a method for structural analysis of crystalline samples in powder form. There exists many geometries and set-ups for powder X-ray diffraction, and the geometric arrangement of an X-ray diffractometer illustrated in Figure 2.5-8 is of the Bragg-Brentano type [68, p. 62]. Its basic function is to irradiate a sample with X-rays and collect the diffracted signal in a range of diffraction angles, 2θ. Firstly, an X-ray tube consists of two metal electrodes in vacuum and X-ray radiation with a range of wavelengths is generated on the surface of the anode. The diffraction technique requires a source of monochromatic X-rays, i.e. of the same wavelength, and this is achieved by using characteristic X-rays and filtering out the rest. Typically, in home laboratories X-ray tubes producing Cu, Mo, Cr and Ag are used. Further, the radiation is collimated when it passes through the soller and divergence slits (Figure 2.5-8) and it comes into contact with the specimen. The diffracted X-rays pass through the receiving slits, then through a monochromator which filters out all radiation except Kα, and enter the detector. The diffraction measurement is done while the sample and the detector are rotated in such a way so that signal from a range of diffraction angles is collected. It is important to note that θ is the angle between the incident X-ray beam and the crystallographic plane in the specimen which diffracts the signal.

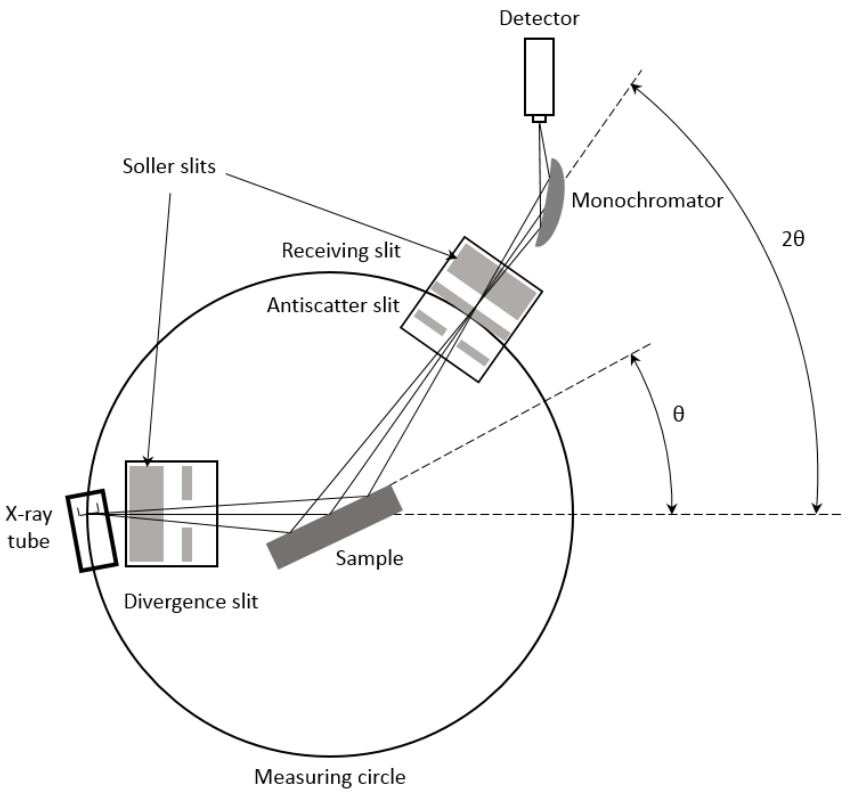

Figure 2.5-8: A schematic diagram of the arrangement of X-ray diffractometer with Bragg-Brentano geometry. The figure is made based on the literature [68, p. 62].

X-ray diffraction is based on wave interference phenomena between two monochromatic waves travelling in the same direction. Depending on their phase difference, the interference can be constructive or destructive, i.e. if they are in phase they will reinforce each other whereas if they are out of phase they will cancel each other out. Being in and out of phase are defined as having a phase difference $n\lambda$ and $\frac{n\lambda}{2}$, respectively for an integer n and a wavelength λ. Any phase difference between these two definitions will result in partial constructive or destructive interference. When two incident X-rays are diffracted by crystallographic planes in a crystalline material, constructive interference between the diffracted waves will occur only when Bragg's law is fulfilled:

$$2d_{hkl} \text{ SIN } \theta = n\lambda \tag{14}$$

where d_{hkl} is the spacing between a series of parallel crystallographic planes with Miller indices (hkl). An illustration of the diffraction mechanism for two waves which are in phase and the geometric conditions from which Bragg's law is derived is reported in Figure 2.5-9 [68, p. 52].

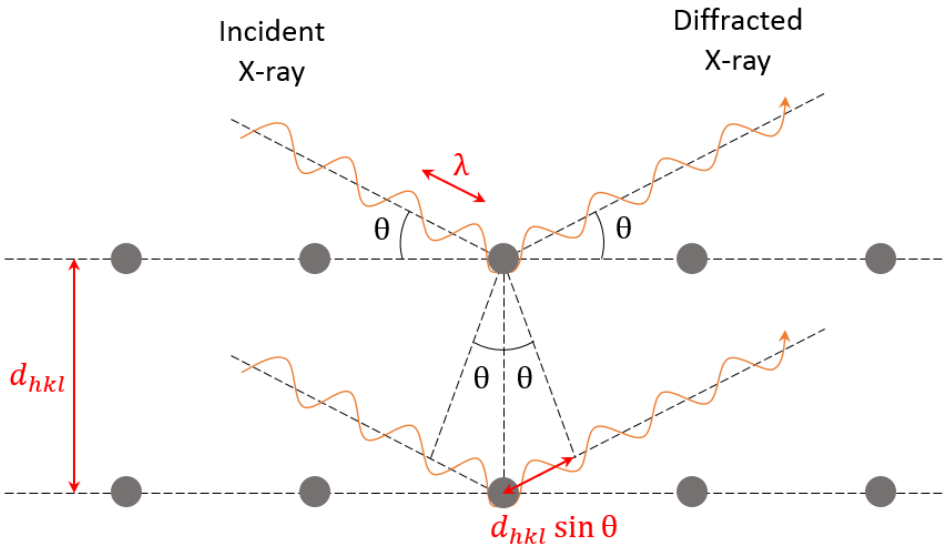

Figure 2.5-9: An illustration of two X-rays (having the same wavelength), which are diffracted by two parallel crystallographic planes with spacing d_{hkl}, and fulfill Bragg's law. The figure is made based on literature [63, p. 46] and [68, p.52].

The spacing (denoted d_{hkl}) between a series of crystallographic planes is obtained from the PXRD measurements and the lattice parameters of the sample can be estimated from it. For a cubic crystal with lattice constant, *a*, the following relationship is given [68, p. 53]:

$$d_{hkl} = \frac{a}{\sqrt{(h^2 + k^2 + l^2)}} \tag{15}$$

Further, the lattice type of the analyzed specimen can be determined from the constructive interferences, which are detected. Structure extinction refers to the interference between scattered X-rays from multiple atoms in one unit cell, which can lead to the extinction of signal from certain crystallographic planes. In order to determined which planes become extinct for specific lattice types, the structure factor, F_{hkl}, is used:

$$F_{hkl} = \sum_{n}^{N} f_n \exp[2\pi i(hu_n + kv_n + lw_n)] \quad (16)$$

where f_n is the atomic structure factor and u_n, v_n and w_n are the atomic coordinates of an atom n in the unit cell. Signal from crystallographic planes (hkl) in a specific lattice type, for which F_{hkl} is equal to zero become extinct and are called forbidden reflections. An overview of the conditions for which reflections are extinct in a simple cubic (SC), body-centered cubic (BCC) and a face-centered cubic (FCC) is reported in Table 2.5-1 [68, p. 60-61].

Table 2.5-1: Structure extinction rules for SC, BCC and FCC lattice types. The table is based on the literature [68, p. 61].

Lattice type	Allowed reflections	Forbidden reflections
Simple cubic (SC)	All h, k and l	None
Body-centered cubic (BCC)	(h + k + l) even	(h + k + l) odd
Face-centered cubic (FCC)	All even or odd	A mixture of even and odd

The reflections in the resulting diffraction pattern should ideally be very sharp (lines), but are in reality peaks with a certain width. There are two factors affecting the reflection width and those are instrumental and particle size. Peak broadening is especially important for the analysis of NPs as the width increases with decreasing particle size. The reason for this is partially destructive interference; see Figure 2.5-10. The curved orange lines represent the incident and diffracted X-rays from a series of planes, which fulfill Bragg's law and thus, have completely constructive interference. Those are the signals which should produce a thin line/sharp reflection in the diffraction pattern of a sample. However, since the incident X-ray beam is not perfectly parallel, there are a range of incident angles (black lines in Figure 2.5-10). In a large particle, there is a high chance of having two incident X-rays which are completely out of phase and will interact destructively. Hence, no signal from these angles will be detected. In a small particle, the chance

of this happening is much smaller and thus, partially constructive interferences from a range of incident angles will be collected in the detector. Hence, the peak broadening [68, p. 68-69].

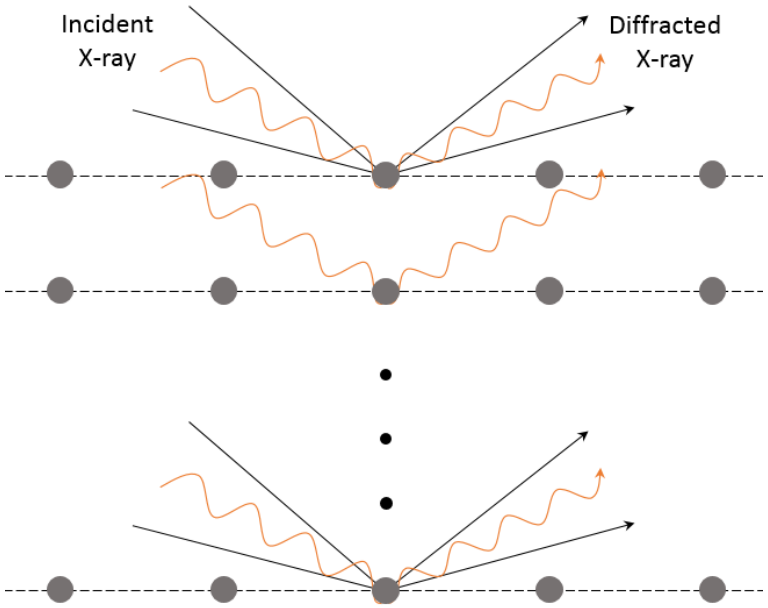

Figure 2.5-10: Diffraction from a large particle (i.e. many parallel planes) illustrating peak broadening with decreasing particle size. The figure is made based on the literature [68, p. 68-69].

For the analysis of the resulting diffraction pattern, Rietveld refinement can be performed. This is a method, which uses mathematical calculations to prepare a theoretical diffraction pattern based on structural data of the sample. The pattern can be refined for a number of parameters so that it looks like the experimental one as much as possible. In this work, the software TOPAS was used to perform Rietveld refinement with structural data for ccp Pt, ccp Ni and ccp Si and fixed temperature- and chemical composition- parameters. Si-NIST [71] is used as a highly crystalline reference material to correct for sample displacement stemming from the broad reflections from NPs. For NPs with nominal compositions $Pt_{100-x}Ni_x$ (x = 80 and 90), the chemical compositions were refined.

The Rietveld refinement method uses a least squares approximation to minimize the difference between the calculated intensity, Y_i^{calc}, and the observed intensity, Y_i^{obs}, in a point, *i*, of the diffraction pattern. The sum for all points across the pattern is given by:

$$M = \sum_i w_i (Y_i^{obs} - Y_i^{calc})^2 \quad (17)$$

where w_i is statistical weight at point i. The quality of the refinement can be estimated visually from the fitting of the calculated diffractogram with the measured one. In addition, it is expressed by a factor R_{wp}, which is given by the following equation:

$$R_{wp} = \sqrt{\frac{M}{\sum_i (w_i Y_i^{obs})^2}} \quad (18)$$

Lower values of R_{wp} indicate that the quality of the refinement is good [72].

2.5.3 Physical Property Measurement System

The physical property measurement system (PPMS) can be used to measure the electronic and magnetic properties of materials. It is common to measure the magnetization, *M*, of a material as a function of temperature, *T*, or applied external magnetic field, *H*. In this master thesis, the field-dependency of magnetization, *M(H)*, was measured and hence, this is described in more detail in this section.

In the instrument, the specimen is held on the end of a thin, rigid sample rod, which is placed within a set of copper coils. The coils are ordered in a first-order gradiometer configuration, which means two sets of counter wound coils are connected in series and separated by several centimeters. This is done to isolate the signal coming from the specimen from the background. The sample holder is translated longitudinally in a rapid and smooth motion while an external magnetic field is applied, which induces voltage in the coil corresponding to the sample's magnetization [73, p. 1-1, 1-2]. In the beginning of the measurement, the applied field is zero and hence, the magnetization in the sample is zero. Then, the applied field is increased to the maximum of the measurement range followed by decrease back to zero. To remove any remnant magnetization in the sample, magnetic field is applied in the opposite direction to the minimum of the measurement range. Finally, the applied field is decreased to zero.

The resulting data from the measurement is the sample's magnetization as a function of the strength of the applied field, usually in the range ± 9 T, at constant temperature. The shape of the magnetization curve depends on the type of magnetism of the material (Figure 2.4-2 (b)) and hence, conclusions about the magnetic properties of the specimen can be made.

3 Experimental

All chemicals and experimental procedures used in the thesis work are presented in this chapter.

3.1 Overview of Used Chemical

An overview of all the chemicals used in this work is reported in Table 3.1-1. All chemicals were used as received.

Table 3.1-1: Overview of the chemicals used in the experimental work of this thesis. See explanations of the alphabetical superscripts at the bottom of the table.

Chemical name and abbreviation	CAS number	Chemical formula	Molar mass [g/mol]	Purity [%]	Supplier
Gold (III) chloride trihydrate	16961-25-4	$HAuCl_4 \cdot 3H_2O$	393.83	99.9	Sigma Aldrich
Platinum (II) acetylacetonate; $Pt(acac)_2$	15170-57-7	$Pt(C_5H_7O_2)_2$	393.29	97	Sigma Aldrich
Nickel (II) acetylacetonate; $Ni(acac)_2$	3264-82-2	$Ni(C_5H_7O_2)_2$	256.91	95	Sigma Aldrich
Chloroplatinic acid hexahydrate	18497-13-7	$H_2PtCl_6 \cdot 6H_2O$	517.9	-	Sigma Aldrich
Nickel (II) chloride hexahydrate	7791-20-0	$NiCl_2 \cdot 6H_2O$	237.69	99.9	Sigma Aldrich
Polyvinylpyrrolidone; PVP10	9003-39-8	$(C_6H_9NO)_n$	10 000[a] 111.14[b]	-	Sigma Aldrich
Polyvinylpyrrolidone; PVP55	9003-39-8	$(C_6H_9NO)_n$	55 000[a] 111.14[b]	-	Sigma Aldrich
Sodium borohydride	16940-66-2	$NaBH_4$	37.83	98.0	Sigma Aldrich
Sodium hydroxide	1310-73-2	NaOH	40.00	99.0	Merck KGaA
1,4-Butanediol; 1,4-BD	110-63-4	$HO(CH_2)_4OH$	90.12	99	Sigma Aldrich
Ethylene glycol; EG	107-21-1	$HOCH_2CH_2OH$	62.07	99.8	Sigma Aldrich
Argon	-	Ar	39.95	99.999	Praxair
Acetone	67-64-1	CH_3COCH_3	58.08	-	VWR
Ethanol	64-17-5	CH_3CH_2OH	46.07	-	VWR

[a]Average molar mass
[b]Molar mass of the monomer

3.2 The Polyol Heat-Up Method

In this section, the experimental procedures are presented in four parts – apparatus and procedure of a typical synthesis, evaluation of reaction kinetics of NP formation, standard synthesis of NPs and a modified synthesis method.

3.2.1 Setup and Procedure of a Typical Synthesis

The apparatus and the procedure of a typical synthesis following the so-called standard polyol heat-up method are presented in this subsection. Figure 3.2-1 shows the apparatus setup, which is used for all experiments in this thesis work. Included are close-up images of a bubbler (Figure 3.2-1 (a)) which is used to visually check if the system is air-tight, a gas adapter (Figure 3.2-1 (b)) which provides Ar gas flow through the system, a three-neck round-bottom flask (Figure 3.2-1 (c)) in which the reaction takes place and a thermocouple inserted in a glass liner (Figure 3.2-1 (d)) which is used to monitor the temperature of the system.

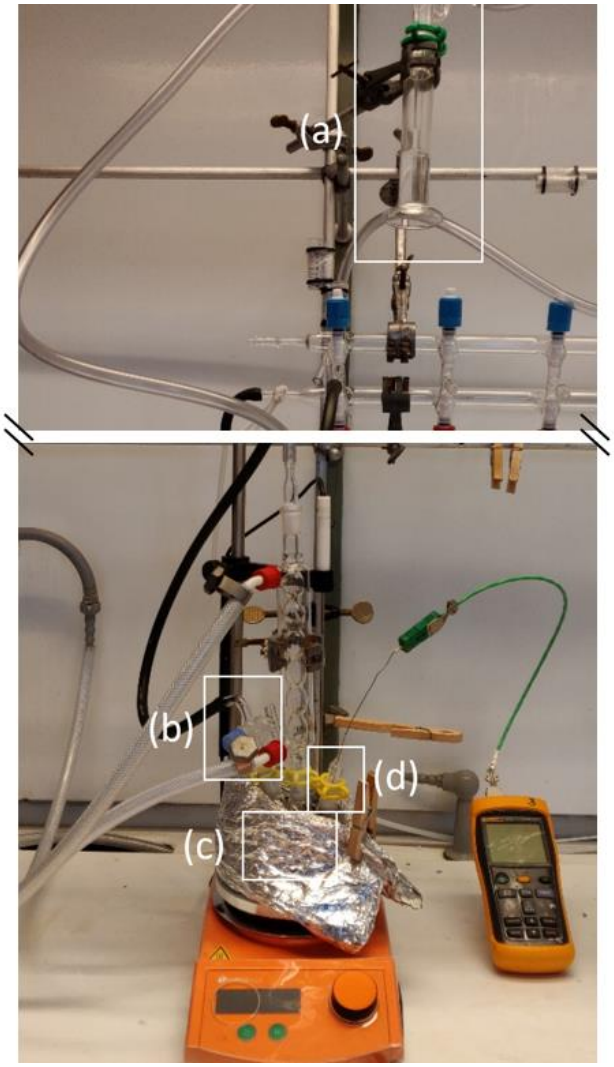

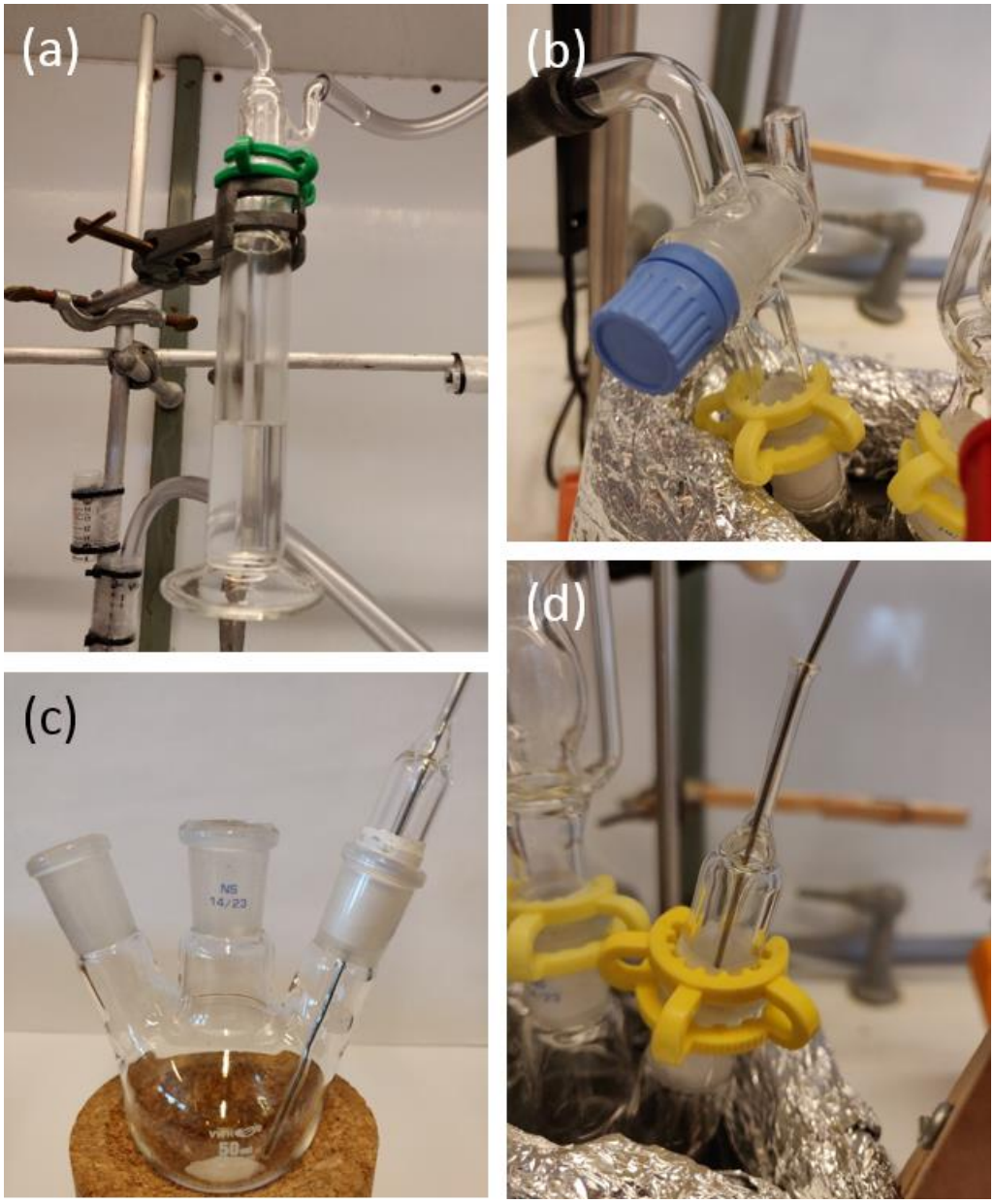

Figure 3.2-1: The experimental setup. Close-up images of the bubbler (a), the gas-adapter (b), the reaction flask (c) and the thermocouple and glass liner inserted in the flask (c and d). The condenser and the bubbler were connected only during the synthesis step (third stage of the procedure). Teflon tape was used in all glass-to-glass connections.

In a typical synthesis, 20 mL solvent was introduced into a 50 mL three-neck round-bottom flask along with a magnetic stirring bar. Then, surfactant was weighed out and transferred to the flask. A gas-adapter was inserted in one side neck of the round-bottom flask, supplying ≈ 200 mL/min Ar gas flow through the system (Figure 3.2-1 (b)). A K-type Fluke 54 II B thermocouple was

inserted into a custom-made glass liner, which in turn was inserted into the flask through the second side neck (Figure 3.2-1 (c) and (d)) to monitor the solution's temperature. The flask was placed on a heating block on a Radleys Carousel Connect heating plate preheated to a given temperature, T_1, and it was fixed to a stand. The flask was isolated with quartz wool wrapped in aluminum foil as shown on Figure 3.2-1 to lower heat loss from the system and the solution was kept at this temperature for 15 minutes under stirring at 1400 rpm. This is referred to as the preheating step and its purpose is to dissolve the surfactant, evaporate water and outgas oxygen.

Then, the round-bottom flask was transferred to a second heating block, which was preheated to a given temperature, T_2. After the solution reached that temperature, metal precursors in targeted molar ratio were transferred to the flask. The solution was kept at this temperature for given time to allow the precursors to dissolve. Hence, this is referred to as the dissolving step. The variation in temperature and time in this step comes from the minimum temperature required for the specific metal precursor to dissolve in the specific solvent in the given time frame.

The flask was then transferred to a third heating block, which was preheated to the targeted reaction temperature, T_3. A condenser was connected and fixed to the flask through its center neck to minimize solvent evaporation; see Figure 3.2-1. The condenser was again connected to a bubbler (Figure 3.2-1 (a)) which allowed to visually monitor whether there were leaks in the system. The solution was kept at this temperature under stirring conditions for 120 min. Finally, the flask was removed from the heating block and the colloidal suspension was let to cool down to below 50 °C. In Figure 3.2-2, a typical temperature-time profile for this type of synthesis is presented.

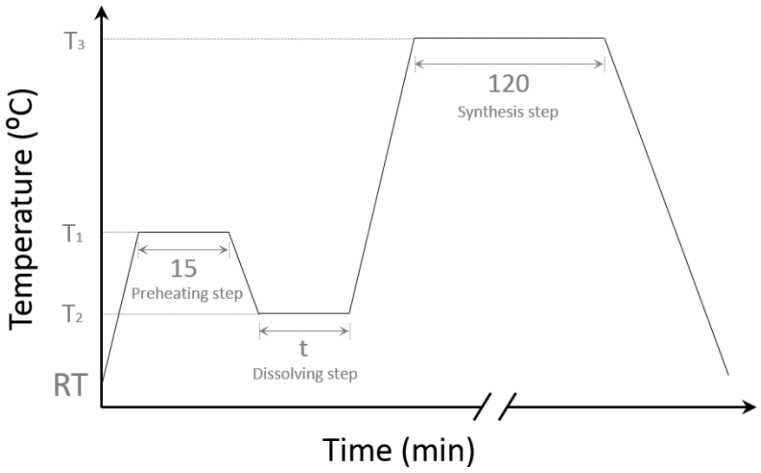

Figure 3.2-2: Temperature-time profile for the polyol heat-up method.

The NPs were washed in order to remove any residual precursors. The colloidal suspension was poured into six 15 mL centrifuge tubes spreading it equally and ≈ 10 mL acetone was added to each of the tubes to achieve flocculation. The tubes were shaken well and sedimentation of the NPs was achieved by centrifugation in an Allegra X-22R centrifuge (4500-7500, 5 min). The supernatant was removed and the washing procedure was repeated two more times.

3.2.2 Reaction Kinetics of NP Formation

Included in this subsection are the experimental details of the reaction kinetics evaluation of NP formation; see Table 3.2-1. Experiments 1-3 studied the reduction kinetics of 0.2 mmol of metal precursors $Pt(acac)_2$ and $Ni(acac)_2$ towards formation of Pt and Ni NPs in the solvents 1,4-BD and 1,4-BD and EG, respectively, in the presence of the surfactant PVP10 with metal ions/PVP monomer ratio 1/10.

Table 3.2-1: Experimental details from the work done on evaluation of reaction kinetics. The following information is given: experiment number, metal precursor, number of moles of metal precursor, solvent, capping agent and metal ions/PVP monomer ratio.

Experiment number	Metal precursor	n_{metal} [mmol]	Solvent	Surfactant	Metal/PVP monomer
1	$Pt(acac)_2$	0.2	1,4-BD	PVP10	1/10
2	$Ni(acac)_2$	0.2	1,4-BD	PVP10	1/10
3	$Ni(acac)_2$	0.2	EG	PVP10	1/10

The experiments were conducted following the procedure described in section 3.2.1 for the first two stages (preheating and dissolving) and then deviating from it. In addition, each of the experiments 1-3 was performed twice – with a quick heating rate and a slow heating rate; see Figure 3.2-3. In the first run, the temperature profile shown in Figure 3.2-3 (a) was followed, i.e. the solution was heated quickly in steps of 10 °C (≈ 10 °C/min) in order to visually determine the approximate temperature at which the solution changes color. In the second run, the solution was first heated quickly in steps of 10 °C (≈ 10 °C/min) and then more carefully in steps of 3 °C (≈ 2.5 °C/min) in the region where the color change was expected; see Figure 3.3-1 (b). Samples were

withdrawn from the reaction mixtures at selected temperatures using a clean glass pipette by quickly removing the thermocouple from the side neck to gain access to the liquid; see Figure 3.2-3 (b and c). The collected samples were photographed for analysis of their colors and SEM samples were prepared for analysis of particle size and morphology (see section 3.3.1).

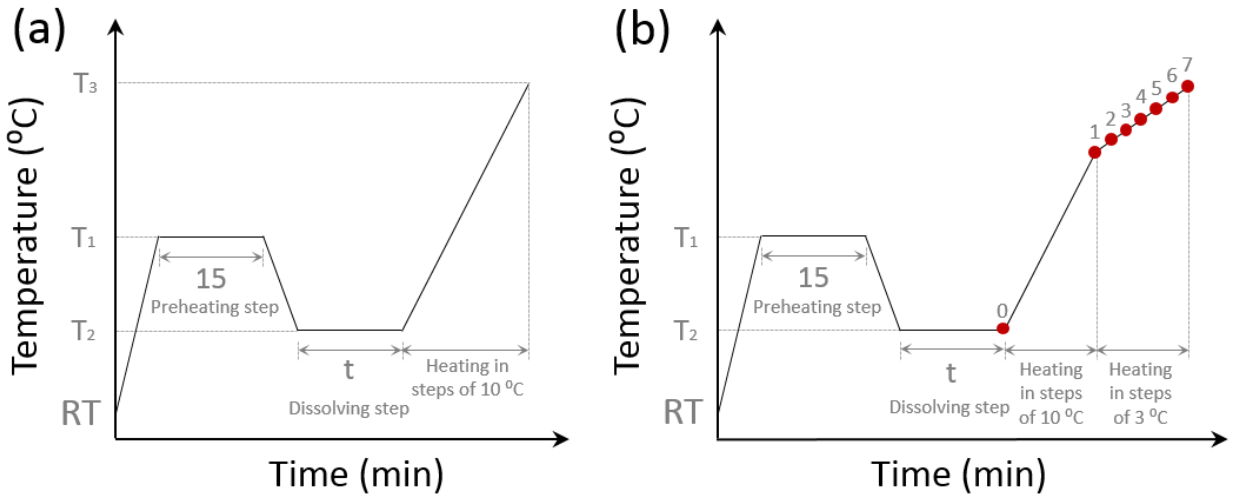

(c)

	T_1 [°C]	T_2 [°C]	T_3 [°C]	t [min]	Temperatures at which samples are collected [°C]							
					0	1	2	3	4	5	6	7
Experiment 1	150	80	200	15	80	184	187	190	193	196	199	-
Experiment 2	150	115	200	15	115	181	184	187	190	193	196	199
Experiment 3	120	95	190	30	95	171	174	177	180	183	186	-

Figure 3.2-3: Temperature-time profiles for the kinetic experiments done with a fast heating rate (a) and a slow heating rate (b). Marked in red are the positions at which samples were collected (b). In addition, a table listing the variables for experiments 1-3 from both heating rates (c).

3.2.3 Standard Synthesis of NPs

Presented in this subsection are the experimental details from the production of $Pt_{100-x}Ni_x$ NPs (x = 0, 10, 20, 25, 30, 40, 50, 60, 70, 80, 90 and 100); see Table 3.2-2.

Table 3.2-2: Experimental details from the synthesis of $Pt_{100-x}Ni_x$ NPs. The following information is given: experiment number, nominal composition, number of moles of $Pt(acac)_2$, number of moles of $Ni(acac)_2$, solvent, surfactant, total metal ions/PVP monomer ratio, metal ions/NaOH ratio, temperatures T_1, T_2 and T_3 and time t. Note that the temperatures and time correspond to the ones in Figure 3.2-2.

Exp. no.	Nominal comp.	n ($Pt(acac)_2$) [mmol]	n ($Ni(acac)_2$) [mmol]	Solvent	Surfactant	Metal/ PVP monomer	Metal/ NaOH	T_1 [°C]	T_2 [°C]	T_3 [°C]	t [min]
4	Pt	0.2	-	1,4-BD	PVP10	1/10	-	150	80	220	15
5	$Pt_{90}Ni_{10}$	0.18	0.02						115		
6	$Pt_{80}Ni_{20}$	0.16	0.04								
7	$Pt_{70}Ni_{30}$	0.14	0.06								
8	$Pt_{60}Ni_{40}$	0.12	0.08								
9	$Pt_{50}Ni_{50}$	0.1	0.1								
10	$Pt_{40}Ni_{60}$	0.08	0.12								
11	$Pt_{30}Ni_{70}$	0.06	0.14								
12	$Pt_{20}Ni_{80}$	0.04	0.16								
13	$Pt_{10}Ni_{90}$	0.02	0.18								
14	Ni	-	0.2								
15	Ni	-	0.2	EG	PVP10	1/10	-	120	95	185	30
16	Ni	-	0.2	1,4-BD	PVP10	1/10	1/50	150	75	220	15
17	Ni	-	0.2	1,4-BD	PVP10	1/10	1/10	150	95	220	30
18	Ni	-	0.1	EG	PVP55	1/10	1/20	120	85	185	15
19	$Pt_{50}Ni_{50}$	0.1	0.1	1,4-BD	PVP10	1/10	-	150	115	220	15
20	$Pt_{10}Ni_{90}$	0.02	0.18	1,4-BD	PVP10	1/100	-	150	115	220	15

Experiments 4-14 studied the change in particle properties with increasing atomic % Ni in NPs produced following the procedure described in section 3.2.1. After the NPs were washed, samples from all were prepared for analysis by means of SEM and PXRD. Additionally, samples from few selected experiments were prepared for analysis by TEM and PPMS (section 3.3).

Experiments 15-18 (Table 3.2-2) studied the change in properties of Ni NPs produced via the procedure described in section 3.2.1 with small changes compared to the Ni NPs prepared in experiment 14. Firstly, the solvent was changed to EG (experiment 15). Then, NaOH (metal

ions/NaOH ratios 1/50 and 1/10 in experiments 16 and 17, respectively) were added to the synthesis mixture before the preheating step (section 3.2.1). Finally, in experiment 18 a few parameters were changed – number of moles of $Ni(acac)_2$ was decreased to 0.1 mmol, the solvent was changed to EG, the surfactant was changed to PVP55 (metal ions/PVP monomer 1/10) and NaOH (metal ions/NaOH ratio 1/20) was added to the reaction mixture after the metal precursor was dissolved. In addition, the temperature-time profile of the last (experiment 18) deviates slightly from the one described in section 3.2.1; see Figure 3.2-4. SEM and PXRD samples were prepared from all (section 3.3).

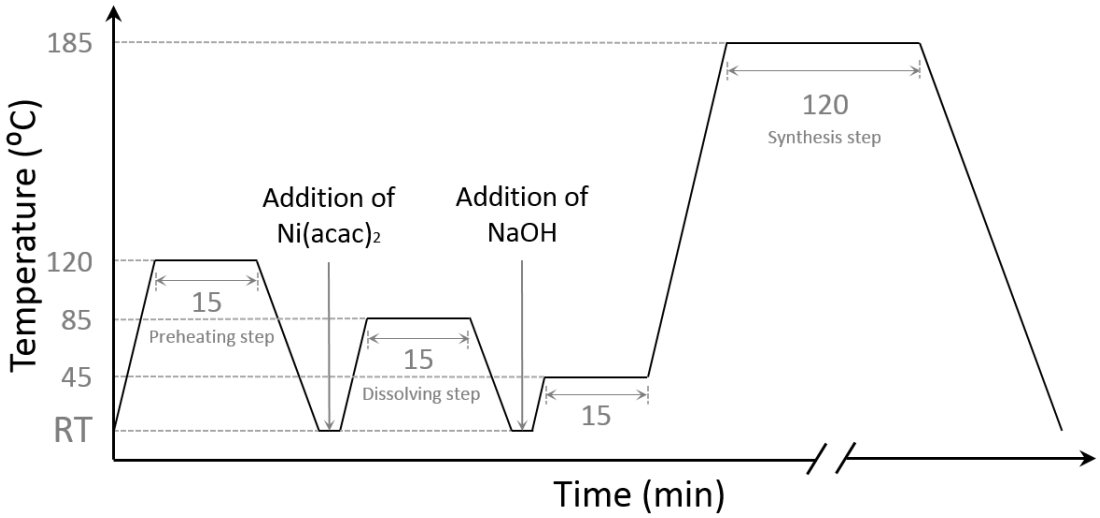

Figure 3.2-4: Temperature-time profile for the synthesis of Ni NPs in the solvent EG with Metal ions/NaOH ratio 1/20 and the surfactant PVP55 (Metal ions/PVP monomer ratio 1/10) (experiment no. 18).

In experiment 19, particle development with increasing synthesis time was studied for NPs with nominal composition $Pt_{50}Ni_{50}$ by collecting samples at selected time points during the synthesis stage of the procedure described in section 3.2.1. The temperature profile for the experiment is reported in Figure 3.2-5 with the time points when samples were collected marked in red. SEM samples were prepared for all time points (section 3.3.1). Based on results from this experiment, a second identical synthesis was performed, but its synthesis time was stopped at 15 min, the colloidal suspension was quenched to RT in ice water and a TEM sample was prepared after the washing procedure (not included in Table 3.2-2 as it was done only for the sample preparation).

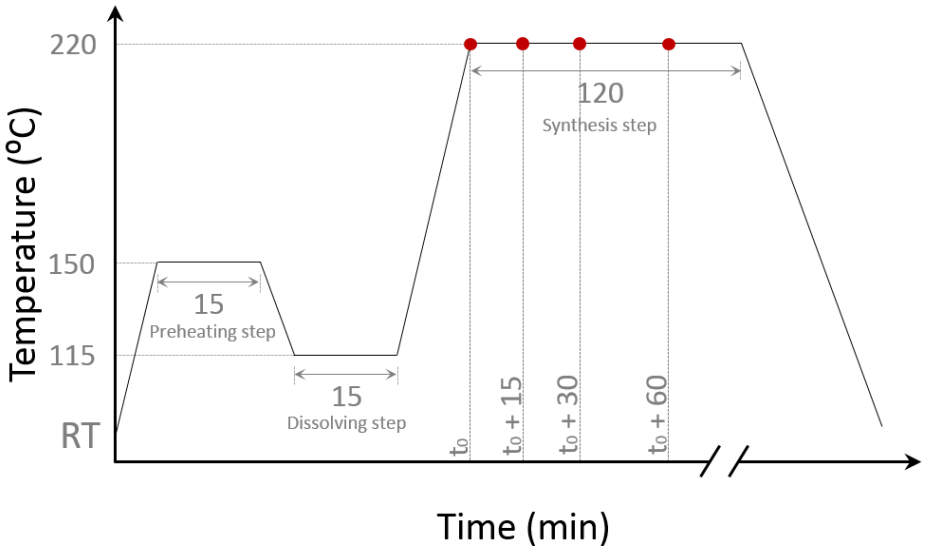

Figure 3.2-5: Strategy for sample collection during the synthesis of $Pt_{50}Ni_{50}$ NPs from the reduction of $Pt(acac)_2$ and $Ni(acac)_2$ in 1,4-BD with PVP10 (Total metal ions/PVP monomer ratio 1/10) (experiment no. 19). Marked in red are the positions at which samples were collected.

In experiment 20, the effect of increased concentration of PVP10 (Metal ions/PVP monomer ratio 1/100) was studied for $Pt_{10}Ni_{90}$ NPs prepared from $Pt(acac)_2$ and $Ni(acac)_2$ in 1,4-BD following the procedure described in section 3.2-1. After the NPs were washed, SEM, PXRD and TEM samples were prepared (section 3.3).

3.2.4 Alternative Polyol Synthesis Method

An alternative polyol synthesis was employed for the preparation of $Pt_{75}Ni_{25}$ NPs. The experimental procedure is described here as it deviates significantly from the one in section 3.2.1. Firstly, 0.045 and 0.015 mmol of $H_2PtCl_6 \cdot 6H_2O$ and $NiCl_2 \cdot 6H_2O$, respectively, were weighed out and transferred to a three-neck round-bottom flask along with a magnetic stirring bar in the glovebox. The flask was sealed by a gas-adapter (closed) in one side neck, a K-type Fluke 54 II B thermocouple inserted in a custom-made glass liner in the second side neck and a glass stopper in the center neck. Then, the flask was removed from the glovebox and transferred to a fume hood where it was fixed to a stand and submerged halfway into an ultrasonic bath. The gas adapter was

connected (open) to a Schlenk line supplying ≈ 200 mL/min Ar gas flow and the glass stopper from the flask's center neck was quickly removed to avoid pressure build-up. 20 mL of EG was introduced into the flask and the ultrasonic bath was turned on to level 9 for 30 min. This is the dissolving step for the metal precursors.

Further, 0.5 mmol of NaOH was weighed out and transferred to a one-neck round-bottom flask with a stopcock-equipped septum inlet, which was connected to the Schlenk line providing ≈ 200 mL/min Ar gas flow. The flask was fixed to a stand and placed on a Radleys Carousel Connect heating plate. 5 mL of EG was added into the flask along with a stirring magnetic bar and stirring conditions were initiated. After the powder was completely dissolved (≈ 15 min), the solution was diluted by a factor of 100 by transferring 0.1 mL to another flask using a clean glass pipette and adding 9.9 mL of EG. This results in a 1 mM solution of NaOH, which is later used for pH regulation.

Then, 0.5 mmol of $NaBH_4$ (total metal ions/$NaBH_4$ ratio ≈ 1/8) was weighed out and transferred to a one-neck round-bottom flask with a stopcock-equipped septum inlet (closed) along with a magnetic stirring bar in the glovebox. A glass stopper was inserted in the flask's neck and the flask was removed from the glovebox and transferred to the fume hood where it was fixed to a stand and placed on a Radleys Carousel Connect heating plate. The septum inlet (open) was connected to the Schlenk line providing ≈ 200 mL/min Ar gas flow and the glass stopper was quickly removed to avoid pressure build-up. 10 mL of EG was added to the flask and the mixture was stirred until the powder was completely dissolved.

Finally, the three-neck round-bottom flask containing the dissolved metal precursors was transferred from the ultrasonic bath to a heating block on a Radleys Carousel Connect heating plate, which was preheated to 70 ^{0}C. 0.2 mL of the prepared 1 mM NaOH solution was added into the flask resulting in pH = 9. After a couple of minutes, 10 mL of the prepared $NaBH_4$ solution was added dropwise (≈ 7 min). Then, the flask was isolated with quartz wool wrapped in aluminum foil to lower heat loss and a condenser was fixed to a stand and connected to the flask through its center neck to minimize solvent evaporation (Figure 3.2-1). The solution was kept at this temperature for 180 min under stirring conditions and the temperature profile for this experiment is illustrated in Figure 3.2-6. After the NPs were washed (section 3.2.1), samples for SEM and PXRD analysis were prepared (section 3.3).

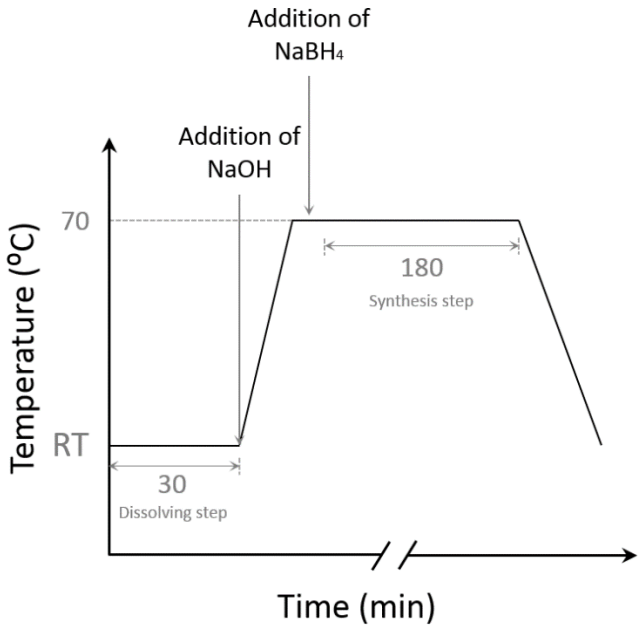

Figure 3.2-6: Temperature profile for the synthesis of $Pt_{75}Ni_{25}$ NPs following a modified polyol synthesis method inspired by the work of Xiong et al. [42].

3.3 Characterization

Technical details regarding the characterization techniques used in this work along with experimental details on sample preparation are described in this section.

3.3.1 Electron microscopy

Analysis by means of electron microscopy techniques was used to study the particle size, morphology and element distribution of the NPs. A typical sample was prepared from either the colloidal suspension directly or the washed NPs which were dispersed in ethanol (Et-OH) with the help of sonication (≈ 1 min). The former was the case for samples collected from the round-bottom flask during the synthesis stage whereas the latter was done for samples collected after the synthesis procedure was completed. The samples for electron microscopy were prepared by placing a drop of the suspension on a carbon coated copper grid (holey carbon, 300 square mesh, Innovative Microscopy Supplies) using a clean glass pipette. Then, the prepared grids were dried

in air (≈ 30 min) followed by drying in the glove box for ≈ 30 min and overnight for analysis by SEM- and TEM-imaging, respectively.

The type of SEM-instrument used in this work is Hitachi SU8230 Ultra High Resolution Cold FE-SEM; see Figure 3.3-1. Before the samples were studied, plasma cleaning (20 watt; 30 s) was done to minimize the carbon contamination. The BF-STEM-detector was typically used for imaging, but for certain samples of NPs it did not provide enough morphological information. In these cases, the SE-detector was used. The SEM-imaging was performed at 25-30 kV acceleration voltage.

Figure 3.3-1: A photo of the SEM-instrument used in this thesis (Hitachi SU8230 Ultra High Resolution Cold FEG-SEM).

The characterization techniques HAADF-STEM and EDX-element mapping were performed on samples using a FEI Titan G2 60-300 kV TEM-microscope, equipped with a CEOS DCOR probe-corrector and Super-X EDS detectors; see Figure 3.3-2. The TEM was used at 300 kV acceleration voltage with a probe convergence angle of 22 mrad. The EDX-element mapping technique was carried out using the software ESPRIT [74].

Figure 3.3-2: A photo of the TEM-instrument used in this thesis (FEI Titan G2 60-300 kV). The photo is taken from reference [75].

Size distribution analysis for histogram preparation was performed using BF-STEM-images of the NPs and the software ImageJ [76]. In order to keep the human error in the measurement from one sample to another approximately constant, all BF-STEM-images used are of the same magnification (300k). The strategy of the size distribution analysis is illustrated in Figure 3.3-3. 250 NPs were measured for the preparation of a size distribution from one sample.

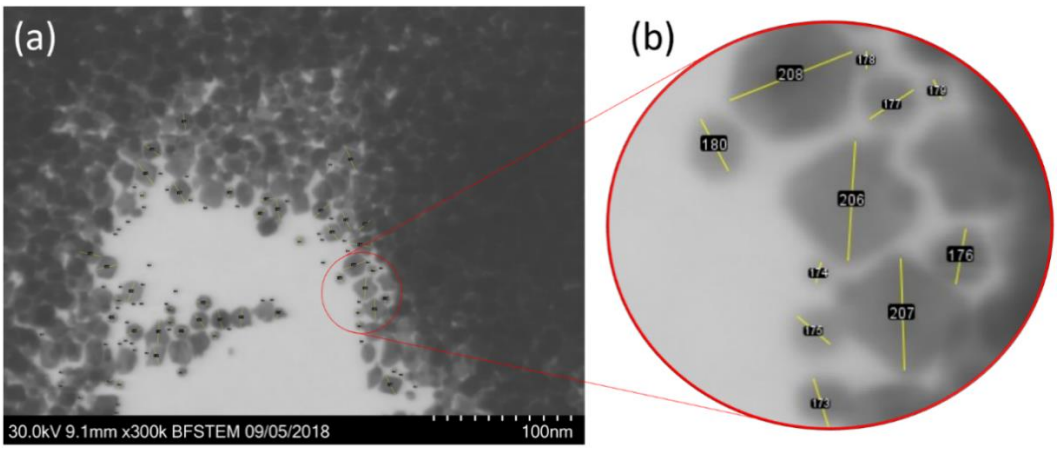

Figure 3.3-3: Strategy of measuring the diameter of 250 NPs for size distribution data collection using the software ImageJ [76].

3.3.2 Powder X-ray Diffraction

Analysis by means of PXRD was used for phase identification and evaluation of the unit cell dimensions. For the preparation of a typical PXRD-sample, the washed NPs were dispersed in Et-OH with the help of sonication (≈ 1 min). Then, a reference material Si-NIST [71] was weighed out and transferred to a mortar (Si-NIST/NPs molar ratio 1/3). The suspended NPs were added to the mortar and the mixture was homogenized using a pestle. Finally, the mixture was dripped on a single-crystal Si sample holder using a clean glass pipette and the sample was dried in air (≈ 15 min) followed by drying in the glovebox overnight.

The XRD-instrument used in this thesis is a Bruker D8 Discover (Figure 3.3-4) in Bragg-Brentano geometry, equipped with a Ge(111) monochromator and a Cu-anode for a monochromatic Cu $K_{\alpha 1}$ radiation with wavelength 1.5406 Å. Two consecutive measurements were done for each prepared sample in the 2θ range 30-95^0. The first was a large-step scan optimized for small NPs whereas the second was a small-step scan optimized for the reference Si-NIST material. The conditions are listed in Table 3.3-1.

Rietveld structure refinement was performed for phase identification and estimations of the unit cell dimensions using the software TOPAS [77]. The *a*-axis of the reference Si-NIST was fixed at 5.43086 Å [71]. The refined parameters were *a*-axis and crystallite size of the NPs, background,

sample height displacement and zero point error. The temperature factor was fixed. Structure data for ccp Pt and ccp Ni was used. For $Pt_{100-x}Ni_x$ (x = 80 and 90), the element composition of the structure data was refined whereas it was fixed for the rest.

Figure 3.3-4: A photo of the XRD-instrument used in this thesis (Bruker D8 Discover).

Table 3.3-1: Conditions used for PXRD-measurements in this work.

Scan optimized for	2θ range [^{0}]	Step size [^{0}]	Step time [s]
Si-NIST reference	30-95	0.016	19.20
NPs		0.100	1152.00

3.3.3 Physical Property Measurement System

A typical sample for PPMS analysis was prepared from the washed NPs, which were dispersed in ethanol with the help of sonication (≈ 1 min). The suspension was transferred to a small glass vial before drying in the glove box overnight. The rest of the sample preparation was done in the glove box. First, one gelatin capsule and the smaller half of a second one were weighed. Then,

the NPs were transferred to the half capsule using a metal spatula and a glass funnel. The whole capsule was connected to the half in such a way so that the NPs were immobilized in-between the two and the capsule was weighed again. Super-glue followed by Scotch-tape were used to seal the gelatin capsule. Finally, the capsule was inserted halfway into one end of a plastic straw and Scotch-tape was used to immobilize it. Outside the glovebox, the straw was cut to a standard length and tweezers were used to poke holes into it.

Magnetization data was measured using a Quantum Design® Physical Property Measurement System (PPMS) (Figure 3.3-5) using the DC Susceptibility (ACMS) option. All samples for DC magnetization measurements were held in gelatin capsules and studied at 300 K for applied fields of up to ± 9 T. In addition, a blank experiment was collected to correct for the diamagnetic contribution. Origin software was used for processing of the acquired data [78].

Figure 3.3-5: A photo of the PPMS-instrument used in this thesis (Quantum Design® Property Measurement System).

4 Results

Results from the experimental work in this thesis are presented in this chapter. The work was initiated by evaluating the reduction kinetics of the metallic precursors $Pt(acac)_2$ and $Ni(acac)_2$ for the formation of free-standing monometallic NPs; see experimental details in section 3.2.2. Pt and Ni NPs were then produced following the polyol heat-up method using our standard conditions. Synthesis of Ni NPs with parameters other than the standard ones were performed with the intention to optimize the method with focus on particle -size and -morphology; see experimental details in section 3.2.3. The experimental work was proceeded with synthesis and characterization of free-standing $Pt_{100-x}Ni_x$ NPs (x = 0, 10, 20, 30, 40, 50, 60, 70, 80, 90 and 100) applying the polyol heat-up method at our standard conditions described in detail in section 3.2.3. The results chapter ends with optimization of the method employed for synthesis of $Pt_{100-x}Ni_x$ NPs by changing key parameters of the polyol method and by employing a new strategy, which has been successful for the production of phase pure $Pt_{100-x}Ni_x$ NPs (x = 20, 25, 33 and 50) in a previous work [42]; see experimental details in sections 3.2.3 and 3.2.4, respectively.

4.1 Pt and Ni NPs Produced via the Polyol Heat-Up Method

In this subchapter, results gathered from the synthesis and characterization of free-standing Pt and Ni NPs by the polyol method are presented. An overview of all experiments performed in this part of the work is given in Table 4.1-1. This includes experimental work done on kinetics evaluations of $Pt(acac)_2$ and $Ni(acac)_2$, synthesis of Pt and Ni NPs via the standard polyol heat-up method and modifications of the synthesis method for preparation of Ni NPs.

Table 4.1-1: Experimental work done on Pt and Ni NPs. In this table, the following information is given: experiment number, experiment type, metal precursor, solvent, surfactant, metal ions/NaOH ratio, analysis methods used, particle size found from size distribution analysis and unit cell dimensions found by means of PXRD. The uncertainty for the unit cell dimensions is only the mathematical one originating from the refinement.

Exp. no.	Experiment type	Metal precursor	Solvent	Surfactant	Metal ions/ NaOH	Analysis methods			Particle size [nm]	Unit cell dimensions [Å]
						Visual	SEM	PXRD		
1	Kinetics evaluation	$Pt(acac)_2$	1,4-BD	PVP10	-	✓	✓	-	-	-
2	Kinetics evaluation	$Ni(acac)_2$	1,4-BD	PVP10	-	✓	✓	-	-	-
3	Kinetics evaluation	$Ni(acac)_2$	EG	PVP10	-	✓	✓	-	-	-
4	Standard synthesis	$Pt(acac)_2$	1,4-BD	PVP10	-	-	✓	✓	17.0 ± 4.0	**ccp:** 3.9221 ± 0.0001
5	Standard synthesis	$Ni(acac)_2$	1,4-BD	PVP10	-	-	✓	✓	67.6 ± 19.3	**ccp:** 3.5277 ± 0.0002
6	Standard synthesis	$Ni(acac)_2$	EG	PVP10	-	-	✓	✓	-	**ccp:** 3.5252 ± 0.0001
7	Modified synthesis	$Ni(acac)_2$	1,4-BD	PVP10	1/50	-	✓	-	-	-
8	Modified synthesis	$Ni(acac)_2$	1,4-BD	PVP10	1/10	-	✓	✓	-	**ccp:** 3.5293 ± 0.0009 ; **hcp:** 2.6490 ± 0.002 and 4.3345 ± 0.0006
9	Modified synthesis	$Ni(acac)_2$	EG	PVP55	1/20	-	✓	✓	-	**ccp:** 3.5255 ± 0.0001

4.1.1 Reduction Kinetics of $Pt(acac)_2$ and $Ni(acac)_2$ towards NP formation

The reactivity of the metal precursors $Pt(acac)_2$ and $Ni(acac)_2$ towards NP formation was studied in the solvents 1,4-BD and 1,4-BD and EG, respectively, in the presence of the capping agent PVP10 (experiments 1, 2 and 3 in Table 4.1-1). Experimental details are given in section 3.2.2. The temperature necessary for the metal precursor to reduce and form nuclei is determined visually by inspecting the change of color of the suspension. For each system, two separate experiments were performed. In the first run, the solution was heated quickly and the approximate temperature where the color changed, was recorded. During the temperature ramping of the synthesis batch in the second run, samples were collected at different temperatures starting a few degrees below the expected nucleation temperature and stopping a few degrees after the suspension had clearly changed color. A reference sample (sample 0) was taken out at the minimum temperature necessary for the specific metal precursor to dissolve in the specific solvent. In addition, all samples were analyzed by SEM imaging to confirm particle formation, and some selected BF-STEM images are reported. For each experiment, the reported images include the first sample in which NPs were detected and the last sample collected in the given temperature range. The selection is made with the intention to show NP development with increasing temperature.

For the reactivity of $Pt(acac)_2$ in 1,4-BD, samples were taken out in the temperature interval from 184 to 199 ^{0}C in steps of 3 ^{0}C, and with a reference sample (sample 0) at 80 ^{0}C; see Figure 4.1-1. The experiment was carried out with a heating rate of approximately 2.5 ^{0}C/min. The color of the $Pt(acac)_2$ solution is changing gradually from the first sample taken out at 184 ^{0}C (sample 1) until the last sample taken out at 199 ^{0}C (sample 6). A careful visual color comparison of the suspensions at 187 ^{0}C (sample 2) and 190 ^{0}C (sample 3), indicates the nucleation temperature to be $\approx$ 190 ^{0}C due to the latter being slightly darker. It is important to note that a more distinct color change was observed in the reaction flask from which the samples were taken out, which could not be easily documented through these photographs. For a direct comparison, the accumulated time it took for the suspension to reach the final temperature was recorded with the intention to keep it approximately constant when experiments on the NP formation from $Ni(acac)_2$ precursor in 1,4-BD, were performed. Since time is a parameter which can affect nucleation and particle growth, in this way, the reaction kinetics of the two precursors could be compared later on.

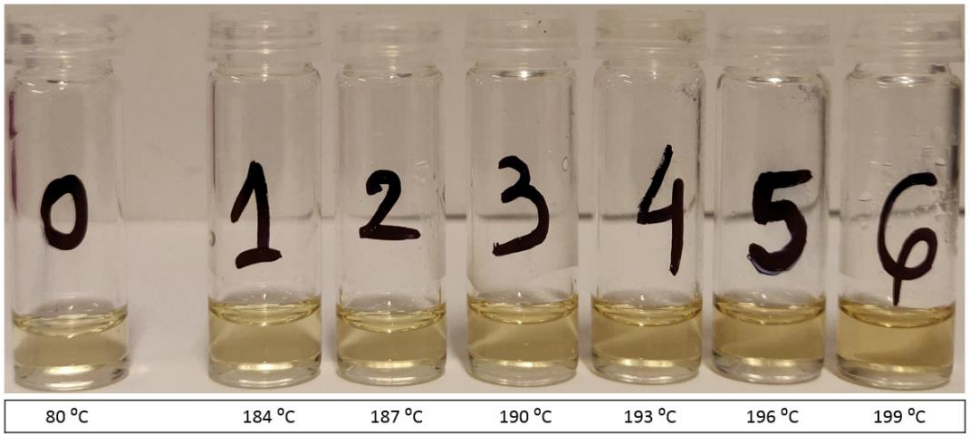

Figure 4.1-1: Color change in samples taken out at selected temperatures in the temperature range from 184 to 199 ^{0}C during the Pt NP formation obtained by reaction from $Pt(acac)_2$ in 1,4-BD in the presence of PVP10. Heating rate is ≈ 2.5 ^{0}C/min.

To confirm the onset temperature of NP formation from $Pt(acac)_2$ in 1,4-BD, all samples (samples 1-6) were analyzed by SEM. In Figure 4.1-2 BF-STEM images of sample number 2 and 6 are reported. BF-STEM images for all samples are reported in the appendix (9.1.1). The first sample in which NPs were detected by means of SEM is the one taken out at 187 ^{0}C (sample 2); see Figure 4.1-2 (a). This confirms that there are NPs in the suspension at 190 ^{0}C (sample 3) as previously suspected from the observed color change, but it also shows that NPs are already formed at 187 ^{0}C which could not be detected visually. The nucleation temperature for $Pt(acac)_2$ in 1,4-BD in the presence of PVP10 is therefore estimated more correctly to be 187 ^{0}C. Figure 4.1-2 shows that reduction of the metal precursor $Pt(acac)_2$ in 1,4-BD following the polyol heat-up method results in formation of small, well-dispersed Pt NPs in the given temperature range. The NPs found in the suspension at 187 ^{0}C (sample 2) shown on Figure 4.1-2 (a) are fewer and smaller than the NPs found in the suspension at 199 ^{0}C (sample 6) shown on Figure 4.1-2 (b). Thus, it was established that with increasing temperature, more nuclei are formed and the NPs grow in size. Note that the reported images are representative and the NPs are too small to prepare size distribution histograms.

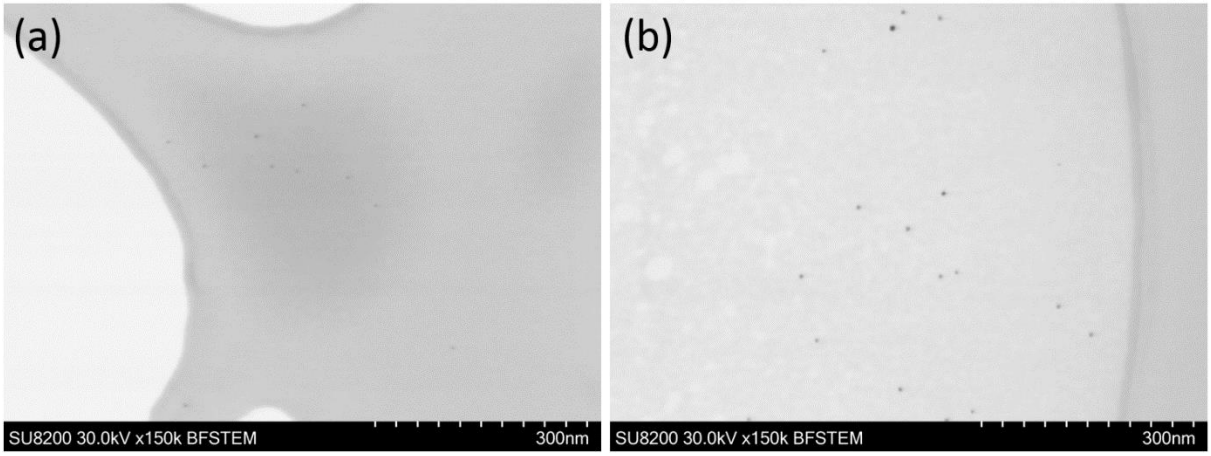

Figure 4.1-2: BF-STEM images of Pt NPs formed from the reduction of $Pt(acac)_2$ in 1,4-BD with capping agent PVP10 at a suspension temperature of 187 ^{0}C (sample 2) (a) and 199 ^{0}C (sample 6) (b).

For the reactivity of $Ni(acac)_2$ in 1,4-BD, samples were taken out at 181 – 199 ^{0}C in intervals of 3 ^{0}C. The reference sample (sample 0) was taken out at 115 ^{0}C; see Figure 4.1-3. The applied heating rate was approximately 2.6 ^{0}C/min. The color of the $Ni(acac)_2$ solution in 1,4-BD changes gradually in the temperature interval from 181 to 199 ^{0}C. The temperature at which the metal precursor starts to reduce and forms nuclei is visually estimated to be approximately 187 ^{0}C by carefully comparing the color of the suspensions taken out at 184 ^{0}C (sample 2) and 187 ^{0}C (sample 3). The latter sample (sample 3) is slightly darker.

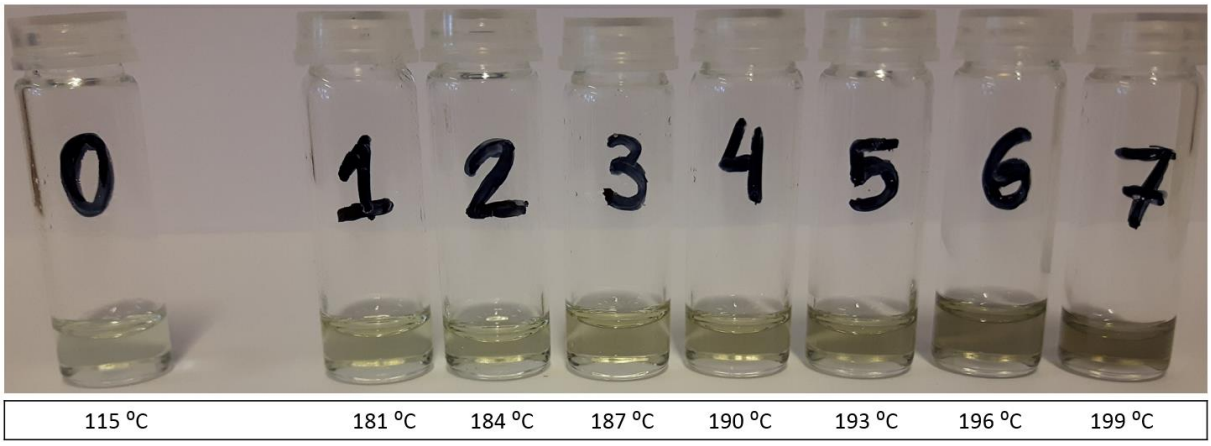

Figure 4.1-3: Color change in samples taken out selected temperatures in the temperature range from 181 to 199 ^{0}C during the Ni NP formation obtained by reaction from $Ni(acac)_2$ in 1,4-BD in the presence of PVP10. Heating rate is ≈ 2.6 ^{0}C/min.

All samples (samples 1-7) were subsequently analyzed by SEM with the purpose to confirm the nucleation temperature of this system. In Figure 4.1-4 BF-STEM images of samples 1 and 7 are reported. BF-STEM images for all samples are given in the appendix (9.1.1). The NPs were first detected by SEM in the suspension taken out at 181 ^{0}C (sample 1); see Figure 4.1-4 (a and b). This confirms the presence of NPs in the suspension taken out at 187 ^{0}C (sample 3) as observed by the change in color and further, the temperature for NP formation is estimated to be 181 ^{0}C. Figure 4.1-4 shows that the reduction of $Ni(acac)_2$ in 1,4-BD with capping agent PVP10 produces agglomerates of small NPs in the given temperature range. The NPs found in the suspension at 181 ^{0}C (sample 1), Figure 4.1-4 (a and b), are fewer and smaller than the ones found in the suspension at 199 ^{0}C (sample 7) shown in Figure 4.1-4 (c and d). It was therefore concluded that with increasing temperature more nuclei were formed and the size of the NPs increased. Note that the reported images are representative and size distribution analysis could not be conducted due to the agglomeration of the NPs. Further, some faceted well-dispersed NPs are present in the suspension at 199 ^{0}C (sample 7), Figure 4.1-4 (d), marked with red circles. Their presence could suggest further faceting of NPs beyond the studied temperature and time ranges. The results from the reduction of $Ni(acac)_2$ in 1,4-BD are the reason behind testing the reactivity of the metal precursor in another solvent (EG) (see below).

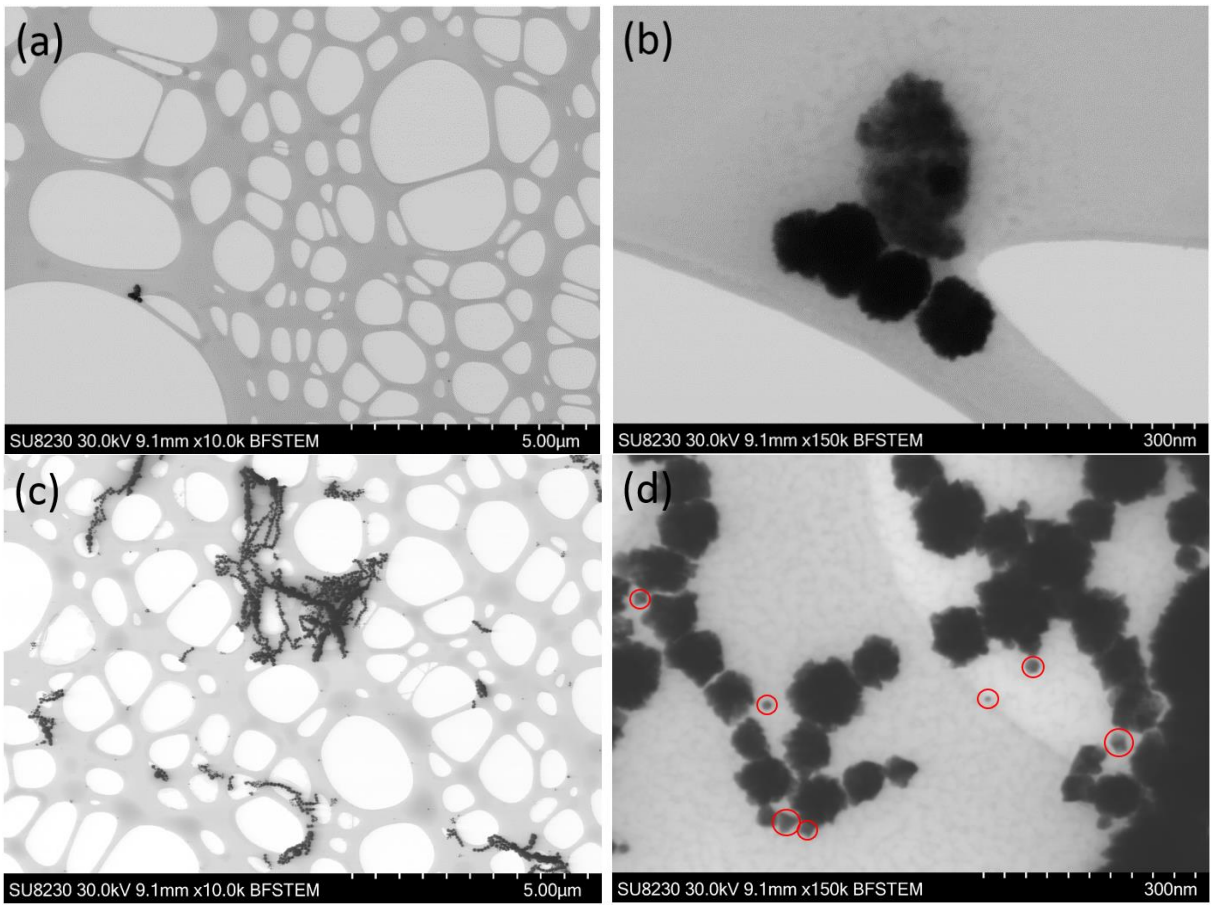

Figure 4.1-4: BF-STEM images of Ni NPs formed from the reduction of $Ni(acac)_2$ in 1,4-BD with capping agent PVP10 at a suspension temperature of 181 ^{0}C (sample 1) (a and b) and 199 ^{0}C (sample 7) (c and d). Some faceted well-dispersed NPs are marked with red circles (d).

Finally, the reactivity of $Ni(acac)_2$ in EG was explored, and samples were taken out in the temperature interval from 171 to 186 ^{0}C in steps of 3 ^{0}C and with a reference sample (sample 0) at 95 ^{0}C; see Figure 4.1-5. The experiment was carried out with a heating rate of approximately 2.5 ^{0}C/min. Figure 4.1-5 shows a gradual color change of the $Ni(acac)_2$ solution in EG upon heating it in the above mentioned temperature interval. The nucleation temperature for this system is estimated to be 183 ^{0}C by visually comparing the colors of the suspensions taken out at 180 ^{0}C (sample 4) and 183 ^{0}C (sample 5).

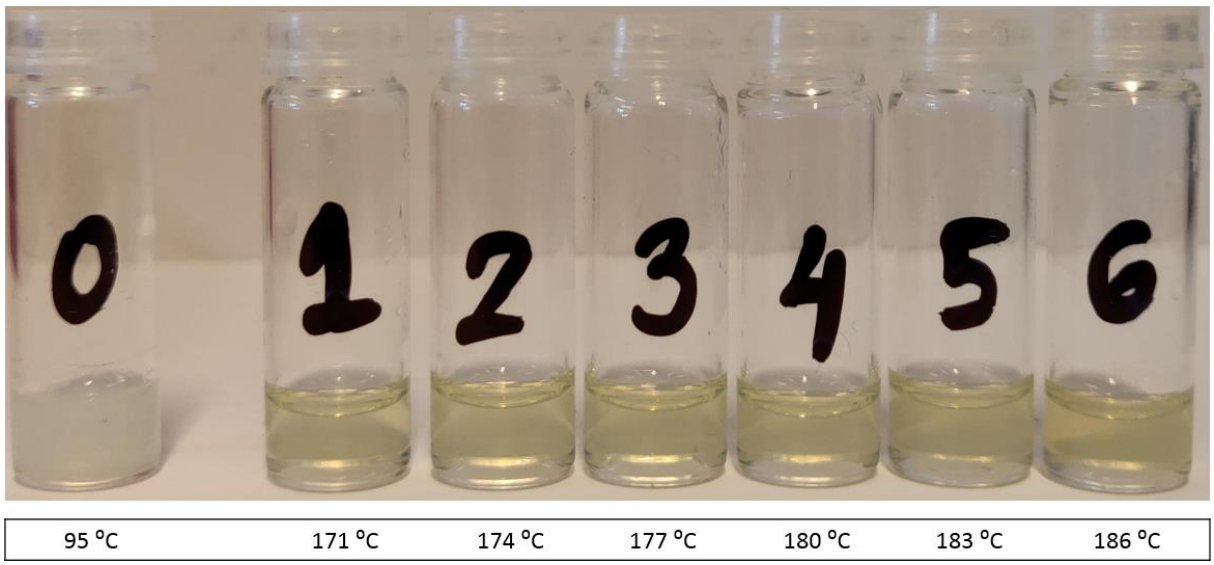

Figure 4.1-5: Color change in samples taken out selected temperatures in the temperature range from 171 to 186 ^{0}C during the Ni NP formation obtained by reaction from $Ni(acac)_2$ in EG in the presence of PVP10. Heating rate is ≈ 2.5 ^{0}C/min.

For the nucleation temperature to be confirmed all samples (samples 1-6) were then analyzed by SEM, and SEM images for samples 1 and 6 are reported in Figure 4.1-6. SEM images for all samples are included in the appendix (9.1.1). NPs were detected by SEM already in the first sample collected in the above mentioned temperature interval, i.e. at 171 ^{0}C (sample 1), Figure 4.1-6 (a). This experiment was attempted a few times with no success to estimate the nucleation temperature for $Ni(acac)_2$ in EG. Each time, samples were taken out at lower temperatures (compared to the previous attempt), but NPs were still found in the first collected sample in the given temperature interval. Further, dissolving of the metal precursor in EG proved to be more challenging than in 1,4-BD. Hence, there could have been heterogeneous nucleation. Figure 4.1-6 shows that the reduction of $Ni(acac)_2$ in EG in the presence of PVP10 results in aggregated NPs in the given temperature range.

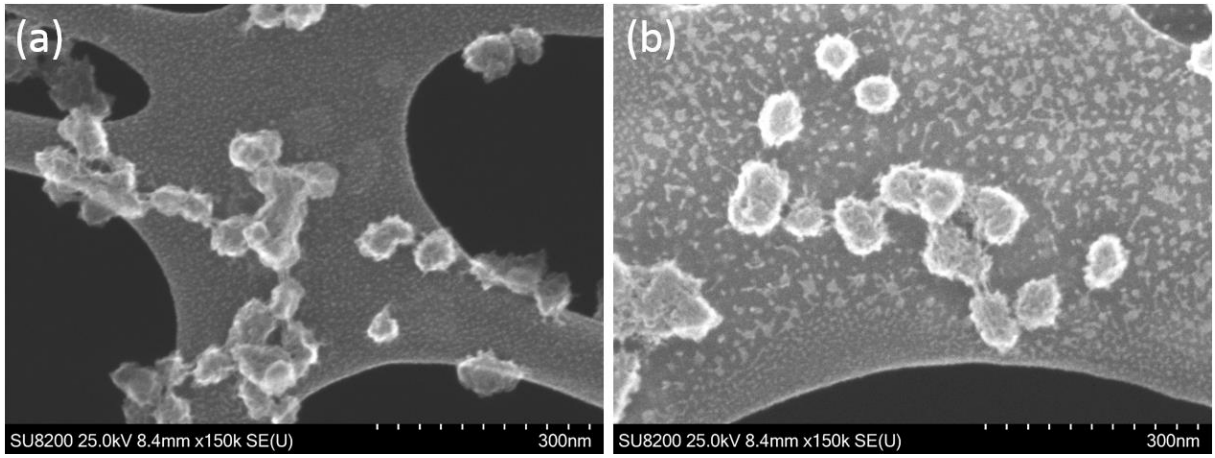

Figure 4.1-6: SEM images of Ni NPs formed from the reduction of $Ni(acac)_2$ in EG in the presence of PVP10 at a suspension temperature of 171 ^{0}C (sample 1) (a) and 186 ^{0}C (sample 6) (b).

The results from the kinetics evaluation experiments on $Pt(acac)_2$ and $Ni(acac)_2$ towards NP formation showed that the nucleation temperatures for the two precursors in 1,4-BD are not too far away. Hence, they could be good candidates for the preparation of bimetallic NPs in this solvent. Further, some faceted well-dispersed NPs were observed in the last collected sample from the reduction of $Ni(acac)_2$ in 1,4-BD, which could suggest further faceting with increasing temperature and/or time. These findings are the basis for the following synthesis using the standard polyol heat-up method.

4.1.2 Pt and Ni NPs Produced via the Standard Polyol Heat-Up Method

Monometallic Pt and Ni NPs were produced following the polyol heat-up method using our standard conditions. Continuing the experimental work presented in subchapter 4.1.1., the solvent used for formation of Pt NPs is 1,4-BD while for the formation of Ni NPs, two solvents were used; 1,4-BD and EG. The capping agent in all three synthesis is PVP10 (experiments 4, 5 and 6 in Table 4.1-1). See experimental details in section 3.2.3. The size and morphology of the Pt and Ni NPs obtained in this part of the work were analyzed by means of SEM imaging; see Figures 4.1-7 and 4.1-8. Then, the NPs were analyzed by means of PXRD for phase identification and unit cell dimension evaluations; see Figure 4.1-9.

Figure 4.1-7 shows that the polyol heat-up method operated at our standard conditions produces well-dispersed Pt NPs with an average diameter of 17.0 ± 4.0 nm from the reduction of $Pt(acac)_2$ in 1,4-BD. Contrary to those results, the same method produces partly agglomerated partly aggregated Ni NPs with an average diameter of 67.6 ± 19.3 nm from the reduction of $Ni(acac)_2$ in 1,4-BD (Figure 4.1-8 (a) and (b)) and even larger and more aggregated NPs from the reduction of $Ni(acac)_2$ in EG (Figure 4.1-8 (c)). Size distribution analysis could not be performed on the latter due to the degree of particle aggregation.

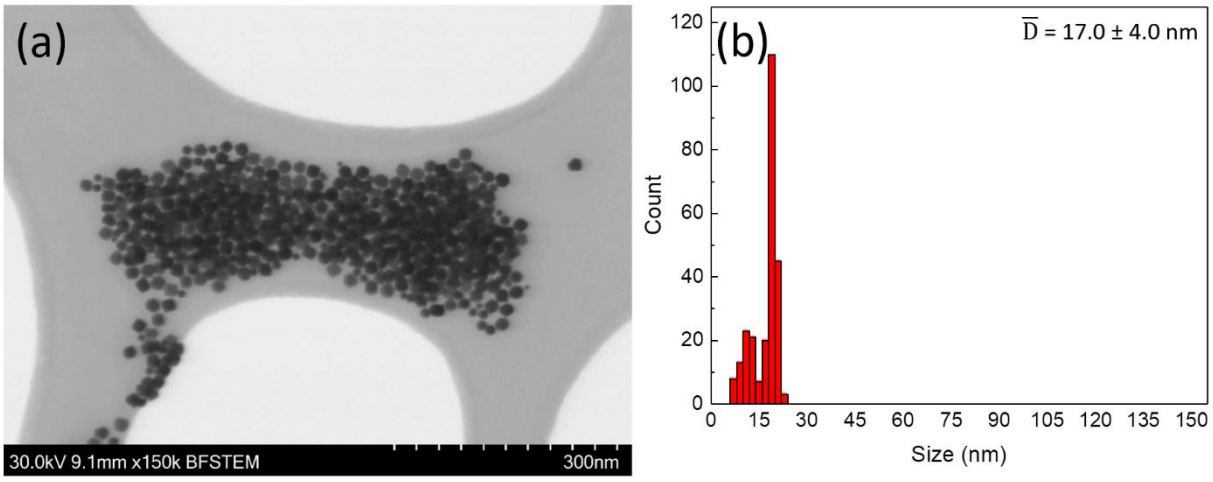

Figure 4.1-7: BF-STEM image (a) and size distribution histogram (b) of Pt NPs formed from the reduction of $Pt(acac)_2$ in 1,4-BD. The histogram is prepared by measuring the diameter of 250 NPs and the calculated average and uncertainty for particle diameter are included.

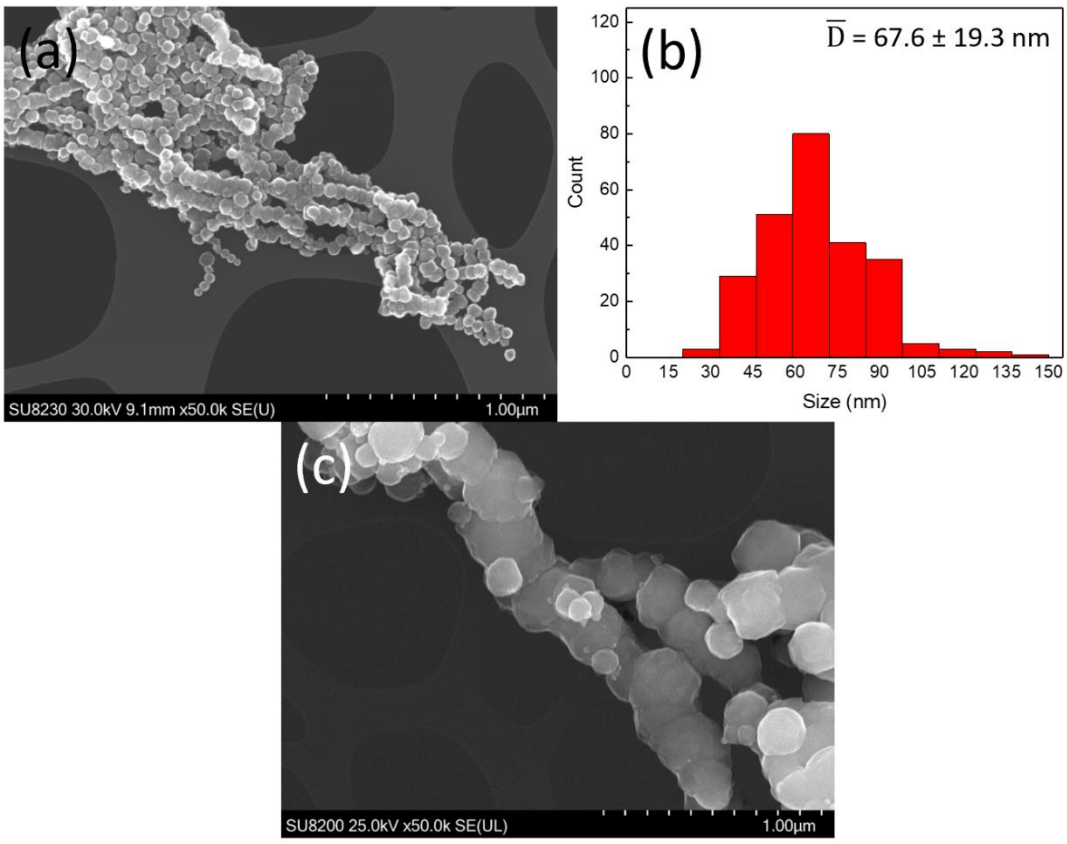

Figure 4.1-8: SEM image (a) and size distribution histogram (b) of Ni NPs formed from the reduction of $Ni(acac)_2$ in 1,4-BD. In addition, SEM image of Ni NPs formed from the reduction of $Ni(acac)_2$ in EG (c). The histogram is prepared by measuring the diameter of 250 NPs and the calculated average and uncertainty for particle diameter are included.

By inspecting the PXRD patterns collected of the three samples (Figure 4.1-9), it was found that only the (111), (200), (220), (311) and (222) hkl-planes are present in all three samples, which shows that the synthesized Pt and Ni NPs are phase pure and that they crystallize with a close packed cubic (ccp) crystal structure. Further, the *a*-axis for the three samples were found to be 3.9221 ± 0.0001 Å for Pt and 3.5277 ± 0.0002 Å and 3.5252 ± 0.0001 Å for Ni produced in 1,4-BD and EG, respectively. These values are in line with the findings of Papa et al. [9] for ccp Pt NPs and Panday et al. [79] for ccp Ni NPs.

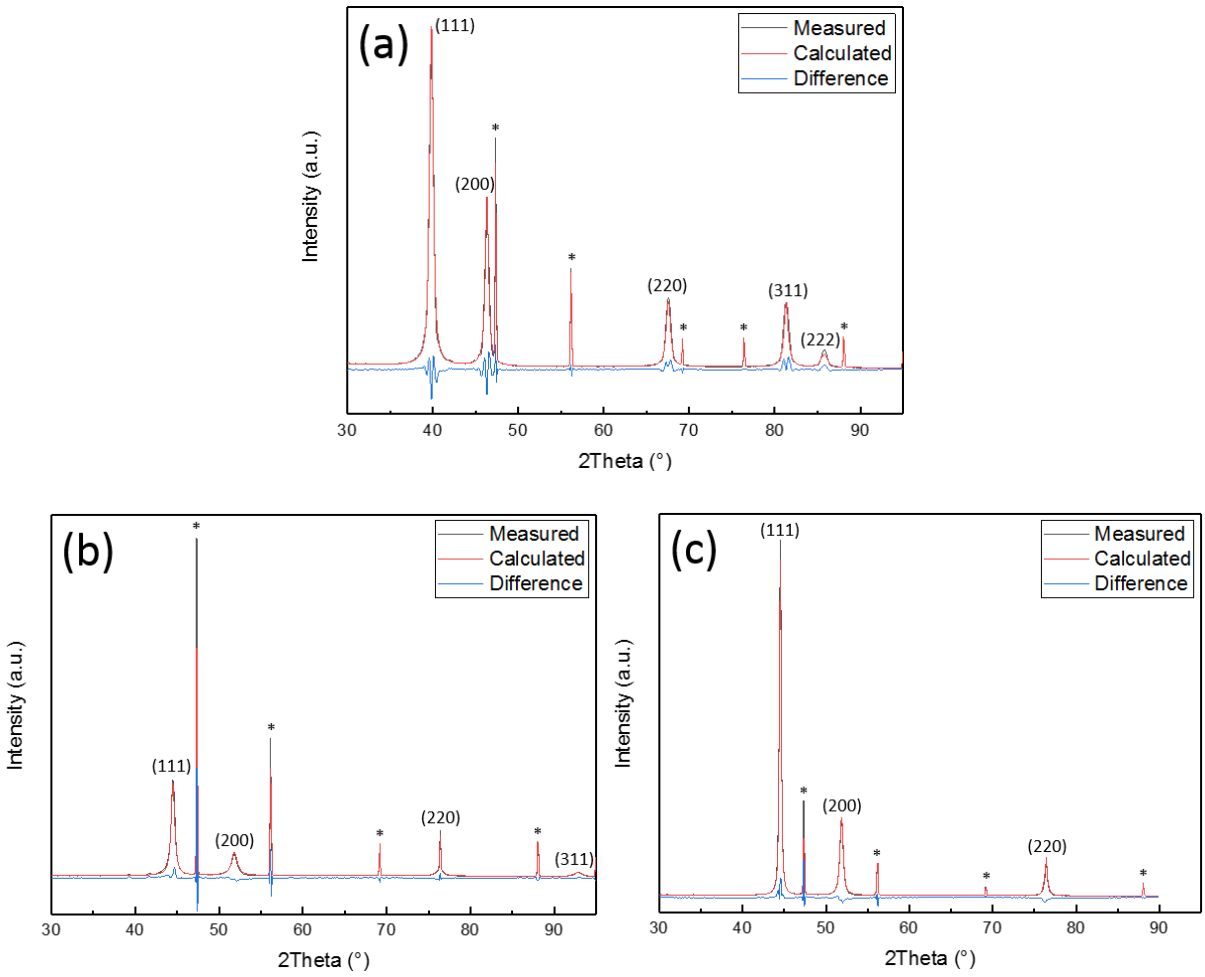

Figure 4.1-9: PXRD patterns of NPs formed from the reduction of $Pt(acac)_2$ in 1,4-BD (a), $Ni(acac)_2$ in 1,4-BD (b) and $Ni(acac)_2$ in EG (c). The measured (black) and calculated (red) patterns as well as the difference between them (blue) are included. *Miller indices of the ccp Pt and Ni phases are included, and the Bragg peaks from a reference Si-NIST sample are labeled with a *.

Based on the results obtained in this part of the work it was concluded that the so-called standard synthesis conditions for preparation of Ni NPs should be revised with the purpose to produce smaller, well-dispersed NPs with a more narrow size distribution.

4.1.3 Tuning the Reduction Kinetics of $Ni(acac)_2$ in 1,4-BD and EG

Our results from sections 4.1.1 and 4.1.2 were not satisfactory for the production of small, well-dispersed Ni NPs by reduction of $Ni(acac)_2$ in 1,4-BD and in EG. Hence, there was a need for optimization of the synthesis method. The first adjustment was to add NaOH as it has been previously shown to increase the rate of the reduction reaction in a polyol synthesis [80]. With basis in the work of Chen et al. [27], the ratio of metal precursor/NaOH 1/50 was our starting point. Ni NPs were produced from the reduction of the metal precursor $Ni(acac)_2$ in the solvent 1,4-BD with metal/NaOH ratios of 1/50 and 1/10 in the presence of the capping agent PVP10 (experiments 7 and 8 in Table 4.1-1). The second adjustment was to change the surfactant from our standard conditions to PVP55 as it has been previously shown to offer better protection against agglomeration in the formation of Ag NPs in the presence of NaOH [80]. Ni NPs were prepared from the reduction of $Ni(acac)_2$ in the solvent EG with metal/NaOH ratio of 1/20 in the presence of the capping agent PVP55 (experiment 9 in Table 4.1-1). See experimental details in section 3.2.3. SEM imaging was used to analyze the size and morphology of the produced NPs; see Figure 4.1-10. Furthermore, PXRD was utilized for phase identification and unit cell dimensions evaluation; see Figure 4.1-11.

Reduction of $Ni(acac)_2$ in 1,4-BD in the presence of NaOH results in aggregated NPs as shown in Figure 4.1-10. For the larger ratio of metal precursor/NaOH of 1/50 which was used, the product was gel-like and it was established by means of SEM imaging that a large part of it was something else than Ni NPs (Figure 4.1-10 (a)). The product of the reduction in the presence of less NaOH (metal precursor/NaOH 1/10) is better in the sense that the aggregates of NPs are smaller and most, potentially all, of the product consists of Ni NPs (Figure 4.1-10 (b)). Figure 4.1-10 (c) shows that the product from the reduction of $Ni(acac)_2$ in EG with metal precursor/NaOH ratio of 1/20 in the presence of the capping agent PVP55 is a mixture of larger faceted Ni NPs and aggregated smaller NPs.

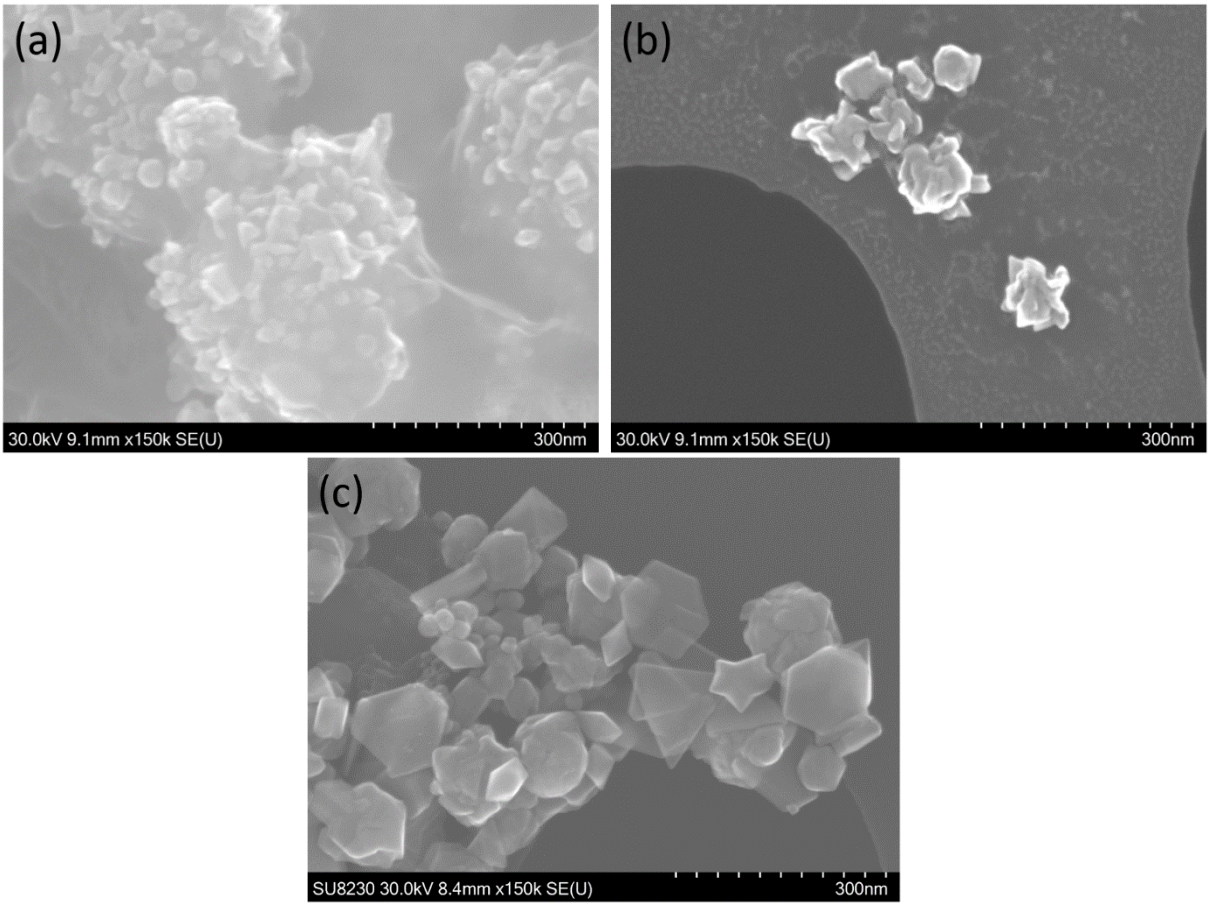

Figure 4.1-10: SEM images of Ni NPs formed from the reduction of Ni(acac)2 in 1,4-BD with PVP10 as surfactant and ratio of metal precursor/NaOH 1/50 (a) and 1:10 (b) and in EG with PVP55 as surfactant and metal precursor/NaOH ratio of 1/20 (c).

Results from the PXRD analysis of the Ni NPs prepared in this part of the work are reported in Figure 4.1-11. The Ni NPs formed by the reduction of $Ni(acac)_2$ in 1,4-BD with ratio of metal precursor/NaOH of 1/50 could not be analyzed properly by PXRD due to the gel-like character of the product. Hence, no diffraction pattern for this sample is reported. There are many Bragg reflections present in the PXRD pattern of the Ni NPs produced by the reduction of $Ni(acac)_2$ in EG with ratio of metal precursor/NaOH of 1/10; see Figure 4.1-11 (a). Beyond the peaks belonging to the Si-NIST reference material, reflections originating from both the ccp and hcp polytypes of Ni are identified. The *a*-axis of the ccp phase was found to be 3.5293 ± 0.0009 Å. The a- and c-axis of the hcp phase were refined to 2.6490 ± 0.0002 Å and 4.3345 ± 0.0006 Å, respectively. Hence, the reduction of $Ni(acac)_2$ in 1,4-BD in the presence of NaOH in the ratio of metal

precursor/NaOH 1/10 produces Ni NPs with both ccp and hcp crystal structures. Figure 4.1-11 (b) shows that the Ni NPs produced from the reduction of $Ni(acac)_2$ in EG with PVP55 as surfactant and ratio of metal precursor/NaOH 1/20 are phase pure. From the presence of the (111), (200), (220) and (311) hkl-planes, it is established that the NPs have a ccp structure. The unit cell dimension of this sample was refined to 3.5255 ± 0.0001 Å. The unit cell dimensions of the Ni NPs prepared in this part of the work are in agreement with unit cell dimensions reported by Panday et al. [79] for the ccp Ni phase and by Gong et al. [81] for the hcp Ni phase.

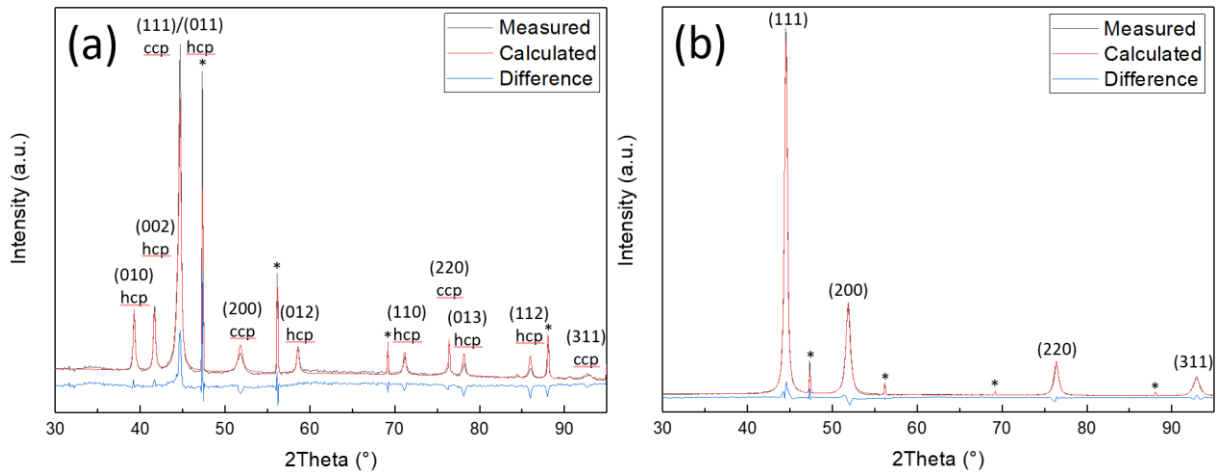

Figure 4.1-11: PXRD patterns of Ni NPs formed from the reduction of Ni(acac)2 in 1,4-BD with PVP10 as surfactant and ratio of metal precursor/NaOH of 1/10 (a) and in EG with PVP55 as surfactant and metal precursor/NaOH ratio of 1/20 (b). The measured (black) and calculated (red) patterns as well as the difference between them (blue) are included. *Miller indices of the ccp and hcp Ni phases are included (only for the ccp in (b)) and the Bragg peaks from a reference Si-NIST sample are labeled with a *.

The modified polyol heat-up method used to synthesize the Ni NPs reported in this part of the work was not used in further experimental work due to the heterogeneous character of the NPs both with respect to morphology and that the samples contained the hcp and ccp polytypes.

4.2 $Pt_{100-x}Ni_x$ NPs Produced via the Standard Polyol Heat-Up Method

Results gathered from the synthesis and characterization of $Pt_{100-x}Ni_x$ NPs (x = 0, 10, 20, 30, 40, 50, 60, 70, 80, 90 and 100) are presented in this subchapter. The observations made for the reactivity of the metal precursors $Pt(acac)_2$ and $Ni(acac)_2$ and the synthesis of Pt and Ni NPs presented in sections 4.1.1 and 4.1.2, respectively, form the basis for this part of the experimental work. A series of NPs with nominal composition $Pt_{100-x}Ni_x$ were produced via the polyol heat-up method using our standard conditions from the simultaneous reduction of the metal precursors $Pt(acac)_2$ and $Ni(acac)_2$ in the solvent 1,4-BD with the presence of the capping agent PVP10, see experimental details in section 3.2.3. An overview of all experiments done in this part of the work is presented in Table 4.2-1. The particle size and morphology of the NPs were mapped by SEM imaging (Figure 4.2-1) whereas PXRD was used for phase identification and unit cell dimension estimations (Figure 4.2-3). In addition, some selected samples were analyzed by HAADF-STEM-EDX element mapping for evaluation of the element distribution (Figures 4.2-5, 4.2-6 and 4.2-7). Finally, PPMS (Figure 4.2-9) was included to the analysis toolbox with the purpose to add extra information of phase composition of the NPs since the magnetic properties of the two end members Pt and Ni are very different.

Table 4.2-1: Overview of the experimental work carried out on $Pt_{100-x}Ni_x$ NPs prepared via the standard polyol heat-up method. The following information is given: experiment number, nominal Pt-Ni composition of the NPs, analysis methods, particle size extracted from SEM and unit cell dimensions determined from PXRD data (phases denoted "Pt-rich", "Pt-Ni" and "Ni-rich"). The reported uncertainties in the unit cell dimensions are the mathematical ones originating from the TOPAS-refinements.

Exp. no.	Nominal comp.	Analysis methods				Particle size and size distribution [nm]				*a*-axis [Å]			Element distribution [atomic % Ni]		
		SEM	TEM	PXRD	PPMS	Mono-modal	Multimodal			Pt-rich phase	Pt-Ni phase	Ni-rich phase	small NPs	intermediate NPs	large NPs
1	Pt	✓		✓	✓	17.0 ± 4.0	11.2 ± 2.1	-	19.4 ± 1.2	3.9221 ± 0.0001	-	-	-	-	-
2	$Pt_{90}Ni_{10}$	✓	✓	✓	✓	8.4 ± 2.8	3.7 ± 0.7	-	9.6 ± 1.5	3.9008 ± 0.0005	-	-	6.9 ± 0.5	-	14.0 ± 0.3
3	$Pt_{80}Ni_{20}$	✓		✓		6.4 ± 2.2	2.5 ± 0.6	-	7.2 ± 1.4	3.8913 ± 0.0004	-	3.581 ± 0.004	-	-	-
4	$Pt_{70}Ni_{30}$	✓		✓		6.4 ± 2.9	2.5 ± 0.6	-	7.9 ± 1.8	3.8720 ± 0.0007	-	3.589 ± 0.003	-	-	-
5	$Pt_{60}Ni_{40}$	✓		✓		7.6 ± 4.1	2.9 ± 0.5	-	10.3 ± 2.4	3.865 ± 0.001	-	3.559 ± 0.003	-	-	-
6	$Pt_{50}Ni_{50}$	✓	✓	✓	✓	6.5 ± 3.9	2.6 ± 0.6	6.2 ± 0.9	11.9 ± 1.2	3.857 ± 0.002	-	3.556 ± 0.002	10.0 ± 1.0	33.7 ± 1.6	58.0 ± 1.4
7	$Pt_{40}Ni_{60}$	✓		✓		6.5 ± 5.0	2.6 ± 0.5	6.7 ± 0.7	14.2 ± 1.9	3.855 ± 0.001	-	3.5427 ± 0.0008	-	-	-
8	$Pt_{30}Ni_{70}$	✓		✓		6.8 ± 5.4	4.6 ± 2.8	-	17.0 ± 2.3	3.857 ± 0.002	-	3.5384 ± 0.0008	-	-	-
9	$Pt_{20}Ni_{80}$	✓		✓		12.3 ± 8.4	4.9 ± 2.0	-	20.9 ± 3.1	-	3.822 ± 0.003	3.5353 ± 0.0004	-	-	-
10	$Pt_{10}Ni_{90}$	✓	✓	✓	✓	19.7 ± 9.4	4.6 ± 1.1	-	25.1 ± 2.9	-	3.76 ± 0.01	3.5309 ± 0.0003	13.2 ± 2.2	-	93.2 ± 3.3
11	Ni	✓		✓	✓	67.6 ± 19.3	-			-	-	3.5247 ± 0.0001	-	-	-

4.2.1 Particle Size and Morphology of $Pt_{100-x}Ni_x$ Nanoparticles

The particle size distribution and morphology of selected compositions of $Pt_{100-x}Ni_x$ NPs (x = 0, 10, 20, 30, 40, 50, 60, 70, 80, 90 and 100) were mapped by SEM imaging (BF-STEM mode), and the particle size distribution histograms were prepared by measuring the diameter of 250 NPs. Obtained results from the analysis work are reported in Figure 4.2-1 using the same magnification on the BF-STEM images and the same scale for the histograms with exception of the one for the Ni NPs. Firstly, it can be noted that the two end members, Pt and Ni (Figure 4.2.1 (a) and (k)), give quite different size distributions and agglomeration. The Pt NPs are well-dispersed over the TEM-grid whereas the Ni NPs are severely agglomerated. The agglomeration in the latter suggests that the Ni NPs could have been magnetized by the magnetic field used for the stirring conditions during the synthesis since Ni is a ferro- or superparamagnet [33], [38]. Further, no systematic trend was observed in the faceting of the NPs by SEM imaging. There is a variety of polyhedral and irregular shapes found for both the two end members. In addition, average particle size of Pt was found to be 17.0 ± 4.0 nm whereas the corresponding value of Ni is 67.6 ± 19.3 nm. The significant difference in average particle sizes for the two metals, prepared at the same reaction conditions, led us to pursuit this. BF-STEM images of the alloyed particles (Figure 4.2-1 (b)-(j)) were therefore collected and carefully analyzed together with the images of Pt and Ni NPs.

As a start, the particle size distributions are considered as monomodal (see Figure 4.2-2 (a)). Firstly, the average particle size decreases from 17.0 to 6.4 nm in the range from Pt to $Pt_{80}Ni_{20}$ NPs. Further, the NPs with nominal compositions in the range from $Pt_{70}Ni_{30}$ to $Pt_{30}Ni_{70}$ have approximately constant average monomodal particle size of ≈ 6.5 nm with a local maximum of 7.6 nm for the $Pt_{60}Ni_{40}$ NPs. It is important to note that this variation falls within the calculated spread of one standard deviation as shown in Figure 4.2-2 (a). Finally, there is a rapid increase in average particle size from 12.3 to 67.6 nm in the range from $Pt_{20}Ni_{80}$ to Ni NPs. In addition, it is observed that the calculated spread of one standard deviation follows a similar trend reaching a minimum for the nominal composition $Pt_{80}Ni_{20}$ and increasing for the rest of the range from Pt to Ni NPs. In summary, the $Pt_{80}Ni_{20}$ NPs have the smallest average particle size and the most narrow size distribution from the series of alloyed NPs when evaluating the data assuming monomodal size distributions.

By visually inspecting the SEM images and the corresponding size distribution histograms in Figure 4.2-1, it can be noticed that many of the samples exhibit multimodal distributions. For this reason, a second analysis is performed by considering multimodal distributions (see Figure 4.2-2 (b)). At this point, it is important to note that the appearance of the size distribution depends largely on the settings for bin width and bin number. The reported histograms in Figure 4.2-1 are set to a constant bin number, hence their width varies from one sample to another. For the preparation of Figure 4.2-2 (b), the number of size-ranges considered for each sample was determined from the appearance of its respective histogram. The size distributions for most of the NPs appear to be bimodal with exceptions for $Pt_{50}Ni_{50}$ and $Pt_{40}Ni_{60}$ NPs, which could be trimodal, and Ni NPs, which is monomodal. In Figure 4.2-2 (b), the average particle size and standard deviation are indicated in red, black and green for the modes at smaller, intermediate and larger particle size, respectively, found in each sample.

Firstly, the average particle size for the larger NPs (marked in green in Figure 4.2-2 (b)) found in each sample, decreases from 19.4 to 7.2 nm in the range from Pt to $Pt_{80}Ni_{20}$ NPs and increases from 7.9 to 67.6 nm in the range from $Pt_{70}Ni_{30}$ to Ni NPs, but there is no clear trend in the calculated spread for these NPs. Further, the change in average particle size for the smaller NPs (marked in red in Figure 4.2-2 (b)) follows a similar curve in the range from Pt to $Pt_{80}Ni_{20}$ NPs, but there is no significant increase observed in the range from $Pt_{70}Ni_{30}$ to Ni NPs as for the larger ones. Finally, the calculated spread of one standard deviation for the smaller NPs is distinctly smaller than the spread for the larger NPs in the range from $Pt_{90}Ni_{10}$ to $Pt_{60}Ni_{40}$ NPs. In summary, most samples of the series of NPs synthesized in this part of the work were found to be bimodal by SEM imaging with growing difference between the two modes with increasing atomic % Ni. NPs with nominal composition $Pt_{80}Ni_{20}$ were found to be the most homogeneous in respect to particle size.

It can be concluded that the polyol heat-up method using our standard conditions produces well-dispersed alloyed NPs with nominal composition $Pt_{100-x}Ni_x$ (x = 10, 20, 30, 40, 50, 60, 70, 80 and 90), which have average monomodal particle diameter in the range from 6.4 to 19.7 nm, but are better described by bi- or tri-modal particle size distribution.

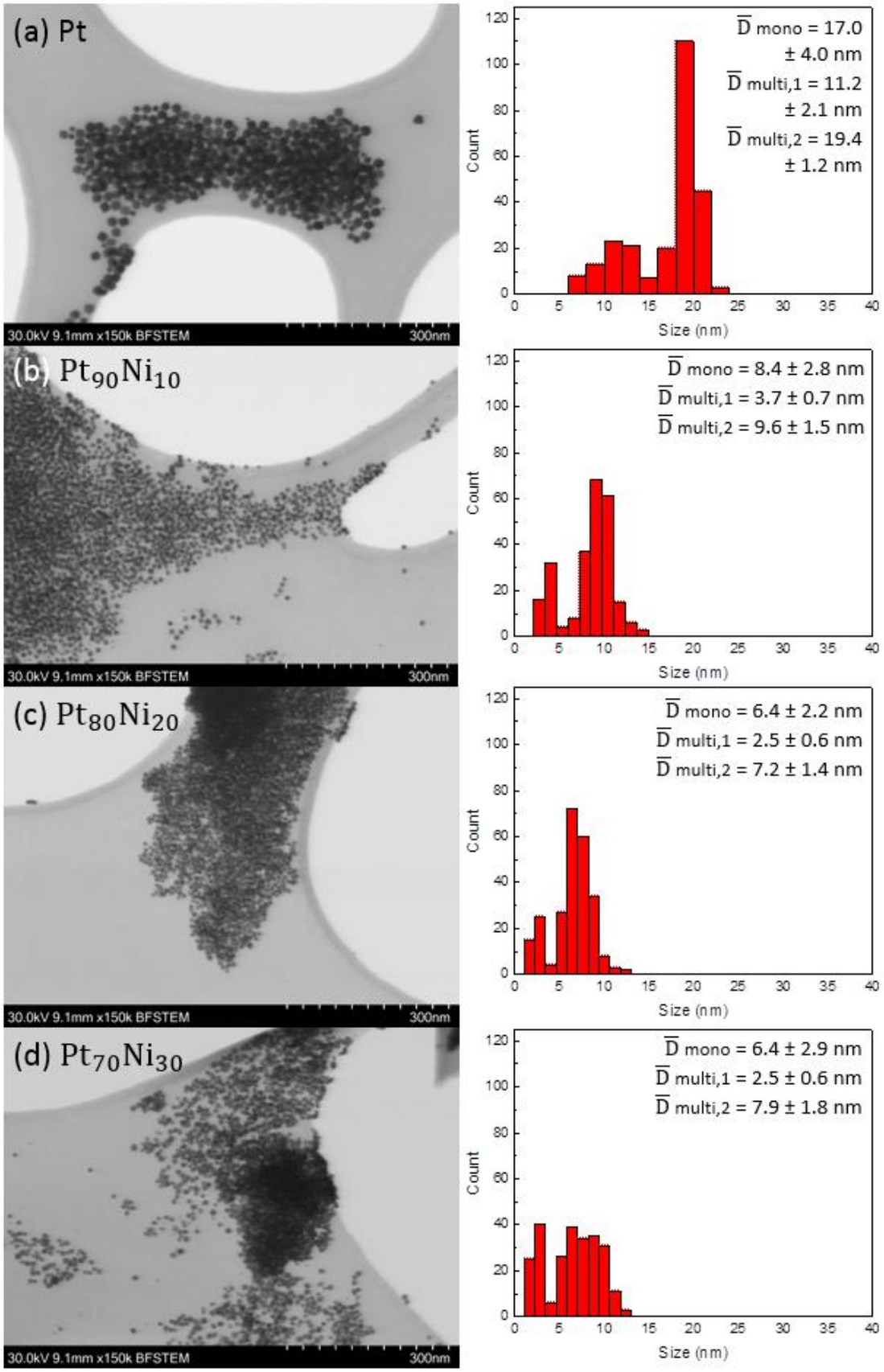
(a) Pt
30.0kV 9.1mm x150k BFSTEM
300nm
D̄ mono = 17.0 ± 4.0 nm
D̄ multi,1 = 11.2 ± 2.1 nm
D̄ multi,2 = 19.4 ± 1.2 nm
Count
Size (nm)
(b) Pt90Ni10
30.0kV 9.1mm x150k BFSTEM
300nm
D̄ mono = 8.4 ± 2.8 nm
D̄ multi,1 = 3.7 ± 0.7 nm
D̄ multi,2 = 9.6 ± 1.5 nm
Count
Size (nm)
(c) Pt80Ni20
30.0kV 9.1mm x150k BFSTEM
300nm
D̄ mono = 6.4 ± 2.2 nm
D̄ multi,1 = 2.5 ± 0.6 nm
D̄ multi,2 = 7.2 ± 1.4 nm
Count
Size (nm)
(d) Pt70Ni30
30.0kV 9.1mm x150k BFSTEM
300nm
D̄ mono = 6.4 ± 2.9 nm
D̄ multi,1 = 2.5 ± 0.6 nm
D̄ multi,2 = 7.9 ± 1.8 nm
Count
Size (nm)

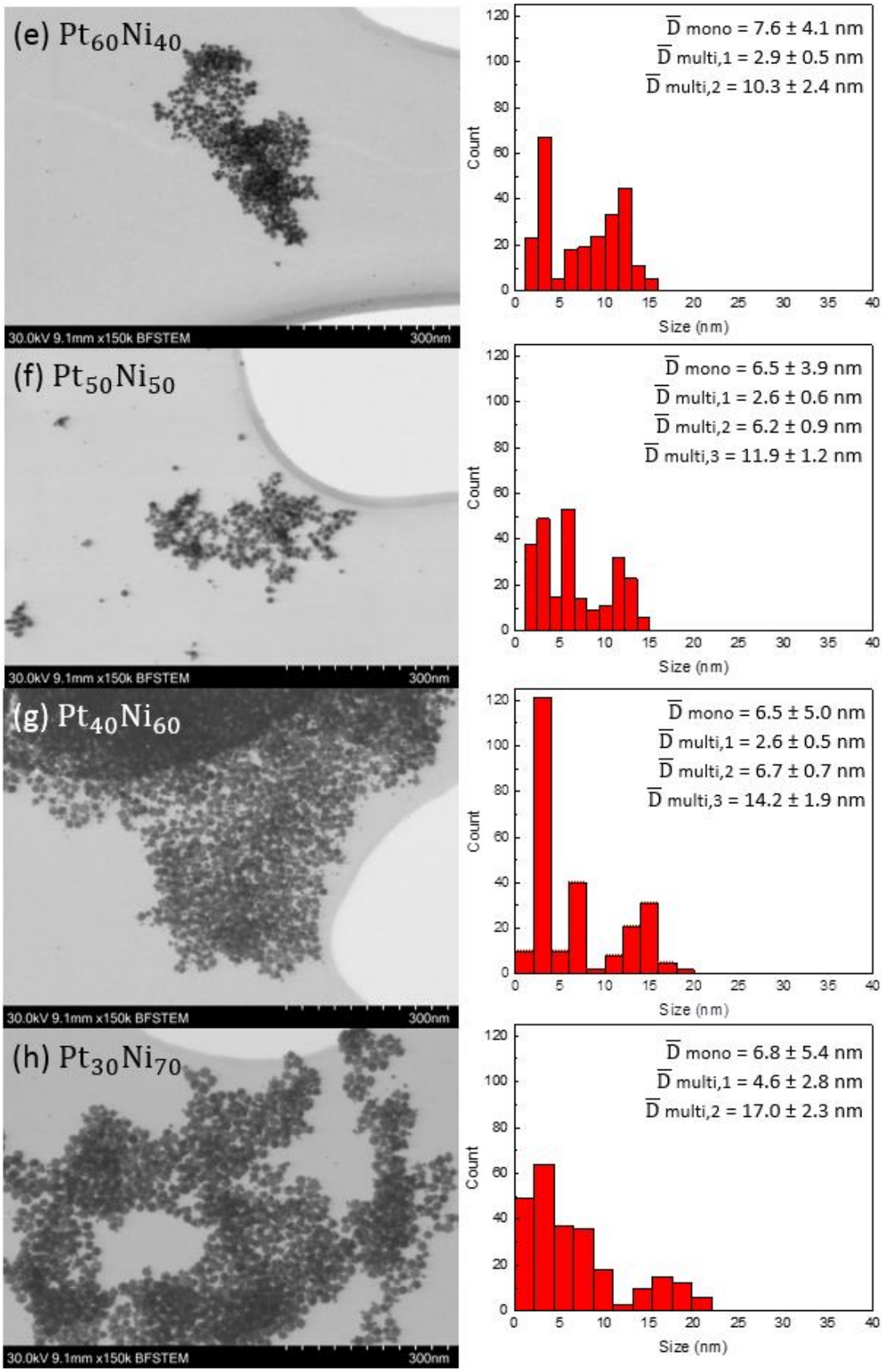
(e) $Pt_{60}Ni_{40}$
30.0kV 9.1mm x150k BFSTEM
300nm
$\overline{D}$ mono = 7.6 ± 4.1 nm
$\overline{D}$ multi,1 = 2.9 ± 0.5 nm
$\overline{D}$ multi,2 = 10.3 ± 2.4 nm
Count
Size (nm)
(f) $Pt_{50}Ni_{50}$
30.0kV 9.1mm x150k BFSTEM
300nm
$\overline{D}$ mono = 6.5 ± 3.9 nm
$\overline{D}$ multi,1 = 2.6 ± 0.6 nm
$\overline{D}$ multi,2 = 6.2 ± 0.9 nm
$\overline{D}$ multi,3 = 11.9 ± 1.2 nm
Count
Size (nm)
(g) $Pt_{40}Ni_{60}$
30.0kV 9.1mm x150k BFSTEM
300nm
$\overline{D}$ mono = 6.5 ± 5.0 nm
$\overline{D}$ multi,1 = 2.6 ± 0.5 nm
$\overline{D}$ multi,2 = 6.7 ± 0.7 nm
$\overline{D}$ multi,3 = 14.2 ± 1.9 nm
Count
Size (nm)
(h) $Pt_{30}Ni_{70}$
30.0kV 9.1mm x150k BFSTEM
300nm
$\overline{D}$ mono = 6.8 ± 5.4 nm
$\overline{D}$ multi,1 = 4.6 ± 2.8 nm
$\overline{D}$ multi,2 = 17.0 ± 2.3 nm
Count
Size (nm)

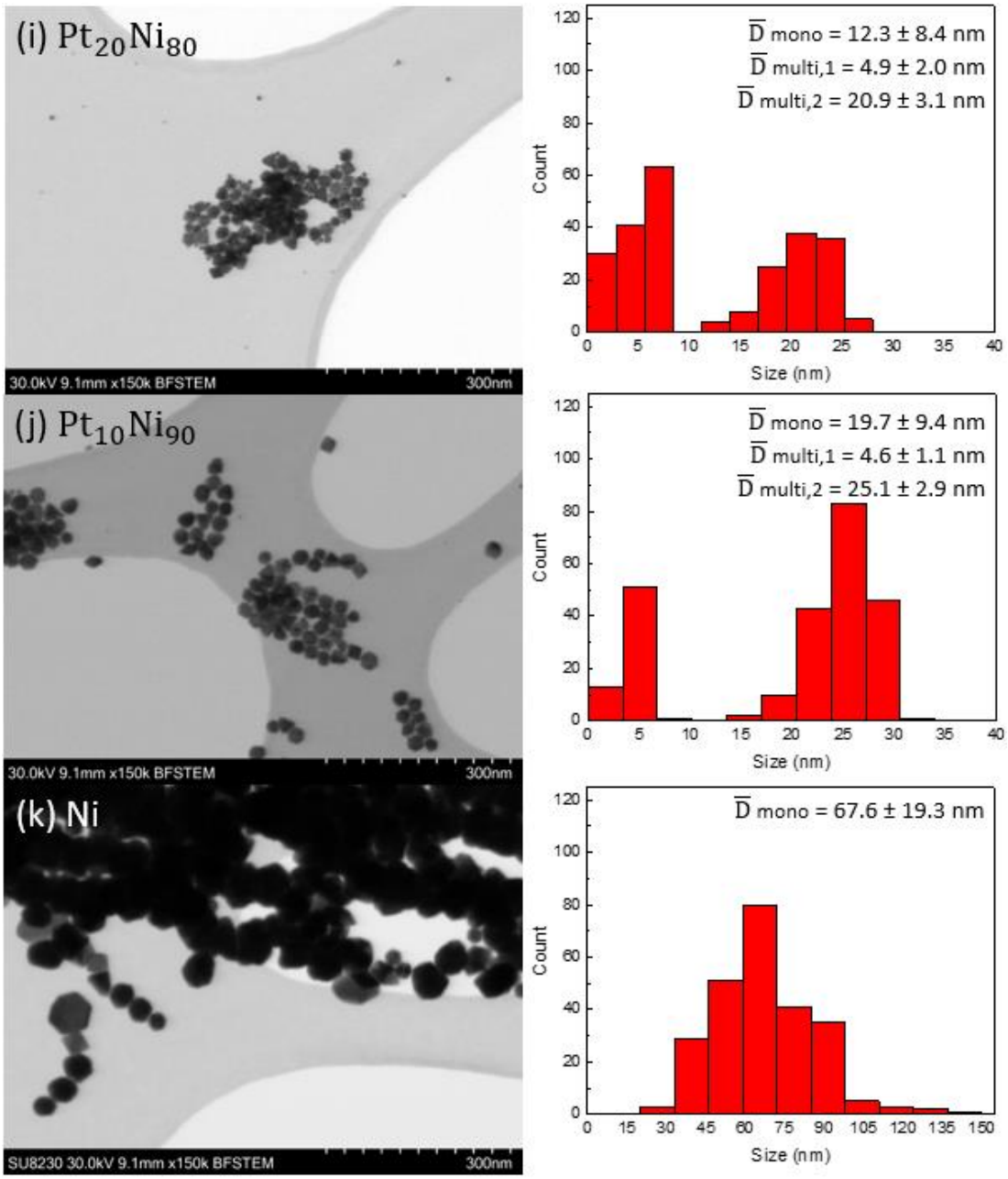

Figure 4.2-1: BF-STEM images and size distribution histograms of NPs with nominal compositions Pt (a), $Pt_{90}Ni_{10}$ (b), $Pt_{80}Ni_{20}$ (c), $Pt_{70}Ni_{30}$ (d), $Pt_{60}Ni_{40}$ (e), $Pt_{50}Ni_{50}$ (f), $Pt_{40}Ni_{60}$ (g), $Pt_{30}Ni_{70}$ (h), $Pt_{20}Ni_{80}$ (i), $Pt_{10}Ni_{90}$ (j) and Ni (k) formed from the simultaneous reduction of $Pt(acac)_2$ and $Ni(acac)_2$ in 1,4-BD in the presence of PVP10. The histograms are prepared by measuring the diameter of 250 NPs and include the calculated average particle size ($\overline{D}$) and spread in the particle size distribution (standard deviation, σ) for both monomodal and multimodal distribution.

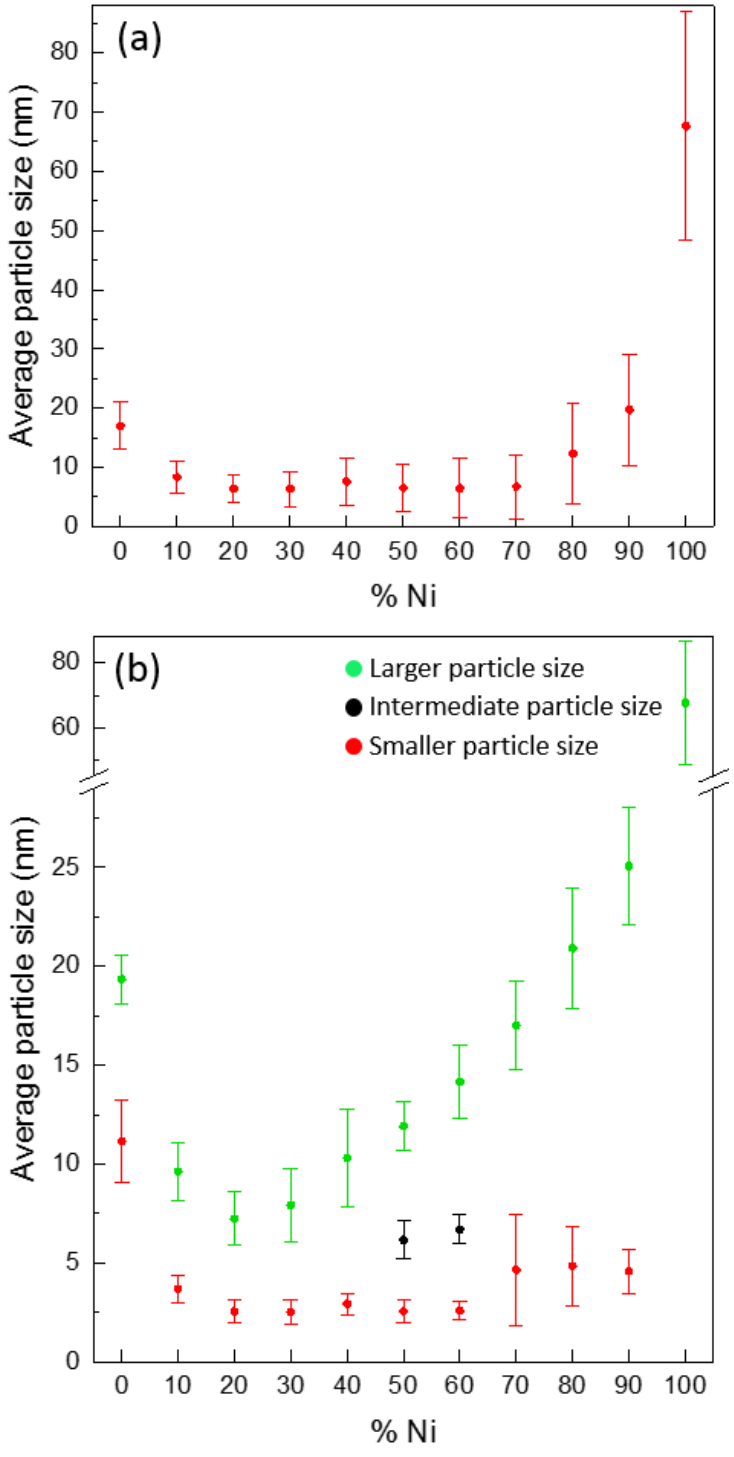

Figure 4.2-2: Average particle size for NPs formed from the simultaneous reduction of $Pt(acac)_2$ and $Ni(acac)_2$ in 1,4-BD with increasing atomic % Ni assuming monomodal (a) and multimodal (b) particle size distributions. The plots include the calculated average particle size ($\overline{D}$) and spread in the particle size distribution (standard deviation, σ).

4.2.2 Phase Identification of $Pt_{100-x}Ni_x$ Nanoparticles

Nanoparticles from the entire $Pt_{100-x}Ni_x$ compositional range (x = 0, 10, 20, 30, 40, 50, 60, 70, 80, 90 and 100) were analyzed by PXRD for phase identification and to estimate the unit cell dimensions. The PXRD patterns of all samples are reported in Figure 4.2-3. The unit cell dimensions were estimated from the TOPAS-refinements and are listed in Table 4.2-1 along with the mathematical uncertainties from the refinements. The variation in the *a*-axes of the various ccp phases versus Ni content (x) for the nominal compositions throughout the $Pt_{100-x}Ni_x$ series is illustrated in Figure 4.2-4.

By carefully inspecting the PXRD patterns collected of the sample-series (Figure 4.2-3), it was found that beyond the peaks originating from the Si-NIST reference material, only Bragg reflections indexed with the Miller indices (111), (200), (220), (311) and (222) from ccp-phases are present. No extra Bragg-reflections originating from NiO or any other impurity phases were identified. By using the PXRD patterns of the two end members (Pt and Ni), diffraction patterns of the alloyed NPs with 20, 30, 40, 50, 60, 70, 80 and 90 atomic % Ni show Bragg-reflections originating from both a ccp Pt-rich and a ccp Ni-rich phase, which suggests that the samples contain multiple metallic ccp phases. Hence, the diffraction data for the alloys are processed assuming they are composed of two or three phases. This results in two or three different values for the *a*-axis for each composition (Table 4.2-1).

It can be visually seen that there are small shifts in the (111) Bragg-reflections (green and red dotted lines included for clarity) in Figure 4.2-3 for all alloyed NPs, which suggests that the metallic ccp phases have different element composition than the end members (Pt and Ni). Figure 4.2-4 shows that the *a*-axis of the Pt-rich phase decreases from 3.9221 ± 0.0001 to 3.857 ± 0.002 Å in the region from 0 to 50 atomic % Ni and reaches a plateau at 50-70 atomic % Ni, which suggests lattice contraction resulting from the introduction of smaller Ni atoms and that a maximum of this is reached. Similarly, the *a*-axis of the Ni-rich phase increases from 3.5247 ± 0.0001 to 3.589 ± 0.003 Å in the region from 0 to 70 atomic % Pt and reaches a plateau at 70-80 atomic % Pt, which suggests that the lattice expands from the introduction of larger Pt atoms and a maximum is reached.

Further, the measured diffraction pattern of the NPs with nominal composition $Pt_{20}Ni_{80}$ did not fit well with the calculated one assuming a Pt-rich and a Ni-rich phases present. Figure 4.2-3 (b) shows that the diffraction pattern of this sample might have additional reflections in between the ones originating from the Pt-rich and Ni-rich phases. The data was, therefore, processed a second time with the addition of a third Pt-Ni phase, but the fit did not improve and the resulting *a*-axis for the Pt-rich phase was estimated to 3.896 ± 0.003 Å, which does not fit with the observed trend. Hence, the diffraction pattern and the corresponding *a*-axes of the first refinement are presented here in light them being more probable. The *a*-axes were refined to 3.822 ± 0.003 Å and 3.5353 ± 0.0004 Å for the Pt-rich and Ni-rich phases, respectively (Table 4.2-1). The former is significantly smaller than the corresponding values from nominal compositions with 50-70 atomic % Ni, which suggests that the two phases present in this sample are rather Pt-Ni and Ni-rich and the estimated *a*-axes are, therefore, presented as such (Figure 4.2-4). Finally, the diffraction pattern of the $Pt_{10}Ni_{90}$ NPs was refined for a Pt-rich and a Ni-rich phase, but the resulting *a*-axis of the former is 3.76 ± 0.01 Å, which is significantly lower than the rest (Figure 4.2-4). Similarly, this suggests the two phases to be Pt-Ni and Ni-rich and the *a*-axes are presented as such.

In addition, of the studied bimetallic compositions only $Pt_{90}Ni_{10}$ visually has Bragg-reflections solely originating from one ccp-phase. This suggests that the NPs in this synthesis batch are single phase and the data was processed assuming a single Pt-rich phase. The *a*-axis was refined to 3.9008 ± 0.0005 Å and since it is slightly smaller than the one for pure Pt (3.9221 ± 0.0001 Å), it suggests lattice contraction resulting from the introduction of smaller Ni atoms. However, it is important to note that the smaller the NPs are, the broader the Bragg-reflections from them appear in the diffraction pattern. Thus, it is possible that very small NPs of a second phase are present, but the signal from these blends in with the background and is not detected.

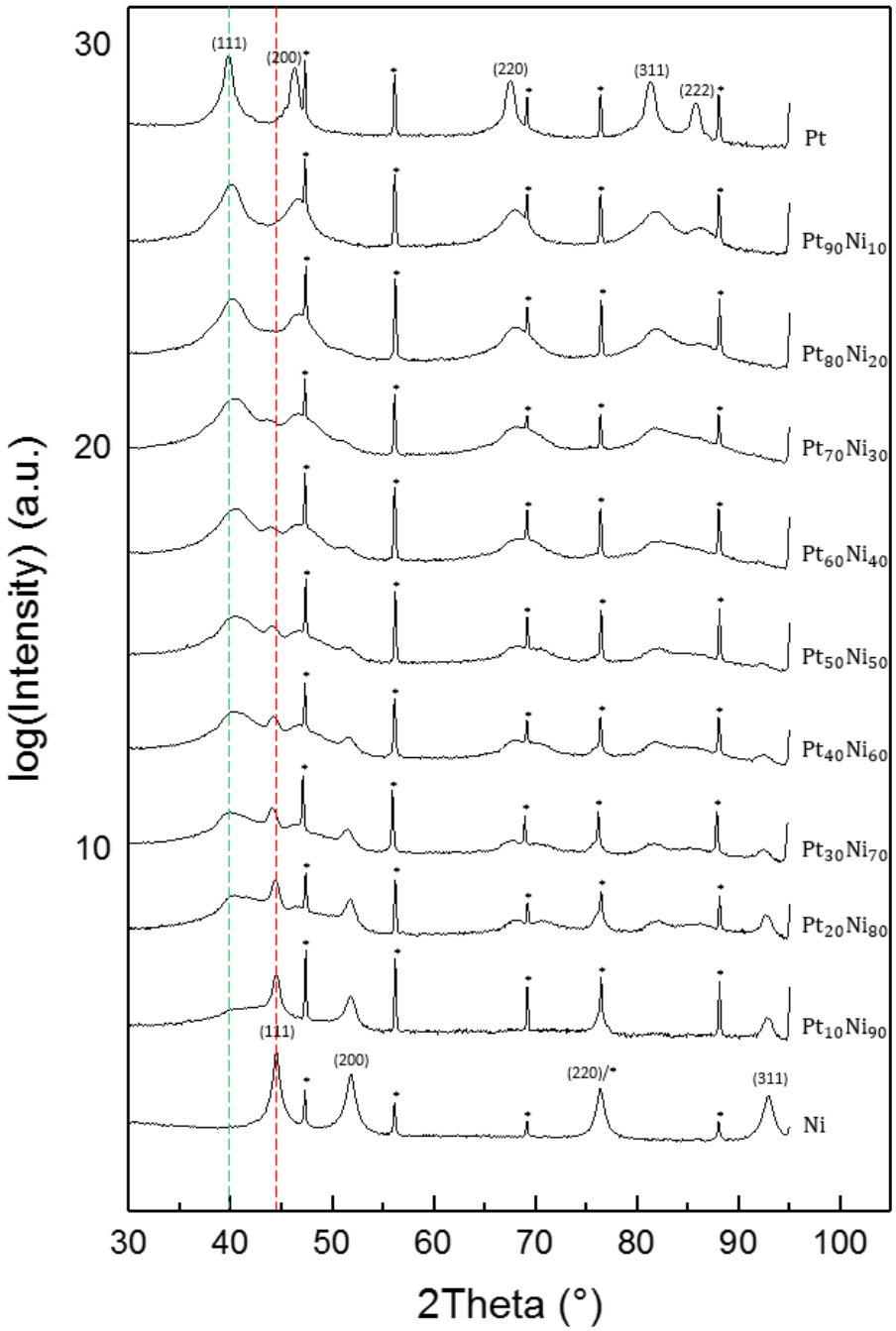

Figure 4.2-3: PXRD patterns of NPs with nominal compositions Pt, $Pt_{90}Ni_{10}$, $Pt_{80}Ni_{20}$, $Pt_{70}Ni_{30}$, $Pt_{60}Ni_{40}$, $Pt_{50}Ni_{50}$, $Pt_{40}Ni_{60}$, $Pt_{30}Ni_{70}$, $Pt_{20}Ni_{80}$, $Pt_{10}Ni_{90}$ and Ni formed from the simultaneous reduction of $Pt(acac)_2$ and $Ni(acac)_2$ in 1,4-BD. *Miller indices of the ccp Pt and Ni phases are included, and the Bragg peaks from a reference Si-NIST sample are labeled with a *. Green and red dotted lines positioned at the Pt and Ni (111) hkl-planes, respectively.

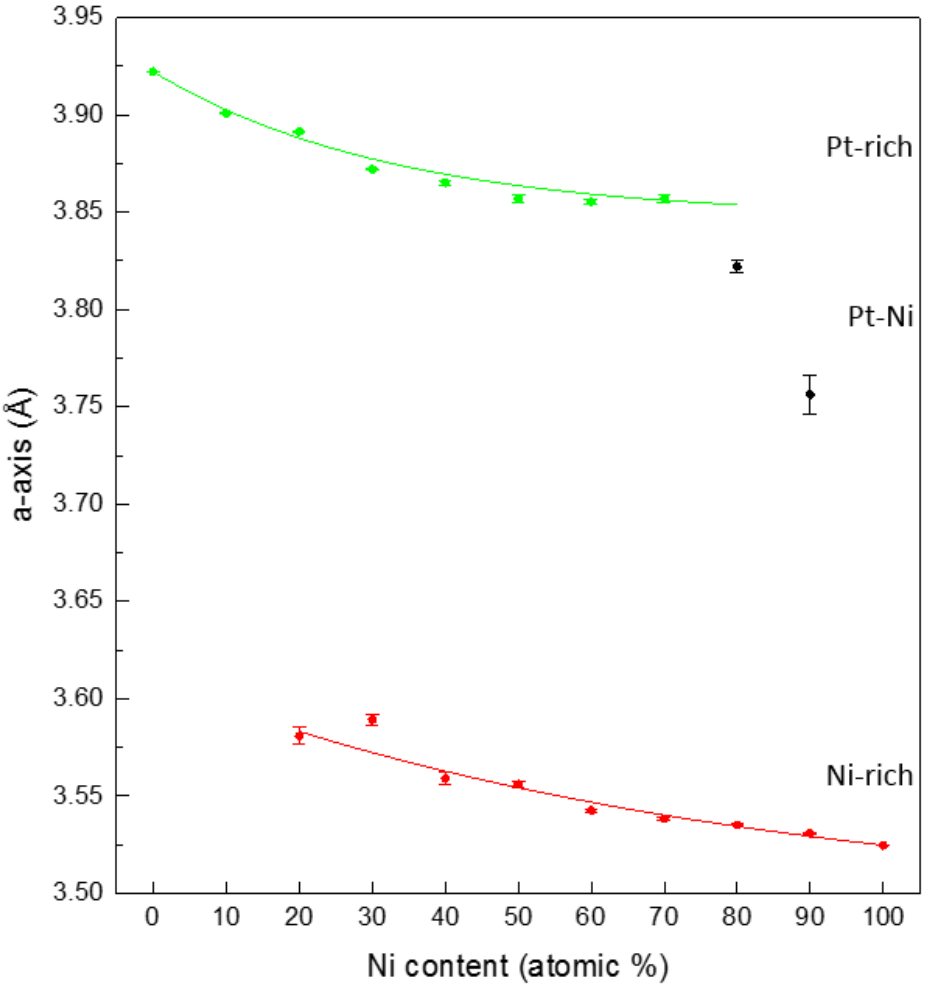

Figure 4.2-4: *a*-axis of NPs formed from the simultaneous reduction of $Pt(acac)_2$ and $Ni(acac)_2$ in 1,4-BD with increasing Ni content in the nominal composition $Pt_{100-x}Ni_x$.

4.2.3 Element Distribution in $Pt_{100-x}Ni_x$ Nanoparticles

HAADF-STEM-EDX element mapping was performed on some selected $Pt_{100-x}Ni_x$ (x = 10, 50, and 90) NPs in order to evaluate their element distribution. The samples were chosen in such a way to get insight to the element distribution throughout the series of the 11 sample compositions analyzed by PXRD (section 4.2.2) without analyzing all of them. Some selected HAADF-STEM-EDX element mapping images for the $Pt_{90}Ni_{10}$, $Pt_{50}Ni_{50}$ and $Pt_{10}Ni_{90}$ NPs are reported in Figure 4.2-5, Figure 4.2-6 and Figure 4.2-7, respectively. The average element compositions for the three nominal compositions were estimated by integrating the EDX signals from multiple regions, and the results are reported in Table 4.2-1. The number of analyzed particles varies from one sample to another depending on the available data. The NPs were divided into smaller, intermediate and larger size based on their respective previously prepared size distribution histograms (4.2.1). Additionally, heterogeneities in the element composition across two individual particles were studied for each nominal composition and the findings for one particle from each composition are reported in Figure 4.2-8. Additional information from the estimation of average element compositions and the rest of the individually studied NPs are available in the appendix (9.2).

Figure 4.2-5 shows that the NPs present in the sample with nominal composition $Pt_{90}Ni_{10}$ have different sizes and element compositions. There are smaller Pt, smaller NPs with Ni-core and Pt-shell (Ni@Pt core@shell), larger Pt and larger Ni@Pt core@shell NPs. Further, some Pt-shells are distributed equally across the particles whereas others are distinctly thicker on one side of the particles than the rest. Finally, it can be visually noticed that two core@shell NPs of similar size have different element composition, i.e. one has a larger Ni-core and a thinner Pt-shell whereas the other has a smaller Ni-core and a thicker Pt-shell. The estimated average compositions for the $Pt_{90}Ni_{10}$ NPs have 6.9 ± 0.5 and 14.0 ± 0.3 atomic % Ni for the smaller and larger NPs, respectively. These estimations show that majority of the Ni atoms are situated in the core of the larger NPs.

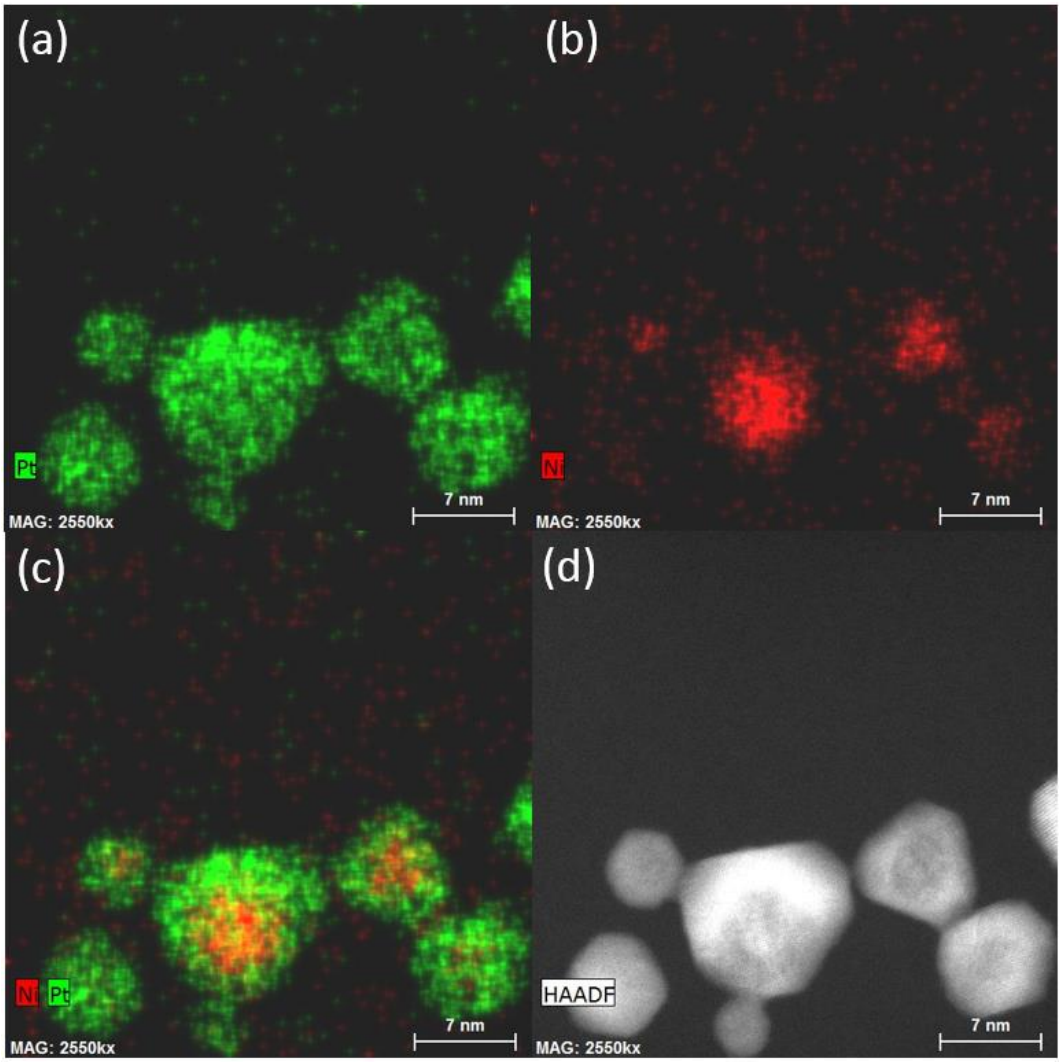

Figure 4.2-5: EDX element mapping of Pt (a) and Ni (b), overlapped EDX image (c) and HAADF-STEM image (d) of $Pt_{90}Ni_{10}$ NPs formed from the simultaneous reduction of $Pt(acac)_2$ and $Ni(acac)_2$ in 1,4-BD in the presence of PVP10.

Figure 4.2-6 shows the element distributions in the NPs with nominal composition $Pt_{50}Ni_{50}$. Firstly, it is noticed that these NPs have a broader size distribution. Further, majority of the smaller NPs are pure Pt, but there are some few that have formed as a solid solution (see Figure 4.2-6, circled in red) whereas all larger particles exhibit Ni@Pt core@shell structure with a Pt-shell which is distinctly thinner than the ones observed for the $Pt_{90}Ni_{10}$ NPs. In addition, there is an intermediate particle size in this sample, which exhibits Ni@Pt core@shell structure with a Pt-shell similar in thickness to the ones observed for the $Pt_{90}Ni_{10}$ NPs. Finally, it can be noted that the distribution in the Pt-shell varies from one particle to another in both the intermediate and the larger ones. The

average element compositions were estimated to have 10.0 ± 1.0, 33.7 ± 1.6 and 58.0 ± 1.4 atomic % Ni for the smaller, intermediate and larger NPs, respectively. The estimated values show that an increasing atomic % Ni is found in particles with increasing size.

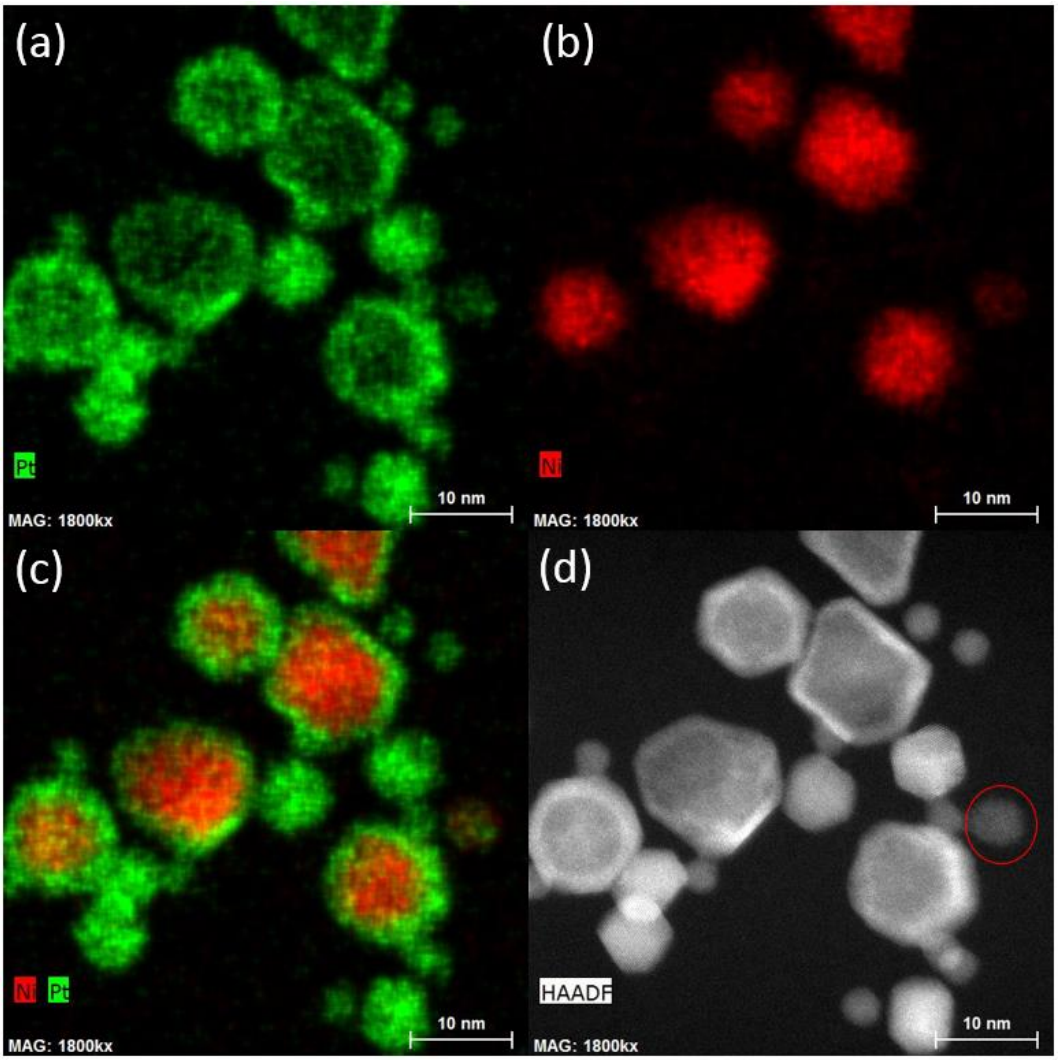

Figure 4.2-6: EDX element mapping of Pt (a) and Ni (b), overlapped EDX image (c) and HAADF-STEM image (d) of $Pt_{50}Ni_{50}$ NPs formed from the simultaneous reduction of $Pt(acac)_2$ and $Ni(acac)_2$ in 1,4-BD in the presence of PVP10. Circled in red is a NP with a solid solution structure.

Figure 4.2-7 shows the EDX element mapping of the NPs with nominal composition $Pt_{10}Ni_{90}$, which reveals two distinct particle sizes with two distinct element distributions. All smaller NPs

are pure Pt whereas all larger ones have Ni@Pt core@shell structure. Further, the Pt-shell in the latter is definitely thinner than the ones observed for both sizes of the $Pt_{50}Ni_{50}$ NPs. The Pt-shells are well-distributed over the Ni-cores and no variation is observed from one particle to another. The estimated average compositions for the $Pt_{10}Ni_{90}$ NPs have 13.2 ± 2.2 and 93.2 ± 3.3 atomic % Ni for the smaller and larger NPs, respectively. These values show that majority of the Ni is found in the larger NPs, but it is important to notice that the quantification of the smaller NPs might not be correct due to too little signal.

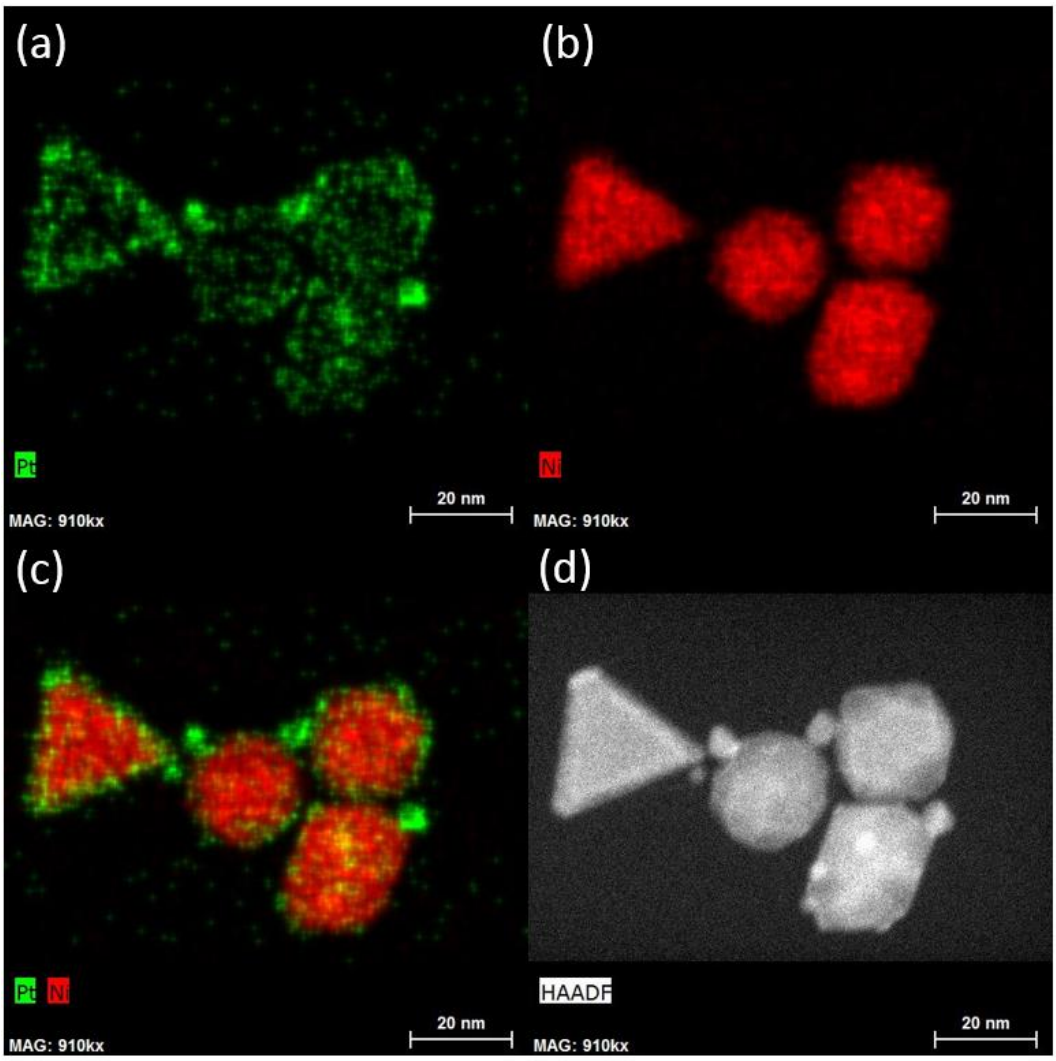

Figure 4.2-7: EDX element mapping of Pt (a) and Ni (b), overlapped EDX image (c) and HAADF-STEM image (d) of $Pt_{10}Ni_{90}$ NPs formed from the simultaneous reduction of $Pt(acac)_2$ and $Ni(acac)_2$ in 1,4-BD in the presence of PVP10.

Finally, overlapped EDX images of individual NPs of nominal compositions $Pt_{90}Ni_{10}$, $Pt_{50}Ni_{50}$ and $Pt_{10}Ni_{90}$ are reported in Figure 4.2-8 along with plots showing the variation in element composition across the particles. The plots were prepared from the average element compositions estimated from each of the squares (numbered green squares in Figure 4.2-8). Hence, the data points are positioned along the x-axis so that they are below the centers of the respective squares. Note that the grey dotted lines, which connect the EDX-images of the NPs with their respective plots illustrate the beginning and end of the measured diagonals and do not represent the exact sizes of the NPs.

Figure 4.2-8 (a) shows a NP with nominal composition $Pt_{90}Ni_{10}$, which has clearly formed a core@shell structure. The EDX analysis shows a Pt-rich shell with $Pt_{83}Ni_{17}$ and $Pt_{88}Ni_{12}$ element compositions at the two ends of the analyzed particle and a Ni-rich core with element composition $Pt_{46}Ni_{54}$. In addition, the fitted curves for Pt- and Ni-content (green and red, respectively) do not intersect with the former being at higher atomic % whereas the latter stays at the lower atomic %. Note that the analysis considers the particle in 2D and part of the measured Pt-signal from the middle comes from the layer of Pt, which lays on top of the core (normal to the paper plane). Hence, the actual core would be richer in Ni than estimated.

The illustrated element distribution across a NP from the batch with nominal composition $Pt_{50}Ni_{50}$ (Figure 4.2-8 (b)), shows a core@shell structure with distinctly larger $Pt_{15}Ni_{85}$-core and a shell with element compositions $Pt_{62}Ni_{38}$ and $Pt_{44}Ni_{56}$ at the two ends. Further, the fitted curves for Pt- and Ni-content barely intersect with the former being at lower atomic % whereas the latter is at the higher atomic %, which is contrary to the analyzed NP with nominal composition $Pt_{90}Ni_{10}$.

Finally, Figure 4.2-8 (c) shows that a NP with nominal composition $Pt_{10}Ni_{90}$, does not have as pronounced core@shell structure as the ones from the $Pt_{10}Ni_{90}$ and $P_{50}Ni_{50}$ batches. The fitted curves for Pt- and Ni-content show relatively small changes in element composition across the analyzed NP with estimated average compositions Pt_3Ni_{97} in the core and $Pt_{25}Ni_{75}$ and $Pt_{13}Ni_{87}$ in the two ends.

Overlapped EDX images and estimated average element compositions at different positions of all the analyzed NPs are available in the appendix (9.2).

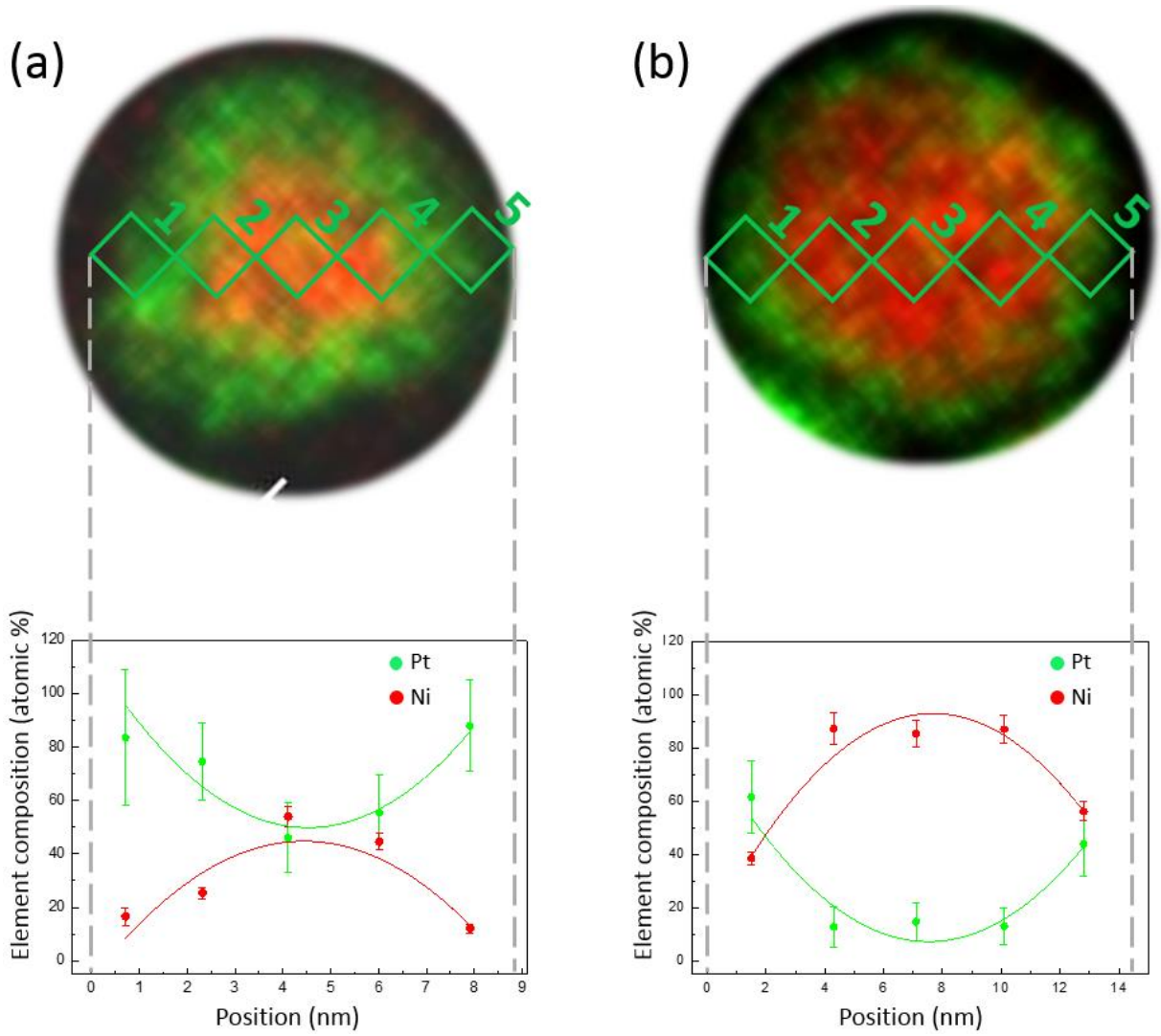
(a)
1
2
3
4
5
Element composition (atomic %)
Position (nm)
Pt
Ni
(b)
1
2
3
4
5
Element composition (atomic %)
Position (nm)
Pt
Ni

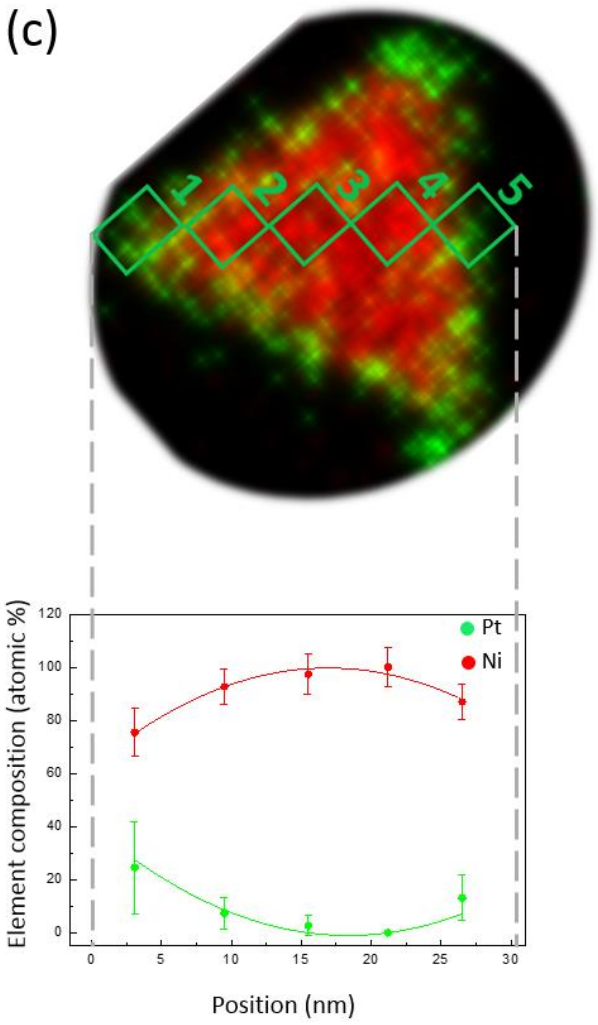

Figure 4.2-8: Overlapped EDX images and element distribution curves along the diameter of NPs of the nominal compositions $Pt_{90}Ni_{10}$ (a), $Pt_{50}Ni_{50}$ (b) and $Pt_{10}Ni_{90}$ (c) formed from the simultaneous reduction of $Pt(acac)_2$ and $Ni(acac)_2$ in 1,4-BD in the presence of PVP10. The plots include the estimated element compositions in 5 non-overlapping regions of the particles and the spread of one standard deviation (σ).

In summary, the HAADF-STEM-EDX element mapping of the alloyed NPs prepared in this part of the work reveals that the three nominal compositions give heterogeneous element distribution and composition of the individual particles. I.e., overall the sample batches are quite ill defined. However, still a trend is seen in the sense that the Ni@Pt core@shell particles tend to form with decreasing thickness of the Pt-shell with increasing atomic % Ni in their nominal composition and thus, the structure type becomes less pronounced. This may be explained from the decreasing amount of Pt precursor available for the formation of the shells. However, it is important to note

that there are some pure Pt NPs even in the $Pt_{10}Ni_{90}$ sample. In addition, it was revealed that the NPs have an increasing content of Ni with increasing particle size for all analyzed compositions. Ni@Pt core@shell NPs have been previously synthesized by Lee et al. [39] from a simultaneous reduction method and by Chen et al. [27] from a sequential reduction method. Our findings are in line with the former.

4.2.4 Magnetic Properties of $Pt_{100-x}Ni_x$ Nanoparticles

Some selected $Pt_{100-x}Ni_x$ NPs (x = 0, 10, 50, 90 and 100) were analyzed by PPMS to study their magnetic properties. The samples were chosen so that one could get insight to the magnetic properties of the entire series without analyzing all of them. Magnetization curves for the Pt, $Pt_{90}Ni_{10}$, $Pt_{50}Ni_{50}$, $Pt_{10}Ni_{90}$ and Ni NPs are reported in Figure 4.2-9 (a), (b), (c), (e) and (g), respectively. In addition, as the magnetization curves for $Pt_{50}Ni_{50}$, $Pt_{10}Ni_{90}$ and Ni NPs are showing hysteresis loops enlarged plots are reported for these compositions in Figure 4.2-9 (d), (f) and (h). The curves show the applied field-dependence of magnetization of the selected NPs. For all data, a correction of the diamagnetic contribution of the sample holder is performed.

Firstly, the magnetization curve for Pt NPs (Figure 4.2-9 (a)) suggests diamagnetic behavior as a net reduction in the magnetic susceptibility is observed with applied increasing magnetic field. This observation is not in line with out expectations, as Pt is reported to be a Pauli paramagnet [16], which should show a very weak but positive susceptibility. However, the diamagnetic behavior can be explained as the Pt NPs are covered with PVP, which is diamagnetic. Similarly, Kozejova et al. [38] report $Pt_{75}Ni_{25}$ NPs supported on Highly Oriented Pyrolytic Graphite (HOPG) to give a diamagnetic behavior. Figure 4.2-9 (b) shows that the $Pt_{90}Ni_{10}$ NPs have spontaneous magnetization when an external field is applied. In addition, there is no hysteresis, which suggests that the NPs are superparamagnetic. The saturation magnetization is very small, and the superparamagnetic contribution is minor, indicating that most of the Ni is incorporated in Pt, which should give a Pauli paramagnetic behavior at this degree of alloying (Figure 1.3-1) [16]. A small fraction of the sample must then contain some Ni rich constituents.

Further, the magnetization curves for $Pt_{50}Ni_{50}$ (Figure 4.2-9 (c and d)) and $Pt_{90}Ni_{10}$ (Figure 4.2-9 (e and f)) NPs show all a saturation magnetization, which suggests that there are at least one

ferromagnetic or superparamagnetic phase for each composition. In addition, there is a very small hysteresis loop, which suggests that the NPs have a ferromagnetic contribution. Finally, Figure 4.2-9 (c and d) shows spontaneous magnetization for the Ni NPs and hysteresis behavior when an external field is applied. Hence, the NPs are ferromagnetic. Furthermore, it can be noticed that the saturation magnetization increases with increasing atomic % Ni in the nominal composition. Overall, the magnetization data for the explored NP samples are not in line with what reported for the bulk Pt-Ni system, whereof alloys up to 70 atomic % Ni are expected to be Pauli paramagnets (Figure 1.3-1) [16].

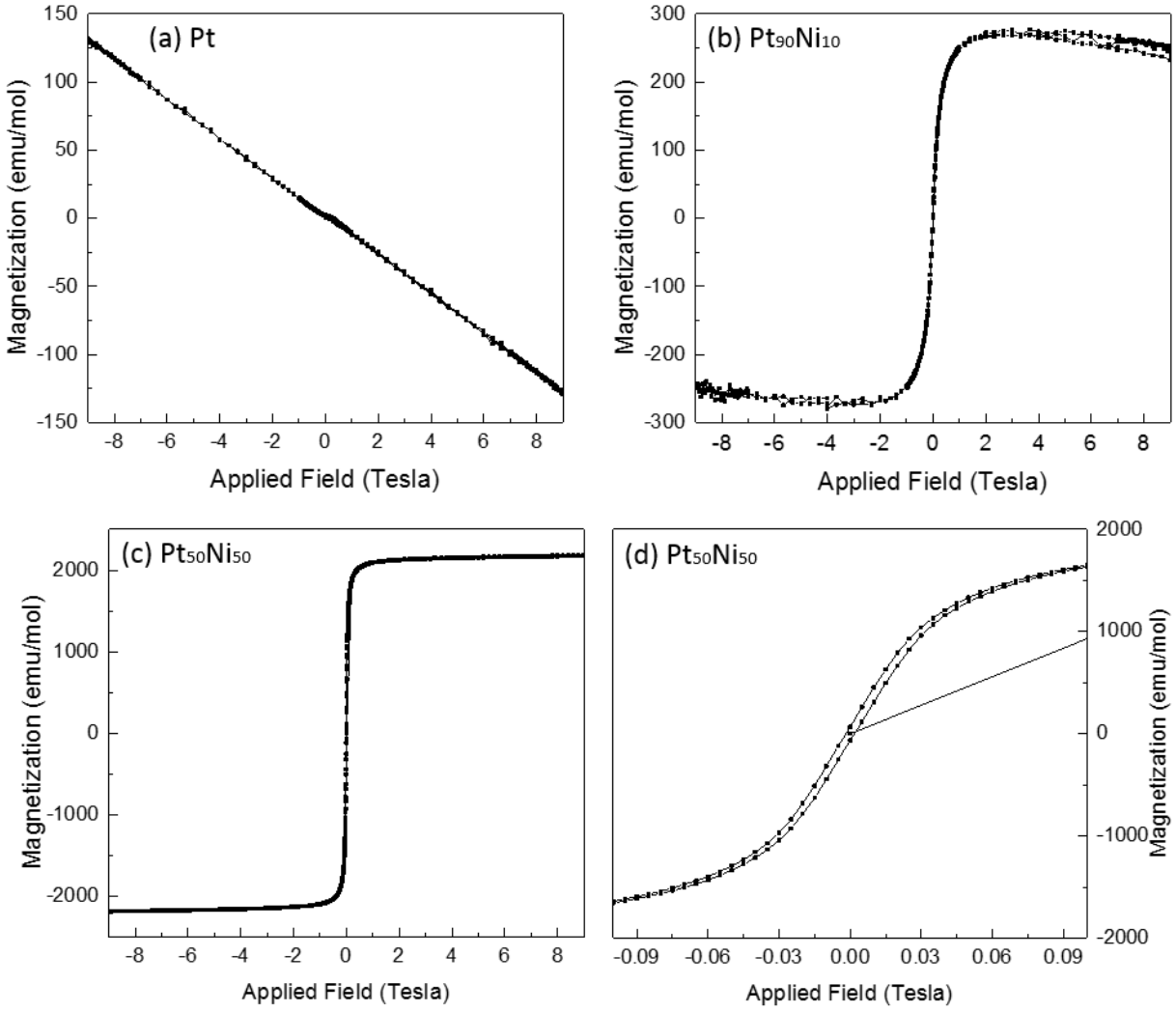

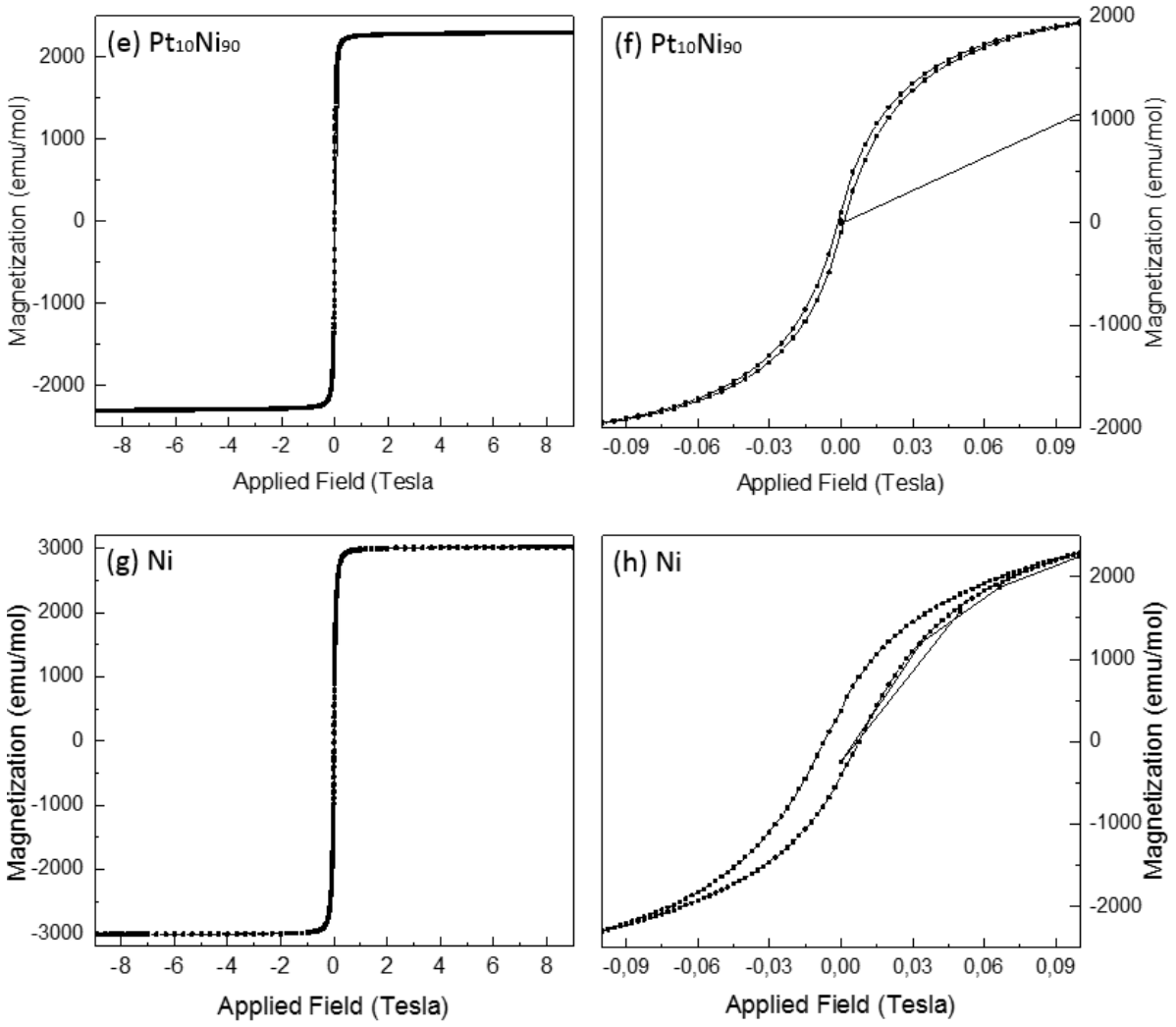

Figure 4.2-9: Magnetization curves measured at 300 K for NPs with nominal composition Pt (a), $Pt_{90}Ni_{10}$ (b), $Pt_{50}Ni_{50}$ (c), $Pt_{10}Ni_{90}$ (e) and Ni (g). In addition, the magnetic hysteresis loops observed in the data for $Pt_{50}Ni_{50}$ (d), $Pt_{10}Ni_{90}$ (f) and Ni NPs (h).

4.3 Optimization of $Pt_{100-x}Ni_x$ Nanoparticles

The results presented in this subchapter are gathered from the synthesis and characterization of free-standing $Pt_{100-x}Ni_x$ NPs (x = 50 and 90) obtained by exploring samples during the propagation of the standard polyol route (subchapter 4.2) or by modifying it. The purpose of these experiments is to produce more homogeneous NPs in respect to particle size and element distribution; see experimental details in section 3.2.3. Additionally, an attempt to employ an alternative polyol synthesis was explored for $Pt_{75}Ni_{25}$, which has been successful for the production of single phase $Pt_{100-x}Ni_x$ (x = 20, 25, 33 and 50) NPs in a previous work [42]; see experimental details in section 3.2.4. In Table 4.3-1 are experimental details summarized together with some of the key findings obtained in the individual experiments.

Table 4.3-1: Experimental work done on $Pt_{100-x}Ni_x$ NPs prepared via the modified polyol heat-up method. In this table, the following information is given: experiment number, nominal composition of the NPs, precursors (in the order: metal precursors, surfactant, solvent, reducing agent, acid/base for pH regulation), total metal ions/PVP10 ratio, synthesis -temperature and -time, analysis methods, particle size found by means of SEM and unit cell dimensions found from PXRD. The reported uncertainties in the unit cell dimensions are the mathematical ones originating from the TOPAS-refinements. See explanations of the alphabetical superscripts at the bottom of the table.

Exp. no.	Nominal comp.	Precursors	Metal ions/ PVP10	Synth. temp. [°C]	Synth. time [min]	Analysis methods			Particle size and size distribution [nm]				*a*-axis [Å]			Element distribution [% Ni]		
						SEM	TEM	PXRD	Monomodal	Multimodal			Pt-rich	Pt-Ni	Ni-rich	small NPs	intermediate NPs	large NPs
1	$Pt_{50}Ni_{50}$	$Pt(acac)_2$ $Ni(acac)_2$	1/10	220	0	✓		✓	8.8 ± 3.5	2.9 ± 0.6	-	10.0 ± 2.3	-			-		
					15[a]		✓		8.3 ± 3.8	3.6 ± 0.9	-	10.9 ± 1.9				36.2 ± 2.4	-	84.6 ± 2.7
		PVP10			30				7.8 ± 3.4	4.0 ± 0.8	-	10.5 ± 1.4				-		
		1,4-BD			60				7.8 ± 3.7	4.5 ± 1.1	-	11.3 ± 1.6						
					120[b]		✓		6.5 ± 3.9	2.6 ± 0.6	6.2 ± 0.9	11.9 ± 1.2				10.0 ± 1.0	33.7 ± 1.6	58.0 ± 1.4
2	$Pt_{10}Ni_{90}$	$Pt(acac)_2$ $Ni(acac)_2$	1/100	220	120	✓	✓	✓	20.1 ± 4.5	5.7 ± 1.3	-	20.7 ± 3.5	-	3.70 ± 0.01	3.5417 ± 0.0007	9.7 ± 1.4	-	88.1 ± 3.0
		PVP10																
		1,4-BD																
3	$Pt_{75}Ni_{25}$	H_2PtCl_6 $NiCl_2{\cdot}6H_2O$	-	70	180	✓		✓	-				3.933 ± 0.004	-	-	-		
		EG																
		$NaBH_4$																
		NaOH																

[a]For TEM imaging, a separate synthesis was performed with synthesis time 15 min, the product was quenched to RT and then washed before it was analyzed

[b]SEM and TEM imaging on this sample already performed in our previous work (section 4.2)

4.3.1 Tuning the Reduction Kinetics of $Pt(acac)_2$ and $Ni(acac)_2$ in 1,4-BD

Our work on optimizing the polyol heat-up method started by studying the propagation of the nanoparticle nucleation and growth during the standard synthesis of the alloyed NPs with nominal composition $Pt_{50}Ni_{50}$ (experiment 1 in Table 4.3-1). Experimental details are given in section 3.2.3. Small samples were taken out from the colloidal suspension at selected time points during the 2-hour-long synthesis. The time points are 0 (sample 1), 15 (sample 2), 30 (sample 3), 60 (sample 4) and 120 minutes (sample 5) with time starting when the suspension had reached the targeted synthesis temperature of 220 ^{0}C. The five samples were analyzed by SEM imaging in order to study the NP growth with time. The obtained results are reported in Figure 4.3-1 using the same magnification on the BF-STEM images and the same scale for the size distribution histograms. The histograms are prepared by measuring the diameter of 250 NPs. Based on observations from SEM imaging, another synthesis was conducted with the same conditions, but it was stopped at 15 min synthesis time and the colloidal suspension was quenched to room temperature. The purpose of the second synthesis was to allow for HAADF-STEM-EDX elemental mapping, which requires the NPs to be washed and the results are presented as if the sample collected at 15 min (sample 2) was analyzed. This analysis was done to study the change in elemental distribution with time by comparison with the sample with standard synthesis time 120 min (sample 5), which was previously analyzed (section 4.2). Additionally, heterogeneities in the element composition across two individual particles were studied and the findings for one particle are reported in Figure 4.3-4. Additional information from the estimation of average element compositions and the second individually studied particle are available in the appendix (9.2).

Firstly, Figure 4.3-1 shows that the NPs collected at 0 min (sample 1, Figure 4.3-1 (a)) are already of significant size, which is visually very similar to the one of the NPs collected at 120 min (sample 5, Figure 4.3-1 (e)), which suggests little particle growth during the synthesis. In addition, the former are distinctly more homogeneous in size than the latter. A careful inspection of the BF-STEM images for all samples indicates that between the synthesis time points 15 min (sample 2) and 30 min (sample 3) the NPs become visibly more heterogeneous with respect to particle size. Further, it was found that the average particle size when considering the distributions as monomodal, decreases from 8.8 ± 3.5 nm to 6.5 ± 3.9 nm from sample 1 to sample 5.

A more detailed inspection of the size distribution histograms reveals that the NPs collected at 0, 15, 30 and 60 min have bimodal size distributions whereas the NPs with synthesis time 120 min have a trimodal size distribution; see histograms in Figure 4.3-1. Contrary to the conclusion about particle size homogeneity based on inspection of the BF-STEM images, the NPs lose their uniformity already in the first 15 minutes. In addition, it is evident that the ratio of larger/smaller NPs decreases steadily from sample 1 (Figure 4.3-1 (a)) to sample 5 (Figure 4.3-1 (e)), which suggests nucleation throughout the entire synthesis. Figure 4.3-2 (b) shows that both the smaller and the larger NPs grow with increasing synthesis time, although the growth is not significant and most of the variations fall within the calculated spread of one standard deviation. The appearance of a third, intermediate, particle size between the samples collected at 60 and 120 min (samples 4 and 5, respectively) suggests that the smaller NPs from the former have grown to this size and the smaller NPs from the latter have nucleated and grown in the last 60 min of the synthesis. This suggests that a shorter synthesis time along with quenching of the colloidal suspension to RT to stop further nucleation and growth of already formed NPs, could result in sample batches with a narrower size distribution.

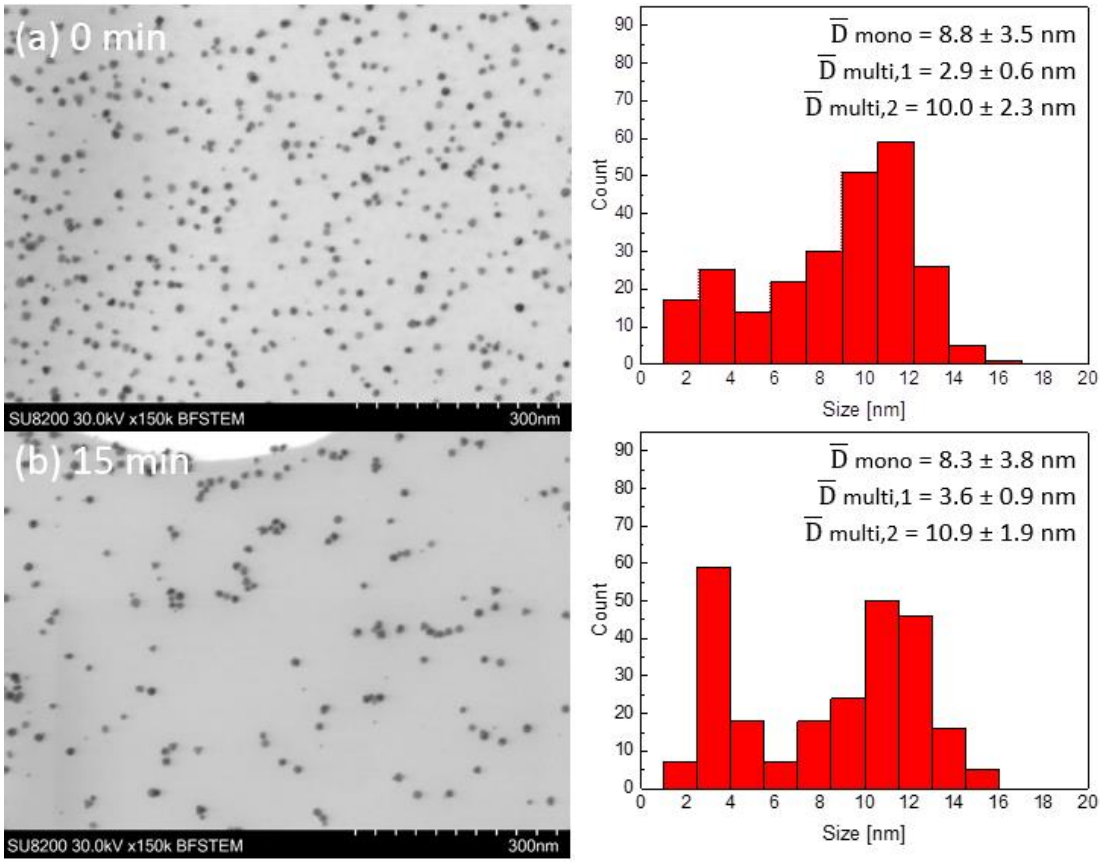

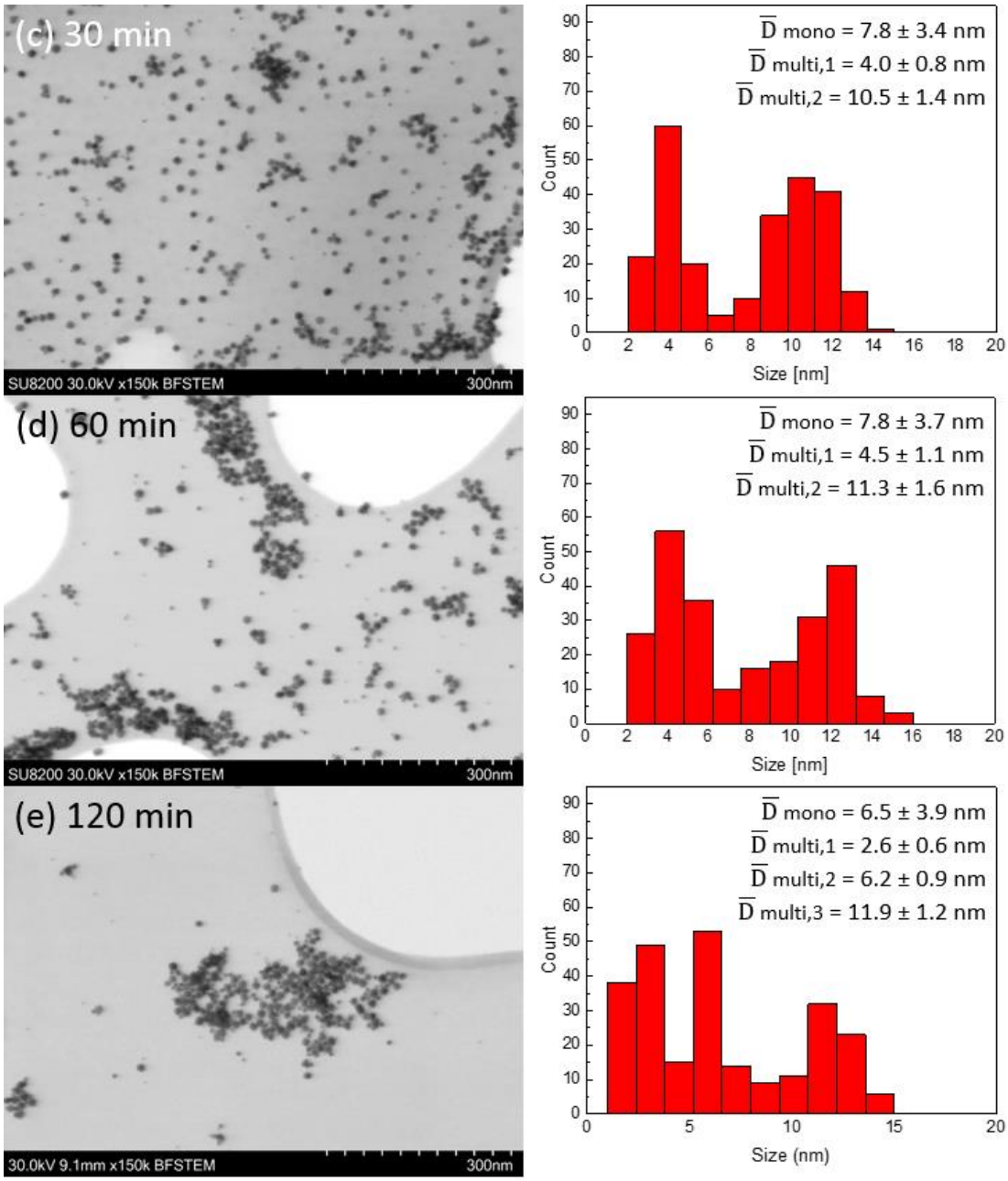

Figure 4.3-1: BF-STEM images and size distribution histograms of $Pt_{50}Ni_{50}$ NPs formed from the simultaneous reduction of $Pt(acac)_2$ and $Ni(acac)_2$ in 1,4-BD with metal precursor/PVP10 ratio 1/10 and synthesis time 0 min (a), 15 min (b), 30 min (c), 60 min (d) and 120 min (e). The histograms are prepared by measuring the diameter of 250 NPs and include the calculated average particle size ($\overline{D}$) and spread in the particle size distribution (standard deviation, σ) for both monomodal and multimodal distribution.

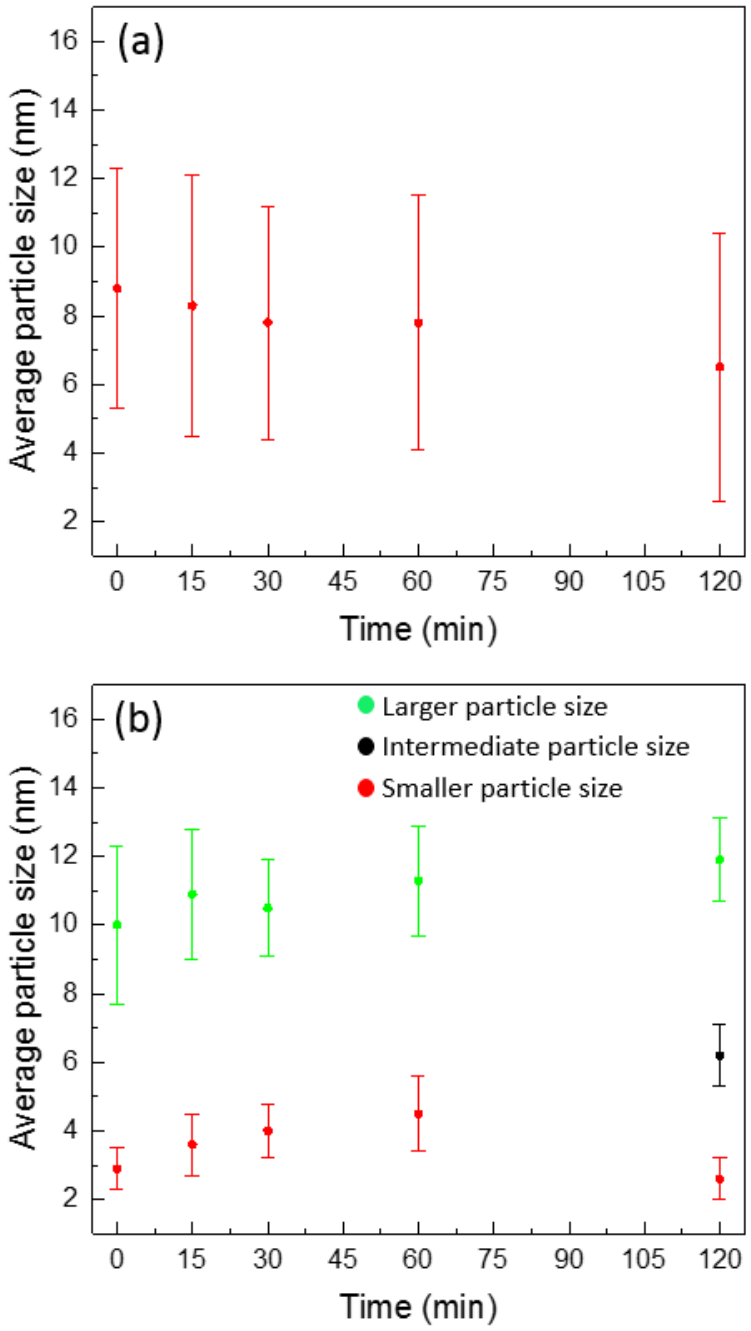

Figure 4.3-2: Change in average particle size for $Pt_{50}Ni_{50}$ NPs formed from the simultaneous reduction of $Pt(acac)_2$ and $Ni(acac)_2$ in 1,4-BD with metal precursor/PVP10 ratio 1/10 with increasing synthesis time assuming monomodal (a) and multimodal (b) particle size distributions. The plots include the calculated average particle size ($\overline{D}$) and spread in the particle size distribution (standard deviation, σ).

Based on the visual estimations obtained from the BF-STEM images and the accompanied particle size distribution histograms, the NPs collected at 15 min (sample 2) were explored further by HAADF-STEM-EDX elemental mapping with the purpose to shed light on possible changes in element content in the various size fractions. Representative images are reported in Figure 4.3-3. The average elemental compositions for the two particle sizes, according to the bimodal size distribution, were calculated from the elemental mappings of multiple analyzed regions. Obtained results are listed in Table 4.3-1.

Figure 4.3-3 shows that there is a variety of NPs present in the sample collected at 15 min (sample 2). Firstly, there is a big difference in elemental composition from one small particle to another. There are some Pt, some Ni@Pt core@shell and some Pt-Ni solid solution NPs. Further, all larger NPs have a Ni@Pt core@shell structure with no visually distinct variations in the Pt/Ni ratio from one particle to another. In most of the larger NPs, the Pt-shell is equally distributed across the Ni-core. In addition, the Pt-shell in a smaller core@shell NP is a lot thicker than the Pt-shell of a larger core@shell NP. The estimated average compositions are 36.2 ± 2.4 and 84.6 ± 2.7 atomic % Ni for the smaller and larger NPs, respectively. These values show that the majority of the Ni is found in the larger NPs. These observations indicate that the Ni-precursor is nucleating faster than the Pt-precursor, and that the nucleation and growth phases are not fully separated.

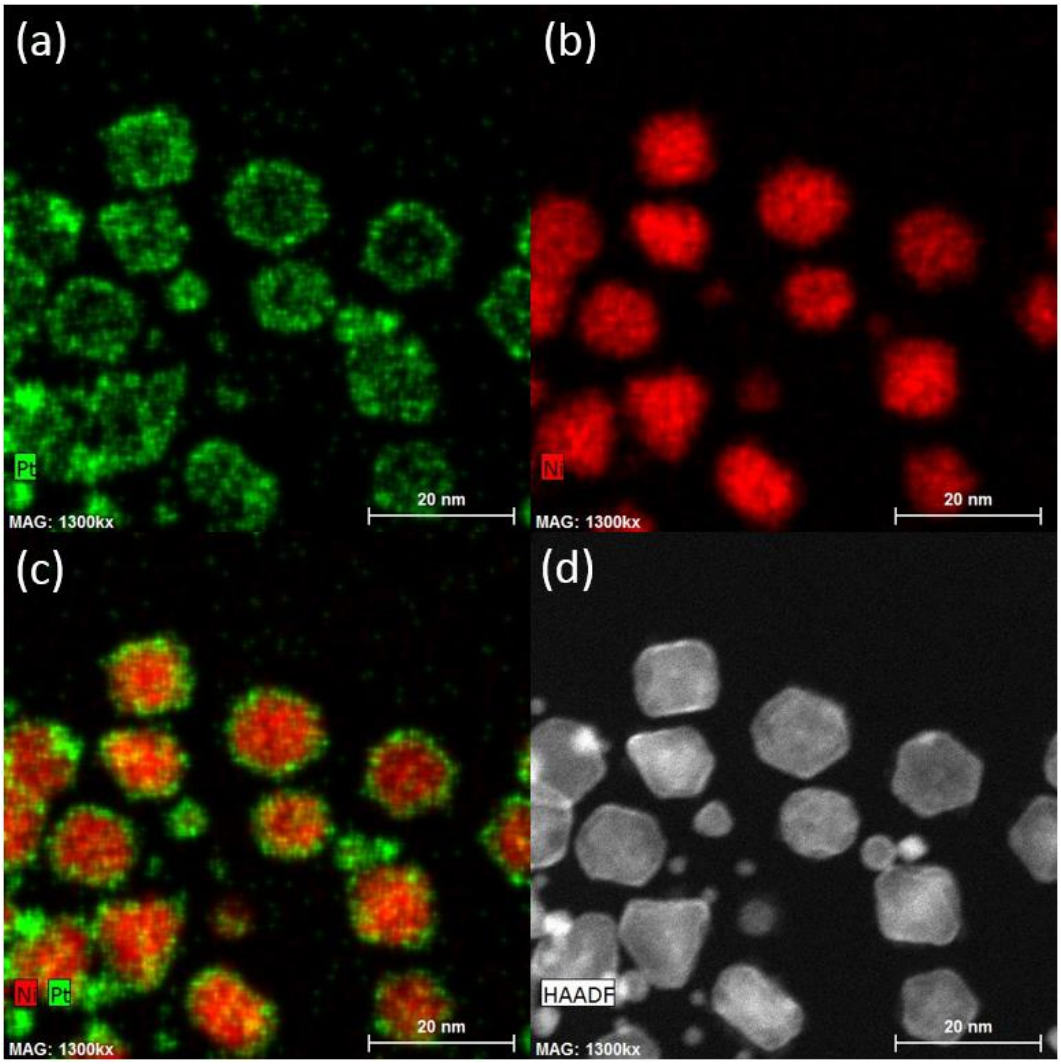

Figure 4.3-3: EDX elemental mapping of Pt (a) and Ni (b), overlapped EDX image (c) and HAADF-STEM image (d) of $Pt_{50}Ni_{50}$ NPs formed from the simultaneous reduction of $Pt(acac)_2$ and $Ni(acac)_2$ in 1,4-BD with metal precursor/PVP10 ratio 1/10 and synthesis time 15 min.

Finally, the overlapped EDX image and a plot of the variation in element composition across a particle from the sample collected at 15 min (sample 2, Figure 4.3-4), show that the particle has a core@shell structure. However, the fitted curves for Pt- and Ni-content (green and red, respectively) show relatively small changes in element composition across the particle with estimated average compositions ≈ Pt_4Ni_{96} (the average value between the studied regions number 2 and 3) in the middle and $Pt_{19}Ni_{81}$ and $Pt_{27}Ni_{73}$ in the two ends. In addition, it can be observed

both visually and from the estimated element compositions that the Pt-shell is not distributed evenly across the studied NP.

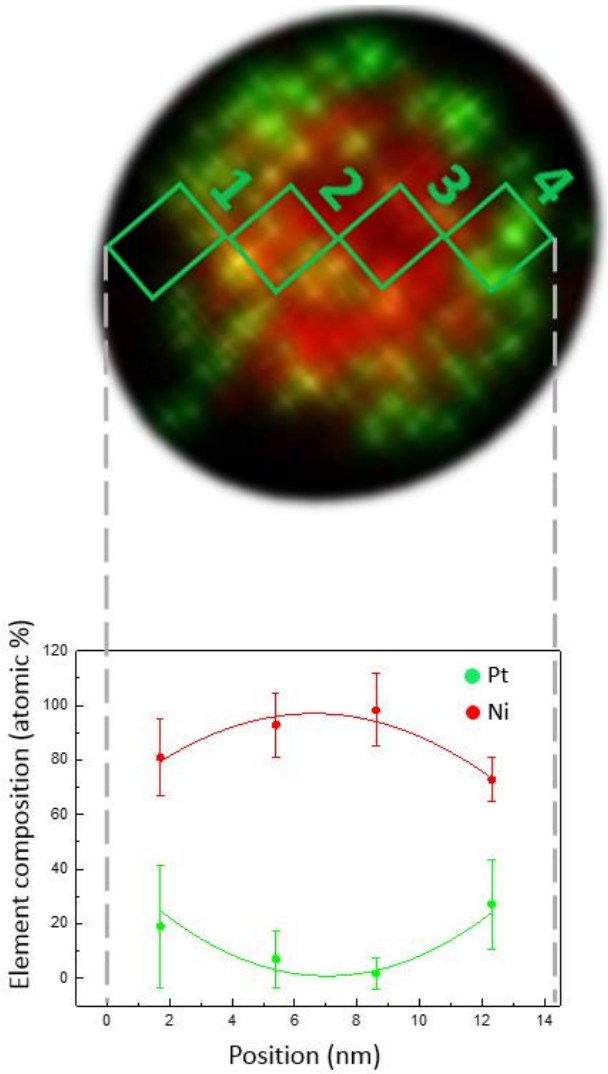

Figure 4.3-4: Overlapped EDX image and element distribution curves along the diameter of a particle with nominal composition $Pt_{50}Ni_{50}$ formed from the simultaneous reduction of $Pt(acac)_2$ and $Ni(acac)_2$ in 1,4-BD with metal precursor/PVP10 ratio 1/10 and synthesis time 15 min. The plot includes the estimated element compositions in 4 non-overlapping regions of the particle and the spread of one standard deviation (σ).

Our work on optimizing the polyol heat-up method continued by increasing the amount of surfactant (PVP10) present during the synthesis of the alloyed NPs with nominal composition $Pt_{10}Ni_{90}$ (experiment 2 in Table 4.3-1) from our standard metal precursor/PVP10 ratio 1/10 to 1/100, else keeping all other conditions identical. This modification was done with the purpose to

produce NPs with a narrower monomodal size distribution, as we know from a previous study that the nucleation kinetics is affected by the quantity of surfactant used [82]. The size and morphology of the NPs were studied by SEM imaging, and a size distribution histogram was prepared by measuring the diameter of 250 NPs. The results obtained from this analysis are reported in Figure 4.3-5 using the same magnification on the BF-STEM image and the same scale on the histogram as the ones presented in section 4.2, so that the results can be easily compared later on. Then, the NPs were analyzed by means of PXRD for phase identification and estimation of the unit cell dimensions; see Figure 4.3-6. Finally, HAADF-STEM-EDX elemental mapping was performed to study the elemental distribution of the NPs; see Figure 4.3-7. The average elemental compositions for the two particle sizes, according to the bimodal size distribution, were calculated from the elemental mappings of multiple analyzed regions. Obtained results are listed in Table 4.3-1. Additionally, heterogeneities in the element composition across two individual particles were studied and the findings for one particle are reported in Figure 4.3-8. Additional information from the estimation of average element compositions and the second individually studied particle are available in the appendix (9.2).

Figure 4.3-5 (a) shows that the $Pt_{10}Ni_{90}$ NPs prepared in this part of the work are faceted and well-dispersed over the TEM-grid. Most of the imaged NPs are of a similar size and there are a few smaller ones. The histogram in Figure 4.3-5 (b) is analyzed in terms of both mono- and bimodal size distributions. Assuming a monomodal size distribution the average particle size is 20.1 ± 4.5 nm. Averages sizes for the smaller and larger NPs assuming a bimodal size distribution are 5.7 ± 1.3 nm and 20.7 ± 3.5 nm. With respect to faceting, no system was observed for the NPs.

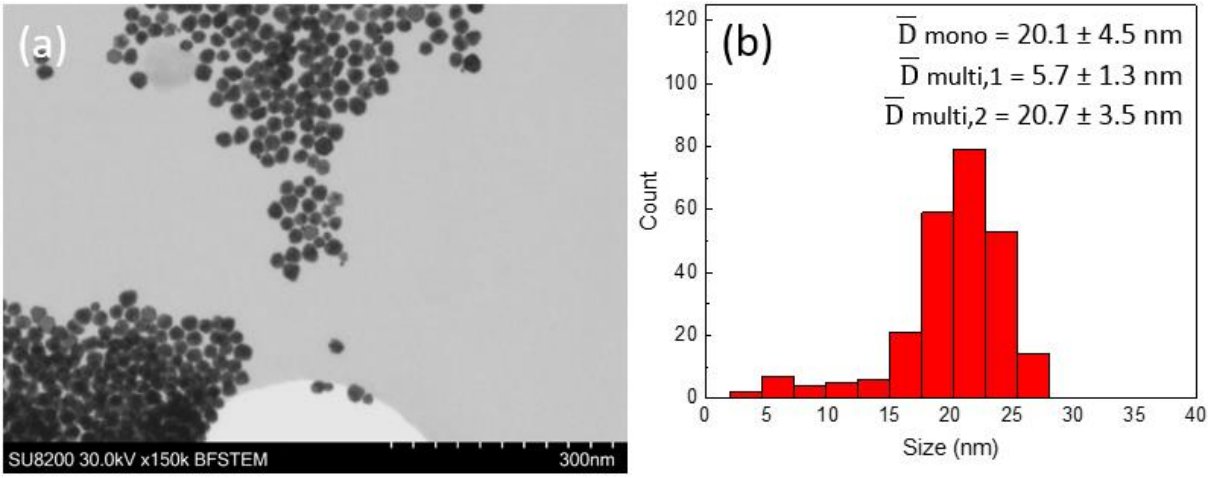

Figure 4.3-5: BF-STEM image (a) and size distribution histogram (b) of $Pt_{10}Ni_{90}$ NPs formed from the simultaneous reduction of $Pt(acac)_2$ and $Ni(acac)_2$ in 1,4-BD with metal precursor/PVP10 ratio 1/100. The histogram is prepared by measuring the diameter of 250 NPs and includes the calculated average particle size ($\overline{D}$) and spread in the particle size distribution (standard deviation, σ) for both monomodal and multimodal distribution.

By inspecting the PXRD pattern of the $Pt_{10}Ni_{90}$ NPs (Figure 4.3-6), it was found that beyond the peaks originating from the Si-NIST reference material, only the (111), (200), (220) and (311) hkl-planes originating from a ccp Ni-phase are present. The positions of the Bragg-reflections are shifted slightly to lower angles compared to those from ccp Ni and no additional Bragg-reflections originating from a ccp Pt-phase or any impurities are present. These results suggest that there is a single, Ni-rich phase and that the lattice expansion is caused by the introduction of some larger Pt atoms in the Ni-lattice. Upon closer inspection of the diffractogram, a small extension of the (111) Bragg-reflection at lower angles can be noticed, which suggests the presence of a second phase. Hence, the TOPAS-refinement on the diffraction pattern was done for two phases. The estimated values for the *a*-axis are 3.70 ± 0.01 Å and 3.5417 ± 0.0007 Å. The former *a*-axis is length somewhere between the *a*-axis for both pure ccp Pt and Ni (3.9221 ± 0.0001 Å and 3.5247 ± 0.0001 Å, respectively). However, the latter value is only slightly larger than the *a*-axis for ccp Ni. Hence, these values suggest a Pt-Ni and Ni-rich phase, respectively. Finally, the background in the PXRD pattern shown in Figure 4.3-6 is quite high and there is a lot of noise. This can be explained by the product's gel-like character and the difficulty to properly prepare a PXRD sample.

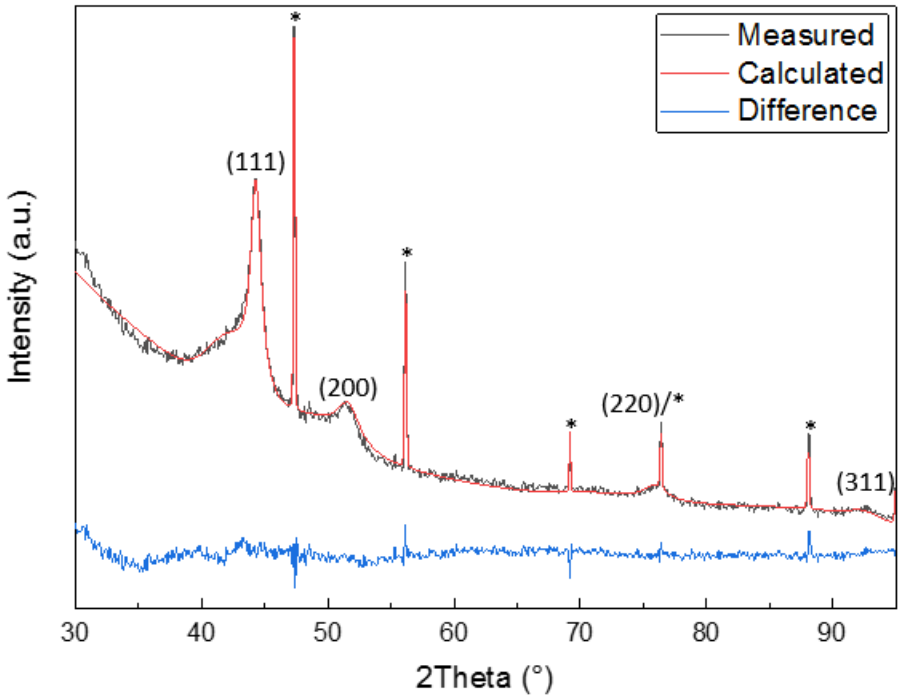

Figure 4.3-6: PXRD pattern of $Pt_{10}Ni_{90}$ NPs formed from the simultaneous reduction of $Pt(acac)_2$ and $Ni(acac)_2$ in 1,4-BD with metal precursor/PVP10 ratio 1/100. The measured (black) and calculated (red) patterns as well as the difference between them (blue) are included. *Miller indices of the ccp Ni phase are included, and the Bragg reflections from a reference Si-NIST sample are labeled with a *.

The HAADF-STEM-EDX images presented in Figure 4.3-7 show that most of the $Pt_{10}Ni_{90}$ NPs have a uniform size with a Ni@Pt core@shell elemental distribution. Some very few NPs are significantly smaller (one shown in Figure 4.3-7) than the main distribution. Elemental mapping shows these to be pure Pt. Further, the Pt-shell in some of the larger NPs is equally distributed over the Ni-core while in others it is distinctly thicker on one side of the particle than the rest. Finally, small variations in the elemental composition from one large particle to another are observed visually. The average elemental compositions were estimated to 9.7 ± 1.4 and 88.1 ± 3.0 atomic % Ni for the smaller and larger NPs, respectively. It is important to note that the accuracy of the calculations depends on the signal available in the analyzed section. Hence, it is possible that the smaller particles are pure Pt and the signal from them is too low to give accurate composition.

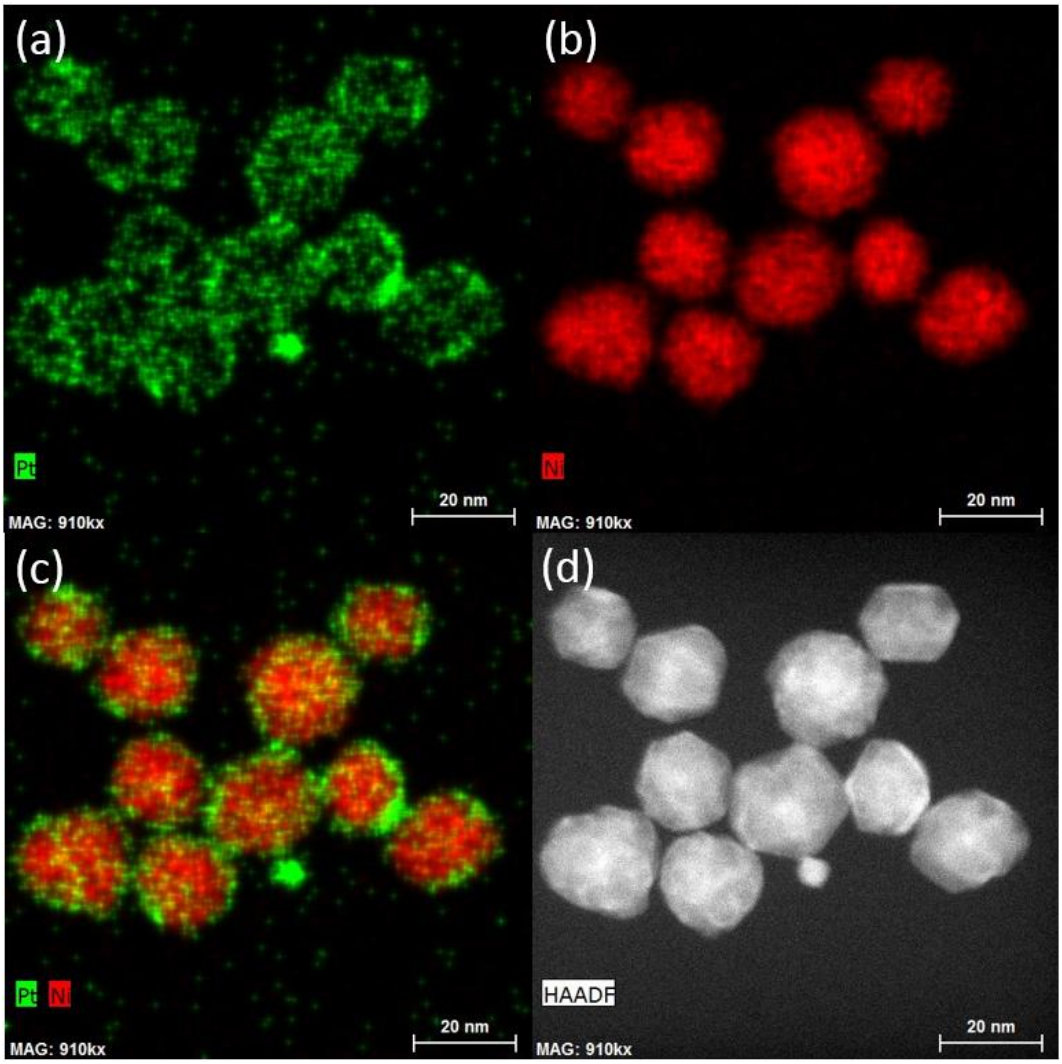

Figure 4.3-7: EDX elemental mapping of Pt (a) and Ni (b), overlapped EDX image (c) and HAADF-STEM image (d) of $Pt_{10}Ni_{90}$ NPs formed from the simultaneous reduction of $Pt(acac)_2$ and $Ni(acac)_2$ in 1,4-BD with metal precursor/PVP10 ratio of 1/100.

Finally, overlapped EDX image and a plot showing the variation in element composition across a single particle are reported in Figure 4.3-8. The obtained data shows a core@shell structure with large variations in the Pt-shell thickness across the particle. The average element compositions were estimated to $Pt_{65}Ni_{35}$ and $Pt_{25}Ni_{75}$ at the two ends of the studied diagonal and $Pt_{11}Ni_{89}$ in the core.

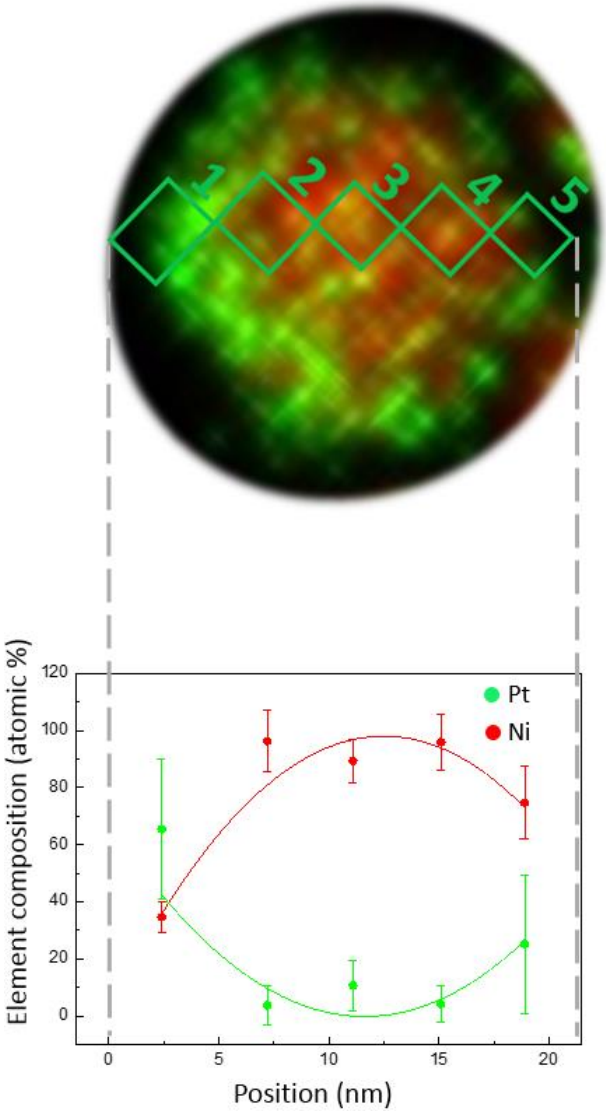

Figure 4.3-8: Overlapped EDX image and element distribution curves along the diameter of a particle with nominal composition $Pt_{10}Ni_{90}$ formed from the simultaneous reduction of $Pt(acac)_2$ and $Ni(acac)_2$ in 1,4-BD with metal precursor/PVP10 ratio 1/100. The plot includes the estimated element compositions in 5 non-overlapping regions of the particle and the spread of one standard deviation (σ).

In summary, the experiment in which particle development was explored with increasing time revealed that batches of NPs with more homogeneous particle size can be prepared for shorter synthesis time. Further, an increased amount of the surfactant, PVP10, was found to steer the reaction kinetics into the production of NPs with narrower size distribution.

4.3.2 $Pt_{75}Ni_{25}$ NPs Produced via an Alternative Synthesis Method

An alternative polyol synthesis route was employed for the preparation of $Pt_{75}Ni_{25}$ NPs as this method has been previously successful for the production of single phase $Pt_{100-x}Ni_x$ (x = 20, 25, 33 and 50) NPs in a previous work [42]. The NPs were produced from the simultaneous reduction of the metal precursors $H_2PtCl_6 \cdot 6H_2O$ and $NiCl_2 \cdot 6H_2O$ in the solvent EG by addition of the reducing agent $NaBH_4$ in the presence of NaOH for pH regulation; see experimental details in section 3.2.4. The size of the NPs was analyzed by SEM imaging; see Figure 4.3-9. Then, the NPs were analyzed by PXRD for phase identification and unit cell dimension evaluations. The obtained diffraction pattern is reported in Figure 4.3-10.

Figure 4.3-9 shows that the employed polyol route produces very small NPs with nominal composition $Pt_{75}Ni_{25}$, which can not be properly analyzed by SEM imaging. Hence, size distribution analysis was not performed on this sample. Further, in some regions of the studied sample the NPs were well-dispersed whereas in others they were agglomerated.

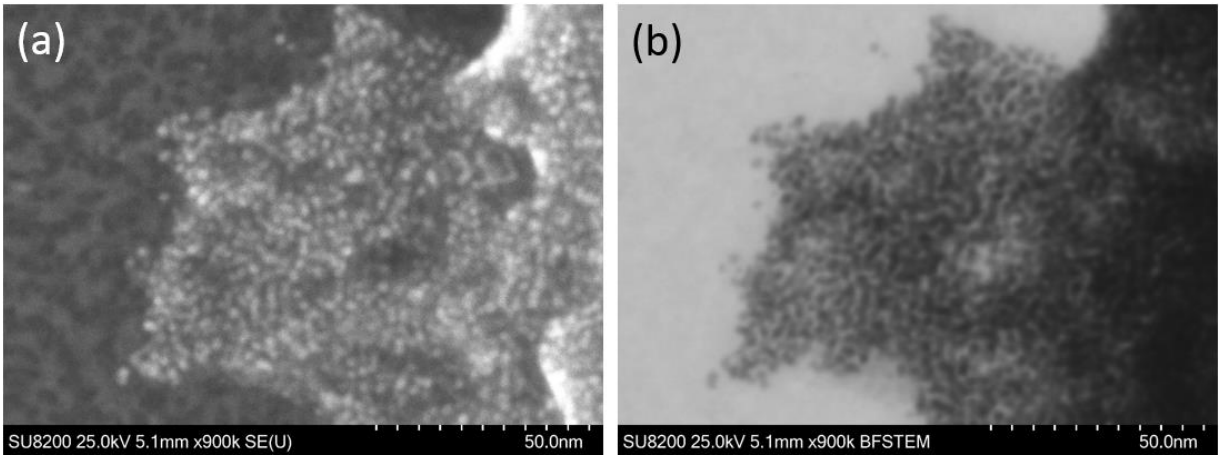

Figure 4.3-9: SEM- (a) and BF-STEM- (b) images of $Pt_{75}Ni_{25}$ NPs prepared from simultaneous reduction of $H_2PtCl_6 \cdot 6H_2O$ and $NiCl_2 \cdot 6H_2O$ in EG by addition of the reducing agent $NaBH_4$ in the presence of NaOH for pH regulation.

By inspecting the PXRD pattern collected from the $Pt_{75}Ni_{25}$ NPs (Figure 4.3-10), it was found that beyond the reflections belonging to the Si-NIST reference material, only (111), (200), (311) and (222) hkl-planes originating from the pure ccp Pt-phase are present. The *a*-axis was refined to

3.933 ± 0.004 Å, which is larger than the one for pure ccp Pt (3.9221 ± 0.0001 Å). This indicates that the prepared NPs are pure Pt rather than the targeted $Pt_{75}Ni_{25}$. In addition, the calculated value for the lattice constant is not in line with the findings of Xiong et al. [42] for NPs of the same nominal composition (3.824 Å), which suggests that the use of a support material might be significant for the preparation of the alloyed NPs.

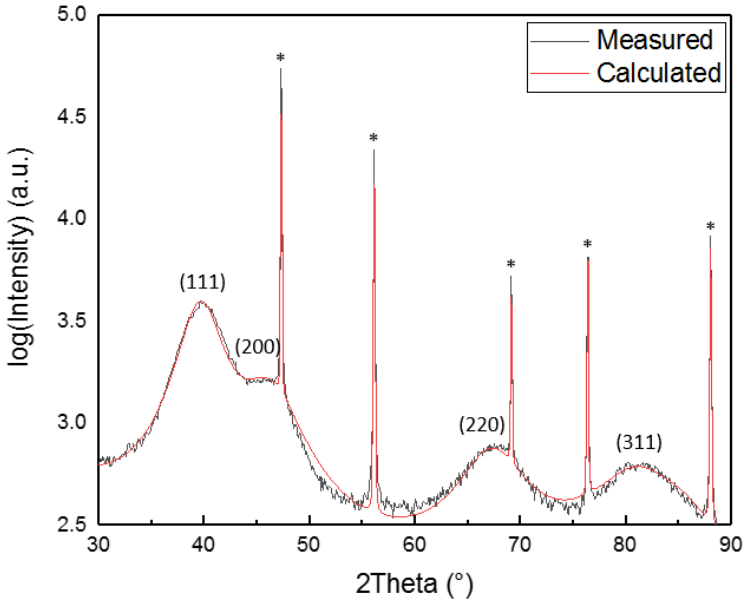

Figure 4.3-10: PXRD pattern of $Pt_{75}Ni_{25}$ NPs prepared from simultaneous reduction of $H_2PtCl_6 \cdot 6H_2O$ and $NiCl_2 \cdot 6H_2O$ in EG by addition of the reducing agent $NaBH_4$ in the presence of NaOH for pH regulation. The measured (black) and calculated (red) patterns are included. *Miller indices of the ccp Pt phase are included, and the Bragg peaks from a reference Si-NIST sample are labeled with a *.

5 Discussion

The primary goal of this master thesis was to explore the suitability of the polyol heat-up method for the synthesis of well-defined $Pt_{100-x}Ni_x$ NPs. In this discussion, some key findings will be considered in detail for that purpose. Firstly, the obtained as-synthesized particles will be fully described with respect to particle size and element distribution by combining information extracted from SEM-histogram analysis, TEM (HAADF-STEM-EDX), PXRD, magnetic measurements and simple kinetic experiments. Subsequently, we will propose a model for the formation of the obtained particles, in terms of a modified LaMer model, which in turn facilitates the understanding of experimental parameters to tune to obtain more homogeneous samples batches. Finally, it will be commented on the powerful combination of characterization techniques used in this work to obtain the full sample characteristics.

5.1 Structural Aspects, Element Composition and Magnetic Properties of $Pt_{100-x}Ni_x$ NPs obtained by the standard heat-up polyol method

Our experimental findings reported in section 4.2 on the simultaneous reduction of $Pt(acac)_2$ and $Ni(acac)_2$ in 1,4-BD with PVP10 (metal/PVP = 1/10) via the standard polyol heat-up method (section 3.2.1) revealed that particle size, number of phases, elemental –composition and –distribution, as well as magnetic properties vary with nominal composition of $Pt_{100-x}Ni_x$ NPs. Furthermore, all compositions turn out to be ill-defined. We base this conclusion on careful analysis of the NPs by combining SEM imaging-histogram analysis, HAADF-STEM-EDX studies, PXRD and structural analysis with magnetic property investigations.

Firstly, SEM imaging combined with histogram analysis revealed that all bimetallic NPs have either bimodal or trimodal particle size distributions (Figure 4.2-1), i.e. the synthesized NPs are heterogeneous with respect to particle size. The $Pt_{80}Ni_{20}$ NPs were found to be the most homogeneous ones with the narrowest particle size distribution and the smallest difference between the two particle size modes (Figure 4.2-2 (b)). However, the overall trend is that with increasing atomic % Ni, the difference between the two particle size modes increases throughout

the $Pt_{100-x}Ni_x$ series (Figure 4.2-2 (b)). Notably, as such, a multimodal particle size distribution, is often an indication of phase segregation.

Further, PXRD measurements in combination with Rietveld refinement showed that there are two or more phases in all alloyed NP batches (Figure 4.2-3). However, the different phases could all be refined with ccp-type structures, where the main difference was the Ni content (or the *a*-axis length). In other words, a standard Vegard law relationship, or a full solid solution, is not formed. Rather, the powder X-ray diffraction analysis shows the samples to be composed of several phases (Figure 4.2-4). The findings from PXRD are in line with our observations from the SEM imaging analysis.

In order to obtain more detailed information on type of phase segregation in the $Pt_{100-x}Ni_x$ particles HAADF-STEM-EDX-elemental mapping were conducted for x = 10, 50 and 90. The analysis revealed that core@shell NPs are formed in all investigated batches (Figures 4.2-5, 4.2-6 and 4.2-7), which supports that there are multiple phases in the product. Additionally, from the combined HAADF-STEM-EDX experiments, it was noted that the larger NPs are richer in Ni than the smaller ones in the same sample (Figures 4.2-5, 4.2-6 and 4.2-7), which suggests that the Ni-metal precursor, $Ni(acac)_2$, has faster kinetics than the Pt one, $Pt(acac)_2$. In addition, it was found that with increasing atomic % Ni, there is an increasing difference in element composition between the smaller and the larger NPs in the same sample (see Table 4.2-1) along with the increasing difference between the two particle size modes observed from SEM imaging (Figure 4.2-2 (b)). The estimated average compositions for NPs with nominal compositions $Pt_{90}Ni_{10}$ and $Pt_{10}Ni_{90}$ are 6.9 ± 0.5 and 14.0 ± 0.3 atomic % Ni and 13.2 ± 2.2 and 93.2 ± 3.3 atomic % Ni, respectively. Hence, the prepared NPs become more heterogeneous with respect to both particle size and element composition with increasing atomic % Ni in the nominal composition.

Finally, magnetic measurements performed by means of PPMS revealed that all the studied alloyed $Pt_{100-x}Ni_x$ (x = 10, 50, 90) NPs give a saturation magnetization. This indicates that all of them have at least one phase, which is ferromagnetic or superparamagnetic. In addition, the observed saturation magnetization increases with increasing atomic % Ni in the nominal composition, which shows that the metallic properties of ferromagnetic/superparamagnetic Ni are reflected in the bimetallic samples whereas the weak Pauli paramagnetic contribution from Pt is hidden. It should however be pointed out that the phases present in the samples cannot be clearly determined using

this characterization technique. It rather tells that all analyzed compositions are giving magnetic properties dominated by Ni rather than Pt.

Based on literature, the heterogeneous nature of the $Pt_{100-x}Ni_x$ NPs does not become surprising as several studies report similar findings (Table 1.3-2). For example, in some studies solid solution for $Pt_{50}Ni_{50}$ NPs has been attempted, but structural data from PXRD measurements shows that a standard Vegard law relationship is not formed. Jiang et al. [23] have reported partial alloying of Pt and Ni with decreasing *a*-axis from Pt to $Pt_{50}Ni_{50}$ (3.920 Å to 3.811 Å). A number of other studies have reported *a*-axis for the $Pt_{50}Ni_{50}$ phase 3.81 Å [24], 3.83 Å [29], 3.84 Å [39], 3.80 Å [39] and 3.80 Å [49]. These values indicate partial degree of alloying between the two metals. Further, Carpenter et al. [29] have also reported that the as-synthesized $Pt_{100-x}Ni_x$ (x = 33, 40, 50 and 67) are not single phase. Further, Bao et al. [24] report the formation of a quasi core-shell configuration for NPs with nominal composition $Pt_{75}Ni_{25}$, where Pt is in the core and NiO_x forms the shell whereas in the work of Park et al. [32] describe $Pt_{75}Ni_{25}$ and $Pt_{50}Ni_{50}$ NPs as alloys of Pt and Ni atoms intermixed with amorphous Ni oxides.

In order to develop the synthesis in a manner that more well-defined NPs can be obtained, an evaluation of the underlying reasons for the uncontrolled NP production is called for.

5.2 Reaction Kinetics of NP Formation via the Standard Polyol Heat-Up Method

In order to get more insight to the NP formation (at standard conditions) the development of particle size and element –composition and –distribution in the NPs with nominal composition $Pt_{50}Ni_{50}$ were studied at selected time points during the synthesis (experiment 1 in Table 4.3-1). SEM imaging showed that the $Pt_{50}Ni_{50}$ samples collected at 0-60 min (Figure 4.3-1 (a-d)) have bimodal size distributions whereas the sample at 120 min (Figure 4.3-1 (e)) has trimodal size distribution. Further, it was noticed that the smaller and larger particle sizes for the samples collected at 0-60 min increased with time and correspond to the intermediate and large particle sizes, respectively, for the sample at 120 min (Figure 4.3-2 (b)). This indicates that in the last 60 min of the synthesis, new, smaller NPs were formed. HAADF-STEM-EDX-elemental mapping (Figure 4.2-6) revealed that the chemical composition of the small NPs is pure Pt. In addition,

when comparing the size distribution histograms, it is noticed that the ratio of small/big NPs increases with synthesis time (Figure 4.3-1 (b and e)), which indicates that nucleation does not occur as a single event.

Further, the element compositions of the large NPs produced after 15 min (Figure 4.3-3) and 120 min (Figure 4.2-6) are very similar both in size and nominal composition, but the Pt-shells are distinctly thicker in the latter. The bimodal distribution analysis of BF-STEM images (Figure 4.3-1 (b and e)) show that the size of the large NPs increases from 10.9 ± 1.9 nm to 11.9 ± 1.2 nm from 15 min to 120 min synthesis time, which is a very small change considering the latter has a lot more time for NP growth. Visually, this change in size is approximately equal to the observed increase in the Pt-shell thickness. In addition, elemental analysis performed on individual NPs across their diameter reveals that the selected NP at 15 min (Figure 4.3-4) has similar chemical composition to the one for the selected NP with nominal composition $Pt_{10}Ni_{90}$ after 120 min (Figure 4.2-8 (c)), i.e. the core@shell structure is much less pronounced as the fitted curves for Pt- and Ni-content are not curved as strongly. This quantifies the visual observations on the thickness of the Pt-shell. Hence, the increasing synthesis time allows for growth of the Pt-shell.

5.3 Underlying Reasons for Uncontrolled Nucleation and Growth of NPs

The conclusions from sections 5.1 and 5.2 is that the produced bimetallic $Pt_{100-x}Ni_x$ NPs are ill-defined, suggesting that the formation and growth of the NPs from the polyol heat-up method with our standard conditions does not follow a simple LaMer model (section 2.1.3). The multimodal particle size distribution and the heterogeneity in the elemental composition indicate that the nucleation and growth steps are not separated. In order to elaborate on this we revisit the results obtained on the reduction kinetics for the metal precursors in the 1,4-BD with PVP10 (metal ions/PVP monomer ratio 1/10) (experiments 1 and 2 in Table 4.1-1). These results confirm that the formation of Ni-atoms, i.e. Ni-monomer, is faster than the formation of Pt-atoms. The nucleation temperature for Pt at our standard conditions was estimated to be ≈ 187 ^{0}C (Figure 4.1-2) whereas Ni NPs were observed already at ≈ 181 ^{0}C (Figure 4.1-4). This implies that the concentration of Ni-monomer is the first to reach the minimum concentration, C_{min}, needed for homogeneous nucleation to occur, described by LaMer's model (2.1.3).

Based on the described observations on kinetics and our knowledge on the heterogeneity of the obtained NPs, our hypothesis is that nucleation occurs in multiple steps and that Ni nucleates first followed by Pt. We can illustrate this by a modified LaMer model; see Figure 5.3-1. Our hypothesis about the nucleation mechanism suggests that the formation of NPs is reaction-controlled. This modified version of the LaMer model can be divided into five regions. In zones I and II, the same processes as discussed in section 2.1.3 are valid, i.e. the solution becomes supersaturated as the concentration of the Ni-monomer increases above its solubility concentration (C_s) and homogeneous nucleation is initiated when it goes over a minimum value (C_{min}) which results in decrease of supersaturation. In region III, the supersaturation of the Ni-monomer decreases to C_{min} whereas the concentration of the Pt-monomer increases above a certain value ($C_{min,\ hetero}$) which is the minimum for heterogeneous nucleation to occur. At this concentration, Pt will nucleate onto the already formed Ni NPs and form a shell. In zone IV, the Ni-monomer can no longer nucleate homogeneously as its concentration is too low whereas the concentration of the Pt-monomer has passed C_{min} and its homogeneous nucleation is initiated. Finally, in region V, the concentrations of both monomers are below the minimum value (C_{min}) and the remaining growth species are consumed in the growth phase. Note that in order to simplify this model, we assume that the minimum concentrations for homogeneous nucleation for Pt and Ni are equal although they might not be in reality. However, our hypothesis need to be verified by further experiments.

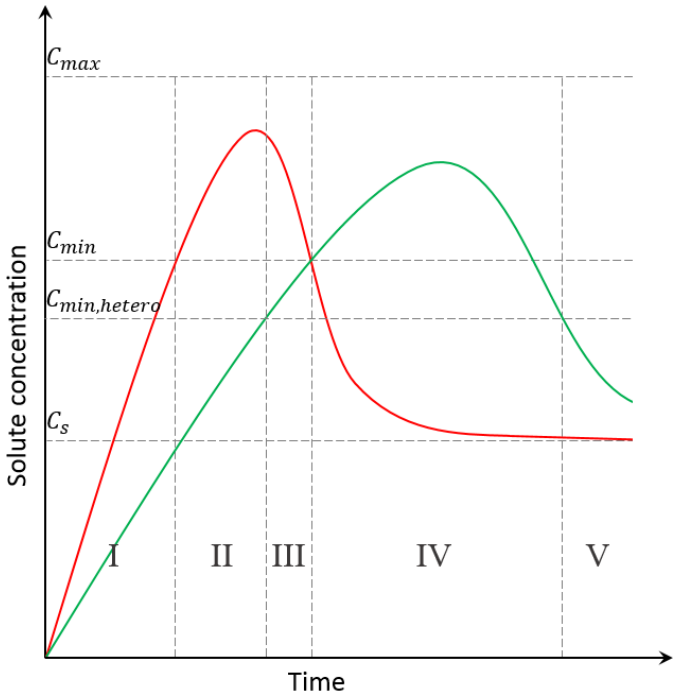

Figure 5.3-1: Modification to the LaMer model to fit our hypothesis about nucleation in multiple steps with Ni (red) nucleating first followed by Pt (green).

5.4 Effects Resulting from Modifications to the Synthesis Method

Our hypothesis proposed in section 5.3 suggests that monodispersed $Pt_{100-x}Ni_x$ NPs in form of a solid solution, is more likely to form if the reaction kinetics of the Pt-metal precursor is tuned/equalized relative to the Ni-metal precursor as well as the reaction time is shortened. With reference to literature [7], [82], we know that the reaction kinetics of the metal precursors may be influenced by the metal/surfactant ratio, type of metal precursor as well as concentration of metal precursor in the solvent. Based on this, $Pt_{10}Ni_{90}$ NPs were studied by changing the ratio of metal ions/PVP monomer from 1/10 to 1/100 (experiment 2 in Table 4.3-1). This composition, should according to the bulk phase diagram give a solid-solution (Figure 1.3-1) [16]. Through comparison of the BF-STEM images and the respective particle size distribution histograms of the NPs prepared with metal ions/PVP monomer ratios 1/10 (Figure 4.2-1 (j)) and 1/100 (Figure 4.3-5), it is noticed that the larger amount of PVP10 gives a significant decrease in the number of the small Pt NPs and the size distribution becomes monomodal. In addition, the approximate range of the

size distribution for NPs prepared with the 1/10 ratio is from 0-35 nm whereas for the ones prepared with the 1/100 ratio it is from 2-28 nm, which indicates that larger amount of PVP10 results in a narrower size distribution. Our findings suggest that the larger amount of surfactant provides better stabilization of the NPs and that a diffusion-controlled regime is entered (section 2.1.2), giving more uniform NP size. However, PXRD analysis gave refined *a*-axes for the NPs prepared with metal ions/PVP monomer ratio 1/10 (experiment 10 in Table 4.2-1) versus 1/100 (experiment 2 in Table 4.3-1) 3.76 ± 0.01 and 3.5309 ± 0.0003 Å for the former and 3.70 ± 0.01 Å and 3.5417 ± 0.0007 Å for the latter. Hence, there is a slightly higher Ni-content in the Pt-Ni phase and a slightly higher Pt-content in the Ni-rich phase for the "1/100" experiment, which suggests that increasing the amount of PVP10 has resulted in two more homogeneous phases. HAADF-STEM-EDX-elemental mapping revealed that the Pt-shells on the NPs in the sample prepared with metal ions/PVP monomer ratio 1/100 (Figure 4.3-7) are slightly thicker than the Pt-shells on the larger NPs prepared with 1/10 metal/PVP (Figure 4.2-7). This is in line with the reduction in number of small Pt NPs and indicates that more of the Pt-monomer has grown on the Ni NPs.

Our experimental findings suggest that the reaction kinetics of the Pt-metal precursor has been trimmed, but it has not been completely optimized since the NPs are more homogeneous in terms of particle size, but still form as core@shell. The phase diagram (Figure 1.3-1) for the bulk Pt-Ni system supports the formation of core@shell because the formation of a solid solution phase is not favorable for low temperatures.

But we shall pay attention to that previous studies have reported both solid solution and core@shell $Pt_{100-x}Ni_x$ NPs. The formation of the core@shell configuration is here discussed solely for work with simultaneous reduction/decomposition of metal precursors. The formation of core@shell has been reported by Lee et al. [39] for $Pt_{50}Ni_{50}$ NPs from an ultrasound-assisted polyol method. Further, the particle shape and the thickness of the Pt-shell along with the *a*-axis varied when the metal precursor was changed from $Ni(acac)_2$ to $Ni(hfac)_2$. Hence, they concluded that the two metal precursors have different kinetics. Further, Hwang et al. [36] report the formation of solid solution core@shell NPs, i.e. core and shell with element compositions $Pt_{96}Ni_4$ and $Pt_{71}Ni_{29}$, respectively, by means of one-pot thermal decomposition method in the presence of CTAC as a surfactant. On the other hand, several studies report the production of single phase solid solution

Pt-Ni NPs (Table 1.3-2). One example is the work of Banik et al. [31], in which $Pt_{100-x}Ni_x$ (x = 10, 20, 30, 50, 70 and 90) were prepared via an aqueous reduction method. It remains open if core@shell configurations or a solid solution is the most stable thermodynamic configuration for $Pt_{100-x}Ni_x$ NPs.

5.5 Suitability of Selected Characterization Methods for Analysis of $Pt_{100-x}Ni_x$ NPs

From sections 5.1, 5.2 and 5.4 discussions on the materials characteristics of mono- and bimetallic $Pt_{100-x}Ni_x$ NPs are given. The detailed sample descriptions became possible since we have combined methods that give complementary detailed information on morphology, element distribution and presence of crystalline phases. SEM imaging has in this work been the "work horse" for evaluating particle size distribution(s) and for a general first glance on the samples. Important input through the histogram analysis with respect to the presence of mono- or polymodal particle size distributions were obtained (Figure 4.2-1). This information turned out to be useful for us when concluding on number of phases present in the samples as well as it gave mechanistic insight to the nucleation and growth process. PXRD gave information on phase content and the average atomic arrangement of the crystalline phases present in the sample. PXRD gave us clear answers to that the bimetallic samples were composed of two or more phases. However, PXRD gave no information how these phases were distributed in the sample batches. Two scenarios are for sure possible; either that individual NPs are composed of one of the phases present or that all NPs have segregated elemental distribution – or are containing more than one phase. To address this question TEM (HAADF-STEM-EDX) is the preferred instrumentation, with sub-atomic resolution. From HAADF-STEM-EDX we could document that the individual NPs were composed of several phases or gave severe element gradients. Finally, PPMS gave supporting information, but due to the complex nature of the samples these analyses became less useful. To summarize, in order to fully describe the as-synthesized NPs, methods that allow you to work on different length scales (SEM versus TEM) for morphological mapping and chemical composition analysis in combination with tools that give direct information on average atomic arrangement is a prerequisite.

6 Conclusions

In this work $Pt_{100-x}Ni_x$ NPs were prepared from the simultaneous reduction of $Pt(acac)_2$ and $Ni(acac)_2$ in 1,4-BD and PVP10 as a surfactant (metal/PVP = 1/10) following the standard polyol route. By combining SEM, TEM, PXRD and PPMS measurements, it was revealed that the bimetallic NPs were ill defined with respect to both NP size and elemental distribution. Most samples turned out to contain several Pt-Ni phases with ccp-type structure, configurated with a Ni-rich core and a Pt-enriched shell as well as the NP size distributions were either bimodal or trimodal. In addition, the overall trend is that the average particle size increases with increasing atomic % Ni in the nominal composition.

The reduction kinetics of the metal precursors towards formation of the monometallic NPs were explored. Visual analysis and SEM imaging revealed that $Ni(acac)_2$ has a faster kinetics than $Pt(acac)_2$. Following these findings, adjusting the reaction kinetics was tried by tuning the metal to surfactant ratio (from 1/10 to 1/100) with the purpose to obtain samples with single-phase NPs with a narrow size distribution. An improved sample quality was obtained with respect to particle size distribution. Unfortunately, the obtained NPs still gave phase segregation; i.e. a core@shell element distribution.

The reduction kinetics of the Pt- and Ni-precursors were furthermore attempted modified by changing the solvent from 1,4-BD to EG, the surfactant from PVP10 to PVP55 as well as NaOH was added for Ni NPs (experiments 16-18 in Table 3.2-2). However, it was concluded that the standard polyol route gave most well-defined samples.

A modified LaMer model (Figure 5.3-1) was proposed to explain the nucleation and growth of the $Pt_{100-x}Ni_x$ NPs at standard polyol conditions. The model suggests that Ni-atoms nucleate homogeneously first followed by heterogeneous nucleation of Pt-atoms onto the formed Ni NPs and finally, homogeneous nucleation of Pt-atoms occurs. The model proposes that tuning the reaction kinetics of $Pt(acac)_2$ with respect to the kinetics of $Ni(acac)_2$ and applying a shortened synthesis time could produce bimetallic NPs with solid solution element distribution, a monomodal and more monodisperse particle size distribution. Our preliminary results, when the reduction kinetics is attempted tuned, show that the $Pt_{10}Ni_{90}$ nominal composition gives a close to

monomodal particle size distribution, in contrast to the bimodal distribution obtained at standard conditions. However, element distribution is still ill-defined.

It has been shown that routine PXRD characterization alone does not give the best insight to element distribution/phase segregation in the $Pt_{100-x}Ni_x$ NPs. In order to describe the synthesized NPs on atomic level HAADF-STEM-EDX-elemental mapping is a prerequisite. Furthermore, combined SEM imaging (BF-STEM) – histogram analysis give valuable insight into particle size distribution complexity, i.e. if the NPs are monomodal or multimodal. Information on the morphology gives in turn insight or indications on number of phases present as well as mechanistic information on the nucleation and growth steps.

Magnetic measurements were performed on selected $Pt_{100-x}Ni_x$ samples (x = 0, 10, 50, 90 and 100). The findings showed diamagnetic signal for Pt NPs and ferromagnetic/ superparamagnetic signal for the remaining analyzed compositions. The obtained magnetic properties reflects the heterogeneity in the element distribution/phase segregation of the bimetallic samples. Furthermore, a diamagnetic behavior for Pt rather than observing Pauli paramagnetism suggests inaccurate background correction or that contribution from the diamagnetic surfactant is covering the Pauli paramagnetic signal from Pt, giving rise to an overall diamagnetic behavior.

7 Perspectives

Our work along with findings from other studies on $Pt_{100-x}Ni_x$ NPs (section 1.3.2) and the phase diagram (Figure 1.3-1) for the Pt-Ni system in bulk show that this system is difficult to control. According to the phase diagram for bulk Pt-Ni, we know that bimetallic Pt-Ni (in bulk) have distinct alloyed phases with solid solutions. In contrast, at nanoscale both full solid solution as well as severe phase segregation is reported. However, due to the nature of the colloidal synthesis, kinetics of the metal precursors play a key role, often giving rise to a less thermodynamic stable element configuration in the obtained NPs. In order to continue the work toward preparation of monodisperse $Pt_{100-x}Ni_x$ NPs with solid solution element distribution, we suggests that the thermodynamic on if the two metals want to mix and form a single phase or segregate at the nanoscale is clarified. Understanding on the thermodynamics can be obtained from e.g. Density Functional Theory (DFT) and operando TEM experiments.

The DFT simulations should evaluate the formation energy of the solid solution versus a segregated situation, and include the NP size into the simulations. Above a critical size, the metallic NPs are expected to follow the phase diagram for bulk Pt-Ni. Hand-in-hand with the DFT simulations, operando TEM of core-shell Pt-Ni NP could be investigated. Following the dynamics in the element distribution as function of time and temperature in the TEM, using the operando gas-temperature cell, may give valuable information on if the two elements tend to mix or not.

Finally, with knowledge on the expected tendency of the two elements to mix on atomic level, new experiments on the reaction kinetics of the metal precursors should be explored, aiming for a single nucleation step followed by the growth step (LaMer theory). Included parameters to explore are type of metal precursor, ratio metal precursor to surfactant, type of surfactant as well as type of solvent.

8 Literature

1. A, A., *Chapter - INTRODUCTION TO NANOMATERIALS*. 2011. p. 76.
2. Faraday, M. and F.V.v. Hahn, *Experimentelle Untersuchungen u\0308ber das Verhalten von Gold- und anderen Metallen-zum Licht. [The Bakerian Lecture, 1857] ... U\0308bersetzt und herausgegeben von F.-V. v. Hahn, etc*.
3. Rao, C.N.R., P.J. Thomas, and G.U. Kulkarni, *Nanocrystals : synthesis, properties and applications*. 2007, Berlin ; [London]: Springer.
4. Sellers, K., *Nanotechnology and the environment*. 2009, Boca Raton: CRC Press. xi, 281 p.
5. Cademartiri, L. and G.A. Ozin, *Concepts of nanochemistry*. 2009, Weinheim: Wiley-VCH ; [Chichester : John Wiley [distributor].
6. Alayoglu, S. and B. Eichhorn, *Rh−Pt Bimetallic Catalysts: Synthesis, Characterization, and Catalysis of Core−Shell, Alloy, and Monometallic Nanoparticles.* Journal of the American Chemical Society, 2008. **130**(51): p. 17479-17486.
7. Bundli, S., *Syntese og karakterisering av Pt1-xRhx nanopartikler. Kolloidal partikkelsyntese, røntgendiffraksjon og elektronmikroskopi*, in *Department of Physics, Faculty of Mathematics and Natural Sciences*. 2016, University of Oslo: Oslo.
8. Jensen, M., *Synthesis and Characterization of Pt1-xPd Nanoparticles and their Suitability for NH3 Oxidation Catalysis*, in *Department of Chemistry* 2018, University of Oslo: Oslo, Norway.
9. Papa, F., et al., *Morphology and chemical state of PVP-protected Pt, Pt–Cu, and Pt–Ag nanoparticles prepared by alkaline polyol method.* Journal of Nanoparticle Research, 2011. **13**(10): p. 5057.
10. Long, N.V., et al., *Novel issues of morphology, size, and structure of Pt nanoparticles in chemical engineering: Surface attachment, aggregation or agglomeration, assembly, and structural changes.* New Journal of Chemistry, 2012. **36**(6): p. 1320-1334.
11. Song, H., et al., *Pt nanocrystals: Shape control and Langmuir-Blodgett monolayer formation.* Journal of Physical Chemistry B, 2005. **109**(1): p. 188.
12. Bathla, A. and B. Pal, *Catalytic Selective Hydrogenation and Cross Coupling Reaction Using Polyvinylpyrrolidone-Capped Nickel Nanoparticles.* ChemistrySelect, 2018. **3**(17): p. 4738-4744.
13. Tripathi, U.N., et al. *Influence of polyvinylpyrrolidone on particle size of Ni nanoparticles preparation*. in *AIP Conference Proceedings*. 2012.
14. Neiva, E.G.C., et al., *PVP-capped nickel nanoparticles: Synthesis, characterization and utilization as a glycerol electrosensor*. 2014: [Amsterdam ;. p. 574-581.
15. Couto, G.G., et al., *Nickel nanoparticles obtained by a modified polyol process: Synthesis, characterization, and magnetic properties.* Journal of Colloid And Interface Science, 2007. **311**(2): p. 461-468.
16. Nash, P. and M.F. Singleton, *The Ni-Pt (Nickel-Platinum) system.* Bulletin of Alloy Phase Diagrams, 1989. **10**(3): p. 258-262.
17. Manoun, B., et al., *Thermal expansion of polycrystalline Ti3SiC2 in the 25 degrees-1400 degrees C temperature range.* J. Am. Ceram. Soc., 2005. **88**(12): p. 3489-3491.
18. Jeon, M.K. and P.J. McGinn, *Composition dependence of ternary Pt–Ni–Cr catalyst activity for the methanol electro-oxidation reaction.* Journal of Power Sources, 2009. **194**(2): p. 737-745.
19. Mishima, Y., S. Ochiai, and T. Suzuki, *Lattice parameters of Ni(γ), Ni3Al(γ') and Ni3Ga(γ') solid solutions with additions of transition and B-subgroup elements.* Acta Metallurgica, 1985. **33**(6): p. 1161-1169.
20. Buschow, K.H.J., P.G. van Engen, and R. Jongebreur, *Magneto-optical properties of metallic ferromagnetic materials*. Vol. 38. 1983. 1-22.

21. Nikiforov, V., A. Morozkin, and V. Irkhin, *Thermoelectric properties of rare-earth alloys.* The Physics of Metals and Metallography, 2013. **114**(8): p. 654-666.
22. Galhardo, T., et al., *Glycerol valorization by base-free oxidation with air using platinum–nickel nanoparticles supported on activated carbon as catalyst prepared by a simple microwave polyol method.* Focusing on Technology Research, Innovation, Demonstration, Insights and Policy Issues for Sustainable Technologies, 2018. **20**(9): p. 2075-2088.
23. Jiang, Q., et al., *Promoting Effect of Ni in PtNi Bimetallic Electrocatalysts for the Methanol Oxidation Reaction in Alkaline Media: Experimental and Density Functional Theory Studies.* J. Phys. Chem. C, 2010. **114**(46): p. 19714-19722.
24. Bao, H.L., et al., *Structure of PtnNi Nanoparticles Electrocatalysts Investigated by X-ray Absorption Spectroscopy.* J. Phys. Chem. C, 2013. **117**(40): p. 20584-20591.
25. Rudi, S., X. Tuaev, and P. Strasser, *Electrocatalytic Oxygen Reduction on Dealloyed Pt 1-x Ni x Alloy Nanoparticle Electrocatalysts.* Electrocatalysis, 2012. **3**(3): p. 265-273.
26. Xu, Y., et al., *Facile one-step room-temperature synthesis of Pt 3 Ni nanoparticle networks with improved electro-catalytic properties.* Chem. Commun., 2012. **48**(21): p. 2665-2667.
27. Chen, Y., et al., *Ni@Pt core-shell nanoparticles: Synthesis, structural and electrochemical properties.* J. Phys. Chem. C, 2008. **112**(5): p. 1645-1649.
28. Wan, J., et al., *Pt–Ni Alloy Nanoparticles as Superior Counter Electrodes for Dye-Sensitized Solar Cells: Experimental and Theoretical Understanding.* Advanced Materials, 2014. **26**(48): p. 8101-8106.
29. Carpenter, M.K., et al., *Solvothermal synthesis of platinum alloy nanoparticles for oxygen reduction electrocatalysis.(Report).* Journal of the American Chemical Society, 2012. **134**(20): p. 8535-8542.
30. Ma, Y., et al., *Modulating Surface Composition and Oxygen Reduction Reaction Activities of Pt-Ni Octahedral Nanoparticles by Microwave-Enhanced Surface Diffusion during Solvothermal Synthesis.* Chemistry of Materials, 2018. **30**(13): p. 4355-4360.
31. Banik, S., et al., *Improved and synergistic catalysis of single-pot-synthesized PtNi alloy nanoparticles for anodic oxidation of methanol in alkali.* RSC Adv., 2016. **6**(95): p. 92490-92501.
32. Kyung-Won, P., et al., *Chemical and electronic effects of Ni in Pt/Ni and Pt/Ru/Ni alloy nanoparticles in methanol electrooxidation.* Journal of Physical Chemistry B, 2002. **106**(8): p. 1869.
33. Du, J.J., et al., *Synthesis, characterization and magnetic properties of highly monodispersed PtNi nanoparticles.* Materials Chemistry and Physics, 2015. **155**: p. 47-51.
34. Zhang, N., et al., *Control of the composition of PtNi electrocatalysts in surfactant-free synthesis using neat N -formylpiperidine.* Nanoscale, 2016. **8**(5): p. 2548-2553.
35. Santos, L.G.R.A., et al., *Oxygen reduction reaction in acid medium on Pt–Ni/C prepared by a microemulsion method.* Journal of Electroanalytical Chemistry, 2006. **596**(2): p. 141-148.
36. Hwang, E.-T., et al., *Synthesis of Pt-Rich@Pt–Ni alloy core–shell nanoparticles using halides.* RSC Adv., 2015. **5**(11): p. 8301-8306.
37. Kim, S.-J., et al., *Radiolytic synthesis of Pd-M (M=Ag and Ni) and Pt-M (M=Ru and Ni) alloy colloids.* Korean Journal of Chemical Engineering, 2006. **23**(3): p. 488-495.
38. Kožejová, M., et al., *Growth of Pt-Ni nanoparticles of different composition using electrodeposition and characterization of their magnetic properties.* Acta Physica Polonica A, 2017. **131**(4): p. 839-841.
39. Lee, E., et al., *One-step sonochemical syntheses of Ni@Pt core–shell nanoparticles with controlled shape and shell thickness for fuel cell electrocatalyst.* Ultrasonics - Sonochemistry, 2014. **21**(1): p. 317-323.

40. Rusnaeni, N., et al., *The effect of NaOH in the formation PtNi/C nanocatalyst for cathode of PEMFC.* Journal of Applied Sciences, 2010. **10**(22): p. 2899-2904.
41. Lin, R., et al., *Rapid microwave-assisted solvothermal synthesis of shape-controlled Pt-Ni alloy nanoparticles for PEMFC.* Electrochimica Acta, 2018. **283**: p. 764-771.
42. Xiong, L., et al., *Pt–Ni alloy nanoparticles supported on multiwalled carbon nanotubes for methanol oxidation in alkaline media.* Current Research and Development in Science and Technology, 2013. **17**(3): p. 805-810.
43. Veera Manohara Reddy, Y., et al., *Ultrafine Pt–Ni bimetallic nanoparticles anchored on reduced graphene oxide nanocomposites for boosting electrochemical detection of dopamine in biological samples*. 2018. p. 16891-16901.
44. Wang, Z., et al., *Glycerol stabilized NaBH<inf>4</inf> reduction for preparation carbon supported Pt-Ni alloy nanoparticles used as oxygen-reduction electrocatalysts for microbial fuel cells.* International Journal of Electrochemical Science, 2015. **10**(3): p. 1953-1965.
45. Yano, H., et al., *Oxygen reduction activity of carbon-supported Pt-M (M = V, Ni, Cr, Co, and Fe) alloys prepared by nanocapsule method*. 2007. p. 6438-6445.
46. Chiwata, M., et al., *Oxygen reduction reaction activity of carbon-supported Pt-Fe, Pt-Co, and Pt-Ni alloys with stabilized pt-skin layers.* Electrochemistry, 2016. **84**(3): p. 133-137.
47. Jeon, T., et al., *Influence of Oxide on the Oxygen Reduction Reaction of Carbon-Supported Pt-Ni Alloy Nanoparticles.* J. Phys. Chem. C, 2009. **113**(45): p. 19732-19739.
48. Jeon, T.-Y., et al., *Effect of de-alloying of Pt–Ni bimetallic nanoparticles on the oxygen reduction reaction.* Electrochemistry Communications, 2010. **12**(12): p. 1796-1799.
49. Yang, H., et al., *Structure and electrocatalytic activity of carbon-supported Pt-Ni alloy nanoparticles toward the oxygen reduction reaction.* Journal of Physical Chemistry B, 2004. **108**(30): p. 11024.
50. Hanprerakriengkrai, S., et al., *Preparation of carbon supported Pt-Ni alloy nanoparticle catalyst with high metal loading using cation exchange resin and its application for hydrogen production.* Chemical Engineering Journal, 2018.
51. Changlin, Z., et al., *Solid-state chemistry-enabled scalable production of octahedral Pt-Ni alloy electrocatalyst for oxygen reduction reaction.(platinium)(Report).* Journal of the American Chemical Society, 2014. **136**(22): p. 7805-7808.
52. Cao, G., *Nanostructures & nanomaterials : synthesis, properties & applications*. 2004, London ; Hackensack, NJ: Imperial College Press. xiv, 433 p.
53. ScienceDirect. *Heterogeneous Nucleation*. [cited 2019 30.04]; Available from: https://www.sciencedirect.com/topics/engineering/heterogeneous-nucleation?fbclid=IwAR122KvyLDi6h2s4smiVm_RXWD89dl9w8yL7Rr827Clfc_2F4S18Iu-F8wM.
54. ScienceDirect. *Ostwald Ripening*. [cited 2019 30.05]; Available from: https://www.sciencedirect.com/topics/materials-science/ostwald-ripening.
55. LaMer, V.K. and R.H. Dinegar, *Theory, Production and Mechanism of Formation of Monodispersed Hydrosols.* Journal of the American Chemical Society, 1950. **72**(11): p. 4847-4854.
56. Schmid, G.n., *Nanoparticles : from theory to application*. 2004, Weinheim: Wiley-VCH. x, 434 p.
57. van Embden, J., A.S.R. Chesman, and J.J. Jasieniak, *The Heat-Up Synthesis of Colloidal Nanocrystals.* Chemistry of Materials, 2015. **27**(7): p. 2246-2285.
58. Fievet, F., et al., *Homogeneous and heterogeneous nucleations in the polyol process for the preparation of micron and submicron size metal particles.* Solid State Ionics, 1989. **32-33**: p. 198-205.

59. Dong, H., Y.C. Chen, and C. Feldmann, *Polyol synthesis of nanoparticles: status and options regarding metals, oxides, chalcogenides, and non-metal elements.* Green Chemistry, 2015. **17**(8): p. 4107-4132.
60. M. Koczkur, K., et al., *Polyvinylpyrrolidone (PVP) in nanoparticle synthesis*. 2015.
61. ScienceDirect. *Polyvinylpyrrolidone*. [cited 2019 30.04]; Available from: https://www.sciencedirect.com/topics/agricultural-and-biological-sciences/polyvinylpyrrolidone.
62. Smart, L. and E. Moore, *Solid state chemistry : an introduction*. 4th ed. ed. 2011, Boca Raton, Fla.: CRC Press ; London : Taylor & Francis [distributor].
63. Owens, F.J. and C.P. Poole, *The physics and chemistry of nanosolids*. 2008, Hoboken, N.J.: Wiley-Interscience. xvi, 539 p.
64. Bentli, I., et al., *Magnesite concentration technology and caustic – calcined product from Turkish magnesite middlings by calcination and magnetic separation.* Separation Science and Technology, 2017. **52**(6): p. 1129-1142.
65. Tilley, R.J.D., *Understanding solids : the science of materials*. 2nd edition. ed.
66. Sydney, U.o. *Scanning Electron Microscopy*. [cited 2019 30.04]; Available from: https://myscope.training/#/SEMlevel_3_1.
67. Chauhan, A., *Deformation and damage mechanisms of ODS steels under high-temperature cyclic loading*. 2018.
68. Leng, Y.a., *Materials characterization : introduction to microscopic and spectroscopic methods*. Second edition. ed.
69. *Lecture notes, FYS4340 - Diffraksjonsmetoder og elektronmikroskopi*. 2018, UiO.
70. JEOL, *Scanning Electron Microscope A To Z Basic Knowledge For Using The SEM*. p. User Guide.
71. *Materials Details SRM 640d - Silicon Powder Line Position + Line Shape Std for Powder Dif*. Available from: https://www-s.nist.gov/srmors/view_detail.cfm?srm=640D.
72. Dinnebier, R.E. and S.J.L. Billinge, *Powder diffraction : theory and practice*. 2008, Cambridge: Royal Society of Chemistry.
73. QuantumDesign, *Physical Property Measurement System AC Measurement System (ACMS) Option User's Manual*. 2003.
74. BRUKER. *ESPRIT 2 Software for Micro- and Nano-Analysis*. [cited 2019 07.05]; A software]. Available from: https://www.bruker.com/products/x-ray-diffraction-and-elemental-analysis/eds-wds-ebsd-sem-micro-xrf-and-sem-micro-ct/esprit-2.html.
75. Haakstad, E., *Titan - mikroskopet som kan <<se>> atomer*. 2015.
76. *ImageJ An open platform for scientific image analysis*. [cited 2019 07.05]; A software]. Available from: https://imagej.net/Welcome.
77. BRUKER. *XRD Software - DIFFRAC.SUITE TOPAS*. [cited 2019 07.05]; A software]. Available from: https://www.bruker.com/products/x-ray-diffraction-and-elemental-analysis/x-ray-diffraction/xrd-software/topas.html.
78. OriginLab. *Origin 2019b Graphing & Analysis* [cited 2019 07.05]; A software]. Available from: https://www.originlab.com/.
79. Panday, S., B.S.S. Daniel, and P. Jeevanandam, *Synthesis of nanocrystalline Co–Ni alloys by precursor approach and studies on their magnetic properties.* Journal of Magnetism and Magnetic Materials, 2011. **323**(17): p. 2271-2280.
80. Chou, K.-S. and Y.-S. Lai, *Effect of polyvinyl pyrrolidone molecular weights on the formation of nanosized silver colloids.* Materials Chemistry and Physics, 2004. **83**(1): p. 82-88.
81. Gong, J., et al., *Structural and magnetic properties of hcp and fcc Ni nanoparticles.* Journal of Alloys and Compounds, 2008. **457**(1): p. 6-9.

82. Bundli, S., et al., *Controlled alloying of Pt-Rh nanoparticles by the polyol approach.* Journal of Alloys and Compounds, 2019. **779**: p. 879-885.

9 Appendix

Reported in this appendix are all the results, which did not fit into the main text of the work.

9.1 Reduction Kinetics of $Pt(acac)_2$ and $Ni(acac)_2$ towards NP formation

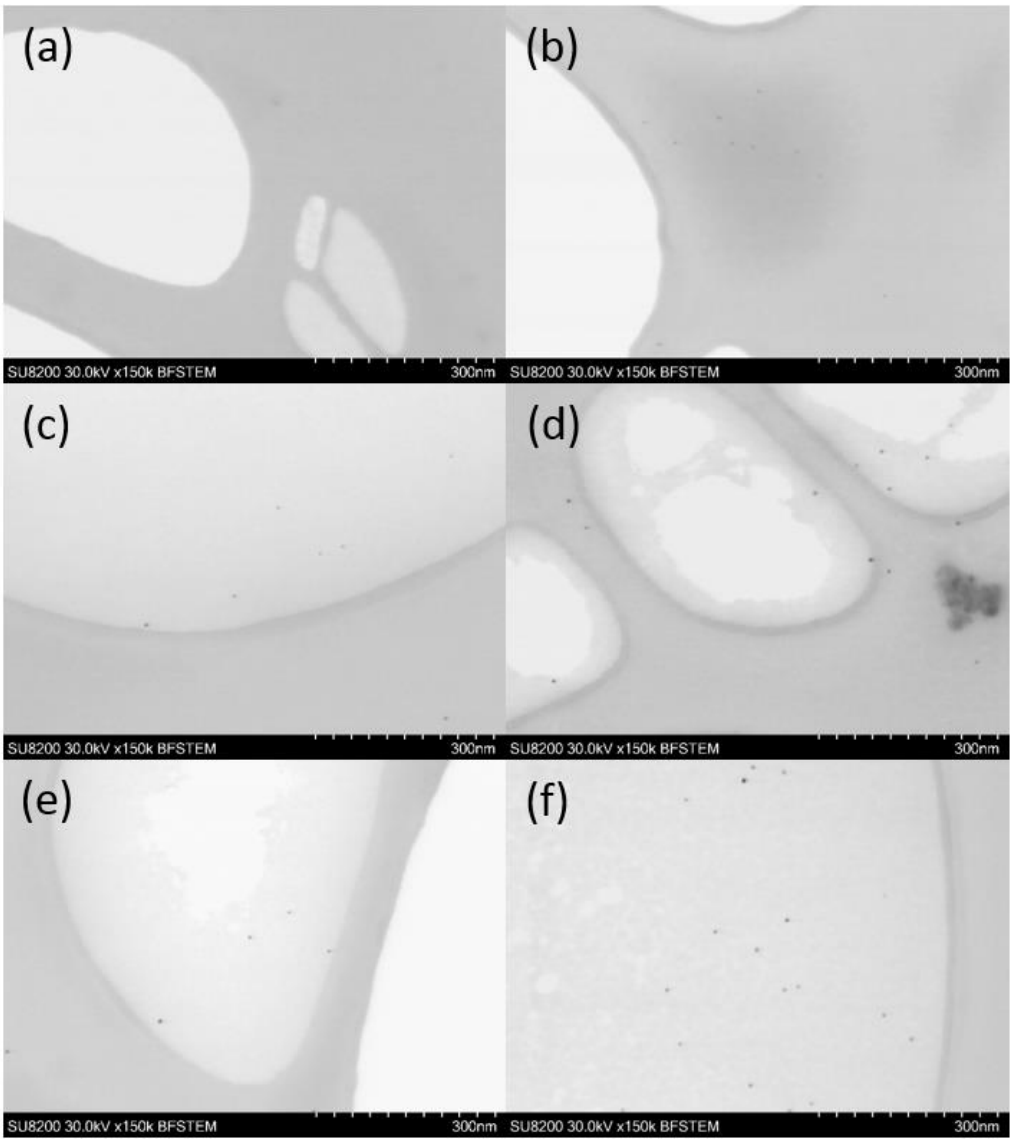

Figure A9.1-1: BF-STEM images of Pt NPs formed from the reduction of $Pt(acac)_2$ in 1,4-BD at a suspension temperature of 184 ^{0} C (sample 1) (a), 187 ^{0} C (sample 2) (b), 190 ^{0} C (sample 3) (c), 193 ^{0} C (sample 4) (d), 196 ^{0} C (sample 5) (e) and 199 ^{0} C (sample 6) (f).

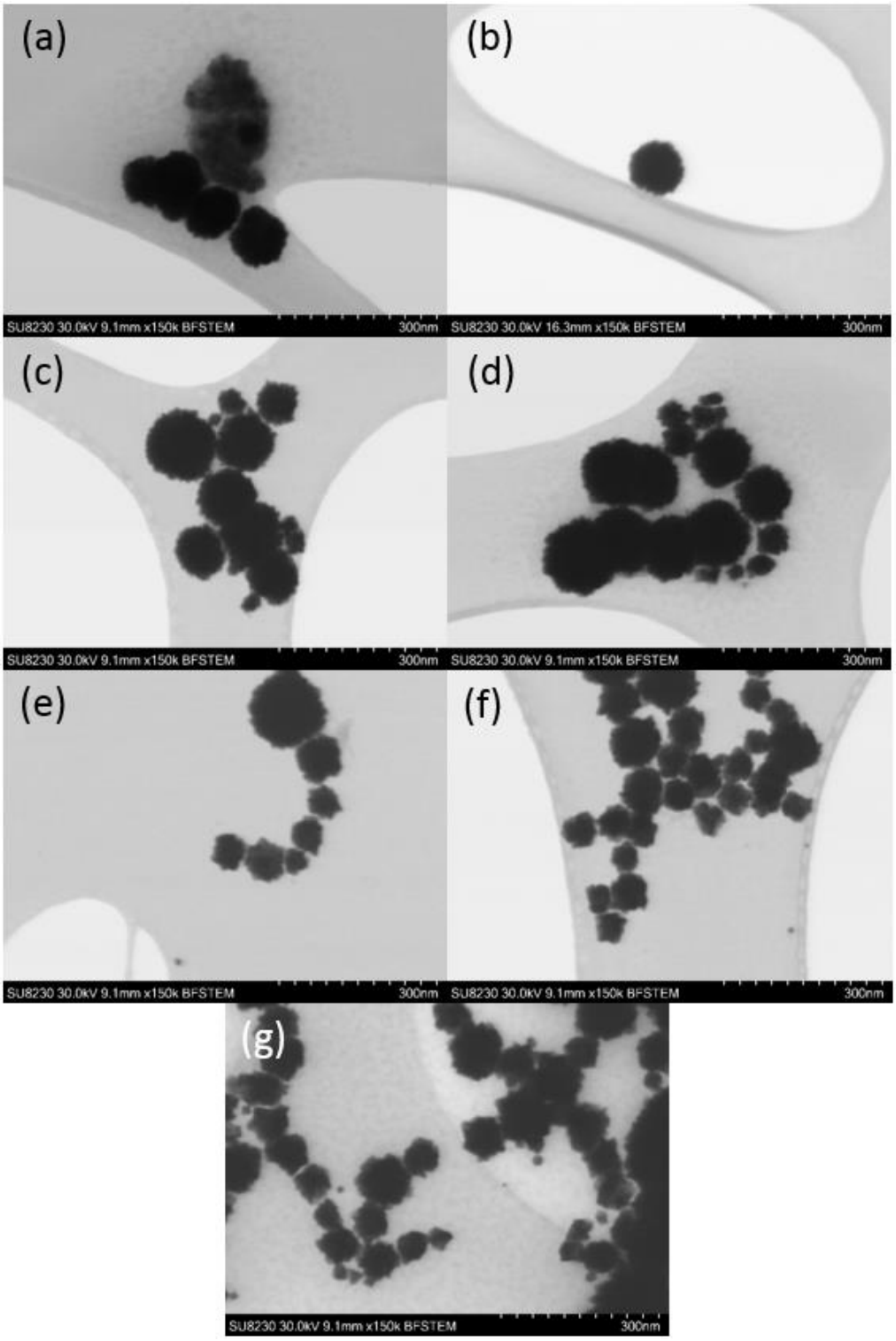

Figure A9.1-2: BF-STEM images of Ni NPs formed from the reduction of $Ni(acac)_2$ in 1,4-BD at a suspension temperature of 181 ^{0} C (sample 1) (a), 184 ^{0} C (sample 2) (b), 187 ^{0} C (sample 3) (c), 190 ^{0} C (sample 4) (d), 193 ^{0} C (sample 5) (e), 196 ^{0} C (sample 6) (f) and 199 ^{0} C (sample 7) (g).

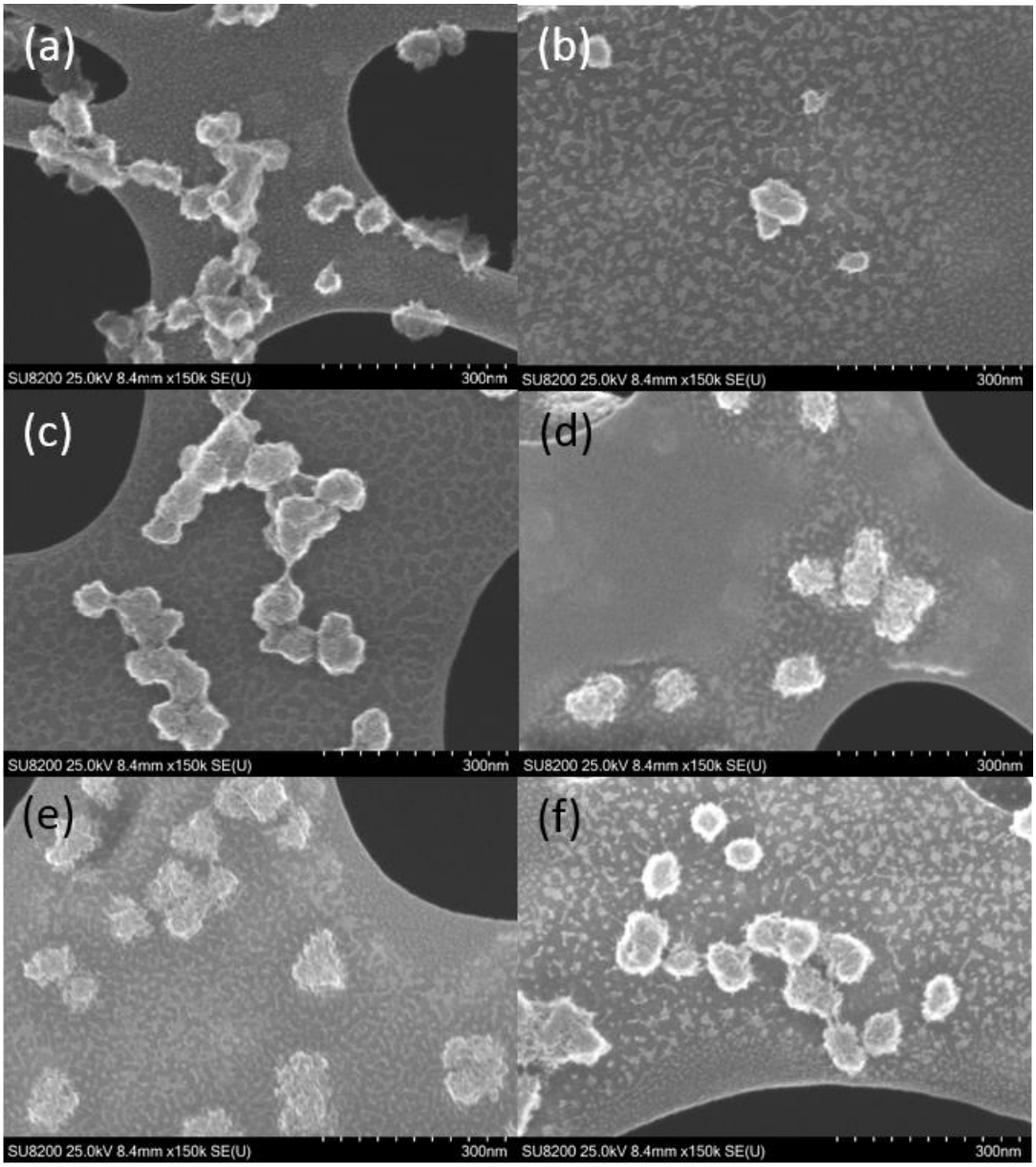

Figure A9.1-3: SEM images of Ni NPs formed from the reduction of $Ni(acac)_2$ in EG at a suspension temperature of 171 ^{0}C (sample 1) (a), 174 ^{0}C (sample 2) (b), 177 ^{0}C (sample 3) (c), 180 ^{0}C (sample 4) (d), 183 ^{0}C (sample 5) (e) and 186 ^{0}C (sample 6) (f).

9.2 $Pt_{100-x}Ni_x$ NPs Produced via the Polyol Heat-Up Method

Table A9.2-1: Average element distribution of NPs with nominal compositions $Pt_{90}Ni_{10}$, $Pt_{50}Ni_{50}$ and $Pt_{10}Ni_{90}$ produced from the simultaneous reduction of $Pt(acac)_2$ and $Ni(acac)_2$ via the standard polyol heat-up method. In addition, element distribution of NPs with nominal compositions $Pt_{50}Ni_{50}$ and $Pt_{10}Ni_{90}$ produced from the simultaneous reduction of $Pt(acac)_2$ and $Ni(acac)_2$ via the modified polyol heat-up method. The distributions were determined from HAADF-STEM-EDX elemental mapping. The spread in atomic % is included (standard deviation, σ).

Type of experiment	Nominal composition	Relative particle size	Element distribution [atomic %]		Number of analyzed NPs
			Pt	Ni	
Standard synthesis	$Pt_{90}Ni_{10}$	Small	93.1 ± 11.5	6.9 ± 0.5	26
		Large	86.0 ± 9.8	14.0 ± 0.3	33
Standard synthesis	$Pt_{50}Ni_{50}$	Small	90.0 ± 15.5	10.0 ± 1.0	10
		Intermediate	66.3 ± 10.5	33.7 ± 1.6	10
		Large	42.0 ± 7.5	58.0 ± 1.4	15
Standard synthesis	$Pt_{10}Ni_{90}$	Small	86.8 ± 30.4	13.2 ± 2.2	4
		Large	6.8 ± 2.7	93.2 ± 3.3	14
Modified synthesis	$Pt_{50}Ni_{50}$	Small	63.8 ± 12.4	36.2 ± 2.4	7
		Large	15.4 ± 4.5	84.6 ± 2.7	25
Modified synthesis	$Pt_{10}Ni_{90}$	Small	90.3 ±17.0	9.7 ± 1.4	1
		Large	11.9 ± 4.0	88.1 ± 3.0	44

Table A9.2-2: Element distribution along the diagonal in single NPs with nominal compositions $Pt_{90}Ni_{10}$, $Pt_{50}Ni_{50}$ and $Pt_{10}Ni_{90}$ produced from the simultaneous reduction of $Pt(acac)_2$ and $Ni(acac)_2$ via the standard polyol heat-up method and $Pt_{50}Ni_{50}$ and $Pt_{10}Ni_{90}$ produced from the simultaneous reduction of $Pt(acac)_2$ and $Ni(acac)_2$ via the modified polyol heat-up method. The distributions were determined from HAADF-STEM-EDX elemental mapping. The spread in atomic % is included (standard deviation, σ).

Type of experiment	Nominal composition	Particle no.	Position [nm]	Pt [atomic %]	Ni [atomic %]
Standard synthesis	$Pt_{90}Ni_{10}$	1	0.7	83.4 ± 25.4	16.6 ± 3.3
			2.3	74.6 ± 14.7	25.4 ± 2.1
			4.1	46.0 ± 13.2	54.0 ± 3.8
			6.0	55.4 ± 14.0	44.6 ± 3.2
			7.9	87.9 ± 17.0	12.3 ± 1.7

		2	0.7	94.3 ± 19.3	5.7 ± 1.3
			2.1	53.7 ± 17.2	46.3 ± 4.5
			3.7	46.7 ± 14.2	53.3 ± 4.1
			5.3	44.3 ± 14.0	55.7 ± 4.2
			7.0	77.0 ± 17.3	23.0 ± 2.5
Standard synthesis	$Pt_{50}Ni_{50}$	1	1.5	62.5 ± 13.4	38.5 ± 2.6
			4.3	12.8 ± 7.6	87.2 ± 5.9
			7.1	14.7 ± 7.1	85.3 ± 4.9
			10.1	13.1 ± 6.8	86.9 ± 5.1
			12.8	43.9 ± 12.3	56.1 ± 3.6
		2	1.2	85.0 ± 24.3	15.0 ± 2.9
			3.7	42.5 ± 12.6	57.5 ± 3.9
			6.5	23.2 ± 8.8	76.8 ± 4.3
			9.5	34.5 ± 10.8	65.5 ± 3.9
			12.5	77.5 ± 17.2	22.5 ± 2.5
Standard synthesis	$Pt_{10}Ni_{90}$	1	3.1	24.6 ± 17.3	75.4 ± 9.1
			9.5	7.3 ± 6.0	92.7 ± 6.6
			15.5	2.7 ± 3.9	97.3 ± 7.5
			21.2	0	100 ± 7.2
			26.5	13.1 ± 8.6	86.9 ± 6.6
		2	2.3	8.6 ± 11.0	91.4 ± 11.0
			7.3	2.9 ± 4.2	97.1 ± 7.8
			12.5	0.7 ± 2.4	99.3 ± 9.0
			17.9	2.5 ± 3.6	97.5 ± 7.3
			23.3	24.3 ± 14.0	75.7 ± 7.2
Modified synthesis	$Pt_{50}Ni_{50}$	1	1.7	19.1 ± 22.5	80.9 ± 14.1
			5.4	7.2 ± 10.4	92.8 ± 11.6
			8.6	1.8 ± 5.6	98.2 ± 13.3
			12.3	27.1 ± 16.3	72.9 ± 7.9
		2	1.8	38.7 ± 20.7	61.3 ± 7.7
			5.3	6.7 ± 9.8	93.3 ± 11.4
			8.7	3.4 ± 7.5	96.6 ± 12.5
			12.3	12.4 ± 18.8	87.6 ± 15.4
Modified synthesis	$Pt_{10}Ni_{90}$	1	2.4	65.4 ± 24.6	34.6 ± 5.2
			7.2	3.7 ± 6.6	96.3 ± 10.7
			11.1	10.7 ± 8.7	89.3 ± 7.7
			15.1	4.1 ± 6.3	95.9 ± 9.7
			18.9	25.2 ± 24.3	74.8 ± 12.7
		2	2.2	29.8 ± 20.4	70.2 ± 9.4
			6.7	5.1 ± 5.6	94.9 ± 7.6
			11.6	5.8 ± 6.3	94.2 ± 7.9
			16.8	6.1 ± 6.6	93.9 ± 8.0
			22.2	37.1 ± 22.0	62.9 ± 8.5

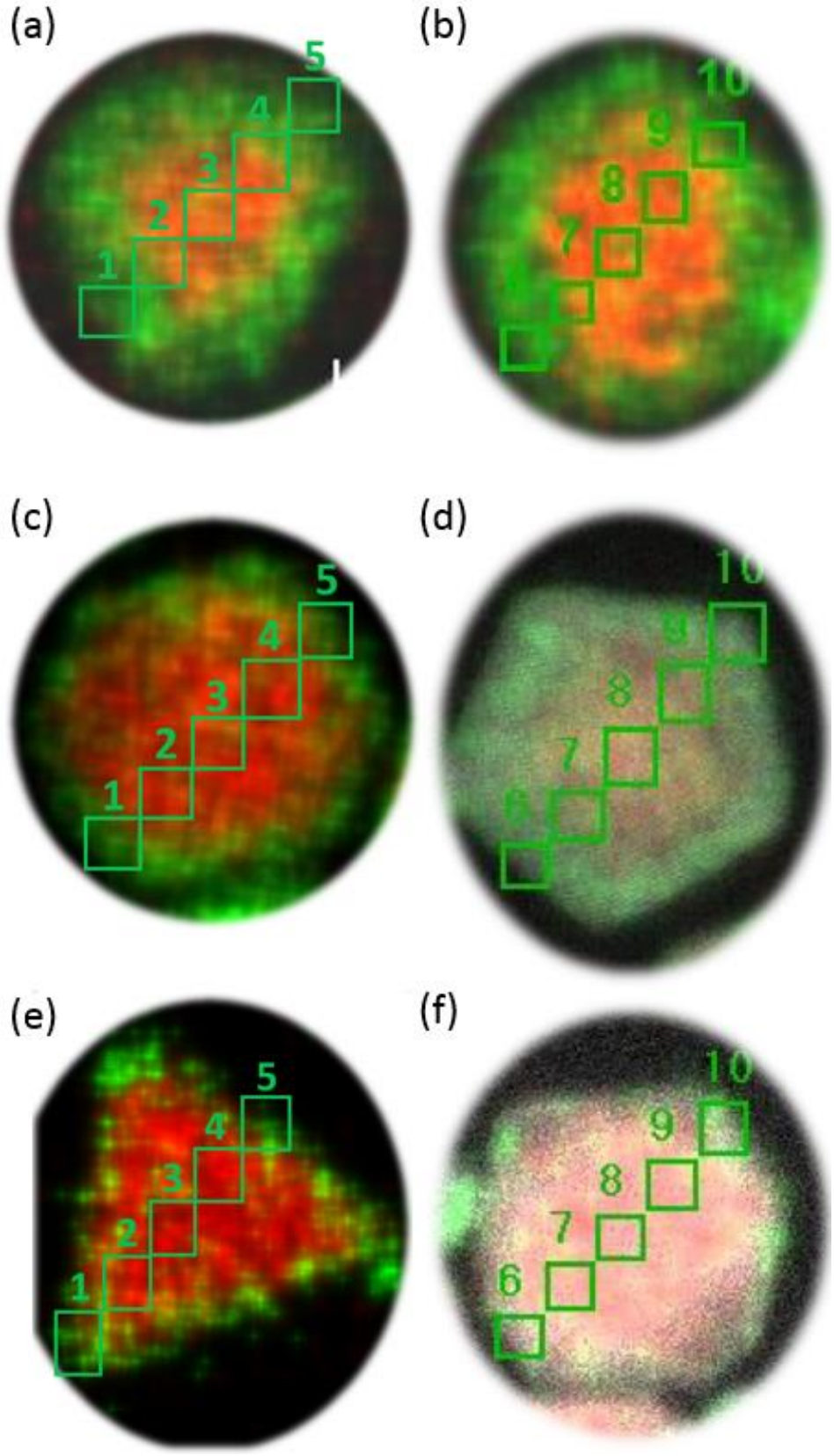
(a)
5
4
3
2
1
(b)
10
9
8
7
6
(c)
5
4
3
2
1
(d)
10
9
8
7
6
(e)
5
4
3
2
1
(f)
10
9
8
7
6

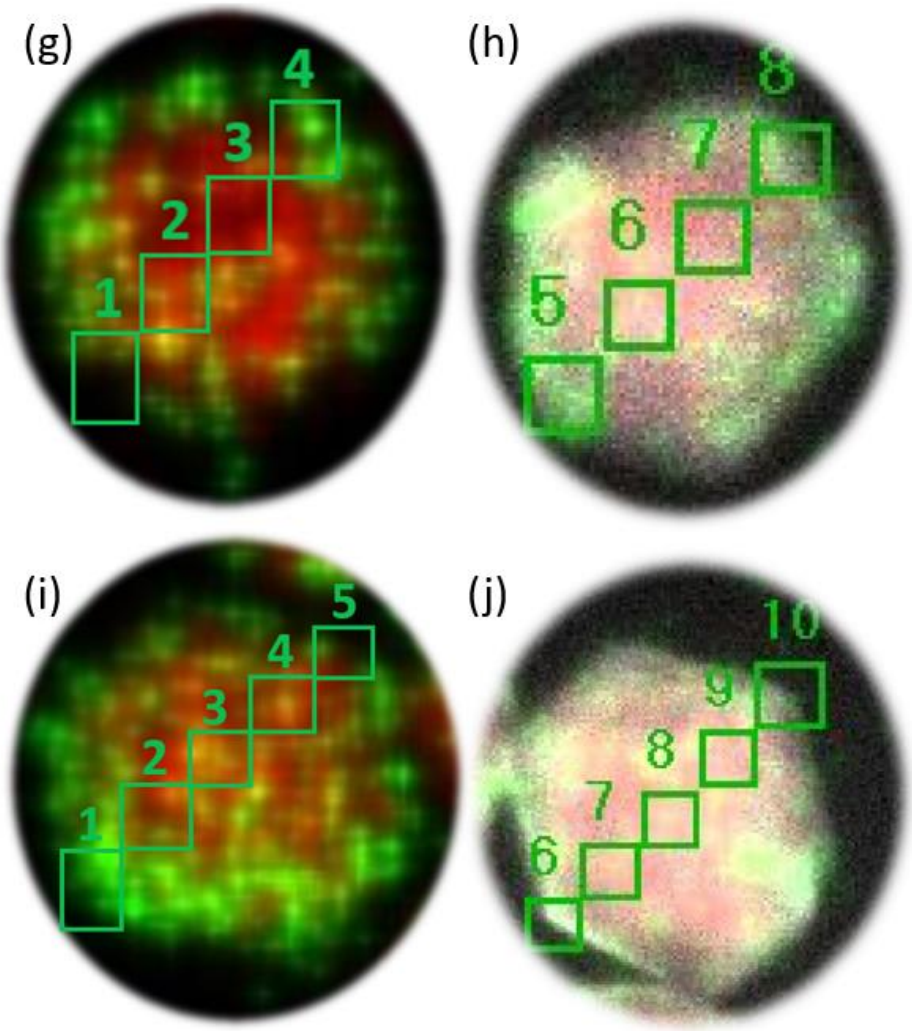

Figure A9.2-1: Element distribution along the diagonal in single NPs with nominal compositions $Pt_{90}Ni_{10}$ (a and b), $Pt_{50}Ni_{50}$ (c and d) and $Pt_{10}Ni_{90}$ (e and f) produced from the simultaneous reduction of $Pt(acac)_2$ and $Ni(acac)_2$ via the standard polyol heat-up method and $Pt_{50}Ni_{50}$ (g and h) and $Pt_{10}Ni_{90}$ (i and j) produced from the simultaneous reduction of $Pt(acac)_2$ and $Ni(acac)_2$ via the modified polyol heat-up method. The distributions were determined from HAADF-STEM-EDX elemental mapping.

9.3 Reduction Kinetics of $HAuCl_4 \cdot 3H_2O$ towards NP formation

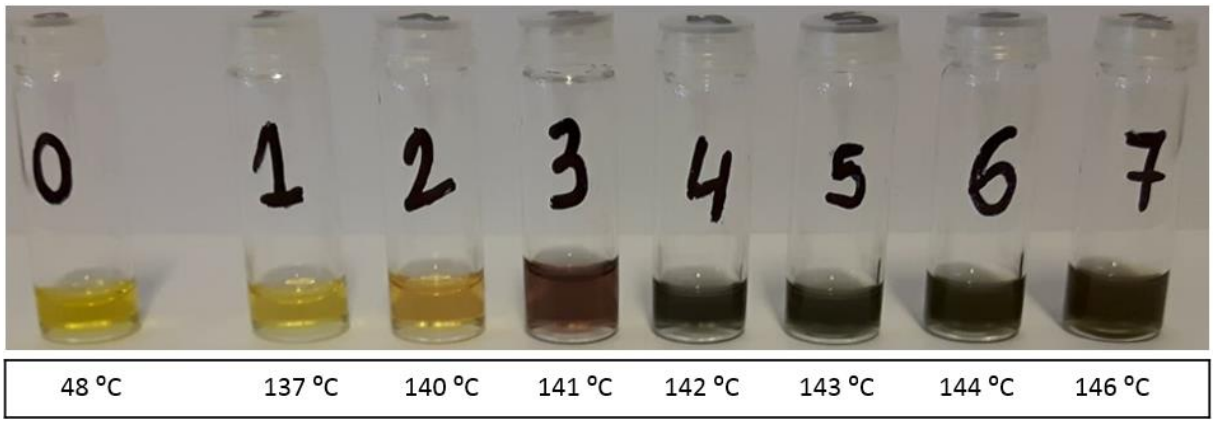

Figure A9.3-1: Color change in samples taken out at selected temperatures in the temperature range from 137 to 146 ^{0} C during the Au NP formation obtained by reaction from $HAuCl_4 \cdot 3H_2O$ in 1,4-BD with metal precursor/PVP10 = 1/100. Heating rate is ≈ 1.3 ^{0} C/min.

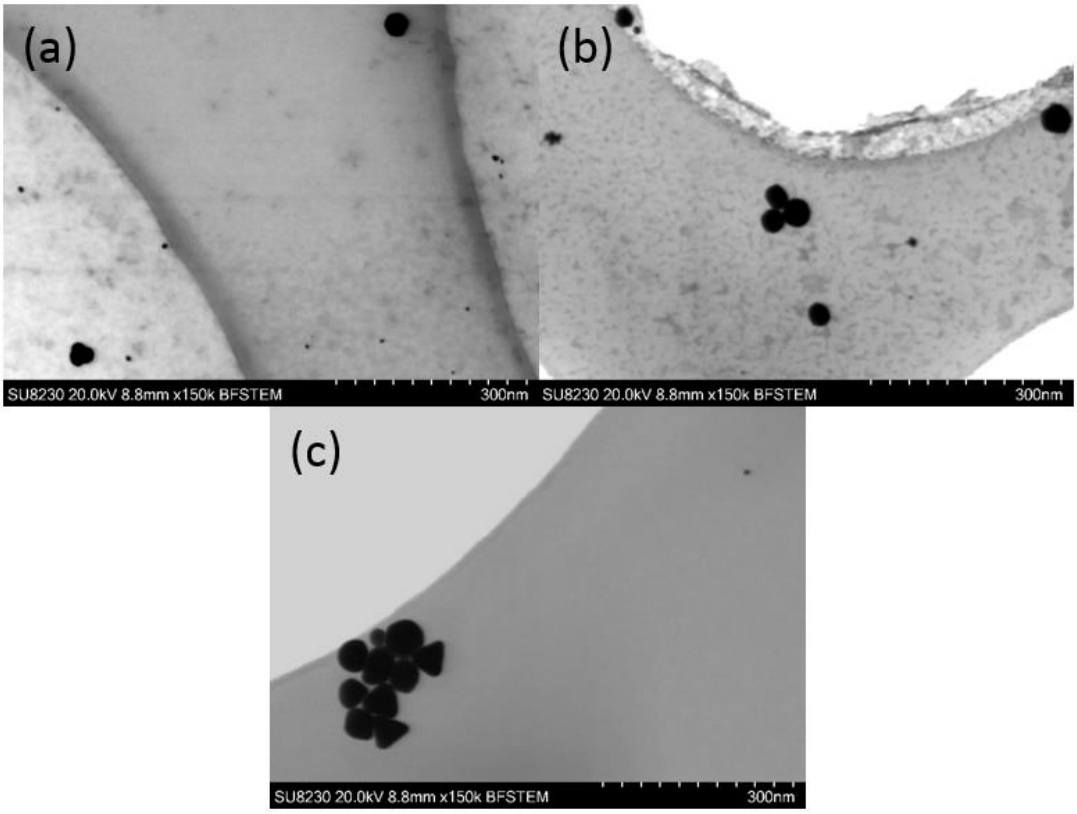

Figure A9.3-2: BF-STEM images of Au NPs formed from the reduction of $HAuCl_4 \cdot 3H_2O$ in 1,4-BD with metal precursor/PVP10 = 1/100 at a suspension temperature of 137 ^{0} C (sample 1) (a), 140 ^{0} C (sample 2) (b) and 142 ^{0} C (sample 4) (c).

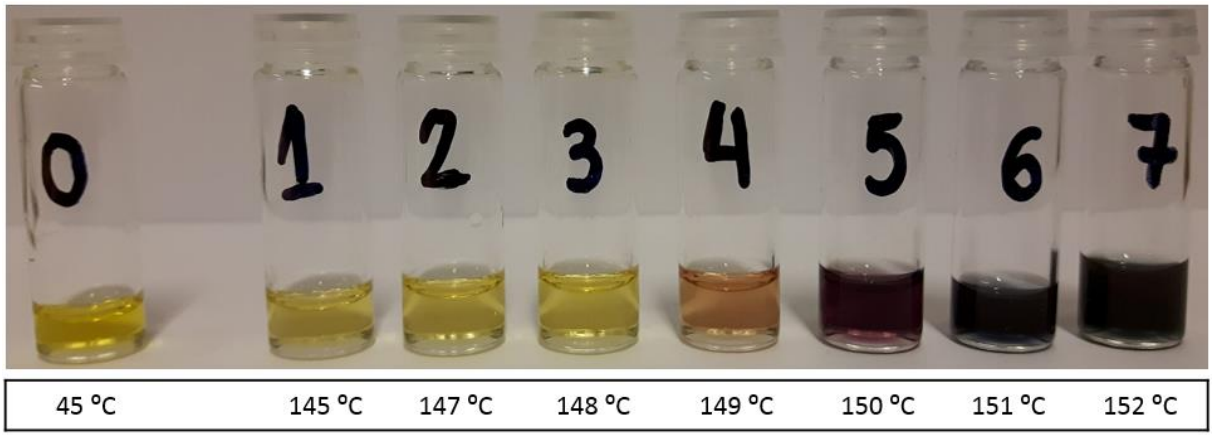

Figure A9.3-3: Color change in samples taken out at selected temperatures in the temperature range from 145 to 152 ^{0} C during the Au NP formation obtained by reaction from $HAuCl_4 \cdot 3H_2O$ in 1,4-BD with metal precursor/PVP10 = 1/50. Heating rate is ≈ 1.2 ^{0} C/min.

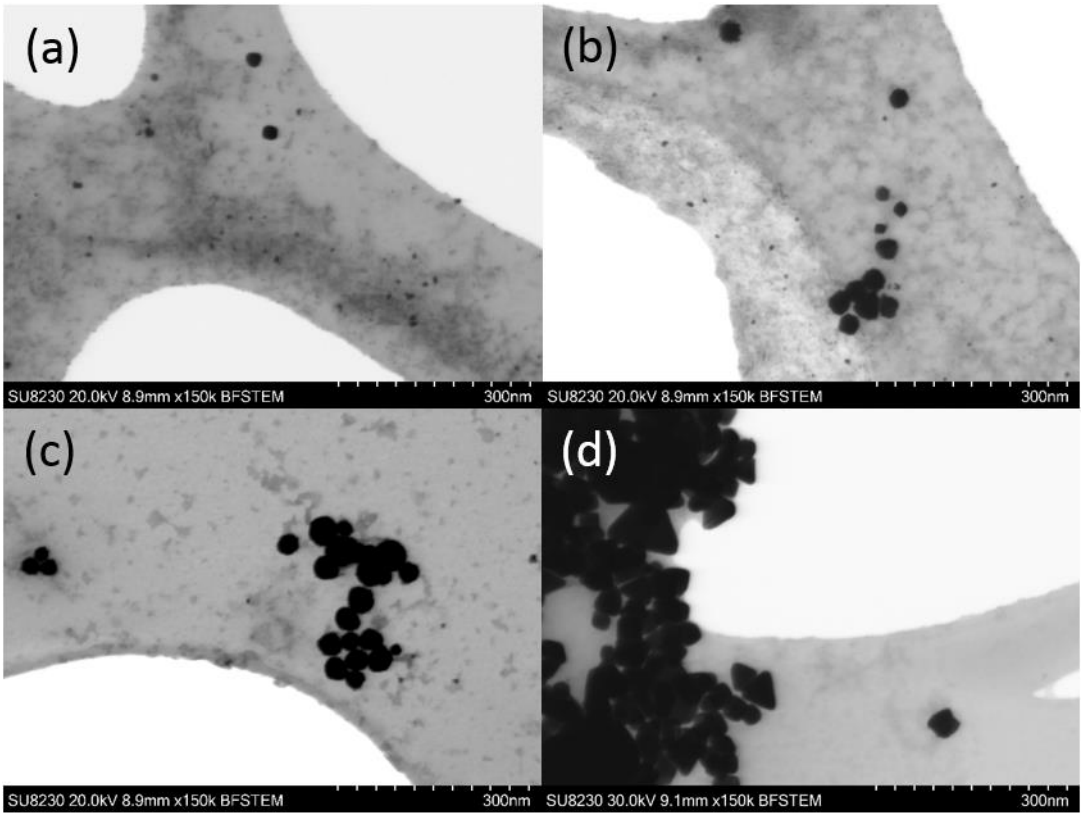

Figure A9.3-4: BF-STEM images of Au NPs formed from the reduction of $HAuCl_4 \cdot 3H_2O$ in 1,4-BD with metal precursor/PVP10 = 1/50 at a suspension temperature of 148 ^{0} C (sample 3) (a), 149 ^{0} C (sample 4) (b), 150 ^{0} C (sample 5) (c) and 152 ^{0} C (sample 7) (d).

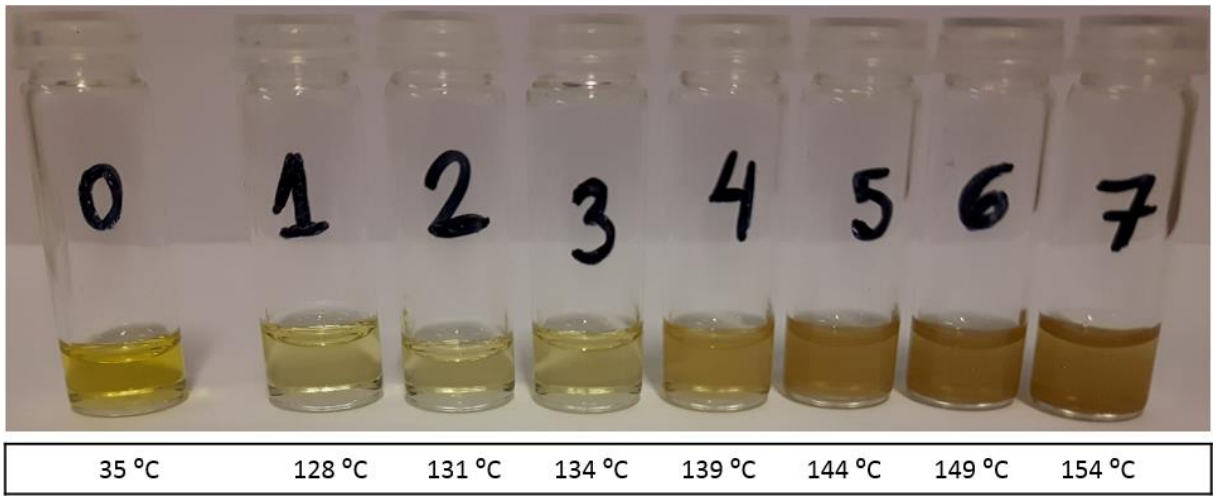

Figure A9.3-5: Color change in samples taken out at selected temperatures in the temperature range from 128 to 154 ^{0} C during the Au NP formation obtained by reaction from $HAuCl_4 \cdot 3H_2O$ in EG with metal precursor/PVP10 = 1/50. Heating rate is ≈ 1.7 ^{0} C/min.

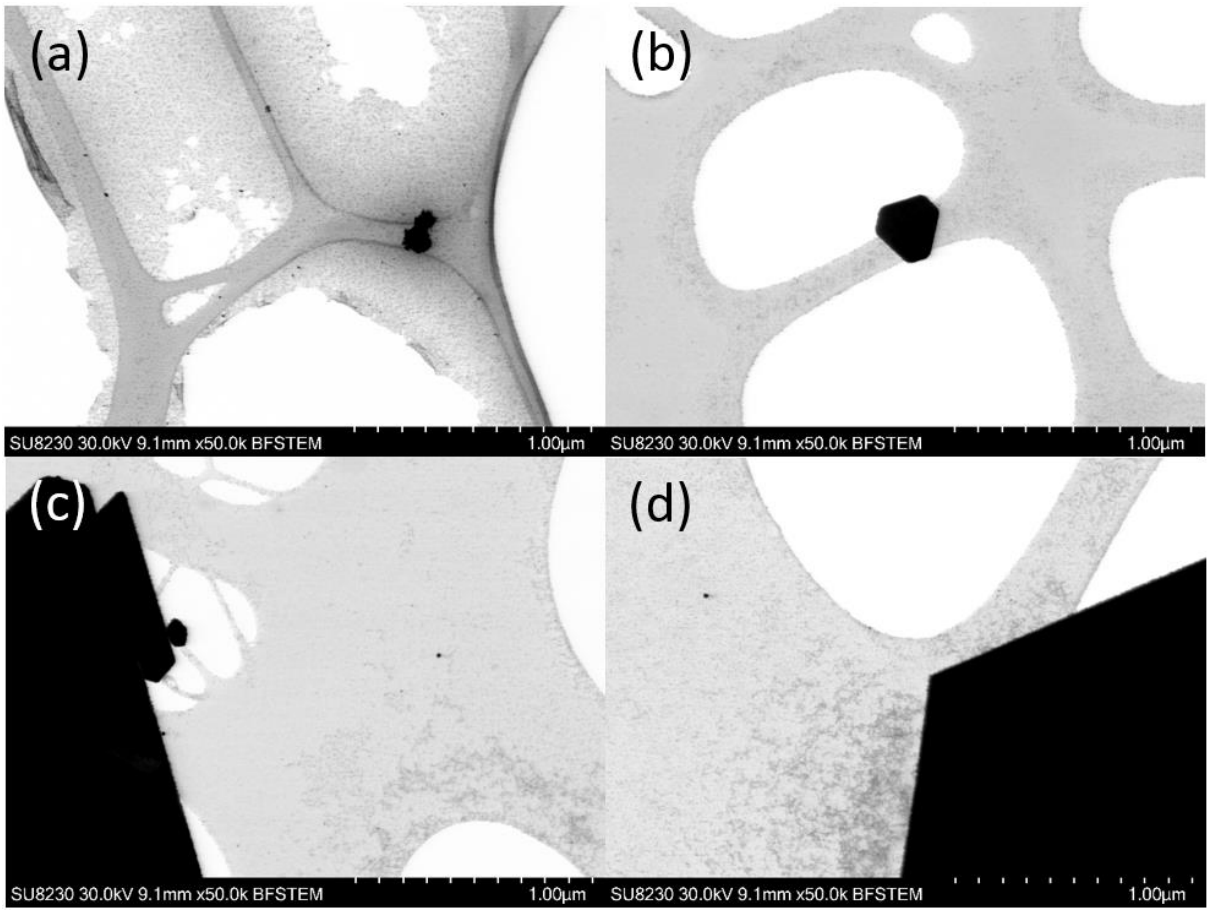

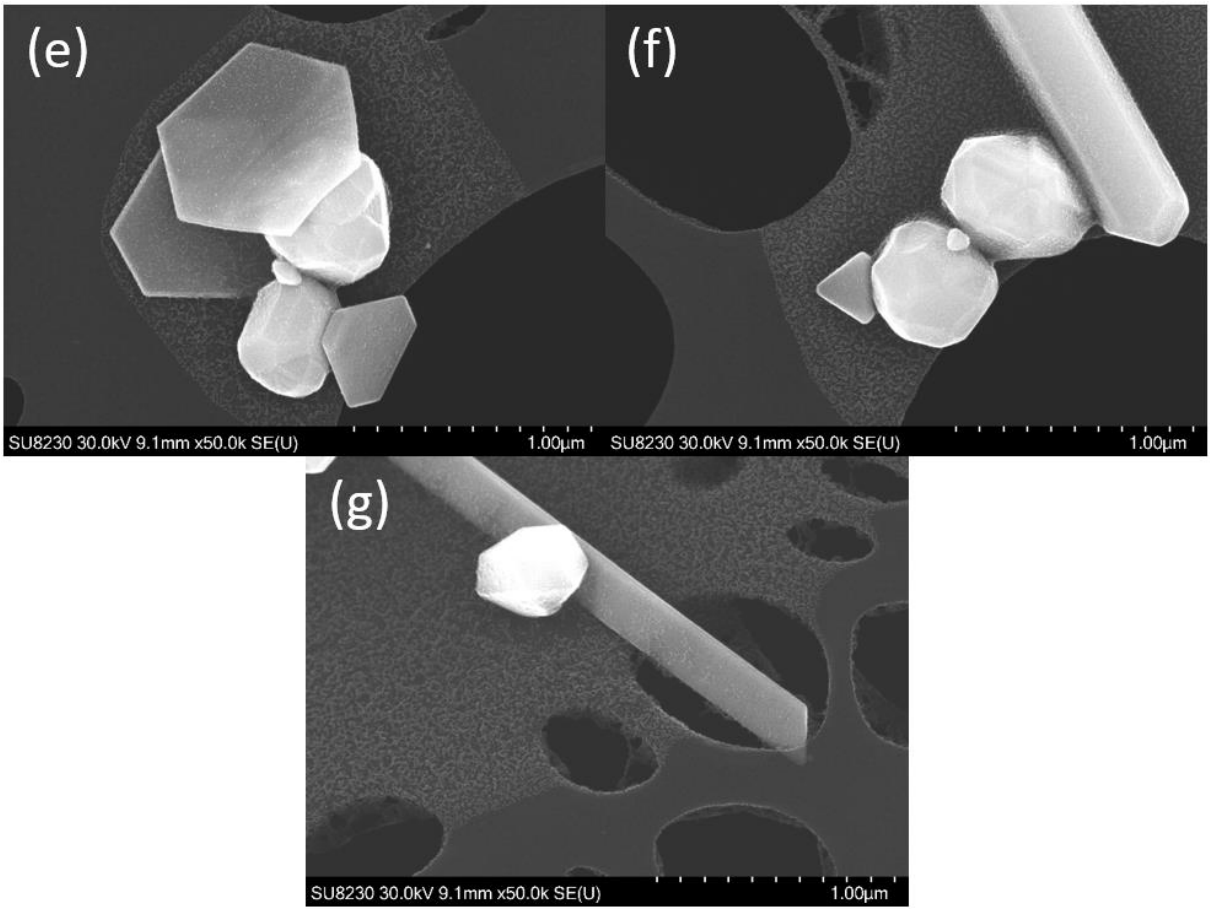

Figure A9.3-6: BF-STEM images of Au NPs formed from the reduction of $HAuCl_4 \cdot 3H_2O$ in EG with metal precursor/PVP10 = 1/50 at a suspension temperature of 128 ^{0} C (sample 1) (a), 131 ^{0} C (sample 2) (b), 134 ^{0} C (sample 3) (c) and 139 ^{0} C (sample 4) (d). In addition, SEM images of the Au NPs at a suspension temperature of 144 ^{0} C (sample 5) (e), 149 ^{0} C (sample 6) (f) and 154 ^{0} C (sample 7) (g).

9.4 Au NPs Produced via the Polyol Heat-Up Method

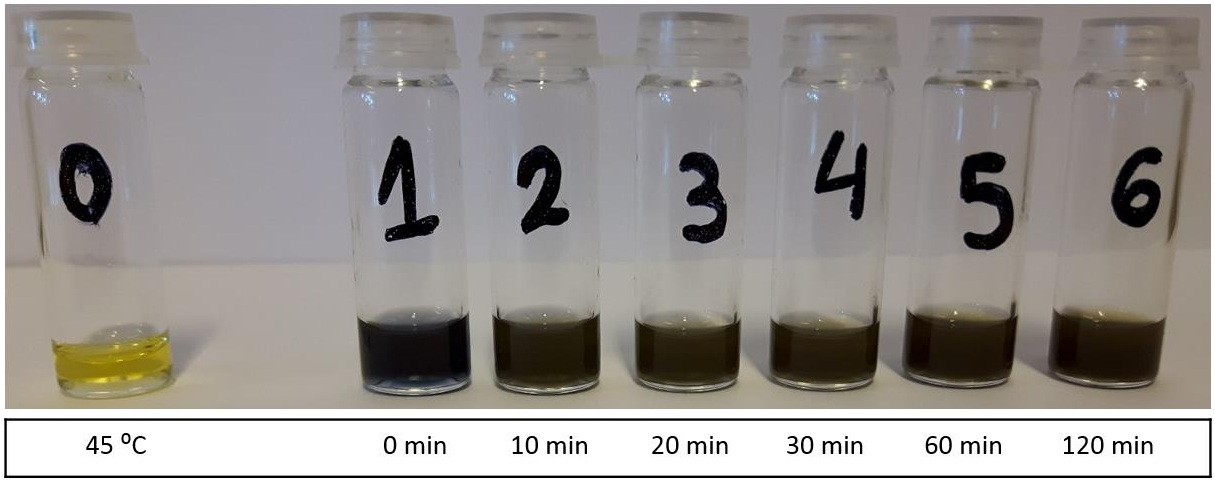

Figure A9.4-1: Color change in samples collected at selected time points in the range from 0 to 120 min during the Au NP formation obtained by reaction from $HAuCl_4 \cdot 3H_2O$ in 1,4-BD with metal precursor/PVP10 = 1/50 at 148 ^{0} C for 120 min.

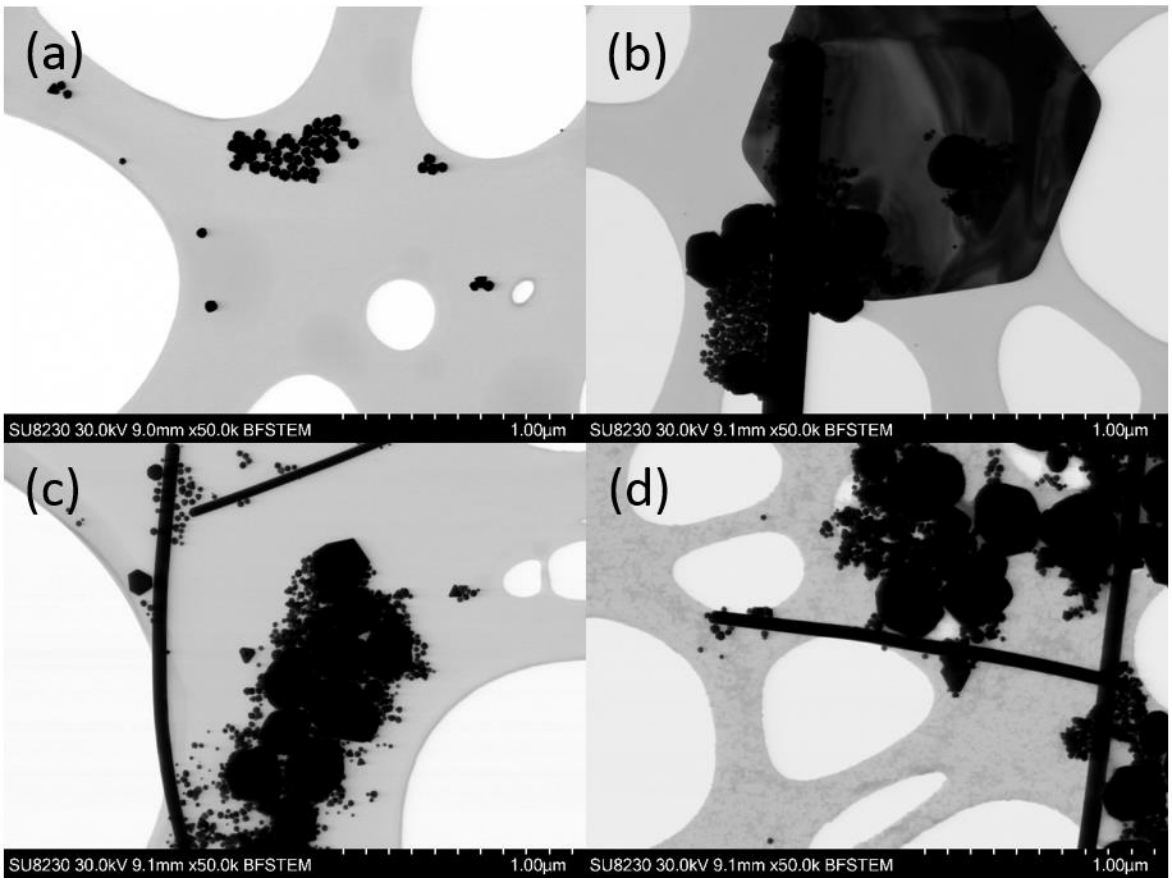

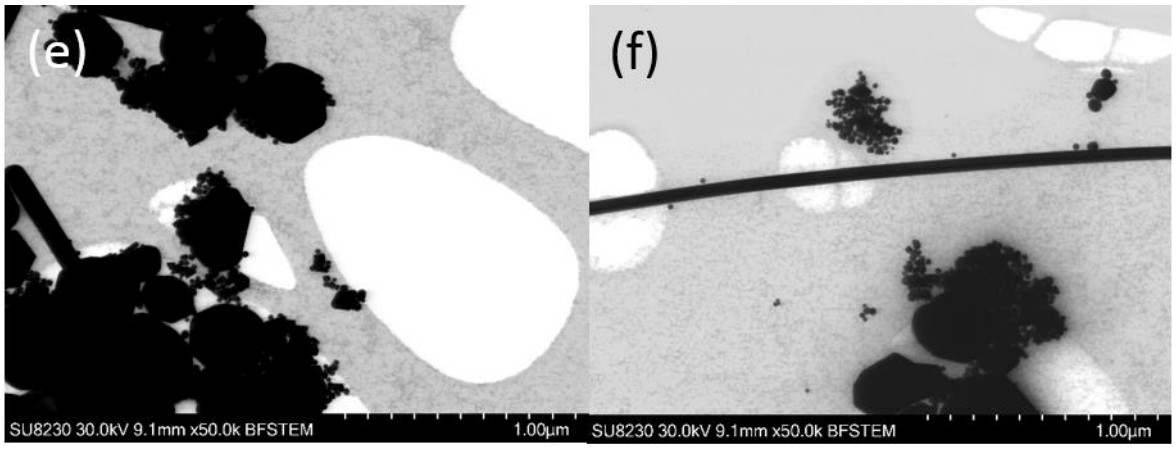

Figure A9.4-2: BF-STEM images of Au NPs formed from the reduction of $HAuCl_4 \cdot 3H_2O$ in 1,4-BD with metal precursor/PVP10 = 1/50 at 148 ^{0} C collected at time points of 0 min (sample 1) (a), 10 min (sample 2) (b), 20 min (sample 3) (c), 30 min (sample 4) (d), 60 min (sample 5) (e) and 120 min (sample 6) (f).

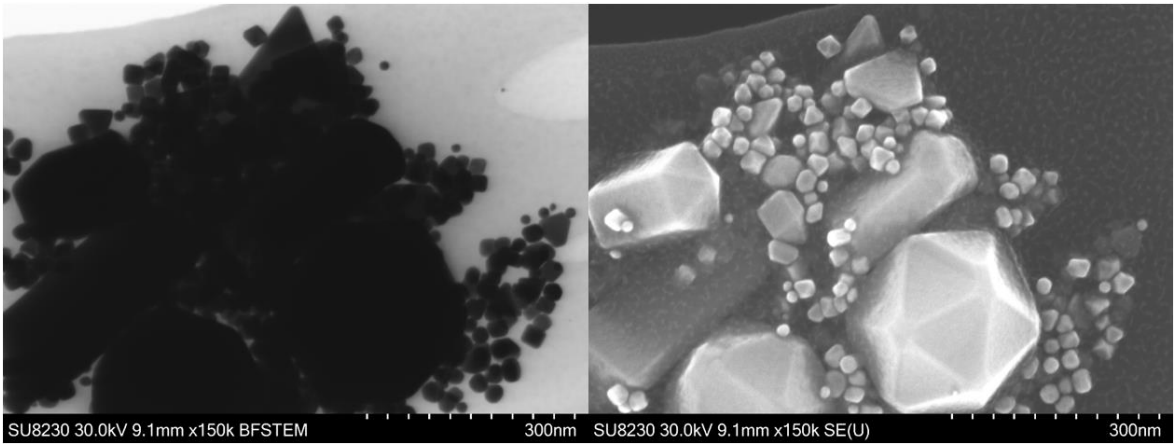

Figure A9.4-3: BF-STEM and SEM images of Au NPs formed from the reduction of $HAuCl_4 \cdot 3H_2O$ in 1,4-BD with metal precursor/PVP10 = 1/50 at 174 ^{0} C for 5 min.